

THÈSE DE DOCTORAT

De l'Université Pierre et Marie Curie en Sciences Physiques

ÉCOLE DOCTORALE : Physique et Chimie de Matériaux

présentée par

Dimitrii TANESE

**“Non-linear dynamics of one-dimensional
polaritons gases in semiconductor microcavities”**

“Dynamique non-linéaire de gaz de polaritons unidimensionnels
dans des microcavités semiconductrices”

Dirigée par Jacqueline BLOCH

Soutenance le 6 Décembre 2013 devant la jury composé de :

M. Jérôme TIGNON
M. Jean DALIBAR
M. Guillaume MALPUECH
M. Nicolas GRANDJEAN
M. Pavlos SAVVIDIS
Mme Jacqueline BLOCH

Président
Examineur
Examineur
Rapporteur
Rapporteur
Directrice de thèse

Contents

| | | |
|----------|--|-----------|
| 1 | Introduction to microcavity polaritons | 15 |
| 1.1 | QW excitons | 15 |
| 1.1.1 | Bulk excitons | 15 |
| 1.1.2 | Confinement of excitons in QWs | 17 |
| 1.1.3 | Light-matter interaction | 18 |
| 1.2 | Photons in microcavities | 20 |
| 1.2.1 | The Fabry-Perot cavity | 20 |
| 1.2.2 | Bragg mirrors | 23 |
| 1.2.3 | Bragg mirror microcavity | 24 |
| 1.3 | Microcavity polaritons | 25 |
| 1.3.1 | Weak and strong coupling | 25 |
| 1.3.2 | Quantum mechanical description of the polaritons states | 26 |
| 1.3.3 | Polaritons as interacting bosons | 29 |
| 2 | Samples and experimental setup | 35 |
| 2.1 | The samples | 35 |
| 2.1.1 | Optical characterization | 36 |
| 2.1.2 | One-dimensional microstructures | 39 |
| 2.2 | Experimental setup | 42 |
| 2.2.1 | The cryostat | 42 |
| 2.2.2 | Excitation | 43 |
| 2.2.3 | Detection | 44 |
| 2.2.4 | Time resolved measurements: the Streak camera | 44 |
| 3 | Polaritons propagation and interaction with defects | 47 |
| 3.1 | Introduction | 47 |
| 3.2 | Polariton propagation | 48 |
| 3.2.1 | Excitation techniques | 48 |
| 3.2.2 | Propagation under non resonant excitation | 50 |
| 3.3 | 1D propagation | |
| | against random disorder | 54 |
| 3.3.1 | Observation of backscattered polaritons | 54 |
| 3.3.2 | Theoretical interpretation: onset of parametric scattering | 58 |
| 3.4 | Conclusion | 63 |

| | | |
|----------|---|------------|
| 4 | Polaritons in a 1D modulated potentials | 65 |
| 4.1 | Introduction | 65 |
| 4.2 | Particles in a periodic potential: | |
| | general introduction | 65 |
| 4.2.1 | The Bloch Theorem | 66 |
| 4.2.2 | Weak potential and tight binding | 68 |
| 4.2.3 | Group velocity and effective mass | 69 |
| 4.3 | Motivations and state of the art | 70 |
| 4.3.1 | Localization of interacting bosons in a lattice | 71 |
| 4.3.2 | Polaritons in a periodic potential: the state of the art | 74 |
| 4.4 | Modulated wires | 75 |
| 4.4.1 | Engineering the potential landscape: modulation of a wire width | 75 |
| 4.4.2 | Characterization in the linear regime | 77 |
| 4.5 | Condensation regime and localization | |
| | under CW excitation | 85 |
| 4.5.1 | Condensation in localized gap states | 85 |
| 4.5.2 | The role of interactions: Bound Gap Solitons | 89 |
| 4.6 | Condensation and localization | |
| | under pulsed excitation | 92 |
| 4.6.1 | Localization and Bound Gap Solitons dynamic | 92 |
| 4.7 | Polaritons Bloch oscillations | 100 |
| 4.7.1 | Overview on Bloch oscillations | 100 |
| 4.7.2 | “Bloch oscillators” structures | 106 |
| 4.7.3 | Bloch oscillations under non resonant excitation: | |
| | acceleration induced by the reservoir | 109 |
| 4.8 | Polaritons in a quasiperiodic potential | 117 |
| 4.8.1 | Quasicrystals and the Fibonacci structures | 117 |
| 4.8.2 | Fibonacci wire | 120 |
| 4.8.3 | Dispersion, eigenstates and energy spectrum in a Fibonacci wire | 121 |
| 5 | A polariton interferometer | 125 |
| 5.1 | Introduction | 125 |
| 5.2 | Measuring and controlling the phase | 125 |
| 5.2.1 | Phase modulation | 127 |
| 5.2.2 | Interaction induced phase shift for polaritons | 127 |
| 5.3 | The interferometer structures | 129 |
| 5.3.1 | The 2 interferometers | 129 |
| 5.4 | Optical control of the polariton phase | 130 |
| 5.4.1 | Interference patterns in the Sagnac interferometer | 131 |
| 5.4.2 | The spontaneous build up of coherence | 132 |
| 5.4.3 | The optical-induced phase-shift | 133 |
| 5.5 | The complete Mach Zehnder interferometer: | |
| | the output modulation | 137 |
| 5.5.1 | Propagation inside the Mach Zehnder interferometer | 137 |

| | | |
|----------|---|------------|
| 5.5.2 | Control of the output intensity | 140 |
| 5.5.3 | MZI as a modulator | 143 |
| 5.6 | Polarization control | 146 |
| 5.6.1 | TE-TM splitting and pseudo-spin precession | 146 |
| 5.6.2 | Pseudospin and phase inside the MZI | 150 |
| 5.6.3 | Control of the output polarization | 153 |
| 5.7 | Towards Berry phase detection | 155 |
| 5.7.1 | The Berry's experiment | 155 |
| 5.7.2 | A polaritonic Berry phase | 156 |
| 5.7.3 | Experimental requirements and limitation | 158 |
| 5.8 | Conclusion | 159 |
| A | Transverse modes switching | 167 |
| B | Correction to the fit of the MZI interferometer transmission | 169 |
| C | Half-solitons | 171 |

Abstract

Microcavity polaritons are mixed light-matter quasi-particles, result of the strong coupling between a photon confined in a Fabry-Perot cavity and an exciton confined in a quantum well. Their non-linearities and their propagation velocity, near the speed of light, make them an ideal system for the study of the physics of gases of interacting bosons, at the edge between non-linear optics and the physics of cold atoms.

This PhD thesis is dedicated to the study one-dimensional polariton gases in semiconductor microcavities. Thanks to the control on the etching of the microstructures, a full engineering of the 1D potential has been obtained and several geometries have been investigated.

We have studied the propagation of polaritons inside photonic wires and we evidenced strong reduction of the backscattering against disorder driven by interparticle interactions.

Polariton condensation has been investigated in a 1-dimensional periodic potential. We have shown how repulsive interactions create localized states inside the energy gap. The nature of these states depends on the relative strength between interparticle interactions and the interactions with the excitonic reservoir. In a time resolved-experiment we have shown the dynamical transition from a regime dominated by interactions with the reservoir to a regime where self-interactions give rise to the formation of gap solitons.

Additionally, the potential induced by the interactions with the reservoir allowed us to combine an energy gradient with the periodic lattice. In this configuration, we have observed polaritons Bloch oscillations. Thanks to the potential engineering, we have also implemented a Fibonacci quasi-periodic potential. In this configuration, we have observed the fractal character of the polariton spectrum.

Finally, we present a polariton interferometer. The optical control of the phase of the polariton flow allows controlling the intensity and the polarization of the beam transmitted through the device. These results reveal the potential of polaritonic microstructures in the implementation of an integrated platform to create and control coherent polariton fluxes.

Résumé

Les polaritons des microcavité sont des quasi-particules mixtes lumière-matière, issue du couplage fort entre le mode optique d'une cavité Fabry-Pérot et un exciton confiné dans un puits quantique. Leurs propriétés d'interaction et leur vitesse proche de la vitesse de la lumière, font des polaritons un système idéal pour l'étude de la physique des gaz de bosons en interaction, à la frontière entre l'optique non-linéaire et la physique des condensats d'atomes froids.

Cette thèse est consacrée à l'étude de gaz de polaritons dans des microcavités semiconductrices unidimensionnelles. Grâce au contrôle de la gravure de microstructures, plusieurs géométries ont été étudiées et une ingénierie du potentiel 1D a été possible.

Nous avons analysé la propagation des condensats de polaritons dans des fils photoniques et nous avons mis en évidence une forte réduction de la diffusion par le désordre due aux interactions entre ces quasi-particules.

La condensation dans un potentiel périodique unidimensionnel a également été explorée. Nous avons montré comment les interactions répulsives génèrent des états localisés dans la bande d'énergies interdites. La nature de ces états dépend de la force des interactions entre particules par rapport à celle des interactions avec le réservoir excitonique. Dans une expérience dynamique nous avons montré la transition d'un régime dominé par le réservoir à un régime où se forment des solitons de gap. De plus, le profil du potentiel induit par les interactions avec le réservoir nous a permis de superposer un gradient d'énergie au réseau périodique. Dans cette configuration, nous avons mis en évidence les oscillations de Bloch de polaritons.

Grâce à l'ingénierie du potentiel, nous avons aussi réalisé un potentiel quasi-périodique de type Fibonacci au sein duquel nous avons observé le caractère fractal du spectre polaritonique.

Enfin, nous présentons un interféromètre à polaritons. Le contrôle optique de la phase d'un flux de particules nous permet de maîtriser l'intensité et la polarisation du faisceau à la sortie de l'interféromètre. L'ensemble de ces résultats montrent le potentiel des microstructures à polaritons pour réaliser une plateforme tout intégrée dans lesquels sont gérés et manipulés des flux cohérents de polaritons.

Introduction

Confinement of light and particles played a crucial role in modern physics, and the control on such confinement often provides an additional manipulation tool for experimentalists to control and manipulate physical systems. A remarkable example is provided both by the solid state physics and by optics, in particular when coming to semiconductors.

The progress in the epitaxial growth allows nowadays the control over semiconductor structures up to the single atomic layer. This gives the possibility to confine the electronic wavefunction of electrons down to two (quantum well), one (quantum wire) or even zero (Quantum dots) dimensions. Light can also be confined down to small dimensions (typically of the order of the wavelength), inside cavities of different shapes (planar cavity, micropillars microdisc, photonic crystal cavity), forcing photons to undergoes up to hundreds of millions of reflections before escaping. This possibility of confining both light and electronic excitations made semiconductors an ideal system to study light matter-interaction.

Light matter interaction is not an intrinsic characteristic of the material used but can be artificially controlled. In 1964 Purcell proposed to alter the spontaneous rate of a dipole by modifying its electromagnetic environment[1]. This general idea has been extensively exploited in the optical range. For instance, the Purcell effect has been applied to study single quantum dots embedded in microcavities [2] and allows producing bright sources of single and indistinguishable photons[3], possible building block for quantum cryptography and quantum computation[4].

If the light matter coupling is strong enough, the emission of light can become reversible. Indeed the photon can be reabsorbed and re-emitted several times before escaping the cavity, thus undergoing several Rabi Oscillations. This regime is known as strong coupling and has been first observed for a set of atoms in a high finesse microcavity [5, 6].

In 1992, C. Weisbusch obtained the strong coupling regime between excitons confined in a quantum well(QW) and photons confined in a microcavity[7]. The reflectivity spectra revealed the formation of new eigenstates named cavity polaritons, mixed light-matter quasiparticles. Since then, the research on cavity polaritons has seen a fast development, taking advantage of the peculiarities of such quasi-particles.

Soon after their discovery, it has been foreseen that under a critical density, polaritons obey bosonic statistics and due to their low effective mass, they are ideal candidates to study bosonic effects in solid state. This bosonic behaviours has been first evidenced in the beginning of 2000, by the generation of parametric oscillations and amplification under resonant excitation [8, 9, 10].

Under non resonant excitation, the bosonic stimulation of the relaxation towards a particular state, together with the spontaneous buildup of coherence, was proposed by

Imamoglu in 1996[11]: the effect, initially named *boser*, is now frequently addressed as *polariton lasing* or *polariton condensation*.

Nowadays, polariton condensates has been observed in several semiconductor systems, CdTe [12] , GaAs [13, 14, 15], , GaN [16] and ZnO [17], from liquid Helium temperature up to room temperature.

Furthermore, polaritons revealed themselves as an ideal system to investigate the hydrodynamic of quantum fluids[18]. The optical control of their momentum, density, phase and spin allowed the observation of superfluid motion[19] and the generation of topological defect like solitons[20, 21, 22] and vortices[23, 24] , approaching the physics investigated in the field of cold atoms. Moreover, their intrinsically out of equilibrium nature[25, 11], due to the energy losses via photon escaping, provides an additional feature, that marks the difference of such system from a more traditional atomic condensate.

They also present enhanced non-linearities which are responsible for the observation of four-wave mixing processes[26], and bistability or and multistability regime[27]. Promising configuration for optoelectronic devices have also been implemented, such as switches[28], transistors[29, 30], resonant tunneling diodes[31], and numerous proposals have been formulated in this direction[32, 33, 34, 35].

In the context of control of polaritons and manipulation of their flow, the confinement of polaritons in lower dimensions present a powerful tool.

In the recent years at the Laboratoire de Photonique et Nanostructure, low dimension polaritons have been widely investigated, thanks to a state-of-the-art fabrication technique. Condensation of 0D polaritons was demonstrated in single micropillar by Daniele Bajoni [15], together with clear effects of non linearities in squared or coupled pillars in the works of Lydie Ferrier and Marco Abbarchi [36, 37]. Polaritons in one-dimension have been studied by the previous PhD of the group, Esther Wertz ,who demonstrated polariton condensation and coherent propagation in wire microcavities[38, 39].

In the present thesis we used these high quality microstructures developped at LPN, to investigate the physical properties of polaritons in various one-dimensional geometries. Engineering the shape of 1D cavities, we address a large variety of fundamental physical problems, ranging from polariton scattering by disorder, condensation in a periodic potential, up to the fractal energy spectrum of polaritons in a quasi-periodic structure. Finally we describe a new polariton device, where the phase of a coherent polariton flow is controlled optically within interferometers.

The structure of the present manuscript is the following.

A general introduction on quantum well excitons and cavity photons is provided in the **first chapter** together with the description of the basic properties of cavity polaritons.

The **second chapter** is dedicated to the description of the structure of the cavity samples used in the different experiments described in the manuscript. Their optical characterization is used to illustrate some essential properties of cavity polaritons. In the second part of the chapter we give a brief presentation of the setup used in our experiments.

In the **third chapter** polariton propagation in one-dimensional structures is addressed. We first give an overview of the state of the art experiments on polariton propagation. We particularly focus on the case of non-resonant excitation and on the results obtained at LPN, just before my arrival in the group, by Esther Wertz in wire microcavities. We then investigate the scattering of a polariton flow with disorder naturally present along a microwire, by analyzing the signal corresponding to backscattered polaritons. A quenching of the backscattering is observed when increasing the polariton density. In collaboration with the group of Guillaume Malpuech in Clermont-Ferrand, we propose an interpretation of this effect based on parametric processes.

The overall subject of the **fourth chapter** is the study of polaritons in modulated potential. The first part is dedicated to polaritons in periodic potentials, obtained using a wire microcavity with a periodically modulated lateral dimension. Here the modified polariton dispersion, in which forbidden energy gaps appear, will allow studying several effects of localization. With the theoretical support from the group of G. Malpuech, we investigate the role of the interactions between polaritons and with excitons in the reservoir, and analyze the nature of the localized states in terms of defect states or bound gap solitons.

In the second part of the chapter, we study polaritons in the presence of a periodic modulation combined with an energy gradient obtained either by adequate shaping of the 1D microcavity profile or exploiting the blueshift induced by the reservoir. The observation of Wannier-Stark ladders and Bloch oscillations will be discussed.

The last part of the fourth chapter is devoted to quasi-periodic structures. A potential landscape reproducing the Fibonacci sequence is expected to give rise to a fractal energy spectrum. We will show evidences of the fractal structure of the polariton spectrum inside such a potential and a direct visualization of the corresponding wave-functions. This work is the result of a collaboration with Eric Akkerman and Evgeni Gurevich from the Technion Israel Institute of Technology, in Haifa, Israel.

The **fifth chapter** presents the implementation of polariton interferometers and their control by optical means. Such structures are used to demonstrate the possibility of inducing a phase-shift of a polariton flow via the interaction with an excitonic population. Such effect is first demonstrated in a Sagnac interferometer and then applied to a Mach-Zehnder interferometer in order to control either the intensity or the polarization of the outgoing beam.

In the conclusion, we give an overview of the results obtained within this work and present all the perspectives that are now envisaged using microstructured microcavities operating in the strong coupling regime.

Chapter 1

Introduction to microcavity polaritons

In this first chapter we will introduce *microcavity polaritons*, mixed exciton-photon quasi-particles. We describe at first their two building blocks: the exciton confined in a Quantum Well (QW) and the photon in a microcavity. Then we illustrate the concept of strong coupling and the polaritons as resulting eigenstates of the system. Their main features will be introduced, especially focusing on their bosonic character and on the interaction properties they present.

1.1 QW excitons

Semiconductors are key material for today's technology. The main characteristic that makes them so interesting is that their band structure presents an energy gap between the last completely occupied band and the first empty one. The ground state of the system is thus characterized by a full electronic band named *valence band* and an empty one, the *conduction band*.

In semiconductors, the width of this energy gap is such that it can be easily overtaken by applying a voltage or by optical excitation. *Electrons* can be promoted to the conduction bands, and the resulting lack of charges in the valence band is represented by *holes*.

In this first section of the chapter we will discuss the first excited state of a semiconductor. In the absence of Coulomb interactions, such first excited state is given by a single electron at the bottom of the conduction band and a single hole at the top of the valence band. But the interaction between the excited electron and all the remaining charges in the valence band results in a picture in which electrons and holes undergo Coulomb attraction: the ground state of the system is at a lower energy and consists in a bound state named *exciton*.

1.1.1 Bulk excitons

In a bulk semiconductor, each electronic band can be approximated by a parabola in the proximity of its maximum or minimum. The electrons in such band can be considered as a free particle with an effective mass directly related to the curvature of the parabola[40]. We consider a direct gap semiconductor, in which the bottom and top of respectively conduction and valence

band correspond to zero momentum $k = 0$. We also choose to note both the effective mass for electron m_e^* and hole m_h^* positive. Their dispersion relation can thus be written as:

$$E_c(\mathbf{k}) = E_g + \frac{\hbar^2 \mathbf{k}^2}{2m_e^*} \quad (1.1)$$

$$E_v(\mathbf{k}) = -\frac{\hbar^2 \mathbf{k}^2}{2m_h^*} \quad (1.2)$$

where E_g is the width of the energy gap and the extreme of the valence band is conventionally set to 0.

As discussed more in detail in 4.2.1, in each band electrons and holes can propagate and their wavefunction can be written respectively in the Bloch form [41] as $\phi_e(\vec{r}) = e^{i\vec{k} \cdot \vec{r}} u_e(\vec{r})$ and $\phi_h(\vec{r}) = e^{i\vec{k} \cdot \vec{r}} u_h(\vec{r})$. The functions u 's are invariant for a translation of a crystal period.

Considering light excitation, in which a photon arrives with energy higher than the bandgap, there's a finite probability of absorption and creation of an electron-hole pair. For conservation of energy and momentum in the absorption process, electron and hole will have opposite momenta, since the photon wavevector can be neglected. If the incident photon has an energy lower than the gap E_g , we observe discrete resonances inside the gap that corresponds to electron hole pair interacting via Coulomb attraction. These bound electrons-holes pairs are named *excitons* and represent the eigenstates of the following hamiltonian that describes the system:

$$H\Psi(r_e, r_h) = \left[\frac{p_e^2}{2m_e} + E_g + \frac{p_h^2}{2m_h^*} - \frac{e^2}{\epsilon |r_e - r_h|} \right] \Psi(r_e, r_h) = E\Psi(r_e, r_h) \quad (1.3)$$

where r_e, r_h and p_e, p_h are respectively the position and momentum vector of electron and hole in the crystal and the value of the dielectric constant ϵ contains the screening effect of the Coulomb interaction due to all the other electrons in the valence band. The eigenstates can be written in the form:

$$\Psi(\vec{r}_e, \vec{r}_h) = u_h^*(\vec{r}_h) u_e(\vec{r}_e) \Psi_{\vec{K}}(\vec{r}, \vec{R}) \quad (1.4)$$

The function $\Psi_{\vec{K}}(\vec{r}, \vec{R})$ is the envelope function, in which $\vec{r} = \vec{r}_e - \vec{r}_h$ and $\vec{R} = \frac{\vec{r}_e m_e^* + \vec{r}_h m_h^*}{m_e^* + m_h^*}$ represent the internal and the center of mass motion of the exciton. Considering \vec{K} the wavevector of the center of mass, one can show that $\Psi_{\vec{K}} = e^{i\vec{K} \cdot \vec{R}} \phi(\vec{r})$ where ϕ is the solution of the equation of an hydrogen-like atom.

Thus the eigenvalues of the exciton are the followings:

$$E = \frac{\hbar^2 K^2}{2M} + E_g - E_b^n \quad (1.5)$$

with E_b^n the exciton binding energy, that depends on the quantum number n following the relation:

$$E_b^n = \frac{R_0}{n^2} \quad (1.6)$$

where $R_0 = \frac{\mu e^2}{2\epsilon^2 \hbar^2}$ is called effective Rydberg constant.

The lowest energy exciton wavefunction is the $n = 1$ ($1s$) state, that reads:

$$\Phi(r) = \frac{1}{\sqrt{\pi a_B}} e^{-r/a_B} \quad (1.7)$$

with $a_B = \frac{\hbar^2 \epsilon}{\mu e^2}$ the exciton Bohr radius, that characterizes the spatial extension of the exciton.

Typically excitons are studied in two limit cases; in ionic crystals they are characterized by strong attraction, and the electrons and holes are strongly coupled and localized in the same crystal cell (Frenkel excitons[42]); in most of the semiconductors the interaction is well screened and spread over several crystal cells (Wannier-Mott excitons[43]). In GaAs, for example, the heavy hole exciton, the one formed by an electron and a heavy hole, has a Bohr radius a_B of around 11 nm and a binding energy of 4 meV. Due to such a low binding energy they require cryogenic temperatures to be observed.

1.1.2 Confinement of excitons in QWs

Confinement strongly modifies the energy configuration of excitons and has also an important impact on the light-matter interactions [44]. Excitons can be confined along one (quantum well), two (quantum wire) or three (quantum dot) dimensions. We discuss the case of quantum wells, where excitons are free to move in a plane.

Such confining structures are obtained by inserting a thin layer (typically few nm) of a semiconductor between two thicker layers of another semiconductor of larger band gap. The resulting potential profile along the growth direction z is schematically represented in figure 1.1, while the potential is constant along x and y directions.

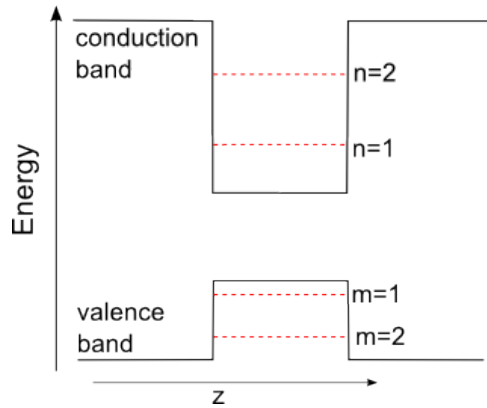


Figure 1.1: Schematic of the unidimensional confining potential created by a QW structure. Red dashed lines represent the energy of confined levels for electron and holes.

Neglecting the Coulomb interaction, the resulting wavefunctions for electrons and holes are plane wave in the x - y plane, of wavevector $k_{||}$, multiplied by the envelope functions $\chi(z)$, labelled with the index n and m , that label the confined state in the z direction [45]. Considering the interaction, the wavefunction of the bound electron-hole pair can be rewritten as:

$$\Psi(\vec{r}_e, \vec{r}_h) = \frac{C}{\sqrt{S}} e^{i\vec{K}_{||} \cdot \vec{R}_{||}} \chi_e^n(z_e) \chi_h^m(z_h) \phi(\vec{\rho}) \quad (1.8)$$

with $\vec{\rho} = \vec{r}_e - \vec{r}_h$ is the in-plane relative position, and $\vec{R}_{||}$ and $\vec{K}_{||}$ respectively the position and the wavevector of the center of mass.

The eigenenergies of the resulting excitons are:

$$E_{exc}^{2D} = E_g + E_n^c + E_m^h + \frac{\hbar^2 K_{||}^2}{2(m_{e,||}^* + m_{h,||}^*)} - \frac{R^*}{(n - \frac{1}{2})^2} \quad (1.9)$$

where $E_n^c + E_m^h$ are the confinement energies of the electron and hole in the quantum well.

To $n = 1$ corresponds the following solution for the hydrogenoid wavefunction: $\phi(\rho) = e^{-\sqrt{\rho^2 + (z_e^2 - z_h^2)}/a_B^*}$ with a_B^* the Bohr radius for the QW exciton. Its value is decreased of a factor 2 with respect to the bulk case $a_B^* = a_B/2$, and for a GaAs QW is around 5 nm. The confinement increases the overlap between the particle wavefunctions with respect to the bulk, and thus the exciton binding energy is strongly enhanced.

Excitons as composite bosons

The exciton, made of two fermionic quasi-particles, behaves as a boson for low particle density. Indeed the creation of an exciton results in a low occupation of each fermionic state of electrons and holes. Consequently, a large number of excitons can be created without feeling the effect of the Pauli exclusion principle. Nevertheless, when strongly increasing the excitations in the system two effects must be taken into account: the screening of the Coulombian interaction and, mainly, the effect of electronic phase space occupation [46, 47]. Both brings to the destruction of the excitonic state and to the generation of electron hole plasma.

An indication of the density corresponding to this transition can be given by estimating the behaviour of the commutator of the operator \hat{B}_k , representing the annihilation of an exciton [46, 47]. Its average value can be written as $\langle [\hat{B}_k, \hat{B}_k^\dagger] \rangle \approx 1 - O(n \cdot (a_B^*)^2)$, with n exciton density. The operator \hat{B}_k behaves as a bosonic operator until the particle density verifies $n \ll 1/(a_B^*)^2$. This limit is known as Mott density. For GaAs QWs this value corresponds approximately to a density of 10^{11} excitons per cm^2 [48, 49].

1.1.3 Light-matter interaction

We have already mentioned that the promotion of an electron from valence to conduction band or viceversa can happen in a radiative process via the absorption or emission of a photon. The process has some selection rules and in the following lines we will introduce the conserved quantity in the transition, with a specific attention to the 2D confined exciton case.

In the dipolar approximation, the Hamiltonian of the exciton photon coupling becomes:

$$H \approx -\frac{e}{m_0} \vec{A} \cdot \vec{p} \quad (1.10)$$

with \vec{A} the vector potential and \vec{p} the momentum operator of an electron of charge $-e$ and mass m_0 . The absorption of a photon is proportional to the matrix element $\langle \vec{K} | \vec{p} \cdot \vec{A} | 0 \rangle$ where $|0\rangle$ is the ground state and $|\vec{K}\rangle$ the excitonic state.

The vector potential has the form $\vec{A} = \vec{\epsilon} A e^{i\vec{q} \cdot \vec{r}}$. Therefore, we obtain:

$$\langle \vec{K} | \vec{p} \cdot \vec{A} | 0 \rangle = \sum_{\vec{k}_e, \vec{k}_h} \langle \vec{K} | \vec{k}_e, \vec{k}_h \rangle \langle \vec{k}_e, \vec{k}_h | \vec{p} \cdot \vec{A} | 0 \rangle \propto \delta(\vec{K} - \vec{q}_{||}) \phi(0) | \langle u_c | \vec{\epsilon} \cdot \vec{p} | u_v \rangle | \left| \int \xi_h^m(z) \xi_e^{n*} dz \right| \quad (1.11)$$

where $\phi(0) = \sum_{\vec{k}} \langle \vec{K} | \vec{k}, \vec{K} - \vec{k} \rangle$, the function u_c , u_v , Ψ , ξ_h and ξ_e are the envelope function already defined above, and where we considered $q_z z \ll 1$ on the spatial extension of the functions ξ .

According to equation 1.11, the coupling of the exciton with the electromagnetic field is determined by the matrix element $\langle u_c | \vec{p} | u_v \rangle$ and by overlap integral $\int \xi_h(z) \xi_e^* dz$.

From the previous expression, the following transition rules can be extracted:

- the in-plane wavevector must be conserved in the transition, that means that the exciton will couple only with photon of the same in-plane wavevector $q_{||}$. But all the values of k_z are possible. This condition, combined with the energy conservation, defines the light cone inside which an exciton can couple with the electromagnetic field: $|\vec{K}| \leq \frac{n_e E_{exc}^{2D}}{hc}$
- For an infinite QW the overlap integral is not zero only in the case of $m = n$, while for a finite but symmetric quantum well, the transition rule imposes simply that m and n have the same parity.
- angular momentum must be conserved in the transition ($\langle u_c | \vec{\epsilon} \cdot \vec{p} | u_v \rangle \neq 0$) and this condition imposes some restriction on the polarization: the angular momentum of the exciton couple is $J = s_e + s_h$ with $s_e = \pm 1/2$ and $s_h = \pm 3/2$. Only the exciton with $J = \pm 1$ are coupled with light. The others are named dark excitons.
- The energy also must be conserved in the transition. The energy of a photon is given by $\frac{\hbar c k}{n}$. This means that excitons with $|K_{||}| > k_{rad}$, where k_{rad} satisfies $\frac{\hbar c k_{rad}}{n} = E_X(K_{||} = 0) + \frac{\hbar^2 K^2}{2M}$, are states not coupled with light.
- An additional selection rules appears when considering also the spin degree of freedom. The angular momentum of the exciton is given by $J = s_e + s_h$. Considering heavy hole excitons, $s_e = \pm 1/2$ and $s_h = \pm 3/2$ are the spin of electron and holes and so for the exciton $J = \pm 1$ or $J = \pm 2$. Since the projection of the angular momentum of a photon can be ± 1 , the state with $J = 2$ they are not coupled to light and are named "dark excitons" [50].

We can define a variable called oscillator strength f , that characterizes the intensity of the coupling to light, given by [51]:

$$\frac{f}{A} = \frac{2}{m_0 E} |\phi(0)|^2 |\langle u_c | \vec{\epsilon} \cdot \vec{p} | u_v \rangle|^2 \langle \chi_{n,e} | \chi_{m,h} \rangle \quad (1.12)$$

The oscillator strength results directly proportional to the absorption probability of a photon going through a QW.

1.2 Photons in microcavities

In this section we will describe the confinement of a photon inside a microcavity structure. The requirement of such a cavity is to have, at the same time, a small effective volume, in order to have a higher electric field created by each single photon, and a long lifetime of the photons inside the cavity, in order to minimize the losses due to the coupling to the free space modes. This conditions can be translated in the requirement of a high reflectivity mirror structure in the spectral range of emission of the QW. For such a purpose, metallic mirrors are not good candidate, because the high absorption coefficient of metals brings to a reflectivity smaller than 95% in the infrared spectral range in which we are interested in.

On the contrary, interferential semiconductor mirrors have many advantages: at first they can be epitaxially grown during the same process and with the same mechanism than the quantum wells and then they have losses due to absorption that are negligible, and this brings to a reflectance coefficient near 100 %.

In order to explain the principle and introduce the essential parameters of a Bragg mirrors cavity, we will first discuss the simple case of a Fabry-Perot cavity. Then we focus on interference phenomena on which the Bragg mirrors are based on and then conclude with the description of a complete semiconductor microcavity.

1.2.1 The Fabry-Perot cavity

In fig. 1.2 we report the scheme of a Fabry Perot resonator. Let's consider two parallel mirrors described by their values of reflectivity and transmission coefficient, respectively, r_1, r_2 and t_1, t_2 .

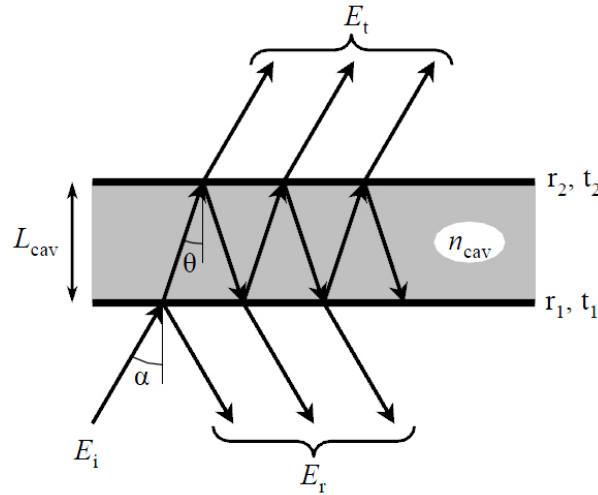


Figure 1.2: Fabry Perot cavity's scheme with metallic mirrors. Figure extracted from [52]

They define a cavity of width L_{cav} , with n_{cav} its refractive index. For instance, we will consider r_1, r_2, t_1, t_2 , complex numbers and $n_{cav} > n_{air}$. Then we consider a progressive

monochromatic plane wave, incident on the surface of the cavity with an angle α . The angle of propagation inside the cavity will be: $n_{air}\sin(\alpha) = n_{cav}\sin(\theta) \Rightarrow \theta = \sin^{-1}\left(\frac{n_{air}}{n_{cav}}\sin(\alpha)\right)$.

We take the incident wave with a transverse polarisation (TE), that means that the electric field is perpendicular to the plane of the figure 1.2. In a single round trip inside the cavity, the wave gains a phase of $\phi = 2\pi(n_{cav}L_{cav}\cos\theta)/\lambda$.

The transmitted wave will be the sum of all the waves reflected and transmitted by the mirrors. We will note the incident electric field with the complex variable E_i and the transmitted one with E_t and then we can write:

$$E_t = E_it_1e^{i\phi}t_2 + E_it_1e^{i\phi}\left(r_2e^{i\phi}r_1e^{i\phi}\right)\dots E_it_1e^{i\phi}\left(r_2e^{i\phi}r_1e^{i\phi}\right)^n t_2 + \dots \Rightarrow E_t = E_it_1t_2e^{i\phi}\left(\frac{1}{1 - r_1r_2e^{2i\phi}}\right) \quad (1.13)$$

If one notes the total phase shift $\phi_{tot} = 2\phi$, the transmission coefficient becomes:

$$T = \left|\frac{E_t}{E_i}\right|^2 = \frac{(t_1t_2)^2}{1 + (r_1r_2)^2 - 2r_1r_2\cos(\phi_{tot})} \quad (1.14)$$

$$\phi_{tot} = 2\phi = 2\frac{E}{\hbar c}n_{cav}L_{cav}\cos\theta \quad (1.15)$$

The reflectance coefficient R will be $R = 1 - T$, since there's no absorption in the mirrors or diffusion at the interface. In fig. 1.3 we report an example of the values of R as a function of the phase shift in a round trip in the cavity.

Some considerations can be done. For some given values of ϕ_{tot} , a constructive interference

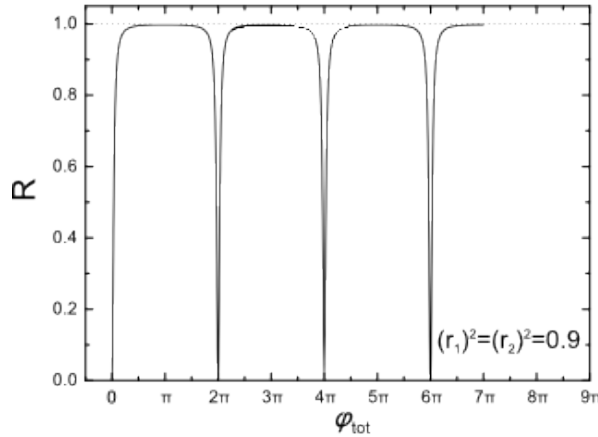


Figure 1.3: Reflectance of a Fabry perot cavity as a function of a phaseshift in a round trip of the cavity. Figure extracted from [53].

phenomenum results into an abrupt decrease of the reflectivity: the value is almost zero for $\phi_{tot} = S \times 2\pi$. Each integer value of S determines a particular cavity mode. In the simpler case of normal incidence, the mode are given by the relation $n_{cav}L_{cav} = S\lambda/2$. In the case of $S = 1$ the cavity is a $\lambda/2$ cavity, the smallest cavity at a given resonance.

In a more general way, we can consider that each reflexion brings to a phase shift, such that the reflectivity coefficient r becomes complex by a multiplication by a phase shift factor $r \Rightarrow re^{i\phi}$, where obviously the phase shift is energy dependent. In this case, the resonance conditions reads:

$$\phi_{tot}(E) = 2\phi(E) + \phi_1(E) + \phi_2(E) = S \times 2\pi \quad (1.16)$$

We will use these equations later, discussing the dielectric mirror structure.

In the case of normal incidence we can define two quantities, ΔE and δE , respectively the interval between two modes, named free spectral range, and the full width at half-maximum FWHM of the reflectance minimum. For negligible losses in the cavity ($r_1 r_2 = 1 - \epsilon$ with $\epsilon \ll 1$), they are given by:

$$\Delta E = \frac{\pi \hbar c}{n_{cav} L_{cav}} \quad \delta E = \frac{\hbar c}{n_{cav} L_{cav}} \frac{1 - r_1 r_2}{\sqrt{r_1 r_2}} \quad (1.17)$$

Two interesting quantity useful to characterize the optical quality of a cavity are the *finesse* F and the *quality factor* Q , defined by:

$$F = \frac{\Delta E}{\delta E} = \frac{\pi \sqrt{r_1 r_2}}{1 - r_1 r_2} \quad (1.18)$$

$$Q = \frac{E}{\delta E} = \frac{s\pi \sqrt{r_1 r_2}}{1 - r_1 r_2} \quad (1.19)$$

The quantity $\frac{\hbar Q}{E}$ gives the cavity photon lifetime τ_{cav} , and similarly, the finesse F is the number of reflection that the photon makes before escaping the cavity.

The finesse parameter is simply related to the characteristic of the mirrors, while the quality factor is proportional to the cavity width and depends on S , that means that it depends on the cavity mode we are considering.

We now take an incident plane wave with an angle of incidence $\alpha \neq 0$ and let us represents its wavevector as $\vec{k} = (k_{||}, k_z)$. Passing from outside (n_{air}) to inside (n_{cav}), the parallel component will be constant while k_z will change. We know that $k_{cav} = n_{cav} k_{air} = \frac{n_{cav} E}{\hbar c}$ and so, imposing the resonance condition for the mode S , we get:

$$\phi_{tot} = S\pi \quad (1.20)$$

$$2k_z cav = L_{cav} = S\pi \quad (1.21)$$

$$L_{cav} \sqrt{\left(\frac{n_{cav} E}{\hbar c}\right)^2 - k_{||}^2} = S\pi \quad (1.22)$$

and finally we get, in the approximation of small incidence angle ($k_{||} \ll k_z$)

$$E(k_{||}) = \sqrt{E_S^2 + \left(\frac{\hbar c}{n_{cav}} k_{||}\right)^2} \approx E_S + \frac{\hbar^2 k_{||}^2 c^2}{2n_{cav}^2 E_S} \quad (1.23)$$

Thus the cavity mode presents a parabolic dispersion, defined by an effective mass, $m_{ph} = \frac{n_{cav}^2 E_S}{c^2}$. The vertical confinement of the photons gives a finite mass for the photon in-plane motion.

1.2.2 Bragg mirrors

A Bragg mirror is a periodic arrangement of dielectric layers with different refractive index n_1, n_2 and width L_1, L_2 , such that $n_1 L_1 = n_2 L_2$. As we have already said, the advantage of cavity made of semiconductor interfaces is that, when used in a energy range below the band gap E_g and so below the absorption edge, their residual absorption due to the penetration of the electric field in the layers is low.

With an argument similar to the previous one used for the Fabry Perot cavity, one can show that, for a given wavelength λ_{Bragg} , the periodic structure will present an enhanced reflectivity for normal incidence when the optical thickness ($n_i \times L$) of each layer is equal to $\lambda_{Bragg}/4$.

In the case of a large number of layers N and normal incidence (such that $1 - R \ll 1$) the reflectivity at $\lambda_{bragg} = \frac{2\pi c}{\omega_{Bragg}}$ is given by:

$$R(\lambda_{Bragg}) \approx 1 - 4 \frac{n_{out}}{n_{sub}} \left(\frac{n_1}{n_2} \right)^{2N} \quad (1.24)$$

with n_{out} the optical index of the external medium, n_{sub} the one of the substrate (in our case *GaAs*). The reflectivity increases with the number of mirrors and with the index contrast between layers. A typical reflectivity curve of 20 pairs Bragg mirror as a function of the normalized frequency ω/ω_{Bragg} is shown in fig. 1.4.

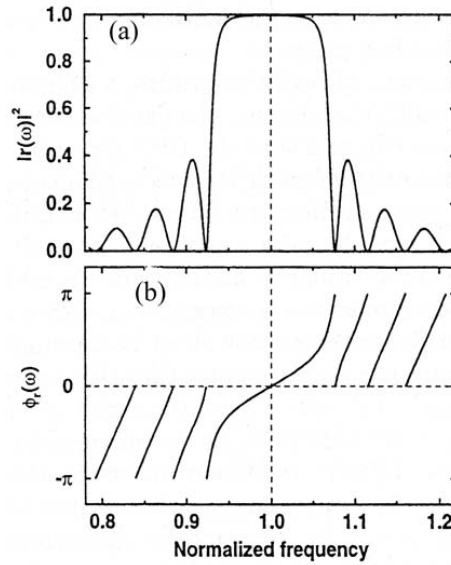


Figure 1.4: Reflectivity and phase shift versus normalized frequency for a 20 pairs Bragg mirror structure, $n_1=3$, $n_2=3.6$. Calculation from ref.[44]

The region of high reflectivity, centered symmetrically around ω_{Bragg} , is called *stop band*. In addition the phase of the reflectivity coefficient r changes with the frequency, and in the stop band is given by the expression:

$$\phi(\omega) \approx \frac{n_{sub} L_{DBR}}{c} (\omega - \omega_{Bragg}) \quad (1.25)$$

where L_{DBR} is the penetration depth of the electric field inside the mirrors and is given by:

$$L_{DBR} = \frac{\lambda}{2} \frac{n_1 n_2}{n_{sub}(n_2 - n_1)} \quad (1.26)$$

1.2.3 Bragg mirror microcavity

We now consider a complete microcavity obtained by the insertion of a layer, in between two Bragg mirrors. This layer is always a semiconductor layer, of width L_{cav} and index n_{cav} . A typical example of the resulting reflectivity spectrum is shown in figure 1.5. One actually obtain a Fabry Perot cavity with a spectral region of high reflectivity, and with a sharp minimum at the wavelength of the cavity mode.

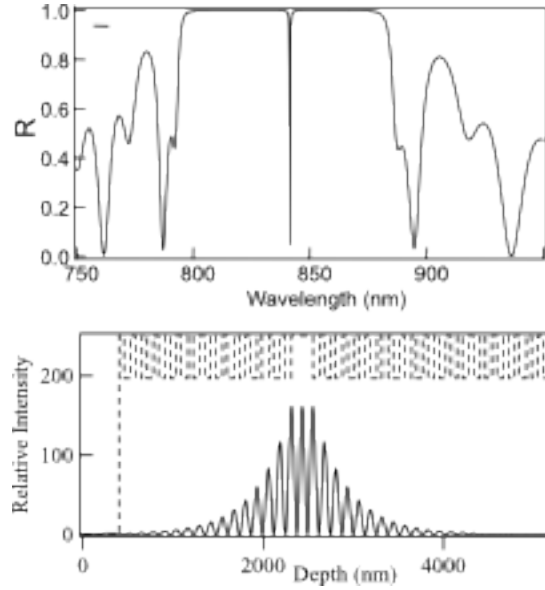


Figure 1.5: Top: Example of reflectivity curve of a Bragg mirror microcavity. The structure consists in a top and bottom mirror with 15 and 21 pairs of GaAs/AlAs, while the cavity layer consists of 240 nm of GaAs. Bottom: Electric field intensity distribution for a wavelength of 841 nm, corresponding to the reflectivity deep. Figure extracted from [54].

The electric field intensity distribution corresponding to the wavelength of the reflectivity deep is also shown in figure 1.5. The mode presents a maximum of the intensity at the center of the cavity layer, but since the electric field penetrates the Bragg mirrors, one can define an effective length $L_{eff} = L_{cav} + 2L_{DBR}$ and the cavity mode energy is given by the constructive interference condition:

$$\left(\frac{\omega^2}{c^2} n_{cav}^2 - k_{||}^2 \right)^{1/2} L_{cav} = S\pi. \quad (1.27)$$

with $S = 1, 2, 3, \dots$

The dispersion of the cavity mode will finally results: $E_{cav} = \frac{\hbar c}{n_{cav}} \sqrt{k_z^2 + k_{||}^2}$.

1.3 Microcavity polaritons

We have presented the two building block of a microcavity structure. Both the QWs and the cavity play an analogous role respectively on exciton and photon by breaking the translational symmetry on the z axis and imposing a confinement that discretize the energetic and photonic levels. We now discuss the case in which the cavity mode is in spectral resonance with the excitonic $1s$ transition. In the cavity, photons can strongly interact with excitons and, if the resonances are sharp enough, the regime of strong coupling can be achieved, in which excitons and photons are no more the eigenstates of the microcavity but they are replaced by half light half-matter quasiparticles, microcavity polaritons.

1.3.1 Weak and strong coupling

A two or more level system such as an atom, can be excited to an excited state and then relax via the emission of a photon. This emission can take place in two regime [55, 56]:

- **weak coupling:** the photon emitted has negligible probability of being reabsorbed by the same medium(irreversible process). The regime is also called perturbative, because the electromagnetic field appears in the Hamiltonian as a perturbative term $w \propto \vec{p} \cdot \vec{A}$ and the first order development gives the spontaneous emission rate (Fermi golden rule),

$$\Gamma = \frac{2\pi}{\hbar} | \langle \Psi_0 | w | \Psi_1 \rangle |^2 \rho(E_{ph}) \quad (1.28)$$

where $\rho(E_{ph})$ is the photon density of states and $|\Psi_0\rangle$ and $|\Psi_1\rangle$ the ground and excited state . In this regime the excitation will be dissipated and the population of excited atoms will decay exponentially.

By acting on the electromagnetic environment, and so on the electromagnetic density of states, one can modifies the transition probability given by the Fermi Golden rule: this is the *Purcell effect* [1] , that consists in an increase or a decrease of the emission probability modifying the density of optical modes.[57, 58].

- **strong coupling:** its is also called non perturbative regime, and corresponds to the case in which the photon emitted can be recaptured and reexcite the medium. In this regime excitation is coherently shifting back and forth between the medium and the mode of the electromagnetic field. These *Rabi oscillations* are dumped by the decoherence present in the system. Energy is therefore dissipated with a time comparable with the coherence time of the uncoupled states. In the spectral domain, Rabi oscillations are revealed by an energy splitting Ω , called *Rabi splitting* or normal mode splitting, and the anticrossing behaviour of the coupled states.

The conditions for achieving the strong coupling regime can be expressed more formally from a semi-classical description of two coupled Lorentz oscillator[44]. By defining the coupling strength between the two oscillator, the cavity photon and the QW exciton $g \propto \sqrt{\frac{f_{osc}}{SL_{eff}}}$, the

Rabi splitting Ω results in:

$$\Omega = 2\sqrt{g^2 - \frac{(\gamma_C - \gamma_X)^2}{4}} \quad (1.29)$$

where γ_C and γ_X are respectively the linewidth of the excitonic and photonic resonances. With $g \ll \gamma_C - \gamma_X$, Ω is purely imaginary, the energy of the system is quickly dissipated, and we are indeed in the weak coupling regime. In the opposite case, with $g \gg \gamma_C - \gamma_X$, Ω the dissipation is sufficiently slow to allow to the energy to be transferred coherently between the oscillators, realizing the strong coupling regime.

The first theoretical discussion of the strong coupling regime in solid state system was made by Hopfield in 1958[59], in which he recognized how, due to translation invariance symmetry in a bulk material, the elementary excitations are mixed exciton-photon states, called polaritons. Polariton luminescence in bulk was observed experimentally in different materials [60, 61, 62], and the polariton dispersion was characterized by polariton-phonon inelastic (Brillouin) scattering [63, 64].

The strong coupling regime was largely explored also in the field of atoms in a cavity, with the theoretical work of Jaymes and Cumming [65], and experimental observation of self induced Rabi oscillations [5] in the group of Serge Haroche, and normal mode splitting [6] in the group of J. Kimble.

In 1992 Claude Weisbuch and collaborators put in evidence the strong coupling regime in a semiconductor microcavity containing QWs and discovered cavity polaritons[7]. In these structures there's a break of the translation symmetry along the z axis (the growth axis). The invariance for translation on the layer plane results in the coupling of an exciton of wavevector $k_{||}$ with photons of the same in plane vector. Besides, the confinement of the photon on the third direction, induced by the cavity, fixes the third component of its wavevector. The result is a one-to-one coupling between exciton in the QW and photon in the cavity.

1.3.2 Quantum mechanical description of the polaritons states

The excitons and the photons inside the cavity constitute a system of two bosonic oscillators coupled through light matter interaction. A quantum mechanical approach, based on the formalism of the second quantization theory, can provide an intuitive visualization of the underlying physics[54]. We introduce the bosonic creation and annihilation operator of a photon of eigenvector $\mathbf{k}_{||}$, $\hat{a}_{k_{||}}^\dagger, \hat{a}_{k_{||}}$ and of an exciton, $\hat{B}_{k_{||}}^\dagger, \hat{B}_{k_{||}}$. The hamiltonian of the system will be:

$$H = \sum_{k_{||}} E_c(k_{||}) \hat{a}_{k_{||}}^\dagger \hat{a}_{k_{||}} + \sum_{k_{||}} E_X(k_{||}) \hat{B}_{k_{||}}^\dagger \hat{B}_{k_{||}} + \sum_{k_{||}} \hbar\Omega_R \left(\hat{a}_{k_{||}}^\dagger \hat{B}_{k_{||}} + \hat{a}_{k_{||}} \hat{B}_{k_{||}}^\dagger \right) \quad (1.30)$$

where the last term represents the coupling between all the oscillators with the same $k_{||}$, with the quantity $\hbar\Omega_R$ that represent the interaction strength.

The previous Hamiltonian can be rewritten as :

$$H(k_{||}) = \begin{pmatrix} E_c(k_{||}) & \hbar\Omega_R \\ \hbar\Omega_R & E_X(k_{||}) \end{pmatrix} \quad (1.31)$$

and can be easily diagonalized in a basis that will be named the polariton basis, in which the creation and annihilation operators are:

$$\hat{p}(k_{||}) = X_{k_{||}} \hat{B}_{k_{||}} + C_{k_{||}} \hat{a}_{k_{||}} \quad (1.32)$$

$$\hat{q}(k_{||}) = -C_{k_{||}} \hat{B}_{k_{||}} + X_{k_{||}} \hat{a}_{k_{||}} \quad (1.33)$$

The two kinds of polaritons created will be called respectively lower and upper polariton (LP, UP), while $X_{k_{||}}$ and $C_{k_{||}}$ are the Hopfield coefficients in the linear combination of exciton and photon states that defines polaritons.

The Hamiltonian in this basis is diagonal and can be simply written as:

$$H = \sum_{k_{||}} E_{LP}(k_{||}) \hat{p}_{k_{||}}^\dagger \hat{p}_{k_{||}} + \sum_{k_{||}} E_{UP}(k_{||}) \hat{q}_{k_{||}}^\dagger \hat{q}_{k_{||}} \quad (1.34)$$

with eigenenergies given by:

$$E_{LP}(k_{||}) = \frac{E_c(k_{||}) + E_X(k_{||})}{2} - \frac{1}{2} \sqrt{4\hbar^2 \Omega_R^2 + (E_c(k_{||}) - E_X(k_{||}))^2} \quad (1.35)$$

$$E_{UP}(k_{||}) = \frac{E_c(k_{||}) + E_X(k_{||})}{2} + \frac{1}{2} \sqrt{4\hbar^2 \Omega_R^2 + (E_c(k_{||}) - E_X(k_{||}))^2} \quad (1.36)$$

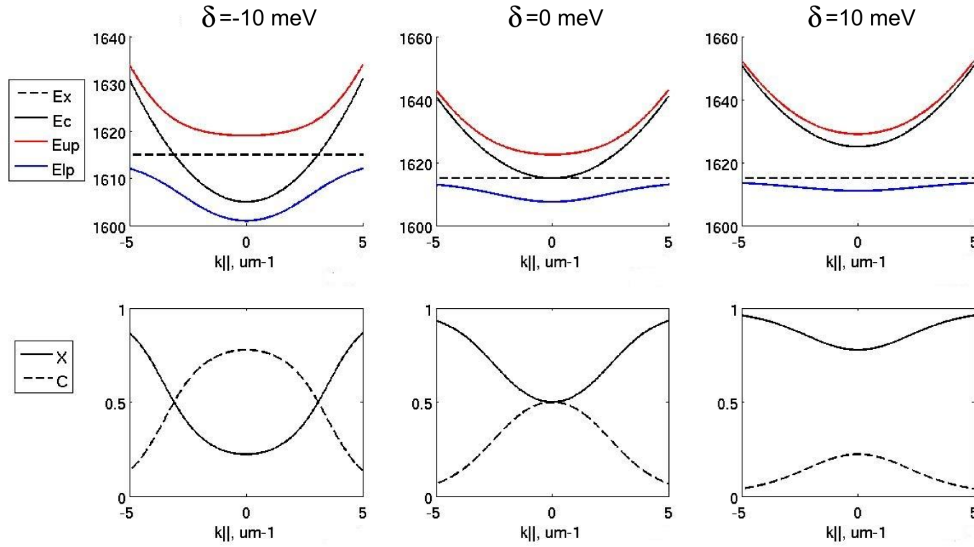


Figure 1.6: Up:Polariton bands and exciton and cavity mode dispersion for several detunings. $\Omega = 15 \text{ meV}$; Down:Exciton (X) and photonic (C) corresponding Hopfield coefficients for the low polariton band

We define the *detuning* δ as the energy difference between exciton and photon mode at $k_{||} = 0$, $\delta = E_c(k_{||} = 0) - E_X(k_{||} = 0)$.

In fig 1.6 we report the in-plane polariton dispersions curve for 3 different values of δ .

The Hopfield coefficients are given by:

$$X_{k_{||}} = \frac{1}{\sqrt{2}} \left(1 + \frac{E_c(k_{||}) - E_X(k_{||})}{\sqrt{4\hbar^2\Omega_R^2 + (E_c(k_{||}) - E_X(k_{||}))^2}} \right)^{1/2} \quad (1.37)$$

$$C_{k_{||}} = \frac{1}{\sqrt{2}} \left(1 - \frac{E_c(k_{||}) - E_X(k_{||})}{\sqrt{4\hbar^2\Omega_R^2 + (E_c(k_{||}) - E_X(k_{||}))^2}} \right)^{1/2} \quad (1.38)$$

These coefficients represent the relative excitonic and photonic fraction of the polariton state.

We can define a LP mass extracted from the curvature of the dispersion, approximated as parabolic around $k_{||} = 0$:

$$E_{LP} \approx E_{LP}(k_{||} = 0) + \frac{\hbar k_{||}^2}{2m_{LP}} \quad (1.39)$$

where the mass is given by the following relation:

$$\frac{1}{m_{LP}} = \frac{X_{k_{||}}}{m_X^*} + \frac{C_{k_{||}}}{m_{ph}} \quad (1.40)$$

with m_X^* the exciton in-plane effective mass. Since $m_X^* \gg m_{ph}$, the polariton mass can be approximated by $m_{LP} \approx \frac{m_{ph}}{C_{k_{||}}}$, and so of the order of the photon mass, around $10^{-5}m_e$.

Also the polariton lifetime can be expressed as a function of the Hopfield coefficient [66]. For the lower branch, its values is given by:

$$\frac{1}{\tau_{LP}} = \frac{X_{k_{||}}}{\tau_X} + \frac{C_{k_{||}}}{\tau_{ph}} \quad (1.41)$$

The lifetime of photons, normally from few ps up to around 30 ps, is much lower than τ_X , typically hundreds of picoseconds, (representing the decoherence induced by the coupling with the excitonic reservoir [66, 67]) and therefore, for detuning δ not too far from zero, we can simplify the expression with $\tau_{LP} \approx \frac{\tau_{ph}}{C_{k_{||}}}$.

Polariton momentum and measure of the dispersion

The finite polariton lifetime results in dissipation of energy via photon emission from the top of the cavity. The photon escaping the cavity has both the same in-plane wavevector and same energy than the polariton that it comes from (see fig. 1.7). Therefore, the angle of emission θ of the photon can be mapped to the value of the polariton in-plane momentum as $\sin(\theta) = k_{||}\hbar c/E(k_{||})$.

Thanks to this relation, the imaging of the far field of the emission spectrally resolved allows a direct visualization of the polariton branches, as reported in figure 1.7.

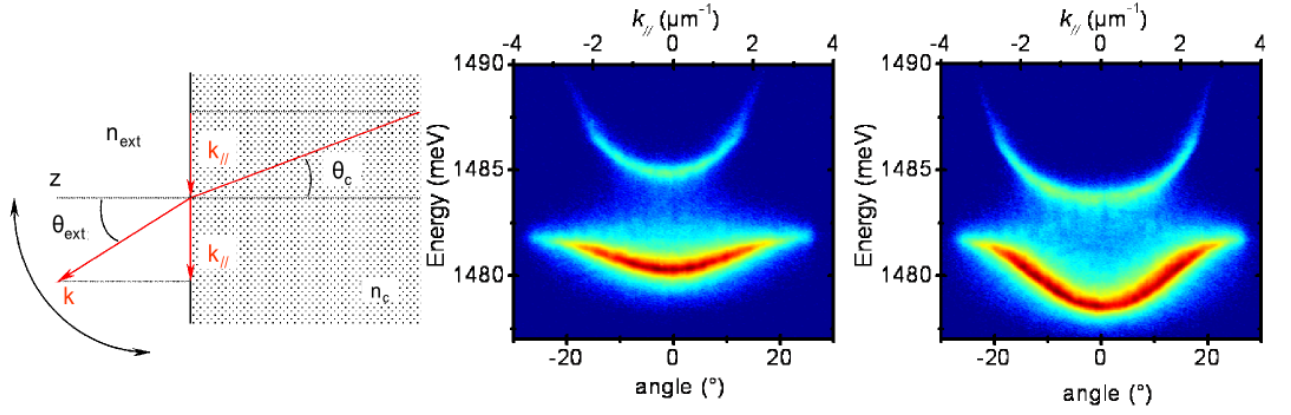


Figure 1.7: Left: Scheme of the photon emission outside the cavity. Figure extracted from [68]. Center and right: Spectral and angular resolved emission from a microcavity at two different detuning ($\delta = -3\text{meV}$ (center) and $\delta = -6\text{meV}$). Both upper and lower polariton branches are detected. Figures extracted from [52].

Polariton pseudospin

The one to one correspondance between excitons and photons coupled in the polaritons state affects also the total angular momentum of the resulting quasiparticles.

We have already discussed how only heavy hole excitons with total angular momentum $J = 1$ are coupled with light. Considering the quantization axis z , the growth axis, this corresponds to the two excitonic state $\uparrow = (J_h^z = \frac{3}{2}, J_c^z = -\frac{1}{2})$ and $\downarrow = (J_h^z = \frac{3}{2}, J_c^z = +\frac{1}{2})$. At normal incidence, photon right-circularly polarized (σ^+) will excite the exciton state \uparrow , and a left-circular polarized one (σ^-), the exciton \downarrow . In-plane projections of the angular momentum can instead be excited with linearly polarized photons.

In the presence of strong coupling, this momentum conservation produces a direct correspondence between the photon polarization and polariton total angular momentum. Since only two possible values are possible, ± 1 , for the polariton angular momentum, it corresponds to a 2-level system that can be described as a $1/2$ *pseudospin*.

The mixed nature of such pseudospin allows it to interact with both an external magnetic field or with the an effective field induced by a polarization splitting of the polariton modes [69, 70]. By resolving the polarization of the emitted photons, the pseudospin dynamics can be observed, as discussed in chapter 5.

1.3.3 Polaritons as interacting bosons

Few years after the observation of the strong coupling in semiconductor microcavities, polaritons started to be seen as good candidates for the observation of bosonic effects in semiconductor materials[11]. As composite bosons, they are expected to obey the bosons statistic, at least for low densities. Consequently, when the occupation factor of a state increases above one, an effect of bosonic stimulation of the relaxation towards such state is expected. The bosonic nature of polaritons was evidenced at first in experiments involving

resonant excitation of the lower polariton bands, triggering parametric oscillation (OPO) and parametric amplification (OPA) [8, 9, 10].

With respect to bare excitons, polaritons present a trap close to $k_{||} = 0$, in which the density of states is 10^4 times lower than for a bare excitonic state. Under non resonant excitation, Imamoglu, in 1996, foreseen that this low effective mass could be favorable for the spontaneous build-up of a highly coherent population in the trap via bosonic stimulation of the polariton relaxation [11]. The signature of such condensation process would be a strong non linear increase of the emission together with the appearance of spontaneous coherence. This new lasing mechanism, without population inversion, was first named *boser*, and later *polariton laser* or *polariton quasi-condensate*.

From the experimental point of view, the achievement of this regime requires a mechanism of relaxation towards the lower part of the polariton band, in order to reach the occupation factor of 1 necessary to trigger the bosonic stimulation [71].

A non-resonant excitation indeed consists in pumping the system around 100 meV above the polariton bands, with an energy corresponding to the first reflectivity deep of the Bragg mirrors, in the high energy edge of the stop band.

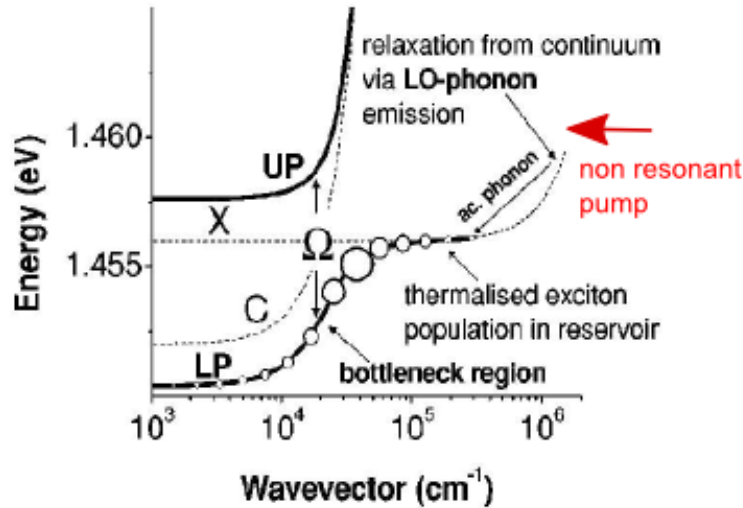


Figure 1.8: Sketch of the polariton relaxation towards the bottom of the LP branch. Carriers are created at high energy by a non resonant pump. They partially thermalize via interaction with phonons. Then competition between acoustic phonon scattering and dissipation could prevent the system to reach thermalization towards the bottom of the LP branch. Figure extracted from [49].

The laser generates free carriers in the QWs, that relaxes via emission of optical and acoustic phonons towards the flat excitonic region of the polariton dispersion, as shown in the picture 1.8. A thermalized excitonic reservoir is then created [72, 54]. The relaxation from the reservoir toward the bottom of the polariton branch via acoustic phonon emission is very inefficient. Indeed because phonon dispersion is very flat as compared to the polariton dispersion, only relaxation with emission of very small energy phonons allows conserving both energy and in-

plane wavevector. As a result, polaritons undergo a relaxation bottleneck[73, 74]. The system is therefore in strongly non equilibrium, the high k -vector state forms the excitonic reservoir in which the population accumulates while the population in the bottom of the band is fixed by the competition between the relaxation from the reservoir to such state and the polariton lifetime.

The dynamic of relaxation has been shown to be accelerated by several factors: interaction with free electrons[75, 76], the rise of temperature[77] and also thanks to polariton-polariton scattering [78]. The latter suggested that by increasing the excitation density, relaxation could indeed be accelerated, but at the same time, excitons density needs to remain below the Mott density, to prevent the transition to the weak coupling regime.

The first experimental observation of polariton lasing was obtained at first by Le si Dang[79] and then confirmed by the works of Jacek Kasprzak in a CdTe cavity [12]. Thanks to the strong binding energy of CdTe-excitons (giving a Mott density ten times higher than GaAs) and a more efficient phonon-mediated relaxation (with respect to GaAs), the authors measured strong non-linear emission from the $k=0$ state of the lower polariton branch, together with a strong increase of the spatial and temporal coherence. Few years later, the use of materials with even higher exciton binding energy, such as GaN [16, 80] and more recently, ZnO [17], allowed the observation of polariton condensation also at room temperature.

In GaAs cavity, the relaxation bottleneck represented a major obstacle against polariton condensation. Indeed, Raphael Butté, in 2002, showed that, increasing the pumping power for a 6 InGaAs-QWs GaAs microcavity, the system enters the weak coupling regime and photon laser is observed[49].

Different approaches have been developed to overcome the bottleneck and to optimize the relaxation process in GasAs based samples.

In the group of Yamamoto in Stanford, the successful approach consisted in pumping the cavity in resonance with the excitonic reservoir, decreasing the density of free charges that contributes to bleach excitonic transition[81].

The group of David Snoke managed to increase the efficiency of the particle relaxation by inducing, via some strain, a potential trap in real space and so to observe strong non linear emission from polariton states[14].

The approach followed at the LPN, in the group of Jacqueline Bloch, consisted in the coupling of a high number of QWs with a cavity of a higher quality factor. The use of 12 *QWs* allowed to increase the Rabi splitting and the total number of excitons in the cavity, enhancing the relaxation efficiency. On the other hand, a nominal quality factor up to 30000 allowed to increase the photon lifetime to more than 10 *ps*.

Before my arrival in the group, Daniele Bajoni in 2008 showed polariton condensation in the discrete modes of a micropillar [15], while Esther Wertz in 2009 demonstrated polariton condensation at the $k = 0$ state of a planar cavity[38]. Later on, different geometries have been investigated, such as coupled micropillars [82], or wire microcavities [39, 83]. The results obtained in 1D will be described in details in chapter 3.

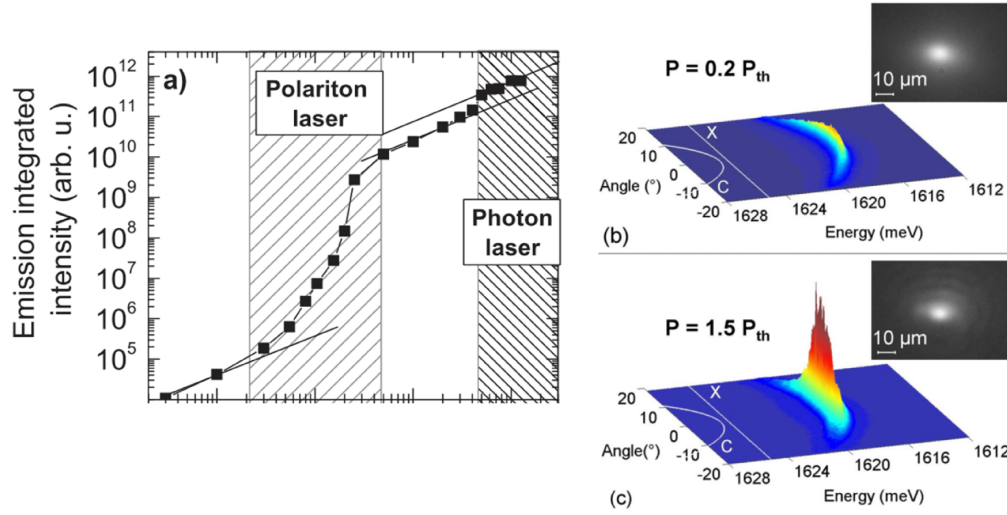


Figure 1.9: Left: Mesures on $6\mu m$ GaAs micropillar cavity (12 QWs, $Q \approx 12000$). Integrated intensity and measured occupancy as a function of the excitation power. Figure extracted from [15]. Right: Mesures on planar GaAs cavity (12 QWs, $Q \approx 12000$). Emission intensity as a function of angle and energy measured below and above the condensation threshold power (P_{th}) for polariton condensation. A macroscopic occupation of the bottom of the band is achieved. Figure extracted from [38]

Polaritons interactions

The Hamiltonian describing polariton states presented in 1.34 is valuable only for low particle density. When increasing the excitation power and so reaching large occupation of the lower polariton bands, we cannot neglect the inner structure of excitons in terms of composite bosons anymore. We already mention the Mott density limit, corresponding to the disappearance of a well defined excitonic bound state. But even before such upper limit, we can reach a regime where the Coulomb interaction between the excitonic part of polaritons must be taken into account.

Indeed in section 1.3.2 we introduced the polaritons states as the eigenmodes of the linear part of the Hamiltonian. A more complete expression can be obtained by taking into account the expansion of the Coulomb Hamiltonian at the second order in the exciton density [84]. The resulting additional term in the Hamiltonian can be expressed, thanks to Bose operators $\hat{B}_{k||}^\dagger$, creator of a 1s exciton; as¹:

$$H_{XX} = \frac{1}{2} \sum_{k,k',q} V_q^{XX} \hat{B}_{k+q}^\dagger \hat{B}_{k'-q} \hat{B}_k^\dagger \hat{B}_{k'} \quad (1.42)$$

The coefficient V_q^{XX} doesn't have a simple expression in the general case, since it includes all the complex effect of interaction and charges exchange (being the dominant term the one of

¹In the present treatment we do not discuss the Hamiltonian term representing the saturation of the excitonic transition with the increase of the optical density, that contribute with a positive term to the interaction constant. The reader can find a detailed discussion of this term in reference [46].

inter-excitons exchange of carriers.) Nevertheless, in the limit of low wave-vector ($q \cdot a_B^* \ll 1$, with a_B^* the exciton Bohr Radius), we can write it as [85]:

$$V_0^{XX} = \frac{6e^2 a_{exc}^{*2D}}{\epsilon A} \quad (1.43)$$

with ϵ the dielectric constant of the material and A the quantification area (the surface of the QW).

This interaction term in the Hamiltonian can be written also using the polariton operators introduced in 1.32 and 1.33. Neglecting any coupling with the reservoir, that we will reintroduce later, and with the upper polariton branch, such term becomes:

$$H_{pol-pol} = \frac{1}{2} \sum_{k,k',q} V_{k,k',q}^{pol-pol} \hat{p}_{k+q}^\dagger \hat{p}_{k'-q}^\dagger \hat{p}_k \hat{p}_{k'} \quad (1.44)$$

with $V_{k,k',q}^{pol-pol} = V_0^{XX} X_{k+q} X_{k'} X_{k'-q} X_k$ is the interaction constant normalized on the polaritons excitonic fractions.

In conclusion, the resulting Hamiltonian represents a system of quasi particle interacting via an effective pair potential. The interaction constant is positive, representing repulsive interactions. In literature the interaction constant is generally indicated with g or α_1 , and can be estimated around $g \approx 2 - 9 \mu eV \cdot \mu m^2$ for GaAs polariton [36].

We finally remark that polariton-polariton interactions present a spin dependence. The discussed constant g or α_1 represent interactions between polaritons of the same spin. The interaction constant for polariton of opposite spin α_2 is theoretically estimated as negative ($\alpha_2 < 0$) and in modulus much lower than α_1 ($|\alpha_2| < |\alpha_1|$) [86]. But the debate on the effective value of such opposite spin interaction constant is still open [87, 27, 88, 89].

Gross-Pitaevskii equation

In the field of quantum gases of matter particles, a classical partial differential equation for the superfluid order parameter was written by Gross[90] and Pitaevskii [91] to describe quantum vortices in liquid helium in the mean field approximation[18]. Indeed, in a condensate phase, the macroscopic fraction of particles that populate the condensate mode behaves in a collective way and the quantum atomic matter field behaves as a classical field [92], expressed with $\Psi(r, t)$, following the Gross-Pitaevskii equation (GPE) that reads:

$$i\hbar\delta_t\Psi = -\frac{\hbar^2}{2m}\nabla^2\Psi + V_{ext}(\mathbf{r})\Psi + \frac{4\pi\hbar^2 a}{m}|\Psi|^2\Psi \quad (1.45)$$

with a the inter-particle scattering length.

Such equation is largely used in the field of cold atom physics and in non-linear optics as well, since it is formally identical to a Maxwell equation for a non linear media[93].

The application of such approach to describe a coherent polariton state requires some corrections . The peculiarities of the polariton system is their dissipative nature. A polariton

population is intrinsically out-of-equilibrium, the system dissipates energy via the photon escaping the cavity and a steady state can only be achieved by continuously replenishing from an external pump [94].

Considering the situation of non resonant pumping, the refilling of the polariton state is provided by the relaxation from the excitonic reservoir. The reservoir itself is then pumped by an external optical excitation. The resulting equation will be defined as a modified GPE or, due to the similarities with the Ginzburg-Landau equation used in the field of non linear dynamical system[95], as complex Ginzburg-Landau equation. Such equation reads[94]:

$$i\hbar\delta_t\Psi = \left[-\frac{\hbar^2\nabla^2}{2m_{LP}} + \frac{i}{2}[R(n_R) - \gamma] + g|\Psi|^2 + 2g_R n_R + V_{ext} \right] \Psi \quad (1.46)$$

The term $-i\gamma$ represents the losses due to the finite particle lifetime $\tau_{LP} = 1/\gamma$, while the term $iR(n_R)$ represents the pumping of the polariton states, corresponding to the process of relaxation from the reservoir of excitons, which population is expressed by the function $n_R(r, t)$.

The evolution of the reservoir population can be expressed in a simple phenomenological model with the following rate equation:

$$\delta_t n_R = P(\mathbf{r}, t) - \gamma_R n_R - R(n_R)|\Psi(\mathbf{r})|^2 \quad (1.47)$$

$P(r, t)$ describes the intensity and the spatial profile of the optical non resonant pump. The population decreases in time due to the finite exciton lifetime, $\tau_X = 1/\gamma_R$ typically of the order of hundreds of ps. But also the stimulated relaxation process plays an important role, and is represented by the term $R(n_R)|\Psi(r)|^2$, in which the relaxation rate is proportion to the spatial overlap between the condensate and the reservoir. Additionally we notice that in 1.46, together with the polariton-polariton interaction terms, also the repulsive interaction between polaritons and the exciton in the reservoir population is taken into account, with $g_R > 0$ interaction constant. This term also will contribute to an overall renormalization of the polariton energies. The last term, V_{ext} represents any possible external potential: it can be a random potential due to the disorder (as discussed in chapter 3), to a controlled barrier [31, 96] obtained for example by the etching of the microcavity (as discussed in chapter 2), or with an optically induced potential [97, 30]. It can also represent a constant acceleration and a periodic or quasi-periodic potential (as discussed in chapter 4).

Until now we mainly discussed the configuration of non resonant pumping. But we already mention other possible approaches to populate the polariton states. By properly adjusting the pump term in eq. 1.46, the condition of coherent resonant driving of the polariton population can also be treated[18]. The resulting GPE equation assumes the form:

$$i\hbar\delta_t\Psi = -\frac{\hbar^2\nabla^2}{2m_{LP}}\Psi - i\frac{\gamma}{2}\Psi + g|\Psi|^2\Psi + V_{ext}\Psi + F_P \quad (1.48)$$

where the pumping of the system now consists of an external incident radiation represented by the term F_P . This pumping configuration will allow to control the polariton density by the pump power, and thanks to the one to one correspondance between the injected photon and the created polariton, also the energy, the wave-vector and the polariton pseudospin can be controlled.

Chapter 2

Samples and experimental setup

In this chapter we present the samples studied during this thesis. The planar cavity structure will be presented first. Then we describe the microstructures obtained by dry etching. The resulting one-dimensional polariton states are introduced.

The second part of the chapter is dedicated to a presentation of the experimental setup and a brief description of its main components.

2.1 The samples

The cavity structure

The cavities investigated during this thesis are *GaAs/AlAs* cavity realized by Aristide Lemaitre and coworkers in the clean room of the LPN.

Two cavities have been studied. The results presented in chapter 3 are obtained on the same sample cavity investigated also during the PhD of Esther Wertz (code 73J125)[38]. All the rest of the presented results (corresponding to chapter chapter 4 and 5), have been obtained on a cavity grown during my PhD (code ABR66), which structure is reported on figure 2.2.).

Both the sample consists in a $\lambda/2$ cavity of *Ga_{0.05}Al_{0.95}As*, with λ the nominal resonant wavelength, 780 nm. The active region consists of 12 GaAs QWs of 7nm width. 4 of them are placed in the center of the cavity, corresponding to the maximum of the electromagnetic field. The other 8, divided in group of four, are placed on the first of the antinode of the electromagnetic field, inside the Bragg mirrors (as shown in figure 2.1).

The Bragg mirrors consist of a periodic sequence of layers of optical width $\lambda/4$ and composition *Ga_{0.05}Al_{0.95}As* and *Ga_{0.8}Al_{0.2}As*.

For the cavity investigated during E.Wertz PhD (code 73J125), the lower mirrors, on the side of the substrate, has 30 pairs, the upper one, 26, and the nominal quality factor results $Q \approx 30000$.

In the more recent cavity (code ABR66), subject of the characterization presented in the following paragraphs of this chapter, the lower mirrors, on the side of the substrate, has 40 pairs, the upper one, 28. Differently from the previous cavity, in which the reflectivity of the top and bottom mirror were identical, here the reflectivity of the lower mirror is higher with respect to the upper one, and this a-symmetrization allows to minimize the photon losses on the substrate

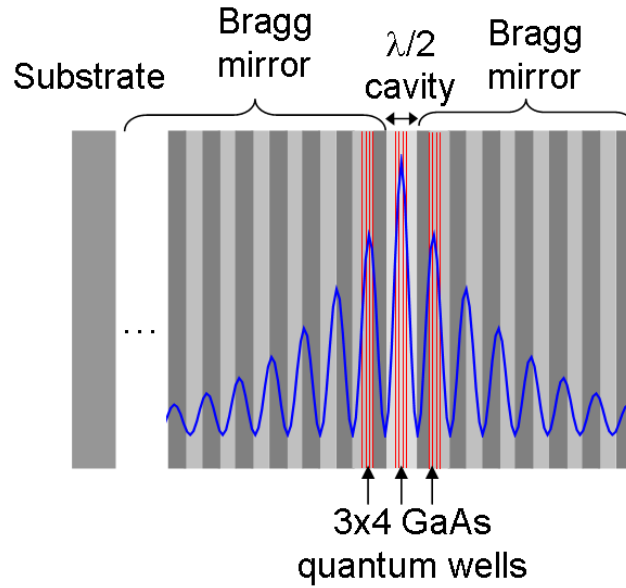


Figure 2.1: Scheme of the cavity sample . The red lines represent the QWs while the blue lines represents the electric field spatial distribution for the wavelength corresponding to the cavity mode.

side. The high number of pairs allows to increase the quality factor of the cavity and so the photon lifetime inside it. The nominal quality factor is $Q \approx 70000$.

The high number of Quantum wells used increases the Rabi splitting between the upper and lower polaritons bands up to $\Omega = 15 \text{ meV}$, making the strong coupling more robust and, at the same time, it allows to introduce a high number of polaritons in the system keeping low the density of excitons in each well.

2.1.1 Optical characterization

The planar cavity

The as-grown wafer is first characterized by reflectivity measurements performed at room temperature. A scan of the whole circular wafer, of radius around 5cm is obtained by Fourier Transform Infrared Spectroscopy (FTIR) and a map of the energy of the cavity mode is extracted. The energy of the cavity varies all over the surface, due to the stop of the rotation of the wafer during the growth. This scan allows identifying the region of the sample where an exciton-photon detuning around zero is expected at low temperature.

The wafer is so clived along the crystallographic axis selecting a region of around 1cm^2 , small enough to be pasted on the cryostat's cold finger and be observed at liquid Helium temperature.

In figure 2.3 we show two examples of polariton dispersion measured at two location of a planar cavity sample. They are obtained by detecting the photoluminescence at 10 K with both

| | Structure nominale | | Répétition du motif |
|------------------|---|-----------|------------------------|
| | Matériau | Épaisseur | |
| Miroir supérieur | $\text{Ga}_{0.8}\text{Al}_{0.2}\text{As}$ | 566.0 Å | x1 |
| | $\text{Ga}_{0.05}\text{Al}_{0.95}\text{As}$ | 650.0 Å | x27 |
| | $\text{Ga}_{0.8}\text{Al}_{0.2}\text{As}$ | 566.0 Å | |
| | $\text{Ga}_{0.05}\text{Al}_{0.95}\text{As}$ | 424.8 Å | x1 |
| | GaAs | 70.0 Å | x4 |
| | $\text{Ga}_{0.05}\text{Al}_{0.95}\text{As}$ | 30.0 Å | |
| | $\text{Ga}_{0.80}\text{Al}_{0.20}\text{As}$ | 369.5 Å | x1 |
| Cavité | $\text{Ga}_{0.05}\text{Al}_{0.95}\text{As}$ | 396.0 Å | x1 |
| | GaAs | 70.0 Å | x4 |
| | $\text{Ga}_{0.05}\text{Al}_{0.95}\text{As}$ | 30.0 Å | |
| | $\text{Ga}_{0.05}\text{Al}_{0.95}\text{As}$ | 366.0 Å | x1 |
| Miroir inférieur | $\text{Ga}_{0.8}\text{Al}_{0.2}\text{As}$ | 369.5 Å | x1 |
| | $\text{Ga}_{0.05}\text{Al}_{0.95}\text{As}$ | 30.0 Å | x4 |
| | GaAs | 70.0 Å | |
| | $\text{Ga}_{0.05}\text{Al}_{0.95}\text{As}$ | 424.8 Å | x1 |
| | $\text{Ga}_{0.8}\text{Al}_{0.2}\text{As}$ | 566.0 Å | x39 |
| | $\text{Ga}_{0.05}\text{Al}_{0.95}\text{As}$ | 650.0 Å | |
| Substrat | GaAs | - | - |

Figure 2.2: Structure of the sample ABR66. It corresponds to the cavity structure used to obtained the results presented in chapters 4 and 5).

spectral and angular resolution. Probing different locations on the sample, both the energy of the excitonic resonance and of the cavity mode change. As a result, the energy of the polaritons states change together with their dispersion. The fitting of the measured dispersion allows extracting the cavity and exciton energy $E_c^{k_{||}=0}$ and $E_X^{k_{||}=0}$ and thus the exciton photon detuning δ .

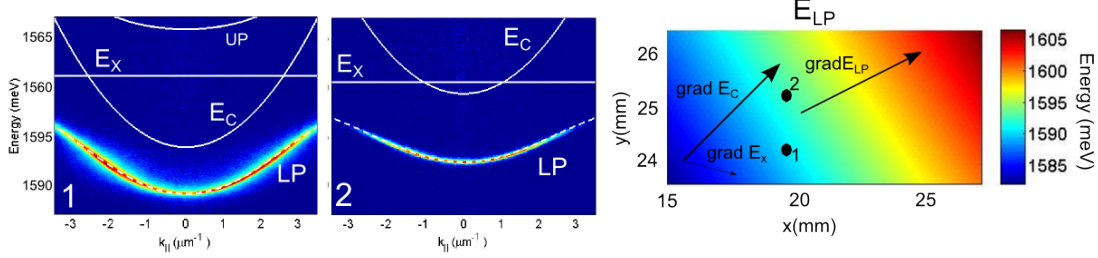


Figure 2.3: Left: Two polariton dispersion collected in two different region of the sample. The fit of the LP curve is obtained by applying 1.35 with $\Omega_R = 15\text{meV}$. (The extracted detuning are $\delta = -7.2\text{meV}$ (left panel), and $\delta = -1\text{meV}$ (central panel)). Right: A colormap of the LP energy at $k_{||} = 0$, results of a scan of the sample surface. The fitting of the local dispersion also to extract also the local values of the excitonic and photonic resonances and deduce their gradient ($|grad E_c| \approx 4.5\text{meV}$, $|grad E_c| \approx 1.4\text{meV}$)

The linewidth of the polariton emission, selected for $k = 0$, is measured $\Gamma = 160\mu\text{eV}$ for the wire in the central panel of figure 2.3, with detuning δ almost zero.

For low wavevector, the broadening is mainly given by the photonic component and at zero detuning such linewidth is twice the linewidth of the cavity mode. For the present case, the measured linewidth would correspond to a cavity quality factor of around $Q = 20000$, corresponding to a photon lifetime around 8 ps. But the linewidth can also be strongly influenced by inhomogeneous broadening [98, 99], mainly given by the fluctuation of width and composition of the QWs. To measure the polariton lifetime, more sophisticated method are required. The method we used is based on the observation of the spatial decay of the signal intensity along polariton propagation. Indeed, given a certain group velocity of propagation v_g , the expected intensity profile for a 1 dimensional propagation would be, $I = I_0 e^{-x/x_0}$, with $x_0 = v_g \cdot \tau$ propagation length.

In figure 2.4, we report the spatially resolved emission of a microcavity excited by a $2\mu\text{m}$ non resonant spot in the $x = y = 0$ point. The excitation is above threshold, and therefore polaritons, as better discussed in 3.2.2, propagates with a given wavevector k and a corresponding group velocity v_g . Here the propagation is radial, and the decrease in the intensity along the propagation will be given by : $I = \frac{I_0}{r} e^{-r/r_0}$ with $r_0 = v_g \cdot \tau$. In order to take into account the intensity decrease with $1/r$ and also to average the effect of some inhomogeneity of the spatial distribution (given probably by few point-like defects along the propagation), we integrated the signal inside a given angle, as indicated in the figure. The resulting emission intensity as a function of the distance from the spot is plotted on the graph of figure 2.4 . An exponential fit allows extracting the value of $r_0 \approx 120 \mu\text{m}$. Given a propagation speed of $v_g = 2.9\mu\text{m}/\text{ps}$,

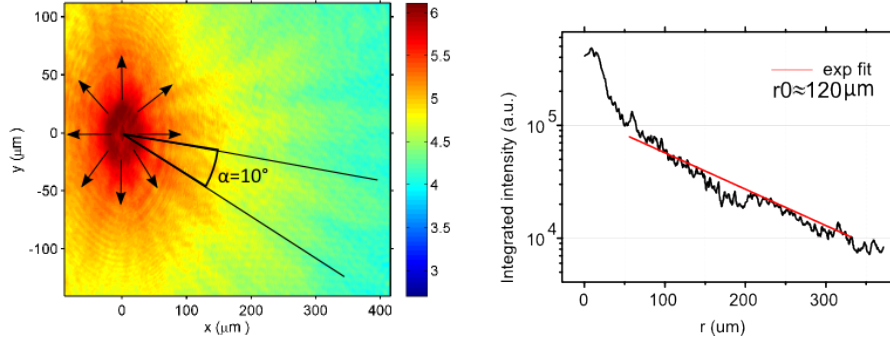


Figure 2.4: Left: Emission from radially propagating polaritons. The excitation spot is placed at $x=y=0$. Right: Integrated emission inside the spherical angle $\alpha = 10^\circ$ shown in the right panel, as a function of the distance from the excitation spot. The red line is an exponential fit, giving a decay length of $r_0 \approx 120$.

this gives a polariton lifetime of 41 ps. Taking into account of the detuning $\delta = -6\text{meV}$ in this region of the sample, we deduce a photon lifetime of $\tau_{ph} \approx 27\text{ps}$. This value corresponds to a cavity quality factor of $Q \approx 65000$, in quite good agreement with the nominal calculated value $Q \approx 70000$.

2.1.2 One-dimensional microstructures

In this work we confine polaritons in one-dimensional microstructures. They are fabricated at the LPN by Isabelle Sagnes starting from the planar cavity using electron-beam lithography and dry etching.

A wide range of one dimensional structures has been realized and will be presented in the manuscript. In figure 2.5 we show a Scanning Electron Microscope image of the resulting sample surface after etching of some one-dimensional micro-structure.

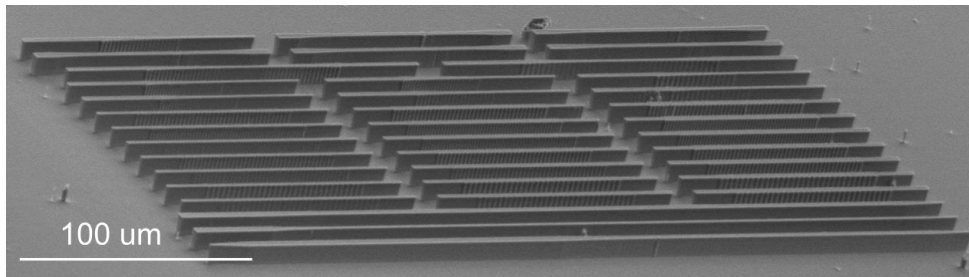


Figure 2.5: Scanning electron microscope image of a microcavity sample surface after etching of several 1 dimensional microstructures.

Polaritons in microwires

We now consider the case of a microcavity wire. The etching confines the optical lateral mode on a further lateral direction and the resulting optical modes are given by:

$$E_c(k_{||}) = \sqrt{E_{C0}^2 + \left(\frac{\hbar c}{n_{cav}}\right)^2 \left[\left(\frac{\pi(j_x + 1)}{L_x}\right)^2 + k_y^2 \right]} \quad (2.1)$$

with $j_x = 0, 1, 2, \dots$ and L_x the width of the wire.

The confinement of excitons, is not affected by the etching, since the lateral size is several order of magnitude larger than the Bohr radius a_B^* .

In the strong coupling regime, the $1s$ excitons undergo a coupling not with one but with several discrete optical modes, and the matrix that describes the coupling (2.2) becomes:

$$H(k_{||}) = \begin{pmatrix} E_c^{j_x}(k_y) & \hbar\Omega_R \\ \hbar\Omega_R & E_X \end{pmatrix} \quad (2.2)$$

This brings to the generation of several polariton subbands: the first three polaritons subbands are visible in the far field emission of a $3.5\mu m$ wide wire, shown in figure 2.6.

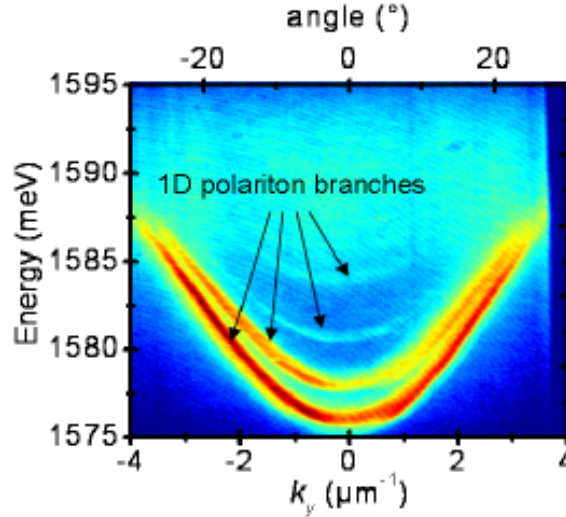


Figure 2.6: Far field emission from a $3.5\mu m$ wide wire (logarithmic color scale). Figure extracted from [52]

In the figure we also notice another difference with respect to the emission from a planar microcavity. We observe a broad emission coming from excitons in the reservoir. This emission arises from in-plane exciton emission refracted on the side walls and redirected toward normal incidence. This emission gives an indication of the energy of the excitonic resonance. The large bandwidth of this emission is probably due to a strain relaxation near the edges.

The measured polariton linewidth at $k = 0$ and zero detuning is also around $150\mu m$, as in the planar sample.

Polaritons lifetime inside microstructures will be evaluated in several way along this thesis, and also further independent measurements of the lifetime in the same sample have been performed in the group on similar microstructures [31, 100]. The resulting values τ_{pol} has been always estimated in the 30-45 ps range.

We conclude that the optical properties of the wire cavities are very similar to the as-grown planar cavity, indicating they have been preserved even after the etching process.

Polarization splitting

In the planar cavity, a polarization dependence of the penetration depth of the optical mode inside the DBRs induces a weak birefringence of the cavity[101]. This results in a splitting between the two linearly polarized optical modes, named Transversal Electric (TE) and Transversal Magnetic (TM). This splitting depends on the incident angle: it is zero at normal incidence and increases quadratically with the photonic in-plane wave-vector $k_{||}$. The strong coupling with the exciton results although into two split LP bands, as shown in the left panel of figure 2.7. The polariton states inherit this polarization splitting from their photon part, as shown in the left panel of fig.1.8. The polarization splitting increases with $k_{||}$ up to a maximum and then, for large angle (not shown), decreases because of the decrease of the photonic Hopfield coefficient[101].

In the case of one-dimensional microcavity structure, the polarization splitting presents a non-zero value at $k_{||} = 0$.

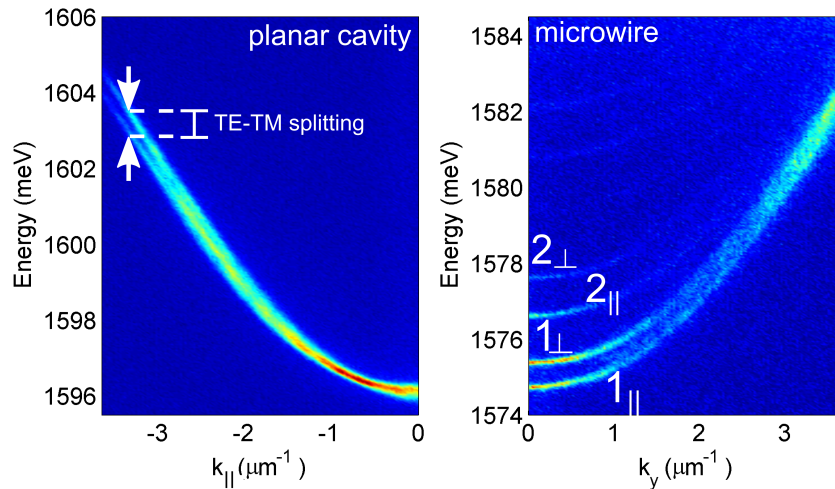


Figure 2.7: Left: Polariton dispersion from a planar cavity. The TE-TM splitting appears for high in-plane wavevector. Right: The sub-bands of a photonic wire are split in linearly polarized sub-bands, parallel and perpendicular to the wire axis.

In the right panel of figure 2.7, we plot the complete band structure for a $3\mu\text{m}$ wide microcavity wire. We indeed observe how each polariton subbands, corresponding to different order of confinement, are splitted in polarization parallel to the wire (lower energy) or perpendicular

(higher energy). The reported wire has a splitting at $k = 0$ of the order of $0,6meV$ for the first mode ($j=1$) and around $0,9meV$ for the second order ($j=2$).

The origin of this splitting is still not perfectly understood and has been well discussed in the thesis of Carole Diederichs[102] and more recently, of Vincenzo Ardizzone [103], in the group of Jerome Tignon at the LPA in Paris.

It has been shown that for a photonic wire, the boundary conditions imposed to the electromagnetic field at the interface between air and semiconductor could result in a polarization splitting also at $k_y = 0$ [104]. But this effect seems to be negligible in our systems.

Some strain relaxation due to the etching could also induce a splitting of the excitonic mode[105]. But considering the lattice parameter mismatch for our quantum well, this effect is expected to be much smaller than $100\mu eV$.

Our experimental observations evidenced the following behaviour:

- the splitting increases with the photon exciton detuning δ ;
- the splitting increases also with the order j of the confined mode, corresponding to polaritons more and more excitonic.
- the orientation of the microwire with respect to the crystallographic axis strongly influences the value of the splitting.

The increase of the splitting with the excitonic component and the influence of the orientation of the structures suggest that the excitonic component must have a key role in the generation of the splitting and the dependence on the orientation of the structure is a signature of the probable role of strain.

A possible interpretation to explain such high values of splitting can relies on previous work of Balili and coworker on a strain induced polariton trap[106]. According to this work, the presence of strain could generate a splitting in the excitonic state but also could bring the energy of light and heavy hole near to each other. The mixing between heavy and light excitons will results in a variation of the oscillator strength for the two polarization and so to an enhancement of the splitting. In this framework, the resulting splitting would be a result of a combination between excitonic and photonic contribution.

In chapter 5, we will describe more in detail the effect of such polarization splittings on the precession of the polariton pseudospin.

2.2 Experimental setup

We now briefly resume the main characteristics of the micro-photoluminescence setup used in the present work. A scheme of such setup is reported on figure 2.8.

2.2.1 The cryostat

All the reported results are performed at a temperature of 10 K. The sample is therefore pasted on the cold Finger of a ST-500 Janis Cryostat mounted on a translational stage. The

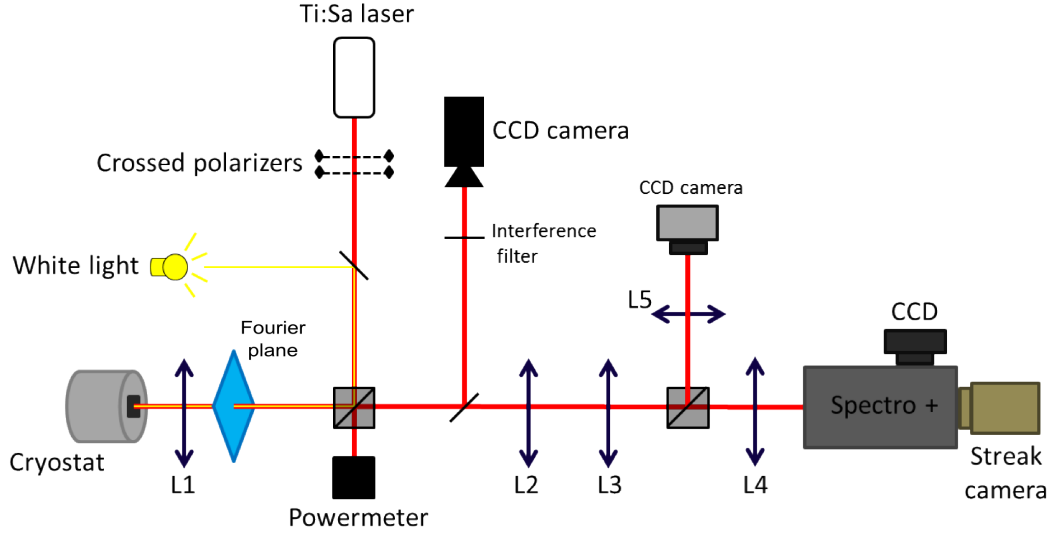


Figure 2.8: Scheme of the experimental setup.

thermal conduction is assured by the use of a vacuum grease (Apiezon N Grease). A constant flow of Liquid Helium is set in order to maintain the cold finger at a temperature $T=10$ K. The chamber is maintained at a high vacuum, at a pressure between 10^{-5} and 10^{-6} Torr, thanks to the use of a Turbo Molecular Vacuum Pump.

2.2.2 Excitation

Three different laser sources have been used to obtain the reported results.

- A CW Ti:Sapphire monomode laser (Matisse-Spectra Physics). The emission is continuously tunable in the spectral range of 690-900 nm.
- A pulsed Ti:Sapphire laser (Tsunami-Spectra Physics). The emission is tunable in the spectral range of $700\text{nm} - 1\mu\text{m}$. The delivered pulsed width is 1.4 ps with a repetition rate of 82 MHz. This laser will be used in the time resolved measurements.
- In the experience requiring a second excitation non resonant spot ($\lambda \approx 730\text{nm}$), together with a resonant one ($\lambda \approx 780\text{nm}$), a CW compact Ti:Sapphire laser (Solstis-M-Squared) with emission tunable in the spectral range of $700\text{nm} - 1\mu\text{m}$ has been used.

The sample is excited at normal incidence. In the case of non resonant excitation the laser is set at around 730 nm, corresponding to the first reflectivity deep of the Bragg mirrors in the presented cavity.

The laser hit a 50/50 cube and the reflected beam is focused on the sample by a microscope objective of large numerical aperture ($N.A. = 0.55$) and focal distance $f_1 = 4\text{mm}$. The resulting size of the spot is around $2\mu\text{m}$. Additionally spherical or cylindrical lenses have been used to increase or reshape the size of the spot in some of the presented experiment. The microscope objective is mounted on translation piezoelectric stage, allowing to place the spot

with micrometric precision. This is essential for properly control the excitation of the micro-structure .

2.2.3 Detection

The emitted signal is collected with the microscope objective, collimated by lens L1 and then sent through one of the optical path schematically represented in figure 2.9, allowing the imaging of both real and reciprocal space.

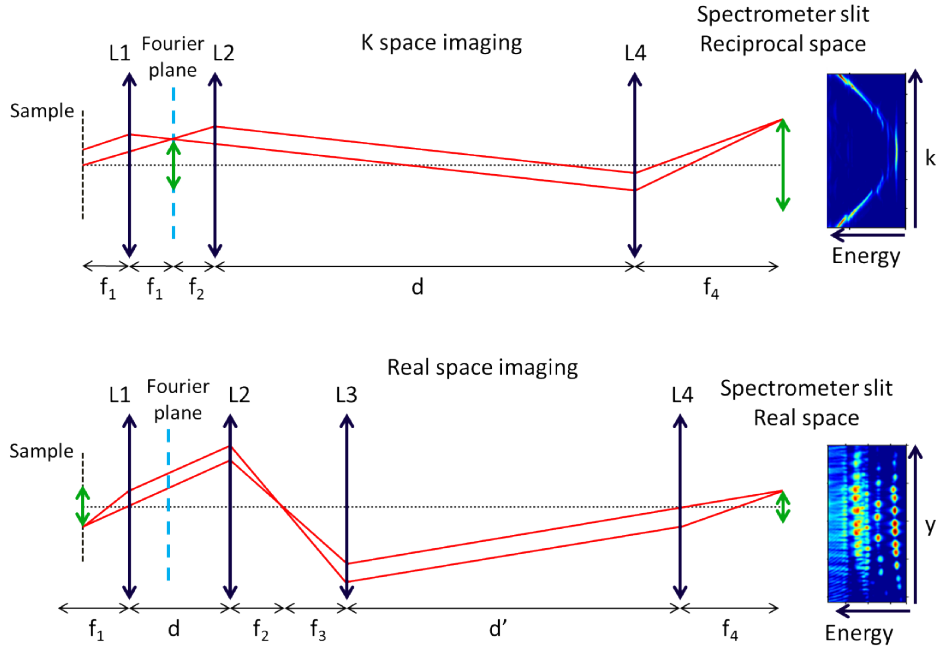


Figure 2.9: Scheme of the optical path for the imaging of real and Fourier space.

The collected signal is focused on the slit of a Spectrometer and then either imaged via a CCD camera, cooled with liquid Nitrogen, or with a Streak Camera (see next paragraph).

The one dimensional microstructure are properly aligned with their main axis parallel to the fenditure objective. To change their inclination, during an experiment, a Dove prism has been placed along the optical path.

A 2D imaging of both Real or Fourier plane was possibly obtained by focusing a fraction of the total signal on an additional CCD camera. This camera were also used to image the surface sample under white light illumination and detect and distinguish the micro-structures.

Eventually, interference filters were placed in front of this camera to get rid of the non-resonant laser signal.

2.2.4 Time resolved measurements: the Streak camera

Time resolved experiment were realized with used of a pulsed Tsunami laser and a Hamamatsu Streak Camera.

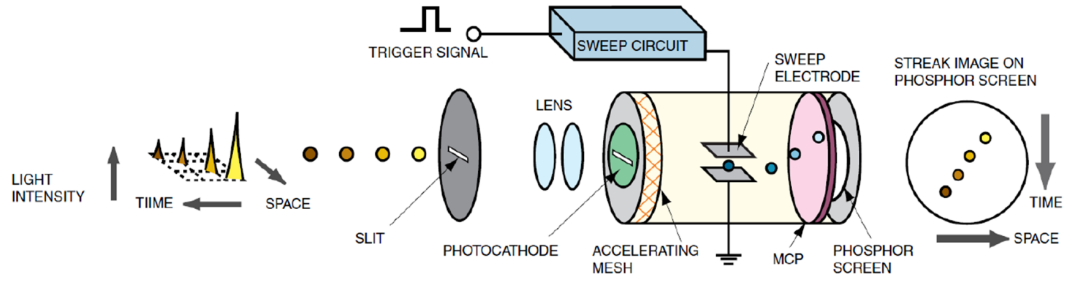


Figure 2.10: Scheme of the operation of the Hamamatsu Streak Camera.

The principles of operation of such a streak camera is depicted in Figure 2.10.

The collected signal hitting the photo-cathode excites photoelectrons inside the streak tube. These photoelectrons are accelerated and they travel inside the tube through a region in which there is an electric field whose strength varies in time (region between the electrodes). Early photons create photoelectrons that encounter a field that deviates them upwards. Photoelectrons created by later arriving photons suffer an electric field that deflect them in a different vertical direction (downwards). In this way, the vertical direction behind the electrodes acquires a meaning of time evolution, while the horizontal axis can represent either a position of the sample or an angle of emission. After the electrodes a multichannel plate multiplies the number of electrons impinging upon it. Finally, the amplified photoelectrons hit a phosphor screen whose light is recorded by a CCD. In the CCD the vertical direction means time while the horizontal direction has the same meaning as the horizontal dimension of the light arriving at the photocathode, which can be wavelength or spatial dimension (real space or momentum space). In this configuration the 1 dimensional structures have their main axis aligned horizontally. The streak camera has also been coupled with a spectrometer in order to detect the time evolution of the emitted signal. In this case, the horizontal axis of the Streak CCD camera corresponds to the energy scale. The detected signal correspond to the region of the sample selected by the thin slit of the spectrometer. By varying the selected point on the sample surface a complete map of time space and energy of the emission is obtained.

The sweeping-voltage frequency that deviates the electrons is synchronized with the repetition rate of the excitation laser via a fast photodiode. In this way, millions of identical measurements (one per excitation pulse) can be performed and signals can be obtained even in low-emission intensity conditions. The largest time window of the streak camera has a size of 2100 ps with a resolution of about 30 ps. However the resolution can be improved below 10 ps by operating the camera in a regime with a smaller time window.

Chapter 3

Polaritons propagation and interaction with defects

3.1 Introduction

The possibility of making polaritons propagating over large distances opens a wide range of possibilities: as photons, polaritons can propagate in a coherent way and with a propagation speed near the speed of light; but with them they bring non linearities orders of magnitudes stronger than other purely photonics systems [9, 107], making possible, for example, the propagation of non linear bistable front in an optical circuit [34, 29]. At the same time, their velocity, their density and also and the potential in which they move in can be optically controlled. Additionally, the escape of the photons from the cavity gives a direct and easy way of detecting the behavior of the system, making a moving polariton gas an ideal playground for investigating non-linear quantum hydrodynamic [18] on one side, and on the other hand to monitor and implement non linearity-based optical devices [31, 28].

In this chapter we will first give a brief overview of the state of the art on polariton propagation. We will discuss and illustrate different excitation techniques, resonant, OPO, and non-resonant excitation, since all of them or the mechanism on which they are based will play a role in the rest of the manuscript.

We will particularly focus on the case of non resonant excitation, presenting results obtained at LPN just before my arrival in the group.

Starting from these results, we then focus on the propagation of polariton gas along a microwires. In this context we will present our observations of the suppression of backscattering by disorder in wires-microcavity. We will discuss why an interpretation in terms of superfluidity is not applicable, and we will propose and illustrate a mechanism for a backscattering quenching based on the onset of spontaneous parametric processes.

3.2 Polariton propagation

Requirements and limitations for observing moving polaritons

The observation of a ballistic propagation of polaritons required the overcoming of several limitations.

The growing process of both QWs and the Bragg mirrors can introduce rugosity on the QWs layers, and at interfaces of the cavity and mirrors's layers. These will result in the generation of local variation of the energy of the polaritonic states. Such fluctuations, if comparable with the polariton kinetic energy, can represent potential wells or barrier forbidding a ballistic motion for polaritons. Such defects, , turned to be helpful to trigger the nucleation of topological defect such vortex and solitons in CdTe[23, 24] and GaAs[21, 20] cavities, but most of the time resulted in uncontrolled spatial inhomogeneity of the polariton density and excluded the possibility of observing free propagation[12].

Furthermore a second intrinsic limitations is imposed by the finite polariton lifetime. Up to recent years, the photon lifetime in the cavity has been limited to few ps[108]. Besides the high propagating polariton speed of typically $2\mu m/ps$, this short lifetime forbids the observation of polariton only few microns away from the excitation region. Nowadays, cavity quality factor reached values near $Q = 10^5$, corresponding to polaritons lifetime longer than 50 ps[109, 110].

GaAs based cavities have presented up to now the best system to study polariton propagation. Propagation lengths longer than $40\mu m$ were observed in cavities grown at LPN, as discussed more in details in this chapter [39]. Analogous propagation lengths have been obtained more recently also in GaAs based cavity grown in the group of Pavlos Savvidis in Crethe. In such samples it has been observed phase-locking between polaritons states generated by laser spots $80\mu m$ far away[111], or polariton spin precession measured up to hundreds of μm away from the excitation[109]. Lately, the group by David Snoke in Pittsburgh University reported high Q factor cavity where polariton signal were detected $1mm$ away from the pump [112]. Additionally, it's worth mentioning that first evidences of polariton propagation has also been obtained and recently presented for ZnO based microcavity[113].

3.2.1 Excitation techniques

An additional and essential requirements for studying polariton propagation is an efficient technique for injecting polaritons with a controlled wave-vector. Several experimental approaches have been used at this purpose.

Resonant excitation

A resonant excitation of the polariton states allow to properly control the propagation velocity of the excited particles. This is due to the one-to-one correspondence between the in-plane $k_{||}$ component of the wavevector of exciting photons from the pump laser and the generated polaritons. It was in this configuration, that Thomas Freixanet and collaborators performed the first studies on cavity polaritons propagation in 2000 [108]: polaritons were injected by pumping resonantly the lower branch with a well defined incident angle. The group

velocity of the wavepacket was measured in time resolved experiments, as shown in figure 3.1, and the dependence of the velocity on the exciton photon detuning was extracted.

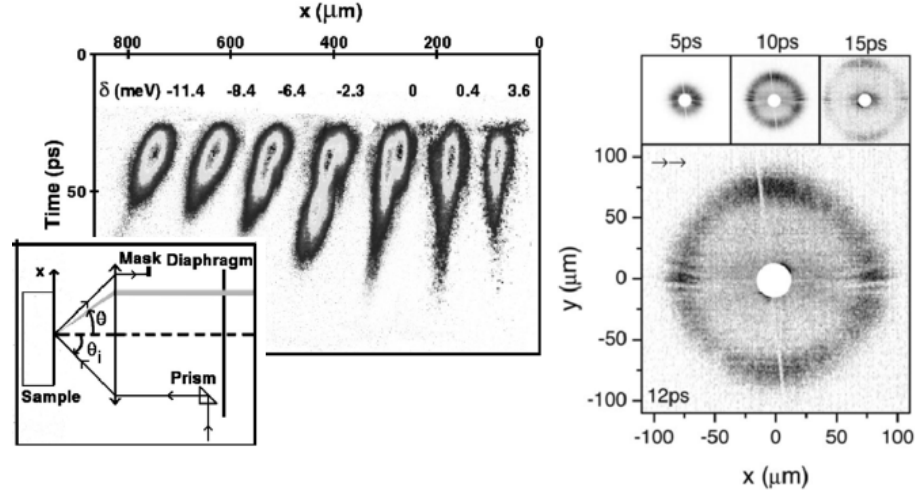


Figure 3.1: Left: Measure of polariton group velocity under pulsed resonant excitation. The incident angle of the excitation laser imposes the k -wavevector of the injected polaritons. Different group velocity are observed by varying the detuning δ . Figures extracted from [108]. Right: Observation of radial polariton propagation under resonant excitation. The laser spot, in the center of the figure, is blocked to do not blur the polariton signal. Figure extracted from [114]

Propagation have been also investigated by Wolfgang Langbein [114]. In this experiment the laser spot was only few microns wide and consequently broad in k space. The selection of the polariton state was so given not by the incidence angle but by solely the pumping laser energy. The possibility of controlling also the initial polarization of the polariton states, allowed W. Langbein to obtain the first evidence of Optical Spin Hall effect[70] in terms of polarization beats observed along the propagation.

We will use an analogous approach for generating polaritons in the interferometer structure discussed in chapter 5.

Triggered OPO

The resonant excitation appears as the most straightforward way to make polaritons flow. But this configuration can presents many difficulties when it comes to the detection of the polariton movement. The energy and polarization of the signal will indeed be the same and so the detection risk to be saturated by the excitation laser signal. In the experiment of Freixanet and Sermage mentioned above, the laser signal was cutted by spatial or angular selection.

An alternative technique to overcome this limitation was developed by A.Amo and D. aniel Sanvitto in the group of Luis Vina in Madrid[115]. The technique is based on optical parametric oscillations (OPO).

Parametric oscillators are non linear resonators in which a coherent pump wave is converted into coherent *signal* and *idler* waves of different frequency. In optics, let's consider a non linear

media, presenting χ^3 non linearities pumped with a laser wave ω_p and inserted in a resonator. A frequency conversion can takes place respecting the energy conservation $\omega_s + \omega_i = \omega_p$. This process is strongly enhanced when signal , pump or idler (ore more than one of them) are resonant with an optical cavity mode. For micro-cavities in the strong coupling regime, the non linearities provided by excitons has been shown to allow a pair scattering, especially under a resonant excitation at energy E_P of the polariton dispersion[9, 10, 116, 117]. Such process must obey the energy and momentum conservation rules, also called phase matching condition:

$$2E_P = E_S + E_I \quad (3.1)$$

$$2\vec{k}_P = \vec{k}_S + \vec{k}_I \quad (3.2)$$

Given the shape of the polariton dispersion, such conditions are more easily satisfied when pumping at the inflection point of the LP dispersion,also named *magic angle*. It provides several pairs of point that satisfy 3.1 and 3.2. It has been shown that increasing the excitation power at the magic angle, a high occupation of the $k = 0$ signal state was achieved (see figure 3.2) . The high population in such state further stimulates the scattering process as a result of the bosonic stimulation. Thanks to a second probe laser placed at the energy of the idler state, an optical parametric amplification was achieved, and high gain, up to 70, was obtained, signature of the bosonic stimulation effects[9, 118, 107].

This effect was exploited later in an experiment of D. Sanvitto and A. Amo to make polaritons flow. The combination of a continuous pumped laser at the magic angle with a probe laser populating the idler state (see figure 3.2) allowed to trigger the optical parametric oscillations (TOPO) and achieve a high coherent population of a signal state with a non-zero wave-vector. Additionally, the population corresponding to the signal state was continuously replenished by the CW pump laser, extended over tens of microns (also shown in figure 3.2). This configuration allowed to observe polariton propagating of a polariton wavepacket against a point like defect, to extract signature of a superfluid motion[115], and more recently was used in the generation of polariton Bright Solitons[22].

3.2.2 Propagation under non resonant excitation

In the following paragraph we discuss more in details another approach for generating a highly populated and coherent flow of polaritons, by using non resonant excitation, based on exploitation of the coexistence of polaritons and excitons in the reservoir.

This approach was developed just before my arrival in the group of J.Bloch. It was the subject of the Phd Work of Esther Wertz, who investigated polaritons in 1D photonic structures.

Condensation regime: real and reciprocal space

In the first chapter we discussed how the bosonic nature of polaritons and their interaction properties allow them to condensate and to obtain a macroscopically occupied single state. Condensation takes place at the $k = 0$ state of the polariton branch. In such a case, polaritons don't possess any kinetic energy and they will necessary stay in the pumping region. This

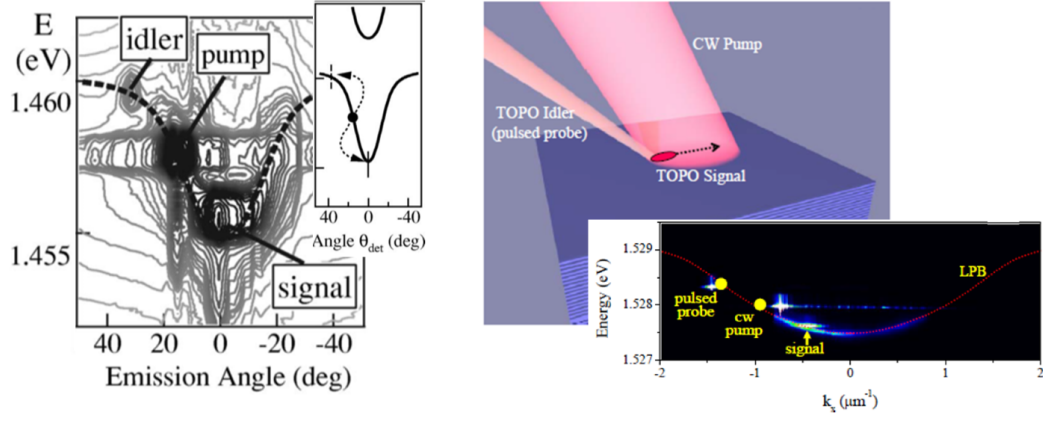


Figure 3.2: Left: PL spectra of a resonantly excited GaAs-based microcavity at the magic angle with a CW laser power above the threshold for stimulated OPO operation. High occupation of the $k = 0$ state is obtained. Figure extracted from [118]. Right: Excitation of propagating polariton via TOPO. A cw pump at the magic angle, together with a pulsed probe laser, generates a propagating signal that is replenished by the pump over several microns. Figures extracted from [119].

description is valuable for the case in which the excitation spot extends homogeneously over a large region of the cavity, that was the case corresponding to figure 1.9.

The behaviour changes drastically in the case of small spot excitation. Let's consider the case of a 1 dimensional microcavity as described in chapter 2, excited with a non resonant spot with a diameter of $2 \mu\text{m}$. For low excitation power, the whole lower polariton branch is incoherently populated with polaritons of several k -vectors. By increasing the excitation density and observing the total emission as a function of power, (fig 3.4) a condensation threshold P_{th} can be identified, corresponding to a strong non linear increase in the intensity, accompanied by a spectral narrowing of the emission.

The corresponding real space image shows the formation of a polariton condensate extending over hundreds of microns (figure 3.3).

By looking at the angle and energy resolved emission above threshold (fig. 3.4) we observe how the emission comes from $k = 0$ in the spot region, confirming how condensation takes place in such a state. But away from the excitation region, polaritons acquire a kinetic energy and a finite k vector.

The role of the excitonic reservoir

To explain this effect we remark how in the spot region, in the case of non resonant excitation, an excitonic reservoir is created. The repulsive interaction between polaritons and exciton of the reservoir results in a renormalization of the polariton dispersion with a local shift E_b towards the blue of the polariton branch (see figure 3.4). The high effective mass of excitons in the reservoir forbids their diffusion over large distances, and consequently the renormalization of the band is no more present outside the spot region. This interaction potential induce an effective force accelerating polariton outside the excitation region. Their potential energy E_b is converted

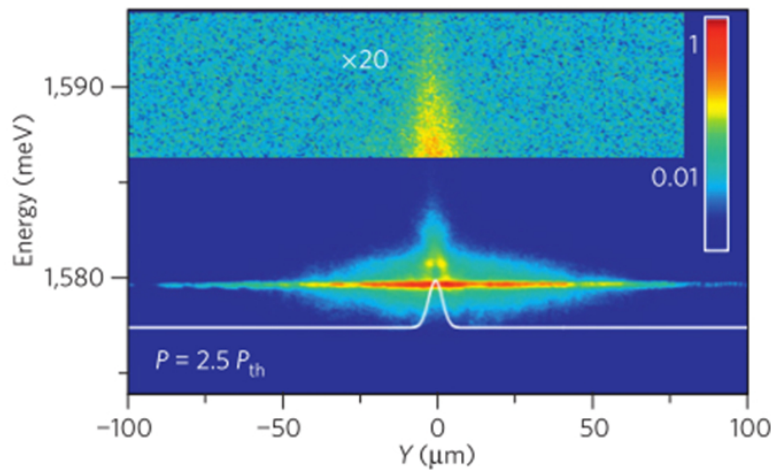


Figure 3.3: Real space emission energetically resolved coming from a microwire excited with a $2\mu m$ non resonant laser spot. The condensate is created at $y = 0\mu m$ and then spreads all over the wire. The contrast of the high energy part of the image is increased to put in evidence the signal coming from the excitonic reservoir, that remains localized in the excitation region. Figure extracted from [39].

in kinetic energy and so polaritons acquire a wave-vector $k = \sqrt{(2m_p E_b)/\hbar}$, as predicted by M. Wouters in [120]. The motion out of the excitation area will be ballistic, allowing the polariton condensate to extend all over the microwire (see figure 3.3).

In figure 3.3 we notice also a signal at the energy of the excitonic transition, collected due to photons emitted by excitonic recombination that escape from the edge of the wire. The localization of this emission confirms the low diffusion rate of the reservoir and its localization in the excitation region.

By varying the excitation power, above threshold, the population of the condensate and of the reservoir changes and so does the local blueshift E_b due to interactions. As it will be illustrated in more details later, this will give us a tool to control the k vector of the propagating polaritons and so the corresponding group velocity of the condensate.

Such local blueshift induced by the reservoir will be later on used in the manuscript not only for putting polaritons in motion but as an optical tool to reshape, from the outside, the potential in which polariton moves and so to accelerate, to slow or to trap them.

Coherent propagation

The propagation of polaritons has also been demonstrated to be coherent over long distances, thanks to an experimental configuration analogous to a Young slit experiment.

As schematized in figure 3.5, one can select two different points over the wire with two micrometric slits. The emission coming from these points interferes and the interference pattern is focused on a CCD. The onset and the maintenance of the coherence all over the wire length were put in evidence (as visible in the graph of fig.3.5).

This coherent propagation will be further exploited in the polariton interferometer presented

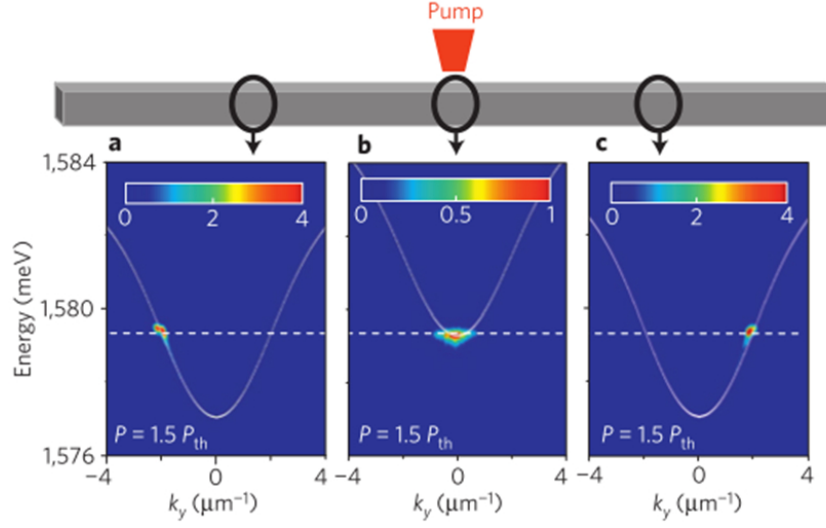


Figure 3.4: Far field emission coming from different region of a microwire. The shifted polariton dispersion is indicated on top of the images to put in evidence the local blueshift of the dispersion curve. Figure extracted from [39].

in chapter 5.

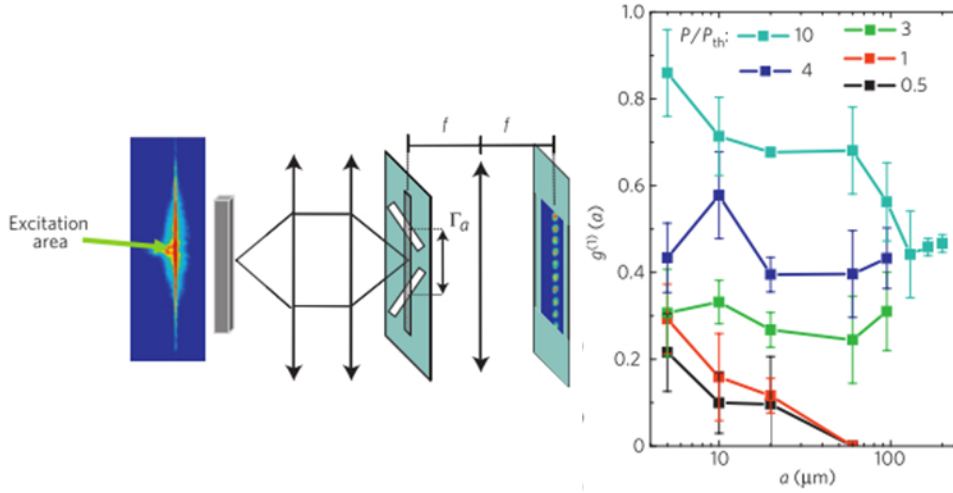


Figure 3.5: Left: Scheme of the double slit experiment for the coherence measurements: interferences between two different point of the wire at distance a are detected. Right: Results of the $g(1)$ measurements as a function of the distance a between the two point for different excitation powers. Figures extracted from ref. [39].

3.3 1D propagation against random disorder

We have presented how the resonant excitation allowed to generate a coherent polariton flow. We have also discussed how the k space imaging spatially selected presented in 3.4 gives a clear indication of the effect of acceleration from the excitation region towards the side of the wire. We now better observe the two panels corresponding to far field emission from the two sides of the spot.

In those images, one should remark that all the emission belongs to polariton with a well defined wavevector, corresponding to polariton moving away from the spot, but no additional components are observed. It seems that polariton propagates ballistically without undergoing any scattering. One indeed could expect that some imperfection on the sample could generate some defects elastically reflecting polaritons. Such disorder could be either too weak or we are in presence of a mechanism that reduces the backscattering probability. To answer such question, we better investigated the far field emission of polariton along their propagation.

3.3.1 Observation of backscattered polaritons

Let's now consider the following experimental configuration, represented in figure 3.6. A 200 μm wire is excited non resonantly with a tightly focused laser spot positioned near one of its edges. Polaritons are then generated in the spot region and propagate far from it, as sketched in figure 3.6.

By a proper positioning of a mask on the optical path of the collected signal, it is possible to imagine the reciprocal space emission of a selected region of the wire and focus it onto the slits of the spectrometer.

Here we select a region of the wire 30 μm long, placed 100 μm away from the excitation spot. In figure 3.6 we plot the real space emission coming from this region corresponding to an excitation laser power below condensation threshold. The polariton dispersion in the spot region is homogeneously populated by an incoherent population. Polaritons with a positive wavevector travels towards the right and reach the observation region. Here, the emission is dominated by polaritons with positive k vectors, populating the right side of the dispersion. But a weaker signals is also collected on the left side of the dispersion, corresponding to contrapropagating polaritons.

One can quantify the relative amount of contrapropagating polaritons by estimating the ratio between the backpropagating polariton signal $I(-k)$ and the forward propagating ones $I(+k)$. This quantity is evaluated for several energies and plotted in the graph of figure 3.6. The value of this ratio below threshold strongly varies from wire to wire, and from the region of wire observed: it depends on the detail of the disordered potential.

The wire reported in the figure is among the one where highest values of backscattering signal were observed. Nevertheless, expect for extremely low kinetic energy ($E_k < 0.2 meV$)¹, we observe how this quantity is low, never higher than 20 %, confirming the high quality of the

¹The investigation of the propagation of polaritons at low kinetic energy $E_k < 0.2 meV$ is an ongoing activity in the group. Preliminary evidences of effects related to the Anderson localization have been obtained.

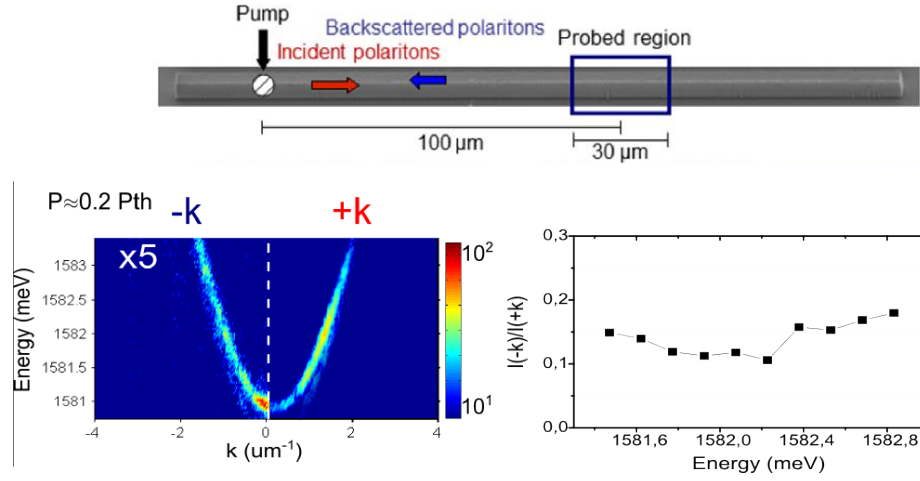


Figure 3.6: Top: Scheme of the experiment: the microwire is excited with a $2 \mu\text{m}$ non resonant laser spot near its left edge while the probed region is $100 \mu\text{m}$ away. Bottom left: Normalized far field emission of the polariton gas collected from the probed region for an excitation below threshold ($P \approx 0.2P_{th}$). The signal from the negative k -vectors side of the dispersion has been enhanced of a factor 5. Bottom right: The backscattering ratio $I(-k)/I(+k)$ evaluated from the left panel, for different values of polariton kinetic energy.

wire. Additionally, we notice how this values does not significantly depends on the polariton energy, as shown in the right panel of figure 3.6

Let's discuss the possible origin of such a signal.

- The large mass of excitons, (10000 times that of polariton), limits their diffusion length[121]. As also confirmed by the spatial profile of the free excitons signal shown in fig.3.3, excitons have a diffusion limited to few microns from the excitation spot. Therefore, in the observed region, at $100 \mu\text{m}$ from the spot, we can exclude any feeding of the polaritons state from an excitonic reservoir.
- One can consider the possibility that polaritons could pass through the observed region and undergo a reflection against the other edge of the wire and then come back generating some negative wavevector signal. This contribution can be estimated considering the distance between the observed region and the edge of the wire (around $100 \mu\text{m}$), a polariton propagation speed of around $2.4 \mu\text{m}/\text{ps}$ and a polariton lifetime of 16 ps [52]. The continuous escape of photons during propagation is responsible for an exponential decay of the population. The given parameters result in a reduction of a factor around 200 between the incoming signal and the signal coming back after a reflection against the edge. The observed contrapropagating signal, of the order of 10% the incident one, cannot be explained by this effect.
- Additionally, one can consider a possible influence of interaction with phonons during polariton propagation. But also this hypothesis can be excluded by considering the time scale characteristic of such interaction, of the order of hundreds of ps [73, 54], much longer than the overall polariton lifetime itself.

We finally attribute this contra-propagating signal to a scattering undergone by polariton against a random disorder potential along the wire. The origin of this disorder can be attributed mainly to weak strain accumulated during the growth of the mirrors and also to the non-intentional rugosity that is formed on the walls of the wires during the lithography and etching process.

The variability of the backscattered signal observed from wire to wire supports the interpretation of such signal as the result of the interaction with a random potential in the sample. But at the same time, these large variations complicates the identification of its nature, either photonic either excitonic [122, 123, 124, 125]. The regular spatial density profiles observed on the wire and the low value of the backscattered ratio, never more than 20%, suggests this disorder to be weak: the theoretical simulation described in the next section, reproduces the backscattering ratio at low power considering a disorder strength around 0,1 - 0,4 meV.

Power dependence of the backscattering signal

Let's now study the effect of the increase of the excitation power and with this, of the polariton density.

Results in figure 3.7 corresponds to the same experimental configuration of figure 3.6 on a slight different wire.

In the upper left graph of the figure, we plot the overall signal collected in the selected region: we can clearly identify a non linear increase of the total emission, signature of the condensation process, and consequently of a higher local polariton density.

In the four lower panels of figure 3.7, we show the reciprocal space emission coming from the observed region. The images are plotted in logarithmic color scale, in order to better visualize the negative k vector side of the dispersion.

In these panels we observe that, increasing the excitation density above threshold, the incident condensate acquires a well defined wave-vector, as discussed in 3.2.2. But by observing the negative k values part of the dispersion corresponding to backscattered signal, a decrease of the backscattered intensity is visible with the increase of the polariton density.

Such a reduction is quantified by plotting the ratio of the backscattered $I(-k)$ to the incident polariton signal $I(+k)$ measured at the energy of the maximum peak signal, as a function of the total polariton density in the probed region. In figure 3.8, we report the value of such ratio. It starts from a value of around 10% below threshold and then is reduced up to a factor of 20 increasing the polariton density ².

Together with this reduction, we observe how the increase of the power also bring to an increase of the reservoir potential in the spot region, and so the kinetic energy and the k vector of the generated condensate. This values are represented in the panel b of figure 3.7, where we observe how they follow the polariton dispersion. This increase continues until the propagating condensate reaches the inflection point of the polariton branch. Furtherly increasing the power, we observe the appearance of several coexisting highly occupied states, at different energies and k -vectors, that we named "relaxed" condensates.

²The residual signal with negative k values is probably generated mostly by the reflection of polaritons against the edge of the wire, as discussed in 3.3.1

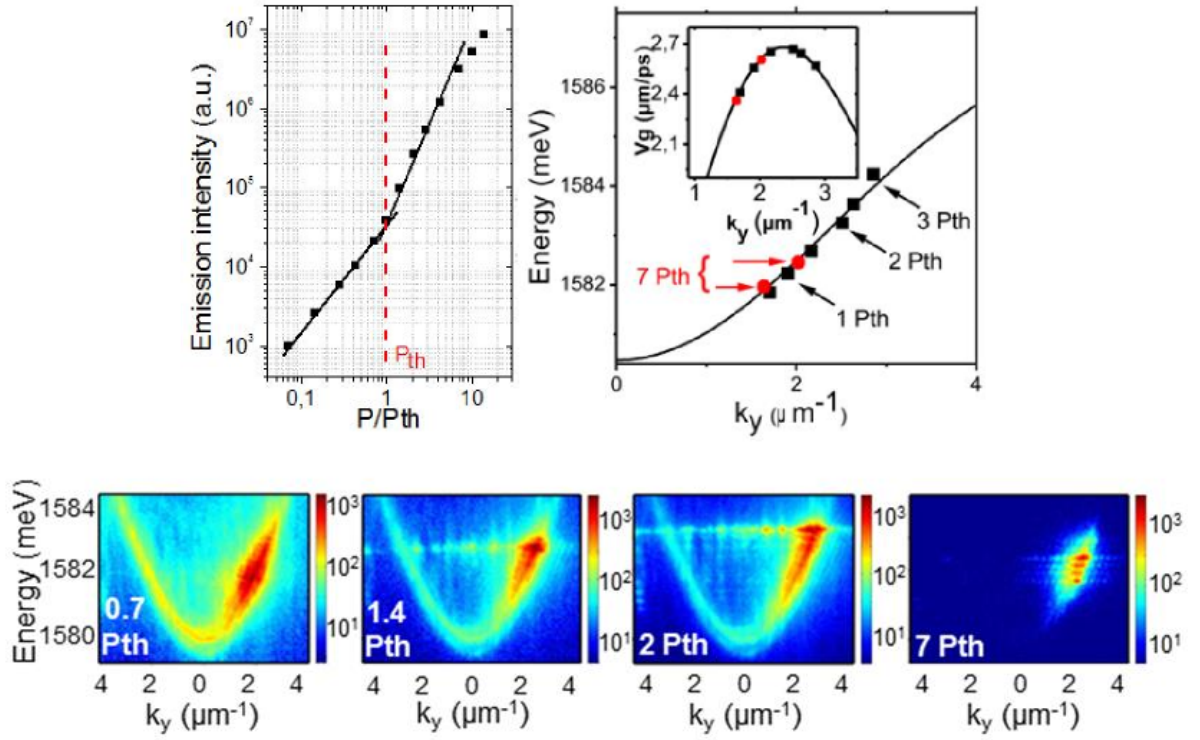


Figure 3.7: Up Left: Emitted intensity in the probed region as a function of excitation power; the red line indicates the condensation threshold. The experimental configuration is the same than figure 3.6. Up right: Energy and momentum of the polariton condensates at different excitation powers, below (black squared points) and above (red round points) the onset for parametric instabilities. The solid line shows the polariton dispersion and the inset the corresponding values of the group velocity. Bottom: Normalized far field emission of the polariton gas collected from the probed region for different excitation power (Logarithmic color scale)

Our interpretation of this energy relaxation effect is based on the onset of a parametric instability process, giving rise to parametric oscillation effect, in analogy to what discussed in section 3.2.1 for resonant pumping of the magic angle.

In our case, the OPO is spontaneously triggered when a sufficient population is accumulated in the condensate and when such a condensate approaches the favorable inflection point of the dispersion. The idler signal, expected at high energy, near the excitonic reservoir, is not visible in the spectra: as in previous OPO experiment, its intensity is expected to be much weaker than the "signal" one due to both the worst outcoupling of highly excitonic polariton state, and the faster scattering of those polaritons towards higher energy and larger momentum states [118]. The absence of an idler emission is, anyway, still a point not completely understood.

We also mention that a possible contribution to the energy relaxation has been proposed in ref. [126] to come also from interaction with the excitonic reservoir.

A better visualization of the resulting condensate energies is given in figure 3.9, where the integrated emission spectra for 3 powers above threshold are reported. The appearance of several equidistant energy peaks is visible for the highest power. But also at lower power, few additional

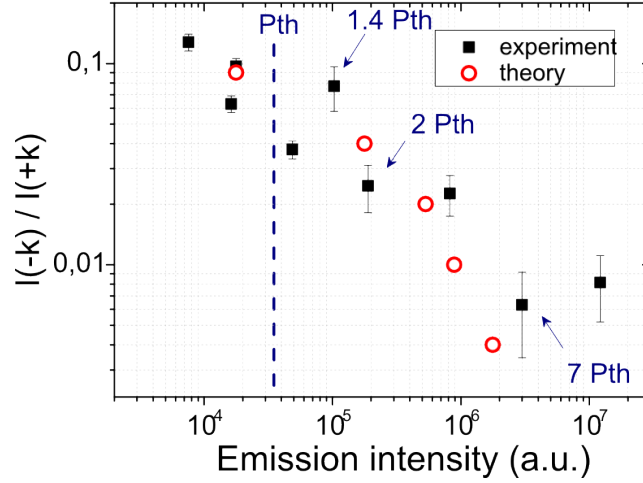


Figure 3.8: Black squares indicates the ratio of the backscattered $[I(k)]$ to the incident polariton signal $[I(+k)]$ in the probed region measured at the energy of the peak signal, extracted from the experiment illustrated in figure 3.7, and plotted as a function of the integrated polariton signal in the observed region. The red circles represents the result of a numerical simulation described later in 3.3.2.

energy peaks are observable. Such equally spaced lines are consistent with parametric processes as will be further detailed later.

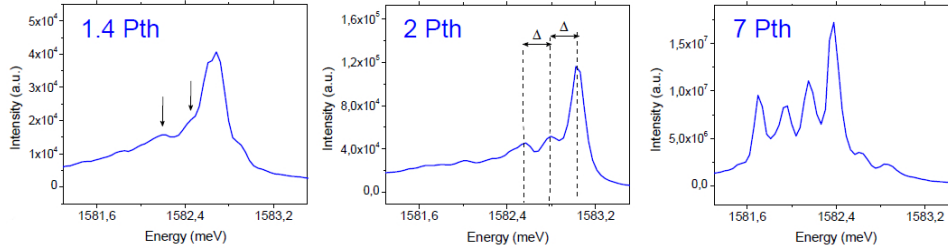


Figure 3.9: Emission spectra for several excitation power corresponding to the panels of fig.3.7. The flashes in the first panel indicates the early appearance of energetically equidistant peak, signature of parametric processes. These peaks become more and more pronounced at higher power.

3.3.2 Theoretical interpretation: onset of parametric scattering

The observed reduction of the backscattered signal when increasing the particle density strongly suggests that polariton-polariton interaction may be involved.

Superfluidity VS supersonic motion

In the framework of interacting bosons, one of the most spectacular features characterizing such systems is a phase transition towards a superfluid state. Superfluidity was originally

observed in liquid helium [127] [128], and then deeply investigated in atomic Bose Einstein condensates [129]. It manifests itself with a vanishing viscosity of the fluid up to a complete frictionless and dissipative-less motion in presence of defects. Such phase transition was first predicted and then observed for 2-dimensional polaritons. In a proposition by Carusotto and Ciuti [130], the Bogoliubov treatement was applied to the polariton excitation spectrum. In this framework, the effect of repulsive interparticle interactions is the renormalization of the band dispersion, as shown in the figure 3.10.

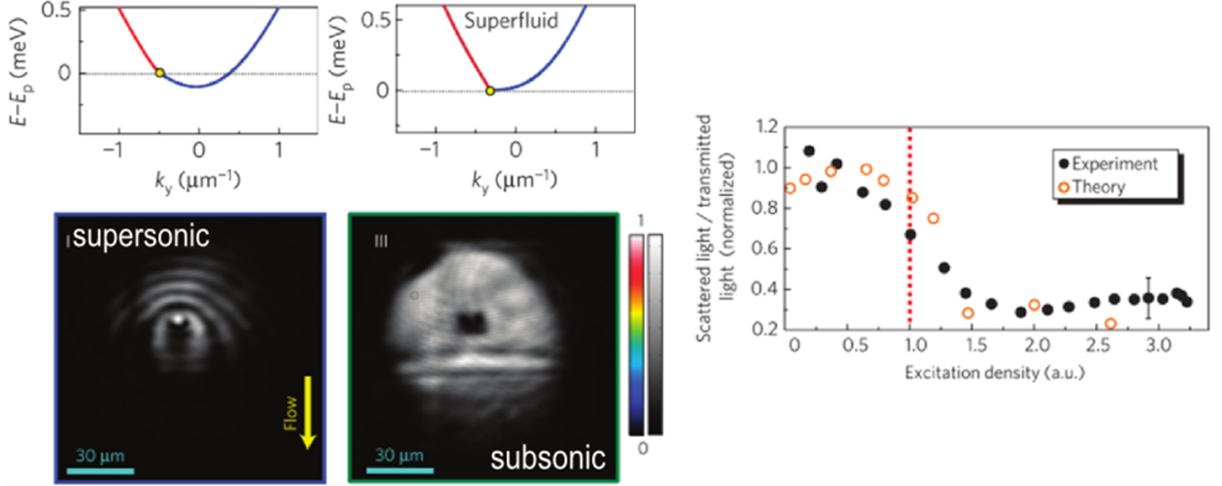


Figure 3.10: Top left panels: Polariton dispersion renormalized by interparticle interaction; on the left a low density regime corresponds to supersonic motion, in which, for the indicated energy, states for elastic scattering are available. On the right the subsonic and superfluid regime is represented, where elastic scattering is not possible anymore. Bottom left panels: Density distribution of a 2D polariton fluid flowing against a point like defect. In the supersonic condition backscattered signal generates Cerenkov interference pattern, while the flow is unaffected in the subsonic regime. Right: Ratio of the scattered polaritons over the incident ones as a function of the excitation power. All figures are extracted from ref [19].

If we consider an impurity as an elastic scattering center, we observe how, sufficiently renormalizing towards higher energy the polariton bands via the interaction energy, one can reach a regime in which no more states are available for scattering. This corresponds to a transition from a Cerenkov regime, to a superfluid one, where the fluid presents no diffusion against the barrier and flows unaffected.

The transition point is given by the Landau criterion[131]: given a certain density of interacting particles n in the condensate, one can define a speed of sound in the system as

$$v_s = \sqrt{gn/m} \quad (3.3)$$

where g is the interaction constant. The Landau criterion states that a superfluid transition can take place only for fluid velocity lower than the speed of sound.

This transition was experimentally demonstrated by Alberto Amo, in an experiment performed in the Laboratoire Kastler Brossel in Paris [19], in which the disappearance of Cerenkov wave was observed together with the collapse of the signal in the Rayleigh scattering

circle moving from supersonic to subsonic propagation (as summarized in the figure 3.10).

Let's now analyze the experimental situation presents in our wire. In 1D dimensional system a phase transition at finite temperature cannot rigourosly exist[132]. This general dogma has been shown to drop in the presence of interaction[133] and it has also been shown that repulsions between particles can lead to an enhancement of transmission of a bosonic particle flow through 1D channel[134].

Even in non-equilibrium system, the Landau-Criterion remains an intuitive picture to identify superfluid-like phases [94, 25].

In our experimental configuration, the propagation speed of the polariton flow is around $2.4\mu m/ps$, that corresponds to a kinetic energy of around $2 - 3meV$ above the $k = 0$ state (fig. 3.7). In order to satisfy the Landau criterion, the interparticle interaction energy required should be of the order of such a kinetic energy.

In the observed region, after $100\mu m$ of propagation from the spot, the polariton occupation factor can be estimated at maximum value of $5 \cdot 10^2$, that corresponds to an interaction energy lower than $0,1meV$ [36].

Additionally, we can notice that, if the interaction energy would have been comparable with the kinetic energy, we should have observed a conversion from potential to kinetic energy during the propagation of the polariton condensate due to the decrease of its density .

This has not been revealed by careful analysis of the far field at different location along the wire. Indeed, if we follow the propagation of the condensate in different point along the wire, what we observe is essentially a constant velocity and a constant k-vector propagation.

We can conclude that the motion in the considered experiment is in the supersonic regime and therefore we can exclude any superfluid effect.

In the following section, we will propose an alternative mechanism, based on parametric processes, to explains the experimental suppression of backscattering.

Interacting particles in a 1D disordered potential

Let's consider a quantum particle in a 1D disordered potential landscape of characteristic strength V_0 .

Even for kinetic energy higher than V_0 , a quantum particle incoming against a potential barrier can either be reflected or be transmitted. In the case of a disorder potential, that can be considered as a random distribution of barriers, the initial wavepacket will split on each potential barrier, into a transmitted part and a reflected part , and interference between them can take place.

This phenomenon results in the well known Anderson localization[135]. In a pure 1D system with non interacting particles in a random potential, all single-particle eigenfunctions are localized, decaying exponentially in space.

Such a configuration has been realized experimentally using a quasi one-dimensional non interacting atomic gas, for which a disordered potential consisting of a speckle pattern was created optically. In the group of Alain Aspect [136] in 2008 (and with a bichromatic potential at LENS in Florence [137]) it has been observed that at short times the wavepacket spreads as

expected, but later on a steady states is formed, and the wavepacket acquires a characteristic exponential shape, with a certain localization length, and the diffusion is suppressed.

But in the case of interacting particles, the situation can drastically changes. Even if disorder can induce localization, repulsive interactions have the opposite effect of delocalization. A transition between localized and extended regime driven by interactions has been both predicted theoretically[133] and observed experimentally in atomic condensate at rest [138], due to an effect based on the spread of the single site localized wavefunctions and hopping of particles between adjacent sites.

It's in this framework that, in collaboration with the group of G. Malpuech in Clermont Ferrand, we propose a possible mechanism to explain the backscattering reduction observed.

We consider the irregular sequence of potential barriers as a lattice in the framework of tight binding model, in which the energy of each site is random, and there's an hopping constant J between sites.

We take for example two sites of energy E_1 and E_2 . If their energy difference is smaller than the hoping matrix element between two states J ($|E_1 - E_2| < J$), a particle can jump from one site to the other with probability P , rapidly decreasing with the energy difference. The probability of making N jumps is then given by P^N , that gives an exponential distribution around the starting site. Let's now extend this picture to a many body situation, in presence of interactions.

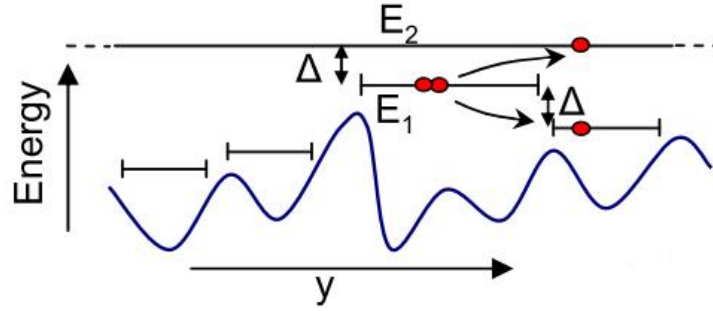


Figure 3.11: Schematic representation of the disorder potential showing the spatial extension of localized states (horizontal bars) while the flashes represent the two particle hopping process.

Interaction can shift the on site energy and so increase the probability of energy match and so of the hopping. In other word, if sufficiently high density of particles gets trapped in the localized sites, a screening of disorder can be achieved.

Secondly, we can include the possibility of a two body process by the onset of an OPO on-site scattering that could populate virtually any site.

The energy conservation for such a two body process (represented schematically in fig 3.11) can be written as : $E_1 + E_1 \Rightarrow (E_1 - \Delta) + (E_1 + \Delta)$, where 2Δ is the energy difference between signal and idler in the parametric process. The condition for hopping then becomes the following: $E_1 \pm \Delta - E_2 < J$, where Δ that can take any values, increasing the hopping probabilities. One should expect that, dealing with a two body-process, such probability would increase non linearly with the particle density. Furthermore, in analogy to the triggered OPO process, a macroscopic

occupation of one or several extended propagating states, can trigger and stimulate the hopping from localized states to such states. This would lower, in ratio, the negative k vector emission coming from localized states and backscattering events.

The 1D character of the system, with respect to the planar case, can enhance the influence of such a phenomena since the reduction of available scattering channels strongly enhances the interference effects.

The low value of backscattering measured in the experiment in the linear regime, suggests the presence of a weak disorder potential, that we can estimate between 0,1 and 0,4 meV thanks to the simulation that will be shown in the next paragraph. Therefore, the kinetic energy in the experiment is much stronger than the localization energy, and the effect of screening of disorder by highly populated localized states is expected to be weaker than that of parametric processes that, by themselves, tend to suppress localization in favour of propagation. Additionally, strong particle localization would result in bright intensity spots in the real space emission along the propagation, not observed in the experiment.

The experimental energy spectra of figure 3.9 confirm the appearance of several highly occupied propagating states.

Already at $1.4P_{th}$, small shoulders next to the main condensate peak appear (see flashes in the central panel of fig. 3.9). This power corresponds to an emission intensity of around 10^5 (see fig. 3.7), and to backscattering ratio that starts to decrease (fig. 3.8). These shoulders evolve into more marked peaks at higher excitation power, and the spectral equidistance between them is a good indication of their origin from parametric processes and that the hopping stimulated toward such propagating states could thus reduce the backscattering signal.

Numerical simulations

In order to support this interpretation, a numerical simulation has been performed in the group of Guillaume Malpuech in Clermont Ferrand. The propagation of a polariton flow through a disorder potential made out of a series of point like defects (δ -functions) has been simulated. . The system is described by two Schrödinger equations representing the evolution of the photonic and excitonic field, coupled via light matter interaction. The lifetime of the particles is taken into account introducing a lifetime for photons and excitons of $\tau_{ph} = 15ps$ and $\tau_{ex} = 400ps$. The disorder is represented by a δ -peaks potential term acting on the photonic field. The height and the density of the peaks are chosen as a fitting parameter in order to reproduce the experimental backscattering ratio at low particle density. One example of the disorder used is represented in figure 3.12.

The results of the simulations of the momenta distribution of the propagating condensate are reported in figure 3.12.

To simulate the experimental conditions for excitation below threshold, the system has been pumped with a pulsed excitation, large in energy and k , resulting in a distribution of positive momenta similar to the experimental one. In this situation, we observe a backscattered signal which intensity is used to calibrate the potential in accord with the experiment.

To simulate the situation above threshold the pumping is cw with a well defined energy and k -vector. In this case we observe how the backscattered signal decreases with increasing the

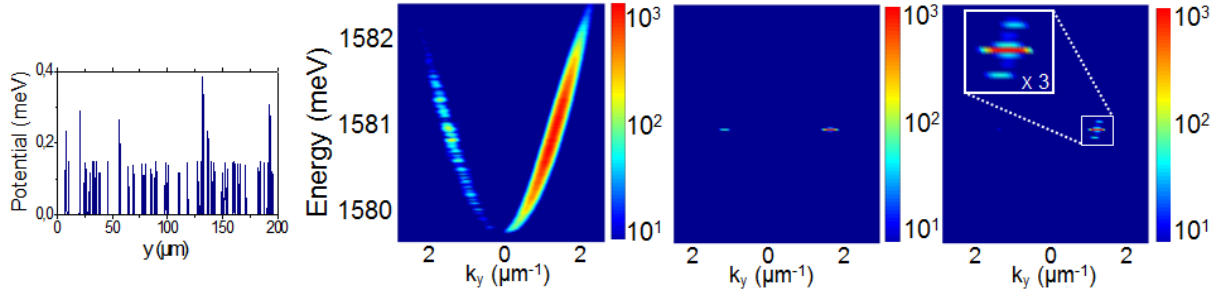


Figure 3.12: Left: Example of a disorder potential used in the model. Right panels: simulation of the polariton far field emission in the disordered potential with increasing polariton density. The backscattered signal progressively decreases. The upper left squared region in the last panel shows a magnification of the lower squared area, putting in evidence the appearance new frequencies, signature of the onset of parametric processes.

polariton density. Moreover, at higher density (right panel of fig 3.12), although the pump is kept monochromatic, we notice the appearance of new frequencies, signature of the onset of parametric processes. The density dependence of the backscattering ratio is plotted together with the experimental data, in figure 3.8. The reported results are the average over 50 different disorder realizations, in order to avoid any effect due to some specific random disorder distribution. The theoretical points reproduce the observed reduction of the backscattered ratio. This good agreement with the experimental results gives strong evidences of the role of parametric processes on the observed experimental backscattering reduction.

3.4 Conclusion

This chapter has been dedicated to the discussion of polariton propagation. The state of the art have been discussed introducing the main experimental configurations used to study a polariton flow, especially focusing on the case of non resonant excitation. Starting from the experiments of Esther Wertz on coherent propagation along microwire, we have focused our attention on the interaction of polaritons with random disorder along the wire. We have shown a strong reduction of the backscattering signal with the increase of the particle density, reaching an almost frictionless polariton propagation in a supersonic regime. We finally propose and illustrate a mechanism for explanation for a backscattering quenching based on the onset of spontaneous parametric processes. These results have been the subject of an article published in Physical Review Letters in 2012 [139]. They are very promising, since they show the possibility of ballistic propagation in a quasi-friction less way in photonic circuits.

Chapter 4

Polaritons in a 1D modulated potentials

4.1 Introduction

In this chapter we explore the possibility of shaping a one dimensional potential for polaritons thanks to the etching of some specific 1D structures.

The first part of the chapter will be dedicated to the study of polaritons in a periodic potential, obtained thanks to a microcavity wire with a periodically modulated lateral dimension. The modified polariton dispersion, in which forbidden energy gaps appear, allows to study several effects related to localization. The interplay between the blueshift induced by the reservoir and interparticle interactions induces the appearance of localized state inside the energy gap. We will show the condensation and localization of polaritons in gap states and the spontaneous formation of defect states and gap solitons.

In the second part we study polaritons in the presence of a potential energy gradient combined with a periodic modulation. This configuration has been obtained either by properly shaping the 1D microcavity profile or by exploiting the blueshift induced by the excitonic reservoir. The appearance of Wannier-Stark states and Bloch oscillations will be discussed.

In the last section we will consider polaritons in a quasi-periodic potential. Barrier and potential wells are ordered in a way that reproduces the Fibonacci sequence. The luminescence from these structures will give direct informations on the density of states, a direct visualization of the polariton wavefunctions and will show evidences of the Cantor-like character of the spectrum.

4.2 Particles in a periodic potential: general introduction

The behavior of a particle in a periodic potential has been the subject of a multitude of studies, initially focused on the investigation of electrons in a solid[40]. The first results belongs to the advent of quantum mechanics and corresponds to the work of F. Bloch, who, in 1929, published a paper in which he described the eigenstates of such a systems [41]. The main results

of the work is today known as Bloch Theorem. In this section we will summarize the key concept related to this theorem and will describe few properties of the particle dispersion and wavefunctions in a periodic medium.

4.2.1 The Bloch Theorem

Let's consider a 1 dimensional Hamiltonian for a particle of mass m in a periodic potential $V(x)$ of period P :

$$\hat{H} = \frac{\hat{p}^2}{2m} + V(\hat{x}) \quad \text{with} \quad V(x + P) = V(x). \quad (4.1)$$

If we consider the translation operator \hat{T}_P such that $\hat{T}_P \Psi(x) = \Psi(x + P)$, it appears clearly that $[\hat{H}, \hat{T}_P] = 0$. The two operators have a common base of eigenstates. Since T_P is a unitary operator, we can write its eigenvalues as $e^{i\theta}$ and define $\theta = Pk$, where k is called **quasi-momentum**[140]. The Bloch theorem states that the eigenstates of the Hamiltonian above can so be written as:

$$\Psi_k(x) = e^{ikx} u_k(x) \quad (4.2)$$

where $u_k(x)$ is a periodic function of period P that must satisfy the Schrödinger equation:

$$\hat{H}_k u_k(x) = E(k) u_k(x) \quad \text{with} \quad \hat{H}_k = \frac{(\hat{p} + \hbar k)^2}{2m} + V(\hat{x}). \quad (4.3)$$

This equation allows, for each k , a discrete number of solutions, that we will label with the index n . Furthermore, from 4.2, it appears clearly that such solutions are periodic in the space of the quasi-momentum k , with a period $2\pi/P$. The values of k can be chosen inside an interval of limits $-\pi/P$ and π/P , named **first Brillouin zone (BZ)**.

The resulting eigenenergies for several values of the index n can be summarized in a family of periodic functions $E_n(k)$, of period $2\pi/P$. The information contained in these function is referred as the band structure of the lattice. For each n , the function $E_n(k)$ represents a set of states that composes the n -th **energy band**. Each of these functions will have an upper and lower limit and the region of energies that do not belongs to any of these families of functions are named **energy gaps**.

These results are valid for any kind of periodic potential, no matter its specific shape. Nevertheless, some particularly regular potential structure allow to more easily compute the band structure. Let's now consider a squared well potential, since it will be the one that will be experimentally investigated in this work.

The Kroenig-Penney Model and the band structure

The case of a squared well potential can be easily solved numerically by a method named Kroenig-Penney model[141]. It is based on the fact that in the case of a squared well potential, of the kind represented in figure 4.1, solutions in each site, 1 and 2, are combination of plane waves of the form respectively $e^{i\alpha x}$ and $e^{i\beta x}$, with $\alpha = (2mE)^{1/2}/\hbar$ and $\beta = [2m(V_0 - E)]^{1/2}/\hbar$. The problem can be numerically solved by imposing the continuity conditions at the edge of the interfaces, in the case of a wavefunction of the form 4.2 [142]. The allowed energy values and the corresponding band structure can be computed.

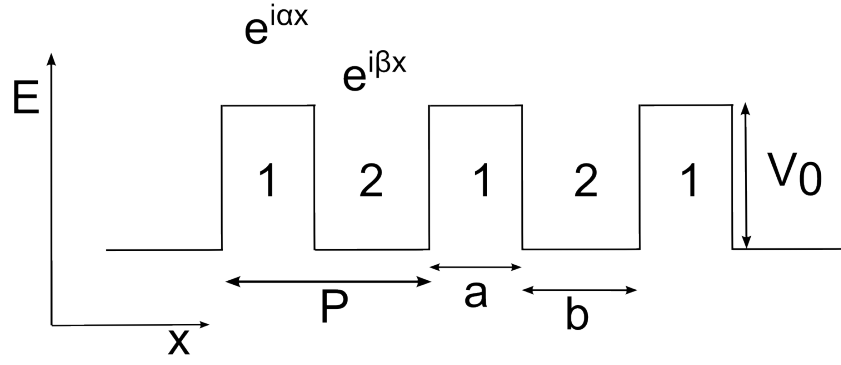


Figure 4.1: Schematic representation of a squared well periodic potential. The potential strength is V_0 , and the period is given by $P=a+b$.

Few examples of typical band structures are reported in figure 4.2, where we use parameters not far from the typical ones for polariton systems.

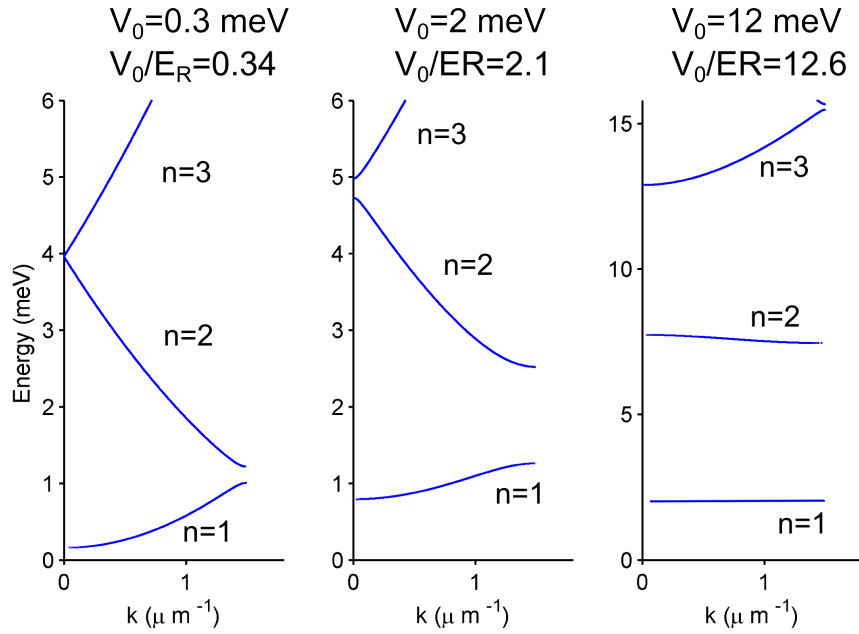


Figure 4.2: Band structure of a squared well lattice calculated with the Kroenig Penney model for different values of V_0 . Parameters: $a = b = 1.05 \mu m$ ($P = 2.1 \mu m$), $m = 9 * 10^{-5} * m_0$. The values of V_0 are shown in the picture.

We clearly observe the appearance of several bands, labelled by the index n , and between them, regions of forbidden energies. In figure 4.2 the height of the potential goes from few tens of meV (panel a) up to 12 meV (panel c). By varying such parameter, the dispersion can be strongly modified, affecting the energy width of the bands, their shapes and the size of the gaps. Such Kroenig Penney calculation will be used all over this chapter in order to either predict the expected polaritonic band structure or to reproduce the experimental polariton dispersions and extract some essential parameters.

4.2.2 Weak potential and tight binding

Let's now consider two essential energy scales in the system. One is given by the amplitude V_0 of the periodic potential and the other corresponds to the kinetic energy of a particle for a quasi momentum corresponding to the edge of the first Brillouin zone, that is called **recoil energy** $E_R = \frac{\hbar^2 k_B^2}{2m}$. Two regimes can be indentified depending on the ratio V_0/E_R .

Let's consider the case of a **weak potential** and the simplest case of a sinusoidal potential of the form $V(x) = V_0/2 \cos(2k_B x)$, where $k_B = \pi/P$. In the case of low values of V_0 , the effect of the lattice can be treated as a perturbation to the case of a free particle, with eigenstates given by plane waves $|k\rangle \propto e^{ikx}$. At the first order, the correction to the energy for the plane wave $|k\rangle$ is given by:

$$\delta E = \langle k | \frac{V_0}{2} \cos(2k_B x) | k \rangle = \langle k | \frac{V_0}{4} (e^{2ik_B x} + e^{-2ik_B x}) | k \rangle \quad (4.4)$$

This expression is incorrect when the two degenerate state $|k\rangle$ and $|-k\rangle$ are coupled to the first order on V_0 , as is the case for $k = \pm k_B$. The hamiltonian must be diagonalized limitedly to this two state as:

$$H = \begin{pmatrix} E_R & V_0/4 \\ V_0/4 & E_R \end{pmatrix} \quad (4.5)$$

which eigenvalues are $E_R + V_0/4$ and $E_R - V_0/4$ and corresponds to respectively a symmetric or antisymmetric combination of the plan waves, $(|k_B\rangle + |-k_B\rangle)/\sqrt{2}$ and $(|k_B\rangle - |-k_B\rangle)/\sqrt{2}$ [143].

The effect of the lattice is to destroy the degeneracy at the edge of the Brillouin zone and to introduce a gap of forbidden energy of width $V_0/2$. In this regime, the bands will be strongly perturbed only in the proximity of the BZ edges [140, 144]. This is well illustrated in the first panel of figure 4.2, corresponding to $V_0/E_R = 0.34$.

Let's now consider the case of a **strong modulation**, with V_0 much higher than E_R , where we can apply the tight binding model[40]. In the case of very deep potential well, we should expect particles to be localized inside this well. At the same time, for a periodic repetition of this wells, the Bloch Theorem requires this solutions to be of the form of Bloch functions (see 4.2), delocalised on the ensemble of the lattice. This two points of view can be joined by introducing the Wannier functions $w_n(x)$ (n being the band index) [145, 140]. They represents functions localized around the site l of the lattice, centered in the position $P * l$, with l integer. Given $\Psi_{n,k}(x) = e^{iPk} u_{n,k}(x)$ the Bloch function in the band n and quasi-momentum k , they Wannier functions of the site l can be defined as defines as:

$$w_{n,l} = \frac{1}{\sqrt{2k_B}} \int_{-k_B}^{+k_B} e^{-ilPk} \Psi_{n,k} dk \quad (4.6)$$

For the first bands, that means for small n , the Wannier functions are strongly localized in each site. The effect of the lattice will so be limited by the small overlap of the different functions centered in each site. It can be shown[146] that we can write the eigenenergies as:

$$E_n(k) \approx E_n + \delta E_n \cos(kP) \quad (4.7)$$

where the center of the bands E_n is the value of the unperturbed state in the single well and the width of the band is proportional to the overlap between functions located in different sites, or in other word, to the tunneling coupling between the sites.

$$\delta E_n = \langle w_{n,l}(x) | H | w_{n,l+1}(x) \rangle \quad (4.8)$$

This situation corresponds to the extreme case represented in the last panels of figure 4.2. Here the high values of the potential $V_0 = 12meV$ (corresponding to $V_0/E_R = 12.6$), reduces the coupling between sites, and so the bands tends to collapse towards the discrete states of a particle in an infinite well.

We will see that different localization mechanism can appear depending of the strength of the periodic modulation.

4.2.3 Group velocity and effective mass

The periodic potential affects fundamentals properties of a particle, such as the effective mass and the group velocity.

One can show that particles inside the bands can freely propagate with a constant wave-vector and group velocity [40]. Such **group velocity** is given by:

$$v_{g,n} = \frac{1}{\hbar} \frac{\delta E_n(k)}{\delta k} \quad (4.9)$$

where n is the index of the band.

In figure 4.3, we report an example of the dependence of v_g on k in the first miniband of the band structure (also shown in the figure). The curves is not monotonically increasing as in the case of a parabolic dispersion, but presents a maximum and then decreases and goes to zero at the edge of the BZ.

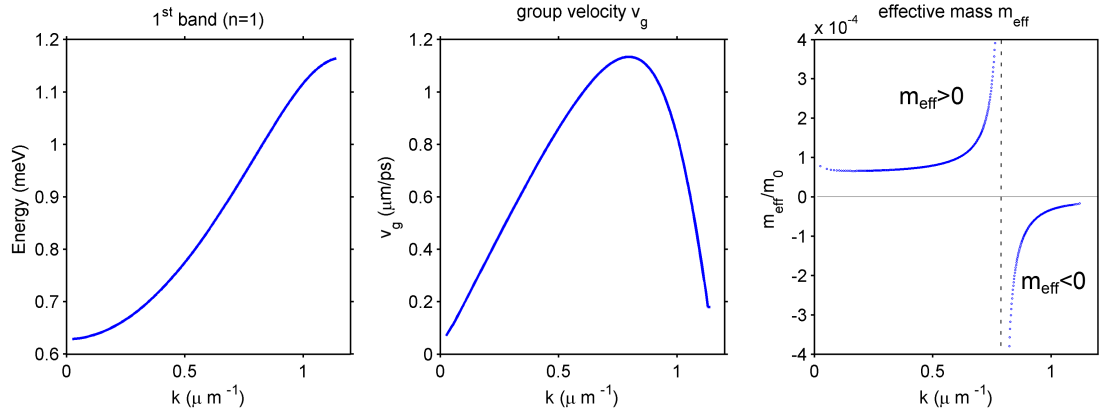


Figure 4.3: Left: First band of a squared well lattice of parameter $P = 2 * a = 2.7\mu m$, $m = 5.6 * 10^{-5} * m_0$, $V_0 = 1.5meV$. Center: Group velocity extracted from the calculated band applying the formula 4.9. Right: Effective mass extracted from the shape of the band obtained applying equation 4.10

Together with the redefinition of v_g , the deviation from the parabolic dispersion induced by the lattice allows the redefinition of an **effective mass**. This will be defined by the expression:

$$m_{eff,n} = \left[\frac{1}{\hbar^2} \frac{\delta^2 E_n(k)}{\delta k^2} \right]^{-1}. \quad (4.10)$$

The values obtained from such expression are reported on the right of figure 4.3. Besides the region numerical divergence, corresponding to the point in which the dispersion is almost linear, the effective mass is well defined and positive on the bottom of the band and furthermore we observe how, both in the case of weak or strong potential, in the proximity of the Brillouin zone edge (where the band can be approximated as parabolic), the curvature of the first miniband changes sign and so the effective mass can be defined and it is negative. This property will also be essential in the case of localization of interacting particles within a lattice.

4.3 Motivations and state of the art

The interest in the shaping of a periodic potential relies in the control that it provides on the particle dispersion relation. From the fundamental point of view, for example, artificial lattices allowed the investigation of several localization mechanism [147, 148] and the implementation and study of Ising and Bose-Hubbard Hamiltonians [149, 150, 151]. In terms of application, they provided, for instance in optics, essential tools for guiding [152], slowing down [153] and strongly confining light [154], enhancing light matter interaction [155].

Periodic lattice for photons have been deeply investigated. At first in arrays of waveguides, coupled via evanescent field, as proposed in 1965 [156] and then implemented few years later with GaAs waveguides [157, 158].

Later photonic crystal have been realized, opening the way to the implementation of lattices of the most various geometries, from 1 to 3 dimensions [159, 160, 161]. In such a structures, a photonic band gap is created (PBG), giving, for given wavelength, a photonic equivalent of an insulator material [162]. Furthermore, one could mention how the anomalous curvatures of the photonic modes opened the way to the flourishing and actual research on metamaterials [163].

Equivalent structures have been realized for electrons: periodic sequence of semiconductors materials, proposed in the '70 as superlattices [164], strongly influences the conduction properties. Negative differential conductivity has been observed as well as electron Bloch oscillations, interesting as potential emitters of THz radiation [165, 166], as discussed later in the chapter.

More recently, cold atoms in periodic lattices have also been subject of interest. The interference pattern generated by two contra-propagating laser forms a lattice for atoms, which geometry, amplitude and period can be controlled at will. This allows the investigation of a large variety of effects: squeezed states [167], Mott-insulator transition [168], Bloch-oscillations [169] together with Landau-Zener tunneling [170].

For all these mentioned systems, a particular interesting field has been the investigation of the several mechanism of particle localization that these systems provide. More specifically, the case of interacting bosonic particles or equivalently, of non linear optical medium, is particularly

rich since the non linearities generates a wide range of peculiar localized states of different nature [171, 172, 173, 161, 173]. On these localization mechanisms we will focus our attention.

4.3.1 Localization of interacting bosons in a lattice

The localization mechanism available for bosonic particles inside a lattice are severals, few of them are purely linear, others are peculiars of interacting particles or non linear medium and are based on the interplay between the band structure and the non-linearities.

Defect states

A case of linear localization mechanism is represented by a defect state. If the periodicity of the potential is perturbed, for example by slightly varying the potential height of one site, a state inside the gap will appear. In analogy with electronic states of donors and acceptors in semiconductors, in which electrons are trapped and don't contribute to conductivity, particle in this state won't undergo any propagation but will be strongly localized nearby the perturbation. The wavefunctions characteristic of such a state presents an exponential decay profile on the side of the perturbation which decay-constant increases with the spectral distance from the band edges [174, 175].

This mechanism has been applied to generate a wide variety of optical cavities, with a low modal volume and high Q factor. In particular in the field of photonic crystal, strong light localization has been obtained by a local variation of the period of the lattice[154], or by slight changes of the refractive index[176]. This confinement has been obtained both in 1, 2 and even 3[162, 159] dimensions. In some cases the perturbation was externally controlled, allowing the implementation of reconfigurable circuits[177, 178].

Let's now consider the effects of the non-linearities and introduce two more classes of confined states : Truncated Bloch waves (also named self trapped states) and Gaps Solitons.

Truncated Bloch states

The generation of truncated Bloch states takes place in the regime of deep potentials coupled with strong repulsive non linearities [179]. Let's consider that the ground state of an individual site (Wannier state) is occupied by a population of interacting bosons. From this state, particles can spread toward the next sites only by Josephson-like tunneling. But this is possible as long as the energy difference between two sites, renormalized by the interaction energy, is smaller than the energy associated with the single particle tunneling, or, in other word, with the width of the band. Otherwise, this tunneling stops, and the population imbalance between adjacent site is locked. The resulting spatial distribution of a cloud of particles presents a flat constant population distributed for a certain number of sites (modulated as "non linear bloch state" [180]), truncated by step edges, through which tunneling is suppressed.

This states has been deeply discussed theoretically in the group of Yuri Kivshar [182, 183] in Camberra, and firstly observed experimentally in atomic condensates in the group of Oberthaler in Heidelberg[181]. In their experiments Rb atoms were confined in a one dimensional trap superposed to an optical lattice. As shown in figure 4.4, by increasing the

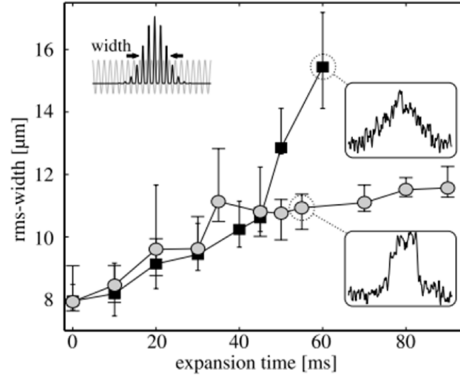


Figure 4.4: Observation of truncated Bloch states (or non linear self trapping) of Bose condensed Rb atoms. By increasing the atom density (from squared to circles), the width of the state decreases and acquires the typical top-flat profile discussed in the text. Figures extracted from [181].

atom densities the self trapping regime was achieved and a top hat profile was observed. Few years later, the same effect has been observed also in arrays of defocusing optical waveguides[184].

Although the basic mechanism for the generation of these states, the self trapping, has been already observed in a polariton system [37], the condition of strong non linearities and, moreover, of deep potential make these states difficult to be generated in our system.

Gap Solitons

Another class of non linear localized states are the Gap Solitons. These states will be the most interesting in our study since the conditions for their formation, namely weak potentials ($V_0/E_R \approx 1$) and weak interactions[179], correspond to our experimental conditions.

Their origin relies on the modified curvature of the dispersion that the lattice generates at the band edge. As already discussed, in the case of the first band ($n=1$), this curvature results in a negative effective mass at the edges of the BZ. Here the dispersion of a wavepacket is anomalous: the time evolution of the wavepacket will go backwards (due to the symmetry of the Schrödinger equation to the inversion $m > 0, t < 0 \rightarrow m < 0, t > 0$). In the presence of interacting particles, the defocusing of the wavepacket due to repulsive interactions can be compensated by the focusing due to the negative mass values and this will generate a non spreading wave-packet named Gap Solitons.

Thus Gap Solitons are non spreading soliton solution of the Gross-Pitaevskii equation (or equivalently, of a Non Linear Maxwell equation) in the presence of a periodic potential, representing a state at the edge of the Brillouin Zone, where a negative (resp. positive) effective mass compensates the repulsive (resp. attracting) inter-particle interactions.

The energy corresponding to these states lies inside the energy gap, due to the interaction-energy shift. Their spatial profile is characterised by an envelope *sech* wavefunction that reads :

$$\psi_{GS}(x) = \sqrt{n} \operatorname{sech}\left(\frac{x}{\xi}\right) \quad (4.11)$$

where $\xi = \hbar^2 / \sqrt{\alpha n |m|}$ is the healing length, with α the interaction constant, m the particle effective mass and n the particle density at the soliton peak [179].

Considering the case of the first band and repulsive interaction, Gap solitons represents stationary solutions for energies lying between the bottom and the middle of the first gap. Their healing length decreases from infinity at the band edge (for low particle density) up to the lattice period at the center of the gap (for high density).

In the reciprocal space their wave functions presents two peaks corresponding to the edge of the Brillouin Zone $k = \pm k_B$.

Gap Solitons have been widely investigated, theoretically and experimentally[185, 179].

The first theoretical proposal was made in 1988 and concerns arrays of waveguides with defocusing non linearities[186]. It's indeed in this system that, 10 years later, the first experimental observation was realized [187] : a large array of waveguides were pumped resonantly at a frequency inside the photonic gap. The signal was then collected after a certain propagating distance and a focusing effect was observed for high optical densities (see figure 4.5). Later, Gap Solitons have been observed in several other photonic systems[148, 188, 173, 189].

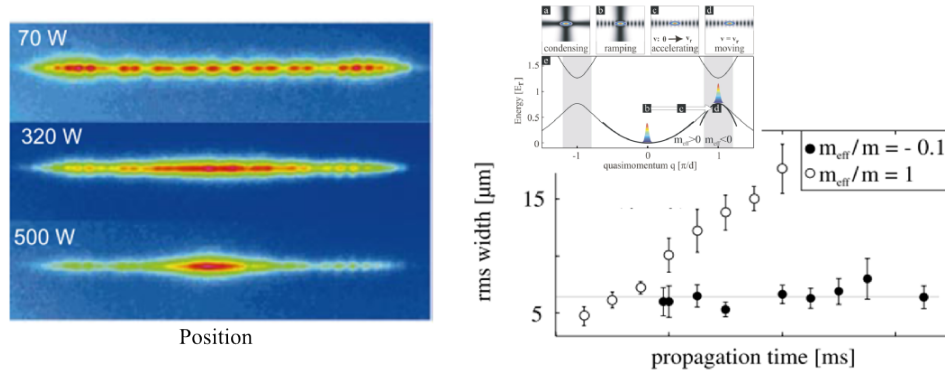


Figure 4.5: Left: Experimental observation of Gap Soliton in AlGaAs waveguide arrays with Kerr non-linearities. Several waveguides are excited. Light propagates inside the waveguide and is collected at the end of the guide. In the left panel we see how increasing the pump power, the beam is more and more focused. Figure extracted from [158]. Right: Observation of Gap soliton for a Rb atomic BEC. On top, the scheme of the experimental approach to bring the condensate from the bottom to the edge of the first miniband: to do that the whole optical lattice is accelerated. In the bottom, effect of the negative effective mass on the expansion in time of the packet of atoms. Figures extracted from [190].

Also atomic BEC have been investigated in region of negative mass of the band structure.

The control of the dispersion of the wavepacket[191] and the formation of Gap Solitons[190] has been achieved. Thanks to an acceleration of the optical lattice the BEC was slowly accelerated and brought adiabatically at the band edge and after that the spreading of the wavepacket was observed revealing non dispersive behaviour (see picture 4.5).

Both these two systems presents some experimental complications for the generation of Gap Solitons. For atoms, since the top band-edge is not the ground state of the system, it is complicated to drive a BEC exactly at this state. For photons, the weak non linearity and the need of pumping the system in the photonic gap, requires high pumping powers. Additionally also the study of the time evolution of the system present some difficulties. In this context, polaritons, with their strong non linearities and their out-of-equilibrium features, can present some advantages in the excitation of such states.

4.3.2 Polaritons in a periodic potential: the state of the art

In the last few years, polaritons in a periodic potential started to be investigated and three main methods has been developed to implement a periodic lattice felt by polaritons.

The first one was developed in 2007 in the group of Y.Yamamoto in Stanford [192]. It is based on the deposition of patterned metallic thin films (20 nm) on the top surface of GaAs based microcavity (see figure 4.6). In the region where the metal is deposited, the cavity mode is red-shifted of around $400\mu eV$. Consequently, the polariton modes are shifted of approximately half of this value. When the metal is deposited in parallel equidistant stripes, it generates a 1D periodic potential in the direction perpendicular to the stripes, while no confinement is present on the perpendicular direction. This method is versatile and allows also the generation of several geometries of 2 dimensional lattices [193, 194, 195].

Although polaritons condensation has been observed in this system, the method presents two main limitations. The metal deposited on the cavity absorbs photons and decreases the polariton lifetime. Additionally, the weakness of the induced potential limits the width of the generated energy gaps to values around $200\mu eV$ (comparable with the linewidth of the polaritonic mode): this factor limits the possibility of investigating localization in states inside the energy gap.

Another method was developed in the group of Paulo Santos in Berlin. It is based on surface acoustic waves, generated over the sample with a deposited piezoelectric material [196]. Such waves travel all over the cavity, inducing a compression and extension of the width of the cavity, the Bragg mirrors and the QWs. Both the excitonic and photonic modes are then modulated periodically with the spatial period of the travelling wave (see figure 4.6). A 1D lattice for polaritons is created and it travels at the speed of the acoustic excitation. Such a method allows to generate a modulation of depth up to few meVs. The possibility of easily acting on the strength of the modulation allowed the investigation of the transition from weak potential to the tight binding regime. Localization of the condensate in each lattice sites could be achieved [197, 196]. Nevertheless, even this system presents some limits. The potential generated is not static but travels over the cavity. Although this movement is slow with respect to characteristic time involved in the system, it is fast with respect to the data acquisition time in the experiments, in which the collected signal must be averaged over several acoustic periods. Additionally, the cavity quality factor ($Q \approx 2000$), limits the photon lifetime to $\approx 3 - 4 ps$ and this complicates

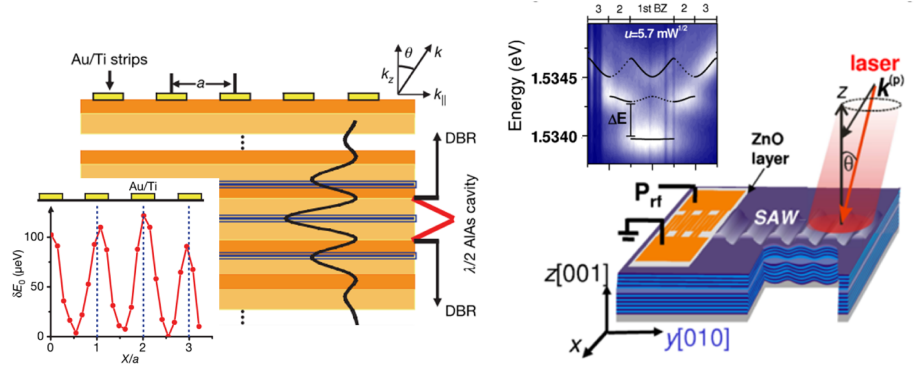


Figure 4.6: Left: Schematic of an array of metal stripes deposited on the cavity. In the inset is shown the induced energy modulation of the polariton states (figure extracted from [192]). Right: Scheme of the experimental configuration for generation of surface acoustic wave propagating over the microcavity. The resulting polariton dispersion is also reported, where forbidden energy gaps appear (figure extracted from [196]).

the investigation and comparison of propagation in the band and localization in gap states.

In the next pages, I will presents how with our approach we tried to overcome some of the limitations of these systems: we obtained a periodic potential in a real 1D geometry (with total confinement on the transversal direction), with a high modulation depth and without sensibly affecting the polariton lifetime.

4.4 Modulated wires

In this section we present our approach for realizing a one dimensional lattice for polaritons, based on laterally modulated wires. We first characterize the polariton modes in the linear regime.

4.4.1 Engineering the potential landscape: modulation of a wire width

The confinement of microcavity polaritons, both in 1D or OD geometry, is associated to an energy blueshift of the ground state, due to the existence of a confinement energy [198]. As already discussed in chapter 2, in the case of a microcavity wire, the energies of the optical modes depends on the lateral size of the wire according with formula 2.1.

In figure 4.7, we show the energy of the optical mode at $k_y = 0$ extracted from wires of different lateral size. The experimental points are then fitted with formula 2.1 for $j = 0, 1, 2$.

We can conclude that the variation of the lateral size of the wire modulates the optical mode states, and thus the polaritonic one.

This dependence of the polariton energy on the size of the wire provides a tool to shape a 1D potential. One can realize defects for a polariton flow, a barrier or a well with controllable size and height [31], or an energy gradient to accelerate or decelerate polaritons.

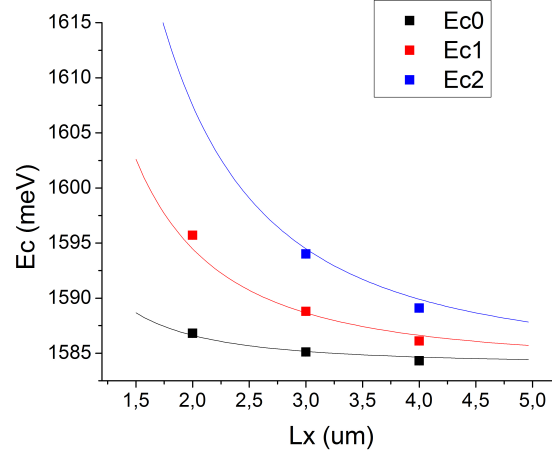


Figure 4.7: Squares: Energy of the several transversal confined cavity mode at $k_y = 0$ extracted from wire of different width. Lines: Curves corresponding to the formula 2.1 for $j = 0, 1, 2$.

Here we show how this method can be exploited to realize a periodic potential for polaritons. We etched some 1 dimensional microcavity with a modulation of the wire width. Figure 4.8 shows a Scanning Electron microscope image of an array of modulated wires.

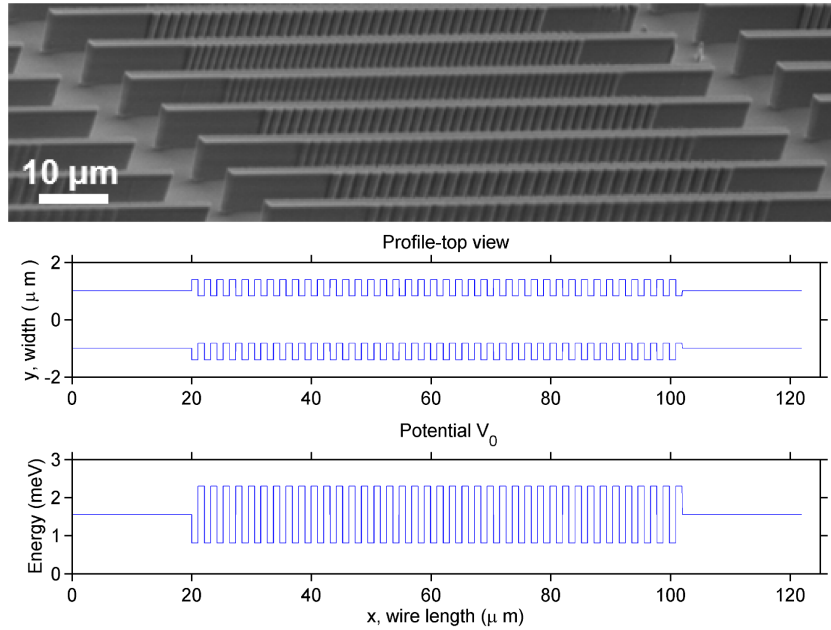


Figure 4.8: Up: Scanning electron microscope image of few modulated wire structures. Bottom: The width profile of a typical modulated wire together with the resulting potential for polaritons. The modulated region is $80\mu m$ long. The period P is $2.1\mu m$.

An exemple of width profile and the corresponding expected potential profile is also reported. The potential is a squared well potential, with a unity ratio between large and thin part, both

of size a . The period of the potential, $P = 2a$, goes from 1.6 up to $2.7\mu\text{m}$.

The height of the potential steps is modulated by two parameters: the strength of the lateral modulation, or the exciton-cavity detuning δ . Indeed, the wire shaping modulates the optical mode energy. If the energy steps is named V_{opt} , the effective potential for polariton is weighted proportionally to its photonic part following the relation $V_0 = |C|^2 V_{opt}$, where C is the photonic Hopfield coefficient of the polariton state.

The present method allows to reach a potential modulation that goes from zero up to 2-3 meVs. The only limitation is given by an upper and lower limit to the lateral size of the wire. A width shorter than $1.5\mu\text{m}$ brings to strong non radiative exciton recombination at the lateral interfaces, while if the wire is too wide, more than $4\mu\text{m}$, the splitting between the first and second order transverse confined mode is too small and the system loses its one dimensional character.

The whole set of etched wires is reported in figure 4.9, together with their main parameters.

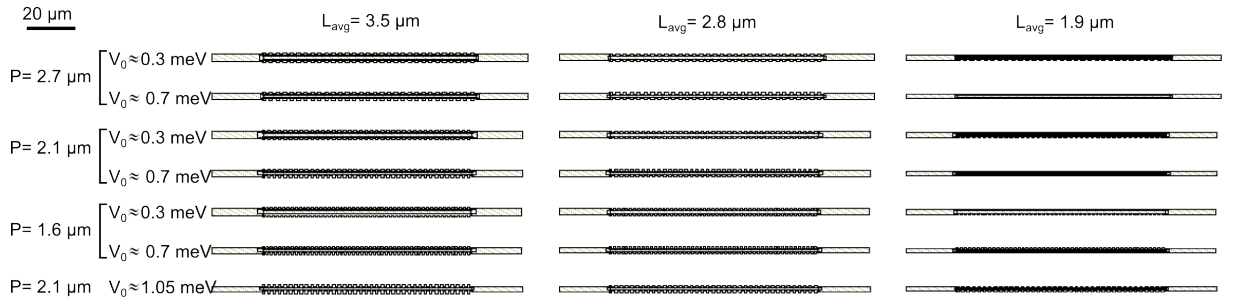


Figure 4.9: Scheme of the etched microcavity mask representing several families of modulated wires. The main parameters are reported in the figure. The values of V_0 corresponds to the estimated potential depth for a cavity-exciton detuning $\delta = 0$. Every combination of the parameters V_0 and period P are reproduced three times by varying the average width of the wire L_{avg} .

4.4.2 Characterization in the linear regime

We now characterize these structures in the linear regime via the photoluminescence signal collected both in real and reciprocal space under non resonant excitation.

The redefined polariton dispersion

In figure 4.10 we report two examples of far field emission from modulated wires, that allows us to directly visualize the polariton dispersion. The measurements put in evidence how the dispersion curve is strongly modified by the lattice.

The continuous dispersion is now cutted in several minibands, separated by the presence of forbidden energy gaps. One can define several Brillouin Zones (BZ), and enhancing the signal for certain energy and angle of emission, the effect of the band folding is visible.

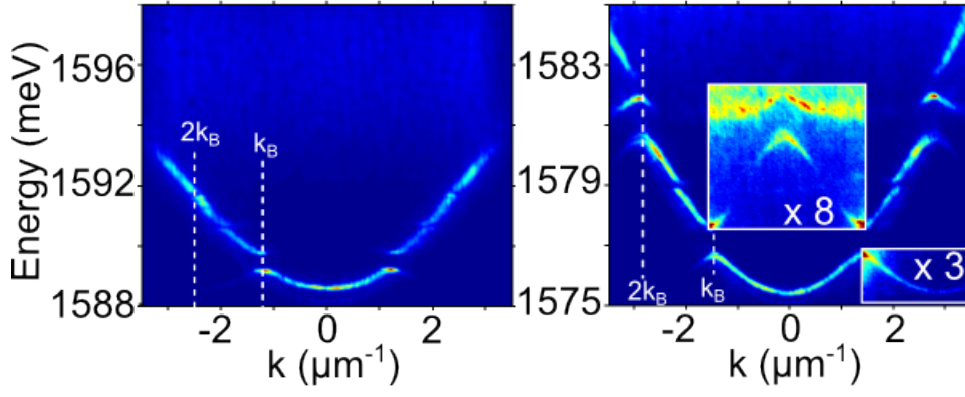


Figure 4.10: Reciprocal space emission measured on a single modulated wire excited non resonantly with low power. The band structure characteristic of a periodic potential is visible. The dashed white line indicates the edges of the 2 first BZs. The signal inside the rectangle in the right panel has been amplified to better show the band folding. Parameters of the wire: Left: $P = 2.7\mu m$, $V_0 \approx 0.9 meV$, $\delta = -1 meV$. Right: $P = 2.1\mu m$, $V_0 \approx 1.5 meV$, $\delta = -9.5 meV$.

Gap and band width

The dispersions obtained from a wide variety of wires of several parameters have been analyzed and the main results are reported in figure 4.11. On the the left graph we show the

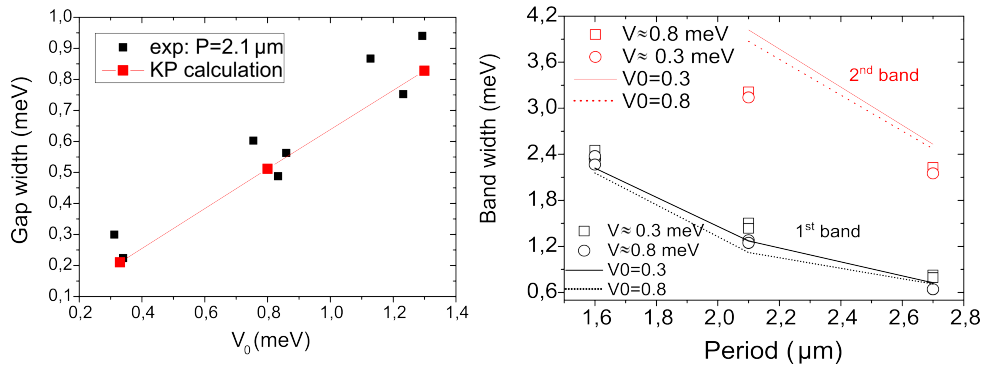


Figure 4.11: Left: Black points: width in energy of the first forbidden energy gap measured for several wire of period $P = 2.1\mu m$. Red points: Kroenig-Penney calculation of the width of the energy gap obtained with parameters V_0 and m_p (polariton mass) extracted according to the geometry of the wire and its detuning δ . Right: Values of the energy width of the first (black) and second (red) allowed energy band. Squares and circles represent values extracted from wire with a modulation depth V_0 around, respectively, 0.3 and 0.8 meV. The solid lines are the results from a Kroenig-Penney calculation.

width of the first forbidden energy gap as a function of the strength of the potential step V_0 . The values of V_0 have been calculated considering the modulation of the optical mode

corrected by the photonic fraction $|C|^2$ corresponding to different exciton cavity detunings δ , different for each wire.

The point shown corresponds to a family of wires with a period of $P = 2.1\mu m$. The width of the gap doesn't change sensibly with the period P of the modulation. On the contrary, it is strongly dependent on V_0 . In the graph we show how we can vary the gap width from 0.2 meV up to almost 1 meV. Its values are, as expectable, slightly higher than $V_0/2$, the value discussed in the beginning of the chapter for a sinusoidal potential of amplitude V_0 .

A Kroenig-Penney calculation has been performed, with parameters given by the expected value of the effective potential V_0 (extracted from the geometry of the wire) and by the polariton mass, both corrected according with the detuning δ of each wire. The obtained results reproduce quite well the experimental points.

On the right part of figure 4.11, we plot the energy width of the first 2 allowed energy bands, which limits corresponds to the polariton energy at $k = 0$ and $k = k_B$ for the first band, and at $k = k_B$ to $k = 2k_B$ for the second one. We plot it as a function of the 3 different periods available on the sample and for values of the potential V_0 around 0.3 and 0.8 meV. The band widths depend weakly on V_0 but mainly on the values of the period P . We also compare our results with a Kroenig Penney calculation obtained varying the period P , and also the potential V_0 and the polariton mass according with the detuning.

The results show how the comparison is satisfying concerning the first band, while it overestimates the width of the second band. This discrepancy can be explained by the fact that the Kroenig-Penney model consider a particle of constant mass, that corresponds to a parabolic dispersion. For polaritons, this approximation is valid for low energy, and so the model works for the first band, while approaching the reservoir the effective mass increases and the model is not adapted anymore. Additionally also the effective amplitude modulation varies with the photonic fraction $|C|^2$, thus with the polariton energy.

Influence of the non parabolic polariton dispersion and of the higher order tranverse modes

To exactly reproduce the observed dispersion curve, a simple KP model is not enough and a more complete one is needed. This is better shown in figure 4.12.

On the left panel we show the experimental polariton dispersion in a modulated wire (same of the right panel of fig. 4.10). In the middle we show a Kroenig-Penney calculation performed to reproduce the experimental dispersion. We observe that the first band is properly reproduced but for higher energies this model is not adapted.

The more complex features observed in the experiments are result of two effects.

One, as already discussed, is the variation of the mass and of the photonic fraction with increasing the energy.

Additionally, the real structure is not fully 1D but allows the existence of several transverse mode. At higher energy this transverse mode plays a role and produce some additional anticrossing and the opening of several gaps. A good reproduction of the experimental dispersion has been obtained by solving two coupled Schrodinger equation for the excitonic and photonic fields, taking into account the real 2D geometry of the wire .

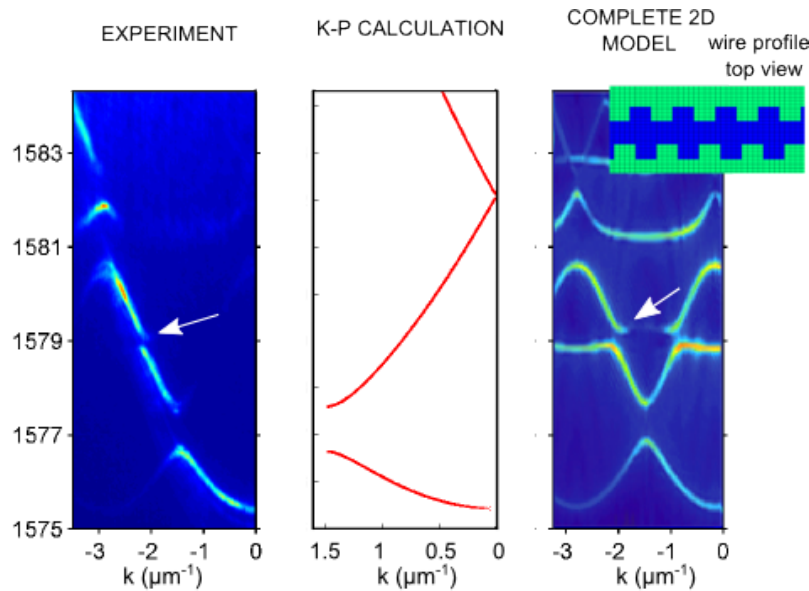


Figure 4.12: Right: Experimental dispersion collected from a modulated wire (same as right panel of fig. 4.10). Center: Best fit of the dispersion obtained from a Kroenig-Penney calculation (the bands are shown in the folded representation). Only the lower energy region of the dispersion is properly reproduced. Right: Simulation of the band structure obtained solving two coupled Schroedinger equations for the excitonic and photonic fields and taking into account the real 2D geometry of the wire. A slight asymmetry in the wire profiles (shown in the inset) has been introduced to reproduce the additional anticrossing indicated by the arrows.

The results are shown on the right panel of figure 4.12, obtained in collaboration with H.Flacy and D. Solnyshkov in Clermont Ferrand. In order to reproduce also the additional anticrossing in the middle of the second band (white arrows in the figure), we had to introduce a slight asymmetry between the modulation on the two sides of the wire, as shown in the inset of the right panel.

We finally remark that, despite the influence of the transverse modes discussed in this paragraph, in most of the presented experiments, the condensates are studied at energy low enough to do not excite any transverse mode of higher order. The 1 dimensional character of the system is preserved.

The ratio V_0/E_R

An essential parameter that will characterize the behaviour of polariton inside these structures is the already discussed ratio V_0/E_R , where E_R is the recoil energy.

In figure 4.13 we report typical obtained values for wires of different width modulation and period. Our structure allows to access values of V_0/E_R going from a minimum of 0.1 up to around unity values (values up to almost 2 can be reached for really negative detuning).

The meaning of this ratio, appears from a better looking to the shape of the first miniband for 2 different wires ,reported also in figure 4.13. For low V_0/E_r values, the polaritons dispersion is

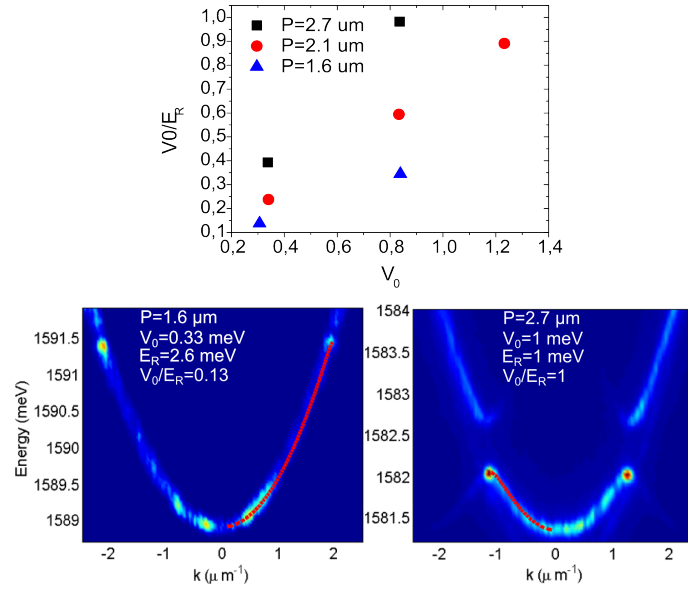


Figure 4.13: Top: Values of the ratio V_0/E_R for wires of different width modulation and period P . Values from 0.1 up to 1 are presented. Bottom: Far field emission from the first miniband of two modulated wires with two different values of the ratio V_0/E_R . The main parameters are reported on the figures and those parameters has been used to obtain the fit of the bands reported on the images with red dashed lines.

almost unaffected, and the minibands is essentially parabolic with a slight curvature only in the proximity of the edge of the BZ. On the contrary, for higher values of the ratio, the curvature of the minibands is more pronounced, acquiring a shape similar to the cosine form expected within the tight binding approach. The curves superimposed to the experimental dispersion in the figure come from a Kroenig-Penney calculation obtained by using the structural parameters of the 2 different wires.

Al tough far from the strict tight binding limits, that would required V_0/E_R of around 10 or higher [143], the values accessible in our structures allows to investigate different regimes. We will highlight the influence of this ratio on the localization of particle in gap states and on the hopping from the first to the second band.

Density of states

In figure 4.14 we show a typical exemple of the total integrated intensity as a function of the energy measured on a modulated wire excited non resonantly at low power. The main graph on the left corresponds to signal coming only from polariton states, obtained correcting the raw emission by substracting the contribution from the excitonic emission (see inset of the left graph of 4.14).

We observe that the polariton emission is not spectrally homogeneous but presents several peaks. These are the manifestation of what in solid state physics are well known as Van Hove singularities after the name of the Belgian physicist who in 1953 introduced them for phonons

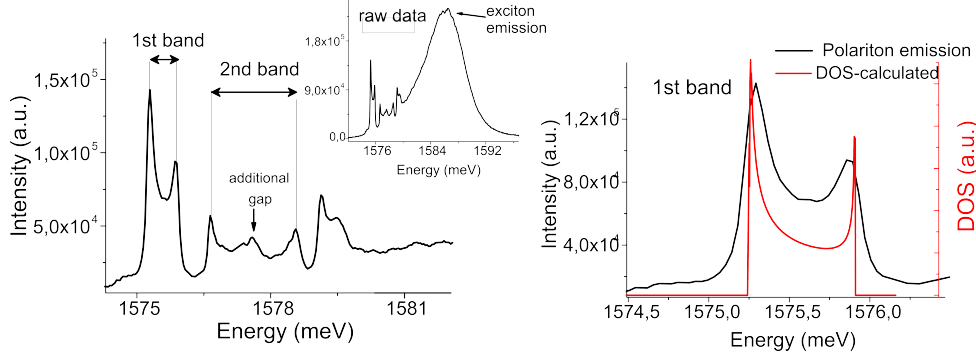


Figure 4.14: Left: Photoluminescence spectra from a modulated wire excited non resonantly at low power. The curve in the main graph represents emission only from polariton states. It has been obtained by subtracting the contribution to the total intensity coming from the excitonic emission. The raw data are represented in the inset. Right: The black curve represents the photoluminescence restricted to the first mini band. The red curve represents the inverse of the derivative dE/dK obtained from a Kroenig-Penney calculation, and so it represents qualitatively the energy dependence of the density of states DOS, according to equation 4.13. The peaks at the edge of the bands represent a divergence of the DOS.

in a lattice [199].

Neglecting the spin degree of freedom, one can construct the density of states defined as proportional to the number of allowed wavevectors in the n -th band in the energy range from E to $E+dE$.

The number of allowed wavevectors is just the volume of a primitive cell in the reciprocal space with $E \leq E(\vec{k}) \leq E + dE$, divided by the volume per allowed wavevector $\Delta\vec{k} = (2\pi)^d/V$, where d is the dimensionality of the crystal.

The expression so becomes:

$$g(E)dE = \int_{\Omega} \frac{d\vec{k}}{(2\pi)^d} \times \begin{cases} 1, & \text{if } E \leq E(\vec{k}) \leq E + dE \\ 0 & \text{otherwise.} \end{cases} \quad (4.12)$$

where the integration is over Ω , an elementary cell in the reciprocal space.

The integral can be transformed in a surface integral on an isoenergetic surface $S_n = E_n(\vec{k}) = E$ within the primitive cell, being n the band index. Given $\nabla E_n(\vec{k})$, the gradient of such surface, one then gets[40]:

$$g_n(E) = \int_{S_n(E)} \frac{dS}{(2\pi)^d} \frac{1}{|\nabla E_n(\vec{k})|} \quad (4.13)$$

which gives the relation between the density of levels and the band structure.

The periodicity of the band structure assures the existence of at least one local minimum and maximum of the energy for each band. The point of minima and the maxima of each band, that often coincide with the edges of the BZs, corresponds to points in which the gradient vanishes and so the density of states has anomalous behaviour, giving rise to Van Hove singularities. In

three dimensions, such singularities are integrable, giving finite values of g_n , but they do result in divergences of the slope dg_n/dE . experimentally they have been observed in optical absorption spectra [200] .

In lower dimensions, 2D and 1D, $g(E)$ is expected to diverge to infinity. This corresponds to anomalies in spectroscopic measurements obtained for example in graphite (quasi-2D)[201] or more recently in graphene [202] . In one dimension, they have also been observed in both optical absorption and photoluminescence [203], for example in single-wall carbon nanotubes.

In the luminescence spectra collected from our wires, the observed peaks correspond to edges of the minibands. We can clearly identify the Van Hove singularity corresponding to the first and second band edges and the additional gap discussed above in the middle of the second band. Also peaks are visible, corresponding to other gaps appearing at higher energies (as visible in fig 4.10). On the right of figure 4.14 we focus on the emission intensity from the first band. The red curves represents the inverse of the derivative dE/dK of the first miniband simulated with a Kroenig-Penney calculation. A qualitative similarity is observed (the height of the divergent peak in the calculated curve is arbitrary and only related to the precision in the numerical calculation).

These results shows that, although we are far from the condition of thermal distribution of the polariton population, the photoluminescence intensity generated at weak non resonant excitation reflects qualitatively the polaritonic DOS in the system.

Linewidth of polariton modes

The periodicity and regularity of the periodic potential directly depends on the precision of the etching. One could expect that some slight imprecision in the shaping of the structures could bring some random variation on the width of the wire and so of the energy depth of the potential well between sites. One could expect an effect of this on the linewidth of the polariton modes.

In figure 4.15 we report the emission corresponding to the polaritonic state at $k_x = 0$, coming from a non modulated (flat) wire and a modulated one ($V_0 \approx 0.8meV$). The two wires have a similar cavity-exciton detuning of around $\delta = -5meV$.

We observe that the flat and modulated wire present similar linewidths, with a slight increase of around 15% for the modulated ones. This is a further confirmation of the regularities of the etched structure.

Propagation in real space

In figure 4.16 we report a typical example of the emission from a modulated wire excited at its center with a $2\mu m$ non resonant laser spot. Together we show also the corresponding band structure collected in the far field emission.

Polaritons inside the bands can propagate away from the excitation region and spread all over the wire. The resulting polariton intensity distribution presents a periodic spatial modulation, with a period that corresponds to the one of the lattice, allowing a direct visualization of the polariton wavefunctions.

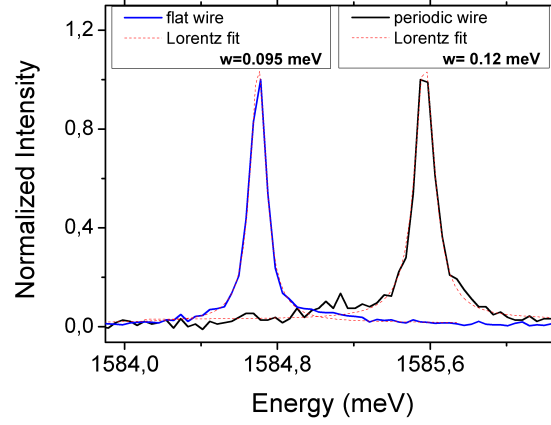


Figure 4.15: Emission line from a polariton state at $k_x = 0$ measured on a non modulated (flat) wire (blue) and a modulated one (black) with $V_0 \approx 0.8 \text{ meV}$. The red dashed lines represent two Lorentzian fit. The resulting width of the emission line is $95 \mu\text{eV}$ and $112 \mu\text{eV}$ for respectively the flat and modulated wire, which is mainly due to inhomogeneous broadening.

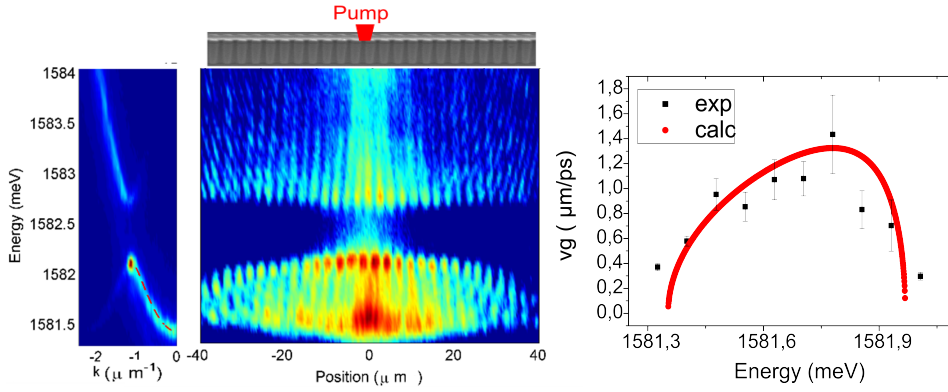


Figure 4.16: Center: Real space emission from a modulated wire of period $P = 2.7 \mu\text{m}$, excited below threshold in the center with a $2 \mu\text{m}$ wide spot. Polaritons are created in the center and propagates all over the wire inside the allowed energy bands. A modulation in the polariton emission is visible, and corresponds to the period of the lattice. Left: The corresponding far field emission, where the band structure is visible. The red dashed line is a fit of the first miniband obtained with a KP calculation (Parameters $P = 2.7 \mu\text{m}$, $m_p = 5.3 \times 10^{-5} m_0$, $V_0 = 0.9 \text{ meV}$). Right: The black points are the experimental values of the group velocity v_g for polaritons in the first miniband extracted by fitting the decrease of the intensity signal along the propagation (a polariton lifetime of 30 ps is considered). The red curve represents the group velocities extracted from equation 4.9 applied to the fit of the miniband.

The signal intensity decreases with the distance from the excitation region. We already discussed how this decrease is related to the finite polariton lifetime and to their propagating

velocity.

In the right graph of figure 4.16, we show the experimental values of the group velocity for polaritons in the first miniband extracted by fitting the decrease of the intensity signal along the propagation and taking into account a polariton lifetime of 30 ps.

The red curve in the graph corresponds to the value of the group velocity calculated from the band obtained in KP calculation with the structural parameters of the wire and applying formula 4.9.

We observe quite a good agreement between the two curves, confirmation that the propagating behaviour is conserved in the modulated wires. The values of polariton lifetime used, 30 ps (corresponding to 40 ps for polaritons at $\delta = 0\text{meV}$), is similar to the one measured on the planar cavity (see 2.1.1) or in other etched structure [31, 100], indication that the modulation doesn't affect the polariton lifetime.

To conclude, in this section we have presented our approach to obtain a 1 dimensional lattice for polaritons. We managed to strongly redefine and modulate the polariton dispersion and the results obtained in the characterization of the polariton states indicates a good control of the parameters of the system. Additionally, the lifetime and the propagation inside the bands seem not to be affected by the periodic modulation.

4.5 Condensation regime and localization under CW excitation

In this section we discuss the condensation regime for polaritons in a 1D periodic potential.

4.5.1 Condensation in localized gap states

Let's consider a modulated wire excited with a $2\mu\text{m}$ non resonant CW laser spot. The spot is centered on a barrier of the periodic potential and its power is progressively increased. The results for few relevant powers are shown in figure 4.17. Below threshold, all the states inside the allowed energy band are populated. In panels c,f of figure 4.17 we focus on the first miniband and the first gap: in the real space emission we observe polariton created in the excitation region and propagating all over the wire as already discussed in details in the previous sections (see 4.4.2).

By increasing the excitation power, we observe a strong non linear increase of the total polariton emission (see panel a), signature of polariton condensation, as already observed and discussed for non modulated wire (see figure 3.7). But here the spatial behavior of condensed polariton drastically changes with respect to the case of non modulated wire. In panel d and e we observe how condensation does not generate a monochromatic flow of polaritons spreading away from the excitation region ,as in the case of flat wire. On the contrary condensation takes place in a strongly localized state, with the energy of such states lying inside the first energy gap (panel b).

The interpretation of these results is the following. The non resonant excitation locally populates the excitonic reservoir. The repulsive interaction between exciton and polaritons and

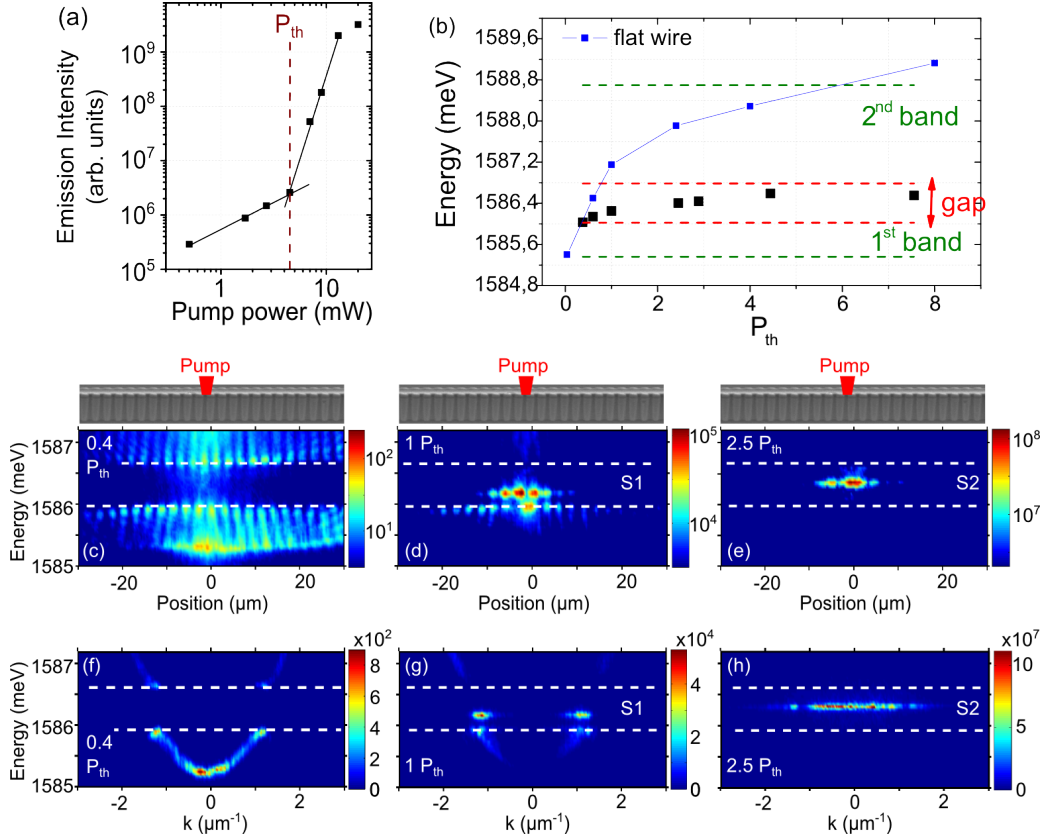


Figure 4.17: A modulated wire is excited with a $2\mu m$ wide cw laser spot centered on a maximum of the periodic potential. (a) Total emission intensity measured as a function of the excitation power. (b) Black points: Energy of the state inside the gap measured as a function of the excitation power. Blue points: typical blueshift measured exciting a non modulated wire. (c-e) Spectrally and spatially resolved emission for three excitation powers (in logarithmic color scale). (f-h) Spectrally resolved far-field emission measured on the same wire for the same excitation powers (in linear color scale); the first minigap induced by the periodicity is indicated with dashed lines. (Parameters of the wire: $P = 2.7\mu m$, $\delta = -5.5 meV$, $V_0/E_R = 1$).

the consequent induced blueshift represents a perturbation to the perfect periodicity of the lattice.

Such additional local potential breaks the symmetry of the lattice and creates some additional localized states, appearing in the energy gap. In panel b we have plotted the energy of the generated condensate as a function of the excitation power (black points). We thus observe that condensation takes place in localized state inside the gap.

Bounding and anti-bounding states

By observing the emission in the reciprocal space, reported in panels g and h of figure 4.17, we observe that by varying the excitation power, condensation is triggered towards two different states, labelled S1 and S2. This two states present in k space two opposite profiles: S1 has two

peaks corresponding to edge of the BZ while S2 presents two minima at the edge of the BZ.

To understand the nature of the two S1 and S2 gap states, we performed some numerical simulation, reported in figure 4.18. In collaboration with the group of G.Malpuech, we

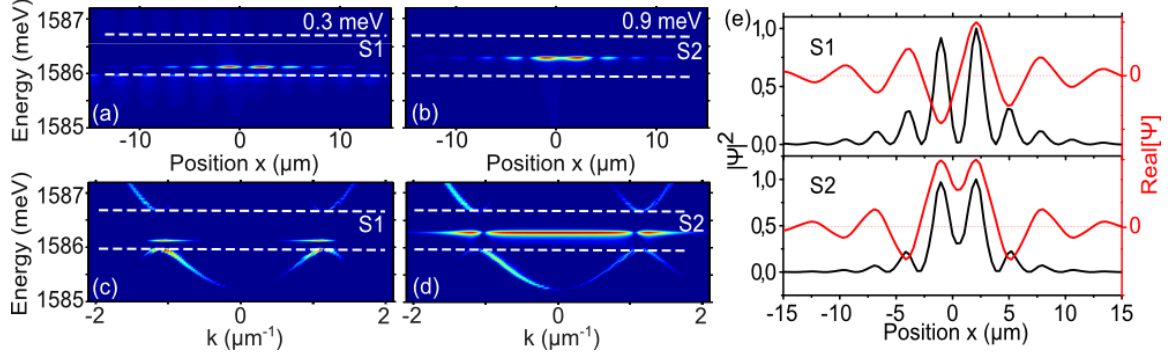


Figure 4.18: Calculated emission distribution in real and in k space solving the time dependent Schrodinger equation including pumping and lifetime, in the presence of both a periodic potential and a Gaussian potential at $x = 0\mu\text{m}$. The height of this potential is 0.3meV for panel a,c and 0.9meV for panel b,d. The pumping is a delta function in time and space which allows exciting the more localized solutions of the spectrum. The white dashed lines indicate the position of the first energy minigap induced by the periodic potential. In panel e we report the density probability (black line) and real part of the S1 (up) and S2 (down) wavefunctions, showing respectively the antisymmetric and symmetric character with respect to the reservoir position (the imaginary parts are not shown but present the same symmetries).

numerically solved a time-dependent Schroedinger equation in the presence of a periodic potential perturbed by a Gaussian potential located on top of a lattice barrier. We neglect firstly interparticle interactions.

The eigenstates of the system are perturbed by the local gaussian. By varying the height of the gaussian potential, we observe the appearance of two different gap states, similar to S1 and S2. The experimental results are well reproduced, in particular the features observed in k space.

From the simulation, we understand that on each side of the potential, a surface state inside the gap is created. Due to the finite size and height of the potential, the two states can couple. The coupling brings to the formation of an anti-symmetric (anti-bonding state) S1, and a symmetric (bonding) state S2. In the simulation, the eigenstates of the system are then excited by a pumping consisting in a delta function in time and space, which favors the excitation of the more localized solutions of the spectrum. For lower potential, the state S1 is located inside the energy gap and so localized and the more favorably excited. Increasing the excitation power, S1 energy increases and approaches the second band, becoming wider. The state S2 instead is in the center of the gap and so is more efficiently excited(panels b,d).

In panels e the wavefunctions for S1 and S2 are shown, both modulus and real part (the imaginary part is not shown but has the same behaviour). The real part for the wavefunctions of S1 and S2 presents respectively antisymmetric and symmetric shapes, reflecting the bonding and anti-bonding character of these states.

The relaxation's kinetic

The discussed gap states are clearly not the lowest energy state of the system. Indeed, due to their finite lifetime, polaritons present out-of-equilibrium features that allows condensation to occur not necessarily in the ground state [82]. The choice of the state in which condensation occurs strongly depends on the relative efficiency of the relaxation from the excitonic reservoir towards the polaritonic state. This relaxation is proportional to the spatial overlap between the reservoir and the final state wavefunctions.

In our experimental conditions, the potential perturbation that generates the gap states is at the same time source of excitons in the reservoir. Consequently, this gap states, strongly localized, will present the highest overlap with the reservoir and so the condensation will be favored towards such states. The efficiency of the relaxation reduces the reservoir population and so the values of the blueshift generated. An indication of this is shown in panel h of figure . The energy of the states excited inside the gap (black points) is much lower then the blueshift generated in a flat wire with a comparable detuning δ (the $k=0$ energy has been set to the same values for the 2 wire): this is an indication of a reservoir more efficiently depleted by the good spatial overlap with the state.

Dependence of the localization on the ratio V_0/E_R

The localization feature in a state inside the gap strongly depends on the wire parameters, and in particular on the ratio V_0/E_R .

On the left column of figure 4.19 we summarize the behaviour of wire with V_0/E_R around unity or larger (panel a corresponds to the wire of fig. 4.17).

We represent schematically the band structure, with dashed horizontal lines, while the black points are the energies of the states generated inside the gap. Even below threshold, a state in the gap appears, and then above threshold condensation takes place in such a state and the energy remains almost stable inside the gap.

The behaviour is different in the right column of figure 4.19. Here we consider wires with small V_0/E_R ratio. In panel c we observe how, even if states in the gap appear below threshold, at condensation power $1P_{th}$, the condensation takes place in a state already inside the second band and the energy continues to increase. Here the width of the gap and consequently the localization of the gap states are not strong enough to trigger condensation on such states. The observed blueshift is comparable with the one of a flat non modulated wire (blue points).

The case of panel d represents a wire where the gap is small and the first band is wide: the observed behaviour is fully similar to what observed in a flat wire. We can measure the blueshift generated by the reservoir below and then above threshold, progressively increasing. Condensation takes place in a state inside the first band and then overcome the gap and create a condensate in the second band.

In panels e and f (corresponding to the wires of panels b and d), we report the real space emission of the wire corresponding to panels, respectively, b and d. We see how strong or weak

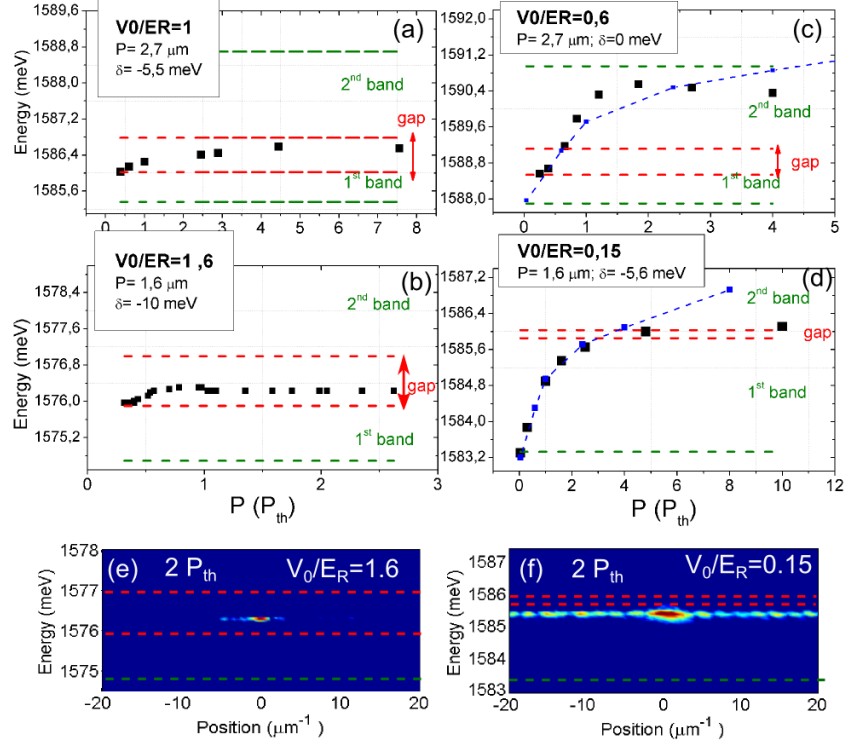


Figure 4.19: In the 4 panels we summarize the behaviour of 4 modulated wires with different values of the ratio V_0/E_R . Panels a,b represents wire with $V_0/E_R \approx 1$, while in panels c-d $V_0/E_R < 1$. The band structure is schematically represented by the green dashed lines, edges of the bands, and the red ones, edges of the energy gap. The black squares represents the blueshift observed by varying the excitation power. In panels c,d this values are reported together with the ones obtained for a flat wire of width $3.5\mu\text{m}$ and $\delta \approx -5\text{meV}$. Panels e and f show the spatial resolved emission corresponding to the wire of, respectively, panels b and d. The red and green lines always represent the edges of the gap and of the bands. The essential parameters of the wires are reported in the figure.

value of V_0/E_R corresponds, respectively, to condensation in a localized or propagating state.

4.5.2 The role of interactions: Bound Gap Solitons

A specificity of our system, with respect to other previous studies of interacting bosons in lattices, is the coexistence of the local excitonic potential together with the polariton-polariton interactions. We already discussed how interparticle interaction can drive localization in gap state named Gap Solitons, characterised by a hyperbolic secant profile with a characteristic size that decreases when going from the low density (bottom of the gap) to the high density limit (centre of the gap). Furthermore, we know that the exclusive presence of an external local potential generates a defect states in the gap, characterized by an exponential spatial decay.

Let's now consider what should be the effect of the coexistence of the two effects on the

spatial profile of the resulting state.

Theoretical background on Bound Gap Solitons

We consider a given number N of bosonic particles inside a lattice, presenting repulsive interaction, being α the interaction constant. We inject them in a region of negative effective mass of the BZ. We also consider the effect of the excitonic potential considering, for simplicity, a delta potential $V\delta(x)$. In such a case, a simple analytical solution of the Gross-Pitaevskii equation (see 1.3.3) is given by a truncated *sech* wave function of the form :

$$\psi(x) = \sqrt{n} \operatorname{sech}((|x| + x_0)/\xi') \quad (4.14)$$

This solution is obtained from boundary conditions: the jump of the derivative at the barrier is proportional to the strength of the barrier potential while far from the barrier, the free Gap Soliton solution remains unperturbed.

The variable ξ' is the characteristic decay length of the envelope function and is linked to the energy of the state as:

$$\xi' = \frac{\hbar}{\sqrt{2|m|E}} \quad (4.15)$$

where E indicates the energy above the upper edge of the first miniband, and is given by:

$$E = \frac{|m| \left(V + \frac{\alpha N}{2}\right)^2}{2\hbar^2} \quad (4.16)$$

x_0 is the truncation coordinate and is given by the expression:

$$x_0 = \xi' \operatorname{arctanh} \left(\frac{1}{1 + \frac{\alpha N}{2V}} \right) \quad (4.17)$$

We can define a variable β as the ratio $\frac{\alpha N}{2V}$, and study the behaviour of the wavefunction for some limit cases. In absence of interaction, $\beta = 0$ and $x_0 \rightarrow \infty$. The wave function is the one of a pure defect state, exponentially decaying on both side of the reservoir. On the contrary, without any excitonic potential V or, equivalently, in the case of strong interaction, $\beta \rightarrow \infty$ and $x_0 \rightarrow 0$. In this case the wavefunction has pure *sech* shape. This is the characteristic shape of a Gap Soliton, (see eq. 4.11), a localised state driven by inter-particles interaction already discussed in 4.3.1. All the intermediate cases, which represent states bound to the perturbation potential V , with a profile modified by interaction, are named Bound Gap Solitons. One can generate a whole family of solutions characterized by a well defined energy in the gap by fixing the quantity $V + \frac{\alpha N}{2}$ and varying the parameters β : this allow to obtain a continuous transformation from an exponential defect state to a free GS.

Few examples of spatial profiles obtained applying the formula 4.14 are reported in figure 4.20 for two different values of E and so of ξ' .

We observe how, by increasing the interactions, the profile deviates from a perfect exponential, gets flatter on top approaching progressively the probability density of the form *sech*², characteristic of a free gap soliton. In the left side of the graph, corresponding to a

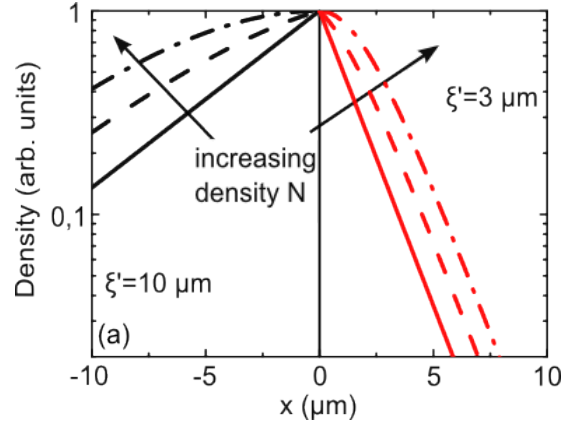


Figure 4.20: Envelope of a Bound Gap Solitons wavefunction, calculated using the formulas from 4.14 to formula 4.17 by progressively increasing the particle density N and so the ratio β . The energy and so the variable ξ' are kept constants. Parameters used: Left side, $\xi' = 10\mu m$, $E = 10\mu eV$. Solid line: $\alpha N = 0$, dashed line $\alpha N = 12\mu eV \cdot \mu m$, dotted dashed $\alpha N \approx 20\mu eV \cdot \mu m$. Right side $\xi' = 3\mu m$, $E = 100\mu eV$, solid line: $\alpha = 0$, dashed line $\alpha N \approx 120\mu eV \cdot \mu m$, dotted dashed $\alpha N \approx 200\mu eV \cdot \mu m$.

energy near to the lower edge of the gap, this variation is particularly clear, while for higher energy, when the size of the state is around 3 microns, the deviation is less pronounced. It's important to notice that changes in the profile occurs even for small values of the non linear term, corresponding to energy shifts of just few tens of microelectronvolts.

Measured spatial profiles of the Gap states

Figure 4.21 shows the experimental profiles corresponding to the gap states S1 and S2 presented in figure 4.21.

The state S2 has an energy close to the center of the gap, corresponding to an energy shift with respect to the top of the first miniband of $E = 0.38meV$. Its intensity profile evidence a strong localisation, with a FWHM of $2.2\mu m$, smaller than the period P of the lattice. For such localized state, we are in the case of the right side of the graph 4.20, where due to the strong localization, it is not possible to see the effect of interactions in the profile shape.

We performed a fit for the envelope of the intensity based on on the formulas 4.15 and 4.14. The result correspond to a curve that is essentially an exponential decay (corresponding to low values of the factor $\beta < 0.05$.)

On the contrary, the state S1 has lower energy, with a value of around $E = 0.22meV$. It's intensity distribution is broader (it presents a FWHM of $6.1\mu m$) and so, although the interaction term is expected to be lower, a deviation from the exponential profile can be evidenced. The envelope of the intensity has indeed the shape of a $sech^2$ function and this is an indication of the role of interaction on the intensity profile and on the formation of a Gap Soliton.

For both states, the exponential spatial decay of the wings of the envelope is found to be around $4\mu m$, not far from the expected values of $\xi = 4.6\mu m$ (for S1) and $\xi = 3.5\mu m$ (for S2),

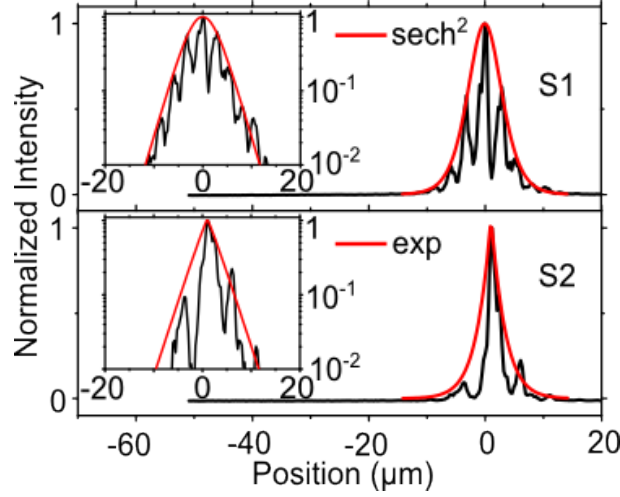


Figure 4.21: The intensity profile of the states S1 and S2 corresponding to figure 4.17. The measured FWHM of S1 and S2 are $6.1\mu\text{m}$ and $2.2\mu\text{m}$. The profiles are fitted by applying formulas 4.15 and 4.14. In order to fit the envelope of the emission, only the intensity at the peaks of the modulated profile are considered. The resulting best fitting function corresponds essentially to a sech^2 for the state S1 and to an exponential for S2. In the insets, the same profiles are shown in log scale.

obtained by applying formula 4.15 (using a polariton mass of $|m| = 0.7 * 10^{-5}m_0$, derived from the curvature of the mini-band at the edge of the BZ).

In conclusion, we have shown how the modulation of the polariton energy changes the spatial behavior of the generated polariton condensate. We discussed how the perturbation to the lattice generate states inside the gap, strongly localized, toward which condensation is triggered. The coexistence of both polariton-exciton and polariton-polariton interaction is unique and specific of our system. It results in the formation of hybrid states named Bound Gap Solitons, bound to the reservoir with a profile analogous to that of a Gap Solitons, dependent on the relative strength of the two interactions.

4.6 Condensation and localization under pulsed excitation

In this section we discuss the condensation of polaritons in modulated wires under pulsed excitation. In this case, both the reservoir and the polariton population evolve in time allowing to explore different regimes by studying the time evolution of the system.

4.6.1 Localization and Bound Gap Solitons dynamic

We now excite a modulated wire by a non resonant picosecond laser pulse and we collect the photoluminescence resolved in time by using a Streak camera (see Chapter 2 for experimental

details).

Dynamics of condensation

In figure 4.22 we summarize the behaviour in time of the integrated photoluminescence signal as a function of the power of the laser beam. On the left graph we report few curves showing

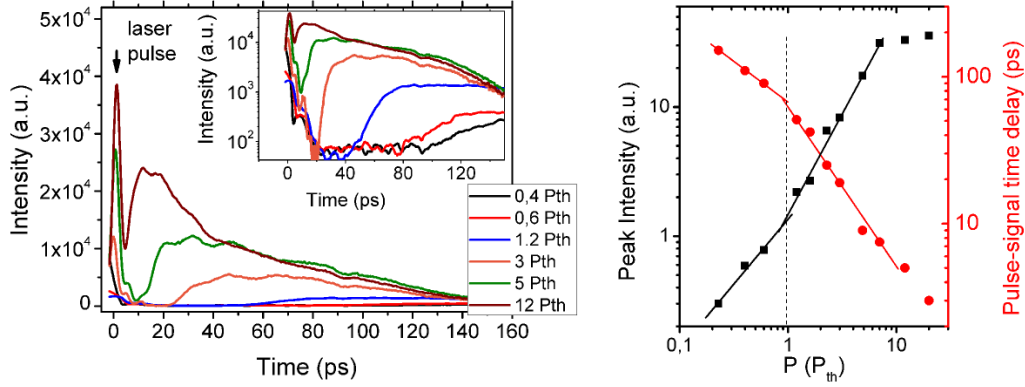


Figure 4.22: A modulated wire is excited with a non resonant ps laser pulse. Its dynamic is resolved in time by the use of a Streak Camera. Left: Total integrated signal emitted from the wire as a function of time for several excitation powers. The peak at $t = 0$ represents reflection of the incoming laser pulse. In the inset the same curve are reported in log scale. Right: Black squares represent the peak intensity of the polariton signal as a function of the excitation power. The red circles show the delay between the pulse arrival and the peak in the emitted polariton signal. Total integrated signal emitted from a modulated.

the typical dynamic of the signal. The ps laser pulse, arriving at $t=0$, populates the excitonic reservoir. Within a certain time delay, excitons in the reservoir relax towards polaritonic states. Below threshold this dynamic is slow, the photoluminescence curve has a long rise time and the photoluminescence signal is weak. On the right of fig. 4.22, we report the value of the peak intensity together with the time delay between the arrival of the pulse and the intensity peak.

By increasing the pump power, the bosonic stimulation accelerates the relaxations from the reservoir toward the lowest energy states and we observe a strong non linear increase of the signal intensity, corresponding to the creation of a coherent polariton population. Parallely, the rising of the signal gets faster, the pulse-signal delay strongly decreases below the time resolution. The signal intensity, after a fast rising, decreases in time due to the finite lifetime of both polaritons and excitons.

It's important to remind that the two populations evolve in time in a coupled way, due to a transfer of particle from the reservoir to the polariton states. As a consequence, although excitons have long lifetime up to 400 ps, the depletion of the reservoir can be much faster due to the stimulation of the relaxation process.

Localization inside the gap

As observed in the case of cw excitation, the spatial behaviour of polariton signal in modulated wire is substantially different from the one observed in a flat wire. In panel a of

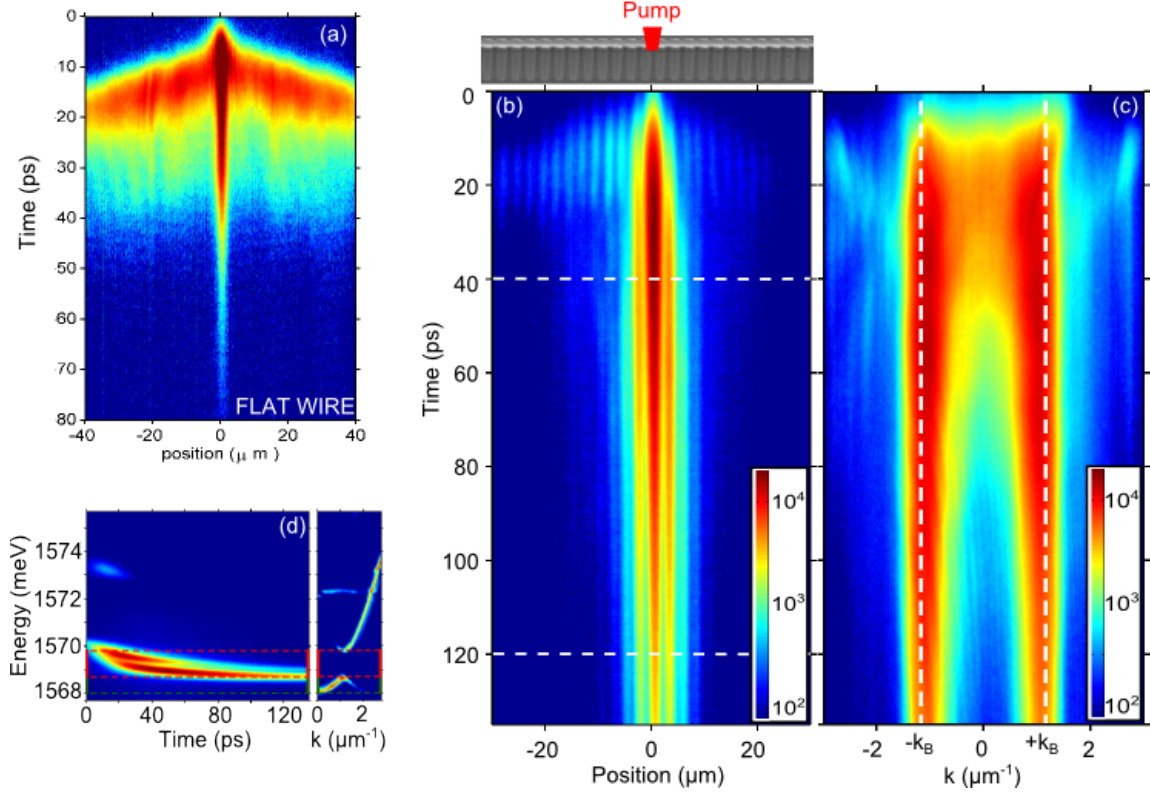


Figure 4.23: Emission under non resonant excitation with a $2\mu\text{m}$ wide pulsed laser spot. (a) Spatially resolved emission measured as a function of time for a flat wire with power $P \approx 3P_{th}$. (b,c) Emission in real and reciprocal space time resolved for a modulated wire excited with a power of $P = 2.5P_{th}$ and spot placed on a maximum of the periodic potential. In (c) the dashed lines show the position of the edges of the first BZ. (d) Energy of the emission as a function of time measured at the center of the wire corresponding to panel b. The dashed lines show the position of the edges of the first BZ. Parameters of the modulated wire: period $P = 2.7\mu\text{m}$, $\delta = -7.5\text{meV}$, $V_0/E_R = 1.5$.

figure 4.23 we show an example of the spatial emission from a flat wire resolved in space and time, excited above threshold. The reservoir blueshift created on the spot region expels polariton from the center. The polaritons outside the spot propagate ballistically and generates the two wing appearing in the figure. The residual reservoir will remains on the spot region and decay with a long lifetime (≈ 200 ps) and, since it is sufficiently highly populated, will continues to populate the polaritonic states. A more complete discussion of the propagation and on the role of the reservoir in flat wire can be found in the Phd thesis of Esther Wertz , and also in [83].

The panel b of figure 4.23 corresponds to a modulated wire excited with a similar the power

($P = 2.5P_{th}$) but that presents a completely different spatial features, showing localization of the emission in the center instead of propagation. In order to completely understand the behaviour of the system, we report also the emission in the reciprocal space (panel c) and the energy of the emission measured in the center of the wire (panel d).

As seen in panel (d) of figure 4.23, for short time delays, a small part of the emission lies in the second allowed band and the corresponding real space image indeed shows a weak signal propagating away from the excitation spot. But the biggest part of the emission remains strongly localized on the spot region in the whole time window. This emission in reciprocal space corresponds to two harmonics located at the edges of the Brillouin zone (white line in panel c), characteristic of the state S1 discussed above.

This shows us that also under pulsed excitation we can trigger condensation into a localized state in the energy gap. But now the system is free to evolve, driven by the coupled evolution of the polariton and excitons populations. Furthermore, the localization of polaritons in the excitation region increases the spatial overlap between the two: this should accelerate the relaxation and so increase in time the ratio between the polariton and exciton density.

Evolution of the spatial profile

Let's now better observe the spatial profiles of the polariton density evolving in time.

In figure 4.24 we report few profiles extracted from panel b of figure 4.23 at different time delays.

At 37 ps, we observe a strongly localized state corresponding to an emission arising from the center of the gap. Later on, the profiles gets slightly broader, together with the approaching of the energy to the bottom of the gap. Interestingly, the shape of the profiles also changes with time. On top of figure 4.24 we report fits of the envelope of the observed spatial distribution applying the formula 4.14 for a bound Gap Solitons attached to a local perturbation. We observe how the envelope progressively changes from an exponential function ($\beta < 1$), typical for a defect state driven by the reservoir, towards a $sech^2$ shaped envelope, typical for a Gap Solitons in which localization is driven by self-interactions. The increase in time of the parameter β , plotted in panel b of figure 4.24 gives a measure of the increase of the relative strength of the interparticle interactions, with respect to the interactions with the excitonic reservoir.

The reservoir indeed gets more and more depleted and the relative strength of interparticle interaction increases: β , despite the large error bars, it is found to increase from almost zero up to a values around 20. From the evolution in time of the size of the state, we can deduce the consequent blueshift, plotted in panel c. To do that we applied formula 4.15 with a values of the mass extracted from the curvature of the band at the edge of the BZ ($|m_p| = 1.7 * 10^{-5}m_0$). The comparison of the obtained values with the experimental blueshift curve extracted from panel d of figure 4.23, is quite satisfying. Additionally, we can combine these values with the ones of the fit parameters $\beta = \alpha N/2V_0$ and obtain an estimation of the relative contribution to the blueshift coming from the reservoir and from polariton self interaction. This is also plotted in panel c, together with the total emitted intensity as a function of time. We can observe that the increase in the self interaction term (orange circles) corresponds quite exactly to the increase in the total emission. This should corresponds to a fast transfer of particle from the reservoir to the polariton states and to a decrease of the

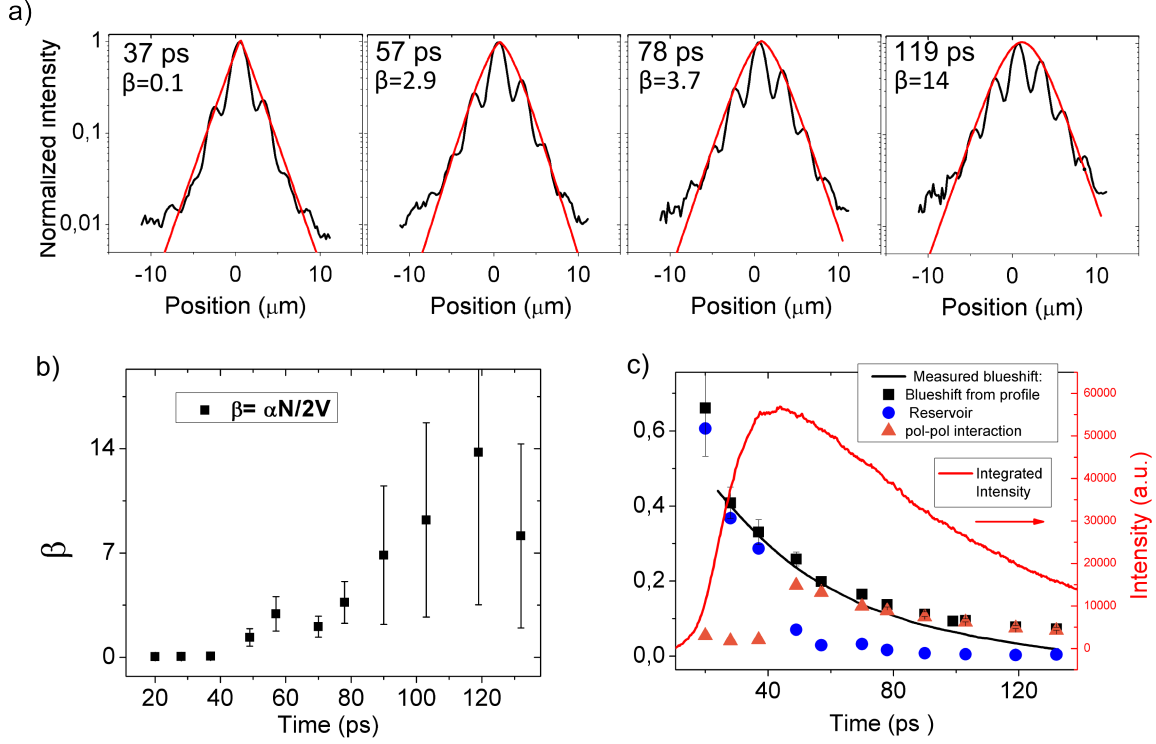


Figure 4.24: a) Normalized intensity profiles extracted from panels b of figure 4.23 at different time delays (black lines). The red lines are fits of the envelope of the profiles obtained applying formula 4.14 and 4.17. In panel b) we plot the values of β obtained from the fit of several spatial profiles corresponding to different time delays. From the extracted size of the observed profiles, we can deduce the corresponding energy blueshift (with respect to the edge of the first band) applying formula 4.15. The results are plotted in black squares in panel c. They are compared to the blueshift extracted from the direct measure shown in panel c of fig.4.23. By combining the values of the extracted blueshift and the values of β , we can derive an estimation of the contribution to the blueshift coming from the reservoir (blue circles) and from the polariton polariton interactions (orange triangles). With a red line we report also the time evolution of the total integrated intensity corresponding to panel b of fig.4.23.

exciton induced blueshift, as obtained and represented by the blue circles. For longer times both contributions decreases, due to finite particle lifetime. The decrease of the total emission at long time presents an exponential decay constant of around 80 ps, that is at least 2 times longer than the expected polariton lifetime. This suggest that still some reservoir is presents and continuously refill the polariton state.

This analysis allowed us to evidence the role of self particle interactions on the nature of the localized state formed. The agreement between the values extracted from the fit and the measured dynamic of both the blueshift and the total intensity is quite satisfactory: it confirms the dynamical evolution from a pure defect state into a Bound Gap Solitons.

Oscillations across the reservoir

We now show different regimes obtained by varying the spot position with respect to the lattice.

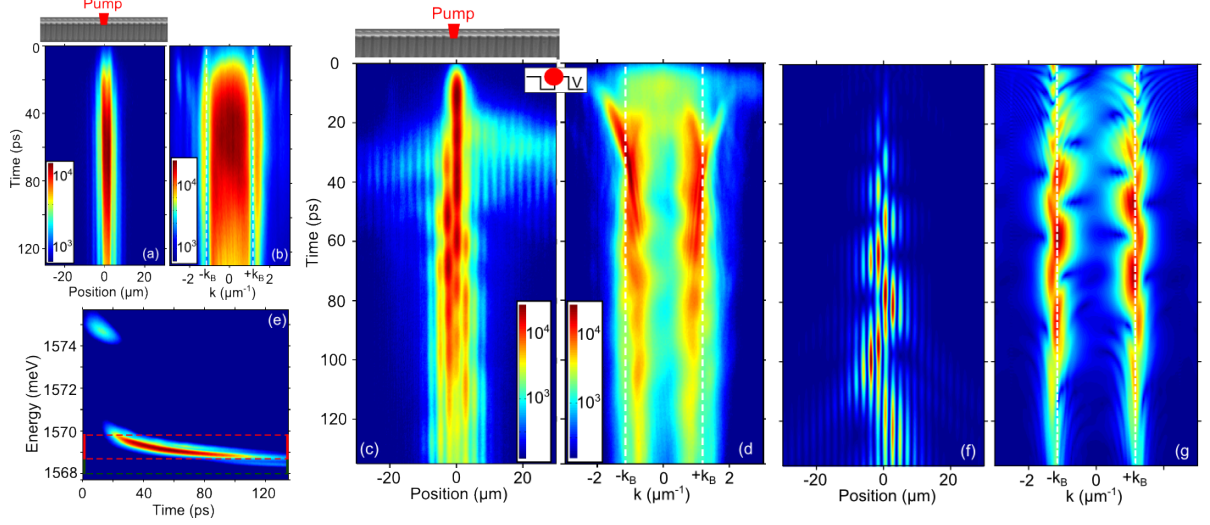


Figure 4.25: a,b) Spatial and reciprocal space emission of the same wire and same excitation power than figure 4.23, but with the spot placed on a minimum of the periodic potential. Here the state S2 is excited. c-d) The same wire is now excited with $P = 4P_{th}$ and the spot is placed in between a minimum and a maximum of the periodic potential and the spatial and reciprocal space emission is reported. e) Energy of the emission as a function of time measured at the center of the wire. f-g) Simulation of the emission both in real and reciprocal space. See text and [83, 110] for more details on the simulation.

In the first two panels a,b of figure 4.25, we show the real and reciprocal space emission of the same wire than figure 4.23, excited with the same power but with a spot centered on a minimum of the periodic potential. This allows to excite the gap state S2, that presents a localized real space emission and in the reciprocal space (panel b) shows the characteristic far field pattern with two minima at $\pm k_B$.

This dependence on the spot position allows us to generate a coherent superposition of two gap states by placing the spot in the middle between a maximum and a minimum of the lattice potential. This is shown in panel c and d and e of figure 4.25. We observe pronounced oscillations both in real and reciprocal space, while the emission energy always remains within the gap. The group of Guillaume Malpuech performed some simulation of our system under pulsed excitation: they reproduced the generation of the state S1 and S2, and also the present oscillatory behavior, shown in panel f and g. The model used is similar to the one presented in [83]: non linearities and also coupling between a local exciton reservoir and the condensate are taking into account and described by the Gross Pitaevskii equation (see [83, 110] for more details on the simulation). A good qualitative agreement with the experiment has been obtained.

The interpretation is that the condensate moves from one side of the reservoir to the other one, passing through the barrier that such reservoir induces. Coherent oscillations between

localized state has already been observed with polariton condensate: they were obtained in a geometry consisting of two coupled traps or two coupled pillars [37, 204]. This was interpreted in term of Josephson oscillations[205], in analogy with the ones observed in atomic gases or liquid helium in double traps [206, 207, 208]. Our situation is analogous: the existence of the energy gap provides the localization needed and the reservoir placed asymmetrically with respect to the lattice provides an energy and spatial splitting between the two states.

Unbinding of Gap Solitons

The simulations revealed also the presence of an additionally regime, corresponding to high polariton density, that is reported in the panel a and b of figure 4.26.

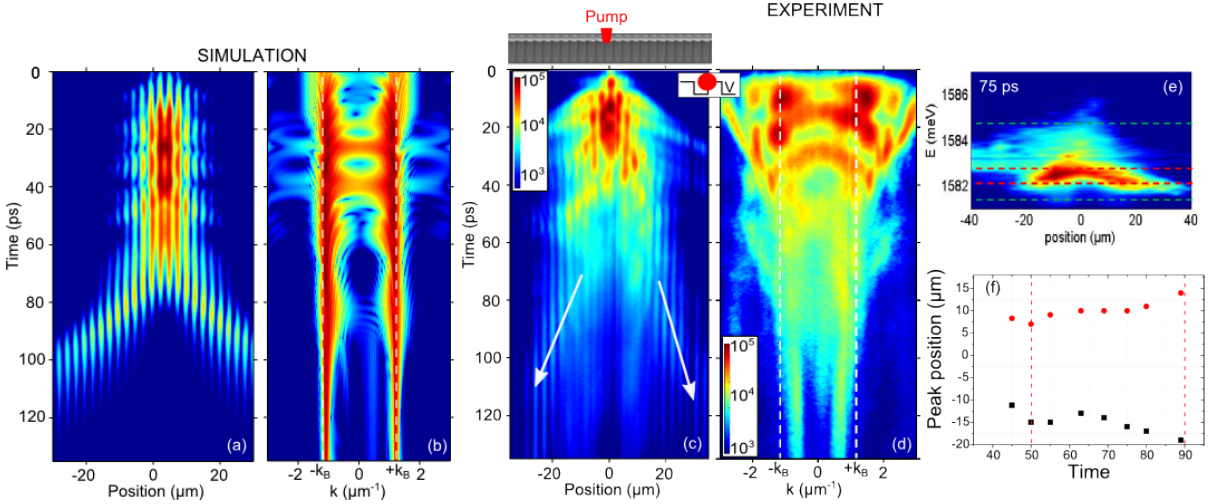


Figure 4.26: a,b): Simulation of the time evolution of the emission in real and reciprocal space (same as panels f-g of figure 4.25) for high excitation density. c-f): Experimental results obtained on modulated wire excited with a $2\mu\text{m}$ pulsed laser spot positioned in between a minimum and a maximum of the periodic potential with power $P = 10P_{th}$. Panels c and d show the spatial and reciprocal space emission as a function of time. Panel e, shows space and energy resolved emission from the wire corresponding to a time delay of 75 ps. The red and green lines represent the edge of, respectively, the gap and the first and second energy bands. We observe how the main emission comes from inside the gap. In panel d we plot the position of the two distinct wavepacket appearing in panel c (evidenced by white arrows) as a function of time. The two vertical lines delimit the interval in which the emission from the two packets lies inside the energy gap. Parameters of the wire: $P = 2.7\mu\text{m}$, $\delta = -3\text{meV}$, $V_0 \approx 0.9\text{meV}$.

Here we observe how, for short time delays the generated gap state remains localized in the spot region, but later on, at around 70 ps, two wavepackets spread away from the central region, while the energy of the polaritons in the packets remains inside the energy gap of the linear dispersion.

This behaviour could be interpreted in terms of moving Gap Solitons. The high excitation region would bring to a quickly depletion of the reservoir in the first 70 ps. Polaritons localized

in the gap wouldn't be attached to the reservoir any more and could unbind a spread away, with a energy given purely by polariton-polariton and placed inside the energy gap, forming a moving free Gap Solitons, as theoretically discussed in ref. [147, 209].

In the experiment we observed a behaviour similar to the simulated ones, reported in panels (c-f) of figure 4.26. The pumping configuration is the one of figure 4.25, but at higher power ($P = 10P_{th}$) and on slightly different wire.

At short times a complex behavior both in real and k-space is observed: this is due to ballistic propagation of high energy polaritons, together with oscillations similar to the case described in the previous paragraph. We won't discuss in detail this regime. We will focus on the fact that after 50-60 ps, the signal in the excitation area vanishes, while two packets seems to move away from the excitation region. The position of the two packets are reported for several time delay in panel f of figure 4.26. The emission has been resolved in time, energy and space. This allows to obtain the complete evolution of the system and to reconstruct a colormap showing the emission, energy and space resolved, for different time delays. An example is reported in panel e. We observe that in a time interval in between 50 and 90 ps the emission comes from inside the energy gap. This means that the polariton wavepackets are unbinding from the reservoir localized in the excitation region, and spreading away, despite having an energy in the gap. Since outside the central region no blueshift induced by the reservoir is expected, this suggests the crucial role of interparticle interactions in the generation of this spreading gap states.

Further investigation of this regime, especially of collisions of this expelled wavepackets[147], would give a better insights on the nature of these states.

Conclusion of the first part

The first part of this chapter has been dedicated to the study of polaritons in a periodic potential.

We introduced our approach to engineer a 1D potential for polaritons, based on the modulation of the wire's width. We have shown how a periodic change of the wire's width generate a lattice and allows to redefine the polariton dispersion by the formation of bands and opening of energy gaps, which widths can be controlled at will.

In the condensation regime, we have shown how the obtained band structure completely changes the spatial behaviour of the generated polariton condensate. Condensation is trigger towards a strongly localized states inside the energy gap, induced by a perturbation to the periodicity of the lattice is introduced. The peculiarities of our system is that, under non resonant excitation, such perturbation is the result of both interactions with the exciton reservoir and from polariton-polariton interactions. We discussed how this can generate hybrid state named Bound Gap Solitons and we observed effects of polaritons non-linearities in the measured spatial profile of the localized states: the correlated time evolution of the excitons and polaritons population allowed us to observe a spontaneous transition from a pure defect state to a Bound Gap Solitons.

The potentialities of the presented 1D potential shaping opens the way to the implementation of a wide range of structures and devices, from a controlled defects[210], to a double barrier operating as a resonant tunneling diode[31]. In the following we present how more complex

potential structure can also be obtained to observe polaritons Bloch oscillation [211] or study polaritons in aperiodic potential.

Especially under pulsed excitation, the mutual time evolution of the excitons and polaritons population allowed us to observe a spontaneous transition from a pure defect state to a Bound Gap Solitons.

4.7 Polaritons Bloch oscillations

This section will be dedicated to the study of the behaviour of polaritons when a periodic potential is combined with an energy gradient.

A by Hugo Flayac[32, 211] to exploit the polariton coherent propagation to observe Bloch oscillation by monitoring the time evolution of a polariton wavepacket.

In this chapter we present two different approaches to obtain a periodic potential combined with a constant acceleration. The first one consisted in the etching of a properly shaped microcavity and in this structure we will proof of the appearance of a Wannier-Stark ladder. The second one is based on the exploitation of the blueshift induced by the reservoir and the energy gradient present at its edges. In this configuration, time resolved measurements will show the generation of Bloch oscillation and will give evidence of Landau-Zener tunneling effect.

4.7.1 Overview on Bloch oscillations

Basic theory

The Hamiltonian that we consider is the following:

$$H = \frac{\hat{p}^2}{2m} + V(\hat{x}) - F\hat{x} \quad \text{with} \quad V(x + P) = V(x). \quad (4.18)$$

where the periodic potential V is superposed to a gradient F , constant in space. The gradient term breaks the translational symmetry and so the Bloch states $|n, k\rangle$ are no more eigenstates of the system. We can ask ourselves how a particle prepared at $t = 0$ in the state $|n, k_0\rangle$ evolves in time. It can be shown [140] that at time t the wavefunction is still in the Bloch form $|\Psi(x, t)\rangle = e^{ik(t)x} |u(t)\rangle$, with the quasi momentum k given by:

$$k(t) = k_0 + \frac{1}{\hbar} \int_0^t F(t') dt' \quad (4.19)$$

As we better discuss later, for low values of F we can neglect the possibility of an interband transition and this means that the $|u(t)\rangle$ corresponds exactly to the function $|n, k(t)\rangle$ (except for a phase factor).

In the case of a force F constant in time, the quasi-momentum is given simply by:

$$k(t) = k_0 + \frac{Ft}{\hbar} \quad (4.20)$$

It means that the quasi-momentum scans the reciprocal space at constant speed, as schematically represented in figure 4.27, where the band structure is reported extended over several BZ.

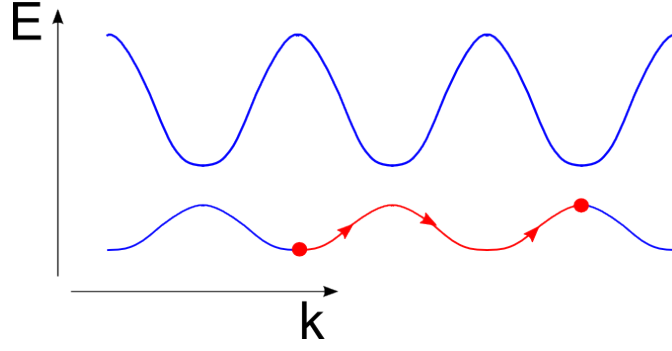


Figure 4.27: Scheme of the trajectory in the reciprocal space of an accelerated particle inside a periodic band structure in the adiabatic approximation.

It is possible to define a characteristic timescale of the system:

$$\tau_B = \frac{2\hbar k_B}{F} \quad (4.21)$$

that corresponds to the time required to an increase of $2k_B$ of the quasi-moment or, in other word, to a complete scan of the first BZ.

The corresponding mean velocity v_g is a periodic function of the quasi-momentum. This means that v_g varies periodically in time, and consequently also the mean value of the position oscillates. This effect, despite firstly predicted by Zener[212], was named Bloch Oscillation (BO), and consists in a constant force that generate, counter intuitively, an oscillating trajectory.

Classical approach and trajectory calculation

The calculation of the particle trajectories, in the adiabatic approximation, can be approached in a complete classical way, in which the operator \hat{x} and \hat{p} can be replaced by number x and $p = \hbar k$, while the information on the band structure will be enclosed in the dispersion relation $E(p)$ [213]. The Hamiltonian becomes:

$$H = E(p) + Fx \quad (4.22)$$

and solutions are given by:

$$x'(t) = \frac{\delta H}{\delta p} = \delta E(p) \delta p \quad p' = \frac{\delta H}{\delta x} = -F \quad (4.23)$$

In the tight binding regime, the dispersion of the first band has the simple expression $E(k) = \frac{\Delta}{2} \cos(pP/\hbar)$ (given also in eq. 4.7), and one can derive analytical solution of the motion equations with initial conditions x_0, p_0 , as done by Hartmann and coworkers, obtaining:

$$x(t) = x_0 - \frac{\Delta}{F} \sin\left(\frac{\omega_B}{2}t\right) \sin\left(\frac{\omega_B}{2}t - p_0\right) \quad (4.24)$$

$$p(t) = p_0 - Ft \quad (4.25)$$

with $\omega_B = \frac{FP}{\hbar}$.

Additionally, in the theoretical work of Hartmann, the evolution of a whole Gaussian packet of initial width Δx_0 and Δp_0 is considered. At $t = 0$ the packet is described by:

$$W(p, x, t = 0) = \frac{1}{2\pi\Delta x_0\Delta p_0} e^{-\left(\frac{(x-x_0)^2}{2\Delta x_0^2}\right) - \left(\frac{(p-p_0)^2}{2\Delta p_0^2}\right)} \quad (4.26)$$

The time dependence of the momentum mean value and width is trivial:

$$\langle p(t) \rangle = p_0 - Ft \quad \Delta p_t^2 = \Delta p_0^2 \quad (4.27)$$

while for the spatial coordinate the result is more interesting:

$$\langle x(t) \rangle = x_0 - \frac{\Delta}{F} e^{-\Delta p_0^2 P^2 / 2\hbar^2} \sin\left(\frac{\omega_B}{2}t\right) \sin\left(\frac{\omega_B}{2}t - p_0 P\right) \quad (4.28)$$

$$\Delta x(t)^2 = \Delta x_0^2 + \frac{\Delta^2}{2F^2} (1 - e^{-\Delta p_0^2 P^2 / \hbar^2}) \sin^2 \frac{\omega_B t}{2} \quad (4.29)$$

Both in 4.24 and 4.29, we observe how the trajectories are periodic functions, with a Bloch period $\tau_B = 2\pi/\omega_B$. But the spatial amplitude and the width of the packet are strongly influenced by the initial width in the momentum space ¹. In figure 4.28 we plotted few results

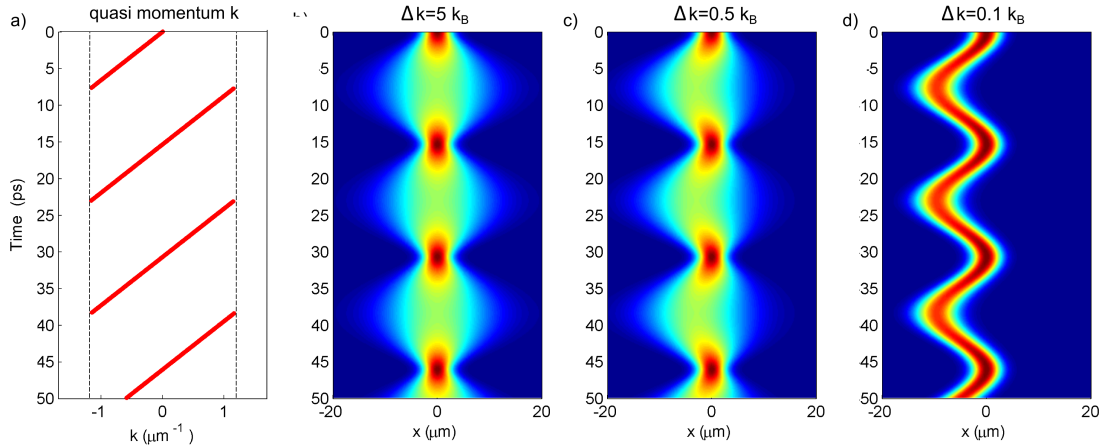


Figure 4.28: Evolution of a Gaussian wavepacket in a periodic potential with a constant gradient obtained applying formulas 4.27 and 4.29. Panel a) shows the mean values of the quasi-momentum (represented folded in the first BZ). Panels b-d) Evolution of the Gaussian wavepacket in real space obtained for 3 different values of the width of the packet in k space (values reported in the figure). Parameters: $\Delta E = 1 meV$, $F = 0.1 \mu eV/\mu m$, $x_0 = 0$, $p_0/\hbar = 0$, $\Delta x_0 = 0$.

in which we simulate the trajectories for different initial conditions. The parameters used are similar to the ones characteristic for a polariton system. By varying the initial width in k space

¹The origin of this effect relies on the variation of the effective mass m_{eff} with k[143]

we can identify a first regime, panel b, in which a large distribution in k , results in a constant position of the wavepacket of oscillating width. This effect is called breathing.

The Bloch oscillations appear when $\Delta p_0/\hbar \ll k_B$. The packet oscillates with a time period τ_B and remains confined in a region of space. The spatial amplitude is given by the expression:

$$L_B = \frac{\Delta E}{|F|} \quad (4.30)$$

This value has an intuitive interpretation: the band structure can be seen as tilted by the gradient force (see figure 4.29). A particle starts at the bottom of the first band, travels at a constant energy, then reaches the gap, is reflected and comes back. The total undergone trajectory is therefore $2 \cdot L_B$.

Although this approach of tilted band is not really rigorous, since it mixes real and reciprocal space, it is the one used originally by C. Zener [212]. We will see how it provides the good picture to interpret experimental spectra.

Above the adiabatic approximation: the Landau-Zener tunneling

The tilted-bands picture given by Zener was initially introduced not to describe the effect of Bloch Oscillations but to investigate the effect of breakdown of the electronic bands under strong electric field in a solid [212].

Up to now we have considered the *single band* or *adiabatic* approximation, with the particle staying always in the same band. But actually there is a non zero probability for the particle to hop to the upper band. This effect is known as Landau-Zener tunneling and is represented schematically in figure 4.29.

According to [212], the probability of hopping to the second band follows the expression:

$$P_{LZT} \propto \exp \left[-\frac{\pi^2}{h^2} \frac{mP\Delta E_{gap}^2}{|F|} \right] \quad (4.31)$$

The formula shows how the probability strongly depends on the width of the gap ΔE_{gap} and also on the strength of the acceleration.

The observation of Bloch oscillations of course requires such a probability to be low, otherwise most of the population would be lost after one or few oscillations.

The Wannier Stark ladder

In the late 50s, Wannier showed that in presence of a constant gradient, Bloch functions are no more stationary states of the system and the continuum of each bands splits in a series of discrete states, equally spaced in energy. An intuitive understanding of this effect can be obtained with the following reasoning. Considering an eigenstate function $\Psi(x)$ of eigenenergy E_0 , the periodicity of the modulation of the potential, allows one to build a complete series of eigenstates by a shift of integer number l of periods P , $\Psi(x-lP)$. This results in the construction of a whole ladder of eigenstates with energies

$$E_{\pm l} = E_0 + lPF \quad \text{with} \quad l = 0, \pm 1, \pm 2 \dots \quad (4.32)$$

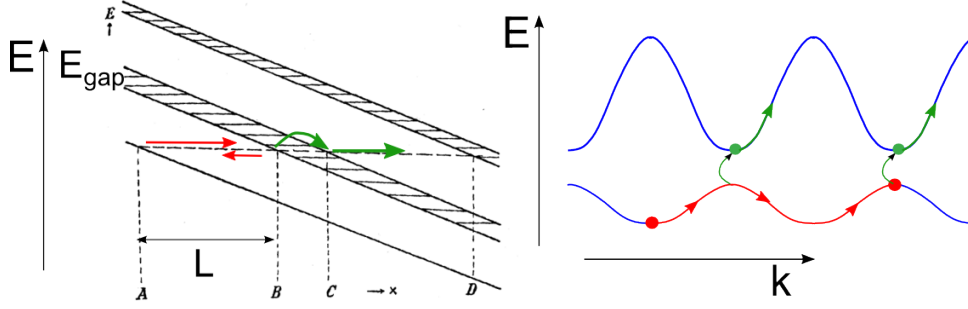


Figure 4.29: Scheme of the Landau-Zener tunneling represented in two different approaches. On the left is represented in the tilted band scheme as introduced by Zener [212]. On the right in terms of particles that follow trajectories inside the periodic band structure. In both the pictures, red flashes indicate Bloch oscillation following adiabatic evolution while green flashes indicate non-adiabatic tunnelling effects.

The complete set of these solutions forms the so called Wannier-Stark ladder². This ladder is, in principle, infinite, with no upper and lower limits. The distance between the levels corresponds exactly to \hbar/τ_B and indeed this ladder can be interpreted as the equivalent of the Bloch Oscillations in the energy domain.

Wannier stark ladder has been observed experimentally in several systems: the first observation was done by Paul Voisin, and consisted in the probe of electronic levels in a semiconductor superlattice [215] by optical absorption. The observation of such states indeed requires that the energy step $F \cdot P$ to be bigger than the linewidth of each electronic states in the crystal, mainly induced by the diffusion of impurities. In other words, we can say that the particle needs to have a sufficiently high coherence length, that allows it to perform a complete Bloch oscillations before being scattered. The superlattice allowed indeed to modulate and increase of around 2 orders of magnitude the value $P \cdot F$, since P is no more the material lattice constant but is the distance between dielectric layers.

A sufficiently coherent length is therefore essential for observing both Wannier Stark Ladder or Bloch oscillations.

Indeed, in system where particles have much longer coherent propagation lengths, such as cold atoms [216] or photonic systems [217, 218, 158], both Wannier-Stark resonances and BOs have been observed.

²The existence of Wannier-Stark ladder has been the subject of a long controversy [214]: indeed formula 4.32 is exact only in the limit of single band approximation. The non zero probability of tunneling to higher bands allows to define such energies only as resonances, corresponding to metastable states of finite lifetime.

Detecting Bloch oscillations

The observations of BOs requires long coherence length compared to the oscillation period (as discussed above), but also a mechanism to induce an energy gradient together with a efficient way to detect the time evolution of the population.

For electrons in bulk or in a superlattice, the gradient is provided by the application of an electric field, while the detection is obtained via quite complicated experimental techniques such four wave-mixing[219] or detection of terahertz emission[165]. For cold atoms acceleration is given by gravity[220] or by an overall shift of the optical lattices[221]: with these approaches BOs have been observed in reciprocal space (see figure 4.30).

More recently, BOs have been studied also in photonic systems, such as waveguide arrays or periodic dielectric layers. The gradient was generated by a linear variation of the optical index obtained either by varying the alloy composition[218, 217] or by a thermic effects[222]. Then the transmission of the device is detected, or, as in the case of reference [222], the output at the end of the waveguide arrays is collected as a function of the propagation time and of the induced gradient. The experiment results are shown in picture 4.30.

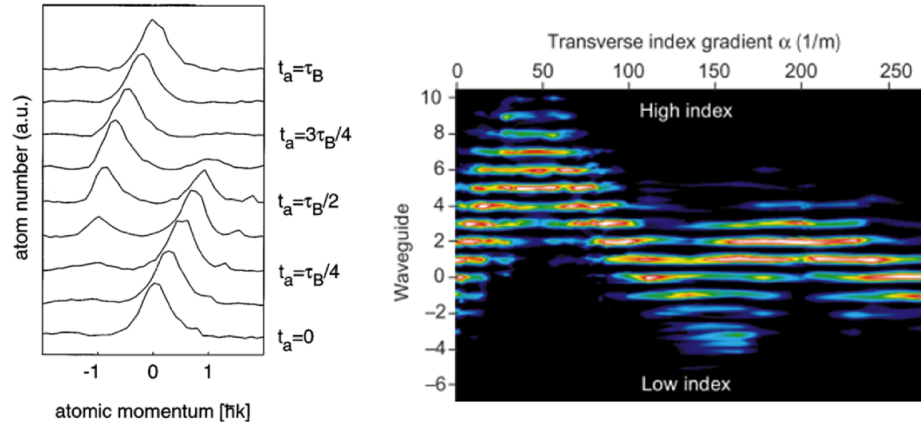


Figure 4.30: Two examples of observation of Bloch oscillations. Left: Bloch oscillations detected following the momentum distribution of ultracold cesium atoms in optical lattice constantly accelerated. Oscillations inside first BZ are observed (figure extracted from [221]). Right: Bloch oscillation inside waveguide arrays. The output of the waveguide is detected as a function of the strength of the gradient in the optical index gradient and oscillations of the center of the wavepacket are observed (figure extracted from [223]).

Despite the fact that a large variety of systems has been investigated, Bloch oscillations have never been observed and studied at the same time in real and momentum space and additionally, the observation in real space are mainly indirect observation, where the evolution of wavepacket is usually studied as a function of the variation of the gradient, while the direct time evolution is not detected.

In this context, polaritons present clear advantages. They have long coherence length typical of photonic systems, and polaritons motion can be easily detected via the signal escaping the cavity, both in real and reciprocal space. In addition, peculiar effect related to the pseudospin

precession have been predicted[32].

4.7.2 “Bloch oscillators” structures

We now describe the first approach that we applied to obtain an energy gradient along a wire based on the etching of specific 1D structure, that will be named “Bloch oscillators”. The Wannier-Stark ladder will be evidenced in the photoluminescence spectra of these structures.

Design of the structures: basic parameters

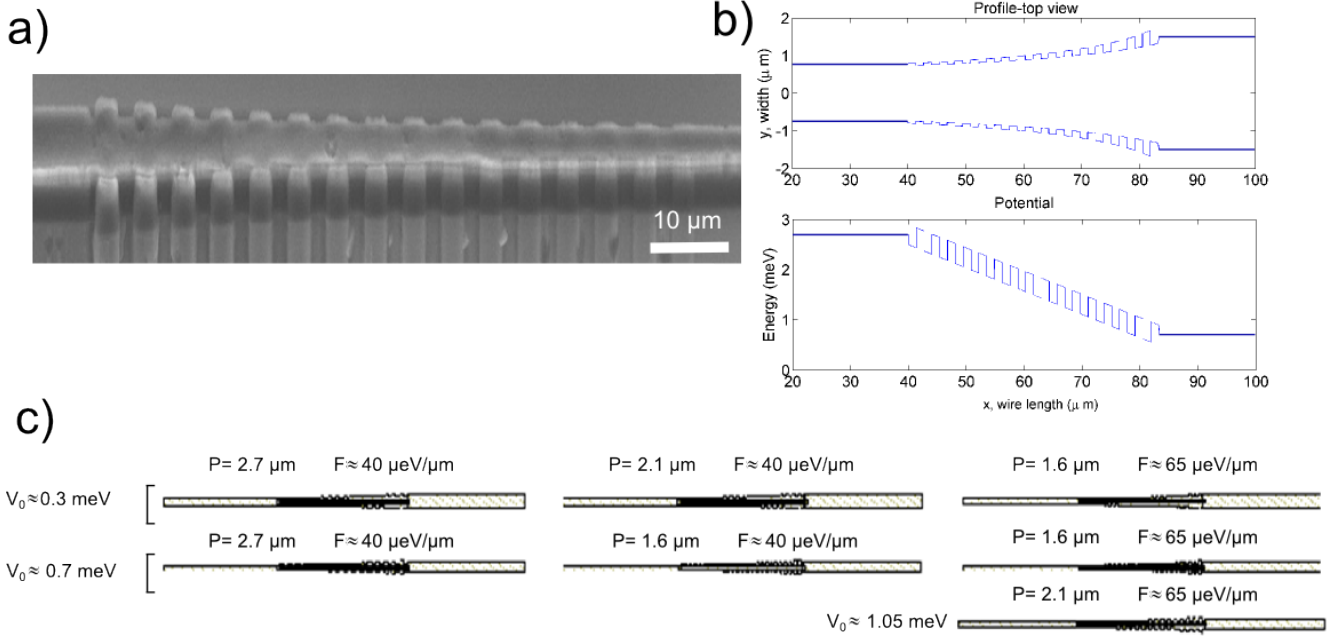


Figure 4.31: 1D structures for the observation of Bloch Oscillations. a) Scanning electron microscope image of one of this structure. b) Width profile and corresponding polariton potential in one of the structure (Parameters: $P = 2.7\mu m$, $V = 0.4meV$, $F = 45\mu eV/\mu m$). c) Scheme of the whole set of structures realized: the essential parameters are reported in the figure.

The lateral width modulation in a wire can be used not only to generate the periodic modulation but also to induce an acceleration for polaritons.

The dependence of the confinement energy with the width L_x (see 2.1), allows to obtain a constant energy gradient when the lateral size of the varies as $L_x \sim L_0/\sqrt{x}$.

Inspired by previous theoretical proposal [211, 224], we realized this kind of lateral modulation at first on the profile of straight wire, where we observed acceleration and deceleration of polaritons traveling through this ramp.

Then, we combined this principle with the periodic modulation, obtaining the structure shown in figures 4.31. By properly adjusting the strength of the width modulation with respect to the local width of the wire, it is possible to obtain a lattice of constant depth V_0 combined with a linear energy profile, or in other word, a constant acceleration (see panel b of figure 4.31).

The purpose of these structures was to observe Bloch oscillations of polaritons and their parameters were set accordingly. In panel c of figure 4.31 we resume the whole set of structures etched on the samples.

The set of adjustable parameters are the period P and the depth of the potential V_0 and also the additional parameter F giving the strength of the acceleration, expressed in $\mu\text{eV}/\mu\text{m}$.

Practically one cannot achieve any value of the acceleration for two reason. A wire larger than $4\mu\text{m}$ reduces the spectral distance between the several confined modes and so the 1D character of the system. A wire thinner than $\approx 1.5\mu\text{m}$ brings to non radiative excitonic recombination and affects polariton propagation.

According with figure 4.7, this limits correspond to confinement energy difference of around 4meV for the optical mode, and $\approx 2\text{meV}$ for polaritons (at detuning $\delta = 0$). The size of the accelerating region is $40\mu\text{m}$ long in all the structures and the maximum values for the acceleration obtained is around $80\mu\text{eV}/\mu\text{m}$ ³.

In figure 4.32 we show how the parameters of the wire influence the two main parameters characterising the BOs: the temporal and spatial period τ_B and L_B . The results shown are directly obtained considering the band structure values illustrated in fig. 4.11 and applying the formula for τ_B and L_B reported in the discussion above.

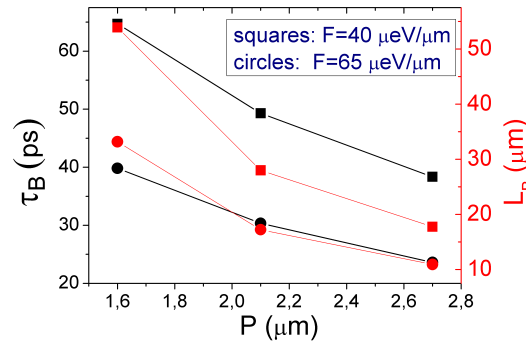


Figure 4.32: Temporal (black) and spatial (red) expected period of BOs, varying the period P of the modulation and for two different values of the acceleration F : $40\mu\text{eV}/\mu\text{m}$ (squares) and $65\mu\text{eV}/\mu\text{m}$ (circles).

The target was to obtain spatial oscillations that could always remain inside the $40\mu\text{m}$ of the modulated region, far from the edges and from the region where the wire gets too thin. At the same time the temporal period shouldn't be too long compared with the typical polariton lifetime of around 40 ps, in order to observe several repetition of the oscillations. The best structures reveal to be the ones with the strongest gradient and higher period. Additionally also the depth of the potential plays a role, since for higher potential, the Landau-Zener tunneling probability decreases.

³Some wires has been etched with values of the width that goes down to $1.2\mu\text{m}$

Observation of Wannier-Stark ladders

The observation of Bloch oscillations requires the excitation of such structure via a pulsed excitation and the detection of the evolution in the picosecond scale. But interesting information can be obtained also by studying the photoluminescence under cw excitation.

In panel a of figure 4.33 we show the emission from the structures excited non resonantly with a $2\mu\text{m}$ spot.

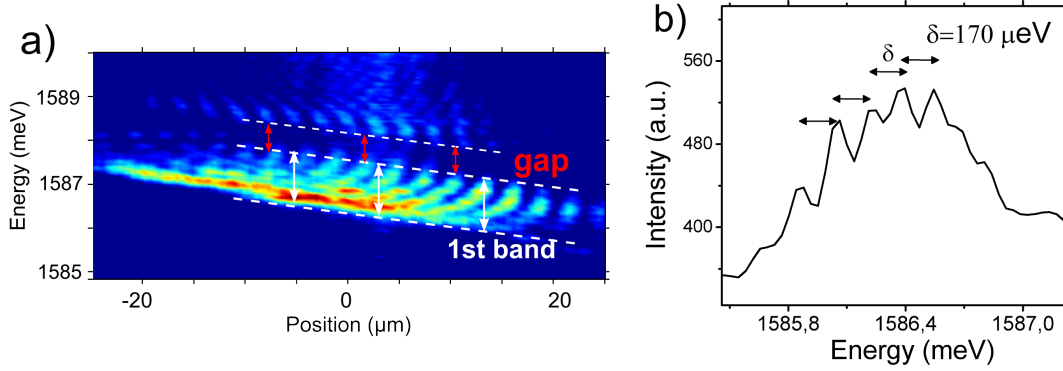


Figure 4.33: a) Emission spatially and energy resolved from a Bloch oscillators excited non resonantly below threshold. The linear gradient is visible and also the band structure can be recognized. The red and green flashes represent respectively the gap and the first miniband that shift according with the gradient. b) Integrated emission spectra from a Bloch oscillators. We focus on the energy of approximately the first miniband. Several equidistant peaks are visible. The distance δ corresponds to $170\mu\text{eV}$, exactly the value characteristic of the Wannier-Stark ladder for this structure.

The presence of the gradient appears clearly in the linear shift of the lowest emission energy. More remarkably, the band structure is still clearly distinguishable, with the energy gap and the first band tilted following the gradient. The picture of Zener reported in the scheme of figure 4.29 is exactly reproduced.

In panels b of figure 4.33 we focus on the emission spectra extracted from a Bloch oscillators at the energy region corresponding to the first miniband.

The spectra collected presents several equidistant peaks. The energy distance between the peaks is measured to be $170\mu\text{eV}$. This value corresponds exactly to the values $F \cdot P = 63\mu\text{eV}/\mu\text{m} \cdot 2.7\mu\text{m} = 168\mu\text{eV}$, where F is directly measured from the tilt of the bands. This suggests that the origin of these peaks are signature of the Wannier-Stark Ladder, seen, as far as we know, for the first time via photoluminescence measurements.

Limitation for the observation of BOs

Although the Wannier-Stark states represent the equivalent of the BOs in the spectral domain, the observation of the oscillations in time, requires different conditions. One needs to follow and distinguish the emission of a single wavepacket in time, if possible both in real and reciprocal space.

The experimental configuration that we used consisted in a resonant excitation provided by a $1.4ps$ pulsed laser, focused down to a spot of size around $2\mu m$ by a microscope objective of $NA = 0.55$. This results in an excitation that will be broad both in energy and in angular distribution: the energy broadening can be estimated around $0.3meV$, comparable with the width of the first band, while the angular distribution corresponds to several k_B . As a consequence, it's hard to resonantly excite a well define state at $t = 0$ and then follows its evolution. Additionally resonant excitation in reflectivity configuration is complicated by the strong intensity of the reflected laser signal. A different approach has then been tried, based on a non resonant excitation.

4.7.3 Bloch oscillations under non resonant excitation: acceleration induced by the reservoir

Here we present observations of Bloch oscillations obtained under non resonant excitation of straight wire, without any gradient on the width. In order to overcome the limitation presented by the "Bloch oscillators" structure, we tried to exploit the blueshift induced by the excitonic reservoir in order to obtain an energy gradient along a modulated wire.

By using a large laser spot the reservoir can be extended over a wide region. The blue-shift that it generates does not represents anymore simply a local perturbation of the lattice, but it shifts the energy of all the sites causing an overall shift of the bands structure. This is represented in figure 4.34, where a modulated wire is shined in the center by $30\mu m$ non resonant laser spot. We can recognize how the band structure is blue-shifted according with the laser shape and at the edge of the spot an energy gradient is induced.

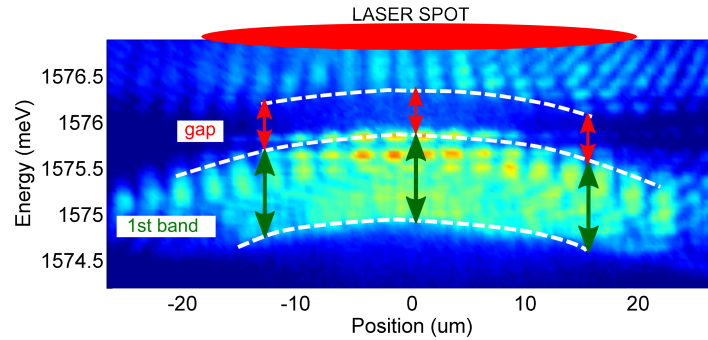


Figure 4.34: Real space emission from a modulated wire excited with a $30\mu m$ wide spot below threshold. The reservoir generates a blueshift of the whole band structure, evidenced by the white dashed line, and therefore an energy gradient is induced on the edges of the spot. The position of the first band and the energy gap are reported respectively by green and red flashes.

This shows how a non resonant excitation, above threshold, could be used at the same time to inject a reservoir that induce a energy gradient, and a condensate with a well defined k vector.

In figure 4.35, we represent the results obtained by exciting a modulated wire with a non resonant pulse at $P \approx 5P_{th}$ focused on a large spot, schematically represented in this figure and

which profile is shown in panel b of fig. 4.36). We monitor the dynamics of the emission in both real space and k-space/

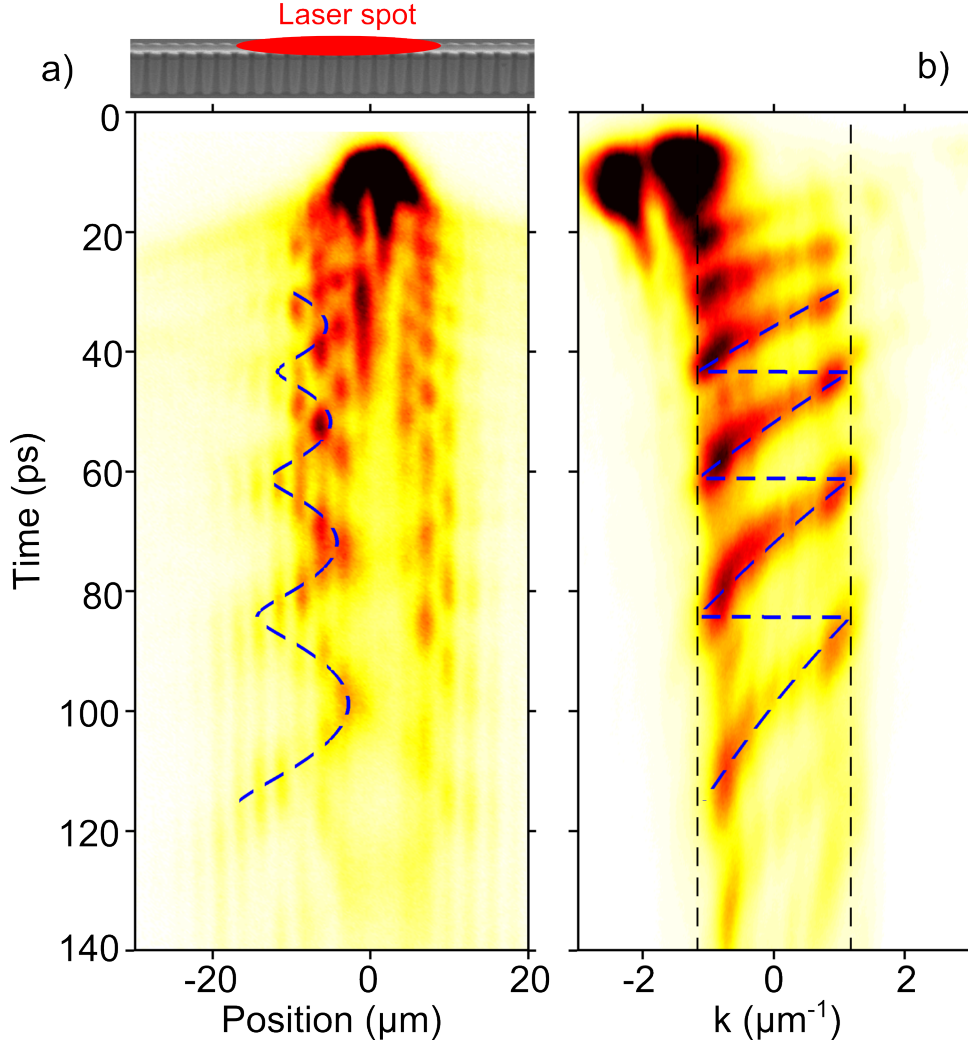


Figure 4.35: a) Real space emission from a modulated wire excited at power $P \approx 5P_{th}$ with a large non resonant spot (spot profile shown in figure 4.36). b) Reciprocal space emission corresponding to the region on the left of the spot in panel a (from $-20\mu m$ to 0). The black dashed lines indicate the edge of the first BZ. Oscillations of the wavepacket inside the first BZ are visible and in real space they correspond to signal that remains confined in a certain region and oscillates in time. Both the spatial and temporal period of the oscillations increase in time. The dashed blue lines presents the result of a numerical calculation based on formula 4.33 and a band structure obtained via a KP calculation (see text for more details). Parameters of the fit: $\tau = 80ps$, $F_0 = 120\mu m$. Parameters of the wire: $P = 2.7\mu m$, $V_0 = 0.85meV$, $m_p = 6.1 * 10^{-5}$, $\delta = -4meV$.

Panel a corresponds to real space emission, while in panel b I plot the k space emission corresponding to the region on the left of panel a.

In both we can recognize an oscillatory behavior: the signal in reciprocal space presents a continuous monotonous variation of the k -vector inside the first BZ, indicated by dashed black lines, while at the edge of the zone one can recognize the jump from $+k_B$ to $-k_B$ typical of a Bloch reflection. In the real space this corresponds to a wavepacket that moves but remains localized in a certain region, following trajectories almost parabolic. These present exactly the same period than the oscillations in the k -space. These oscillations are triggered only on the left of the spot due to its asymmetric shape.

The energy gradient induced by the reservoir accelerate polaritons away from the spot region, but then when the acquired wave-vector reaches the edge of the BZ, it changes sign abruptly, and so the speed of the wave-packet is inverted generating the observed oscillations also in real space. During the time evolution, the reservoir gets depleted thanks to the relaxation and exciton recombination. The values of the potential gradient decreases in time, and so both the temporal and spatial period of the oscillations increase, according with formula 4.21 and 4.30.

To quantitatively reproduce the observed oscillations, we performed some simulations starting from the specific parameter of the wire used. The model proposed by Hartman in [213] and described in the introduction is not appropriate anymore, since it was based on an acceleration constant in time. Therefore, we performed a more general numerical calculation. By starting from the structural parameters of the wire we obtained the band dispersion from a Kroenig Penney calculation. Then, from the band shape, the group velocity is deduced, and so all the kinematic can be derived. Parallely, we consider the existence of a energy gradient which dependence in time is extracted from the measurements of the energy and time resolved emission. In panel (a) of figure 4.36 we show the energy of the emission at $k = 0$ corresponding to panel (b) of figure 4.35. The decrease of the energy with time can be fitted by an exponential with decay constant $\tau = 80ps$, as shown in the panel. This will be the decay rate of the acceleration used in the model. In panel (a) we also report with horizontal lines the energies corresponding to the gap and the band for the unaffected band structure: it's important to underline that although most of the signal have energies inside the gap, we can still consider polaritons as inside the first miniband since the whole band structure is blue-shifted by the reservoir.

The exponential decay of the acceleration, that reads $F(t) = F_0 e^{-t/\tau}$, gives an evolution of the quasi-momentum that can be written as:

$$k(t) = k'_0 + \frac{1}{\hbar} \int_0^t F(t') dt' = k_0 - \frac{\tau F_0}{\hbar} e^{-t/\tau} \quad (4.33)$$

From this, we deduce $v_g(t)$. Then, the real space trajectories are calculated. The parameter k_0 is the wave-vector at the beginning of the oscillations and this can be deduced from the k -space emission. Therefore, the only fitting parameter is F_0 , is the initial value of the acceleration.

The results are reported superposed to the experimental datas on figure 4.35 starting from a time delay of around 30 ps, since before oscillations are too fast and small to be identified.

We can see how the experimental trajectories are well reproduced both in real and reciprocal space: the period of the oscillations increases in time and the corresponding oscillations in real space get larger. This is due to the decay of the reservoir population.

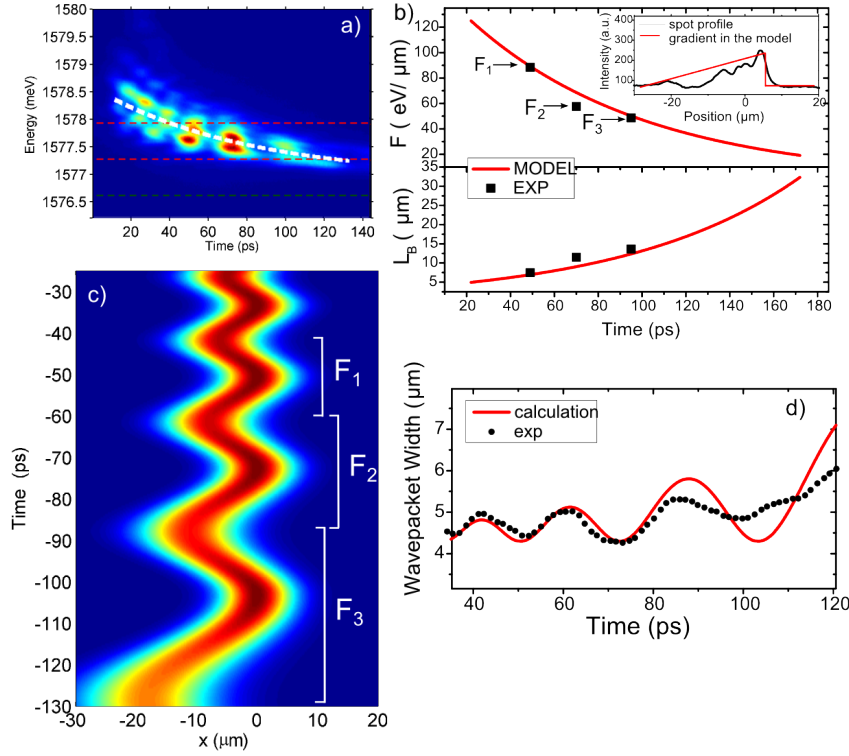


Figure 4.36: a) Energy of the emission at $k = 0$ corresponding to the right panel of figure 4.35. The green and red lines represent the limits of respectively the first miniband and the energy gap corresponding to the wire excited at low excitation power. The decrease in energy is fitted by an exponential of decay constant $\tau = 80ps$, shown with a white dashed line. b) In the upper graph, the black squares are the values of the acceleration deduced using formula 4.21 from the measured time period for the 3 more clear oscillations in figure 4.35 (centered in 50 ,70 and 94 ps). The red line shows the time dependent values of the acceleration used in the model to reproduce the trajectories shown in 4.35. c) Wavepacket evolution in real space calculated applying the semi-classical model of ref.[213]. The gradient $F(t)$ used is a step-like function, with values constant in each oscillation. The values are the ones extracted from the experimental results indicated by the arrows of panel b. d) Black points show the measured width of the wavepacket during the oscillations. The red curves is the calculated one corresponding to panel (c). Parameters of the calculation: $\Delta E = 0.62meV$, $\Delta x_0 = 4.5\mu m$ $\Delta k_0 = 0.15k_B$.

In panel (b) of figure 4.36 we explicit some key parameters of the oscillations. From the temporal period of the 3 oscillations that appear more clearly in the experiment, we deduce the value of acceleration F . The points are reported in the graph, together with the curve representing the values of F used in the calculation. The agreement is very good. In the inset we show the spatial profile of the excitation spot while the red line is the approximation to a linear profile used in the calculation. Additionally, also the values of the spatial amplitude of the oscillations are extracted and compared with the values obtained by the model applying 4.30.

Calculation and experimental results are in good agreement. The model can reproduce

the observed behavior, and this, remarkably, with only a single fitting parameter F_0 , while all the others numerical values put in the models are extracted from independent measurements. The values F_0 , defined as the value of the acceleration at the beginning of the first oscillation ($t \approx 30$ ps), is $F_0 \approx 100 \mu\text{eV}/\mu\text{m}$. Considering the observed spot extension of around $20 \mu\text{m}$, this corresponds to an initial maximum blueshift of around $20 \mu\text{m} \cdot 100 \mu\text{eV}/\mu\text{m} = 2 \text{ meV}$, not far from the blueshift of around 1.5 meV , with respect to the bottom of the band, observed at $t = 30$ ps in panel a of figure 4.36.

Additionally, we also measured and try to reproduce the width of the wavepacket during the oscillations. To do this, we apply the model by Hartmann [213] described in 4.7.1, considering the gradient $F(t)$ as a step-like function, constant for each oscillation period, with values corresponding to the one extracted from the experiment (see panel b of figure 4.36). We will then apply formulas 4.29, with Δ the measured width of the band.

The result in real space is shown in panel c of figure 4.36, in which the oscillations of figure 4.35 are qualitatively reproduced. We analyze the time evolution of the width of the wavepacket, reported in panel d. The oscillations in the width of the wavepacket observed in the experiment (black points) are well reproduced by the calculation taking as parameters $\Delta x_0 = 4.5 \mu\text{m}$ and $\Delta k_0 = 0.15 k_B$, the latter compatible with the width observed in k-space. A discrepancy is observed at the end of the third oscillations since the signal is weak and the estimation of the position and of the width of the wavepacket is imprecise.

Overall, the agreement between observation and numerical simulation provides a clear confirmation that the observed oscillations can be interpreted in terms of Bloch oscillations. They are drive by an energy gradient induced by the reservoir and they are observed at the same time in real and reciprocal space.

The ratio L_B/τ_B

Bloch oscillations have been observed also in wires with different potential period P from the one of fig. 4.35. An example is reported in figure 4.37 for a wire with $P = 2.1 \mu\text{m}$.

In reciprocal space the oscillations are now wider, according with a larger BZ. Also in real space at least two oscillations are visible. The same calculation discussed above has been performed for this wire and the results are shown in blue lines in the figure.

We notice how the ratio between the two parameters that characterize the oscillations, L_B and τ_B , gives:

$$\frac{L_B}{\tau_B} = \frac{1}{2} \frac{\Delta E}{\hbar k_B} \quad (4.34)$$

This quantity, homogeneous to a velocity, depends purely on the wire parameters and is independent from the value of the gradient F , that in our analysis is the only fitting parameter used to describe the trajectories.

In figure 4.38, we show this ratio corresponding to the two considered wires (fig. 4.35 and 4.37), result of the average over the oscillations visible in each wire. We plot it as a function of the ratio $\Delta E/\hbar k_B$ and we observe how they lay on the line of slope 1/2 according with 4.34.

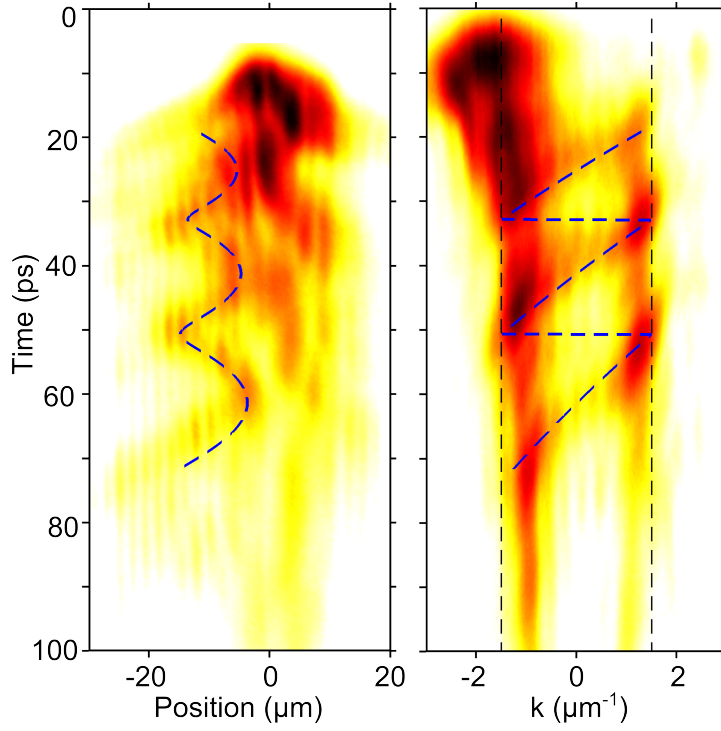


Figure 4.37: Left: Real space emission of wire with $P = 2.1\mu m$, excited with a large non resonant excitation spot. Right: Reciprocal space emission corresponding to the region in real space between $-20\mu m$ and $0\mu m$, the region where oscillation takes place. The dashed blue lines indicates the trajectories obtained by numerical calculation as described in detail in the text relatively to fig. 4.35. Parameters of the wire: $P = 2.1\mu m$, $V_0 = 1.25meV$, $\delta = -4meV$, $\Delta E = 1.04meV$. Parameters of the model: $F_0 = 140\mu eV/\mu m$, $\tau = 85ps$.

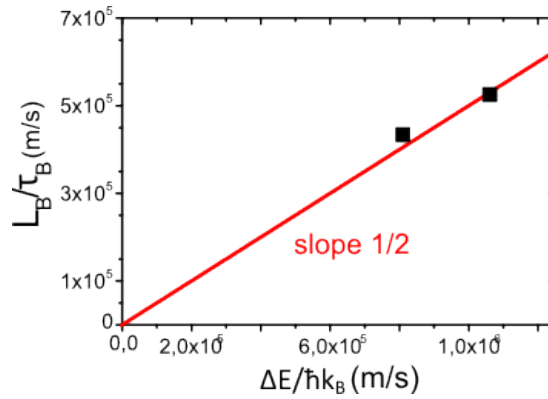


Figure 4.38: Black points represent the ratio L_B/τ_B for two different wire of different period extracted from the observation of BOs in figure 4.35 and 4.37. These values are plotted as a function of the ratio $\Delta E/\hbar k_B$ extracted from the wires' dispersions. The red line is a line of slope 1/2 according with 4.34.

Only two points are present on the graph since oscillations have been observed for wire with $P = 2.7\mu m$ and $P = 2.1\mu m$ but not with the third available period in the sample $P = 1.6\mu m$. As discussed for the effect of localization in the gap, the ratio V_0/E_R plays an important role. Wires with $P = 1.6\mu m$ have a much higher E_R values and so a ratio V_0/E_R is too low: the particles do not undergo Bloch reflection at the BZ but they can more easily jump on the second band via Landau-Zener tunneling.

Observation of Landau-Zener Tunneling

Let's now discuss the signal observed not where oscillations takes place but outside this region, further from the excitation region.

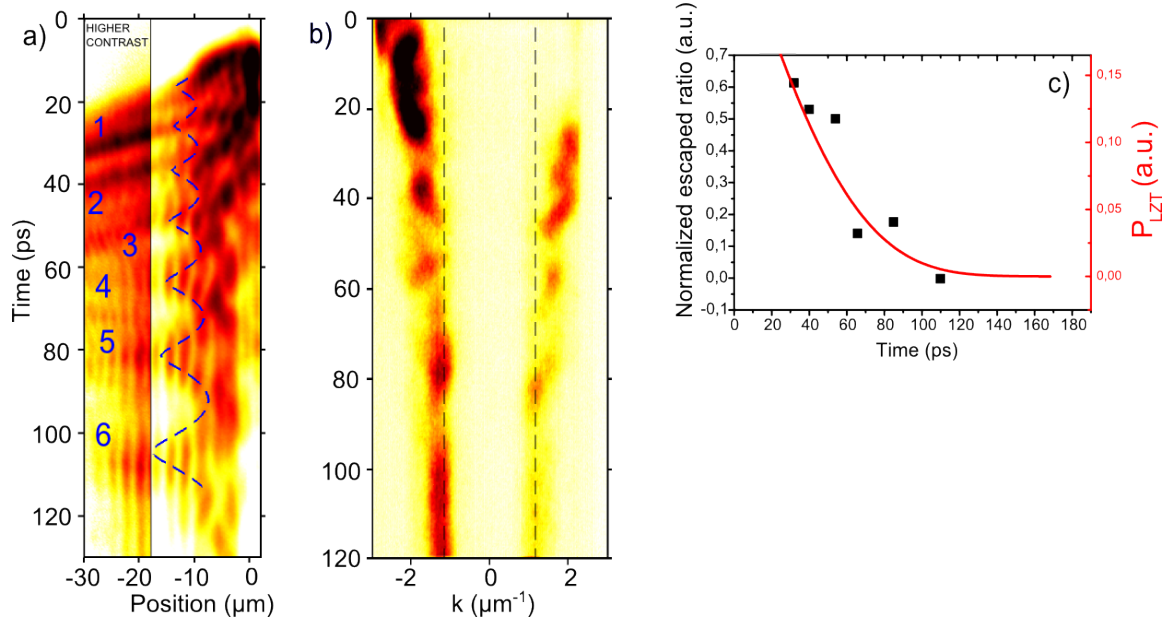


Figure 4.39: Panel a) Real space emission of a modulated wire, with experimental conditions similar to figure 4.35. Bloch oscillations are observed and fitted with the blue dashed line (obtained with the numerical calculation already discussed). The signal outside the oscillation region is enhanced with a better contrast. Several ejected beams can be identified and labelled from 1 to 6. Panel b) Typical emission in k-space coming from a region right outside the oscillation region. For practical reason, this figure doesn't belong exactly to the same set of measurements than the one in panel (a), but it represents qualitatively the same situation. Signal is collected from outside the first BZ, indicated by the black dashed lines. Panels c) Black squares represent the intensity of the ejected beam normalized over the total integrated intensity. They are plotted as a function of the time of their emission. The red curve is proportional to the expected Landau-Zener tunneling probability, obtained applying formula 4.31 and with the gradient F used in the calculation of the oscillations in panel a (exponential decay constant $\tau = 80ps$).

This is done in figure 4.39, where oscillations in real space are observed in a region from

-20 to 0 μm , while the contrast is enhanced outside this region. This allows to observe how at each oscillation, at the time when reflections takes place, a certain amount of particles are not reflected but propagates straight away. This signal can be interpreted in terms of Landau Zener tunneling from the first to the second band. During the time evolution, this effect seems to be weaker, and this is in accordance with formula 4.31, since the acceleration progressively decreases. Additionally, this interpretation can be confirmed from the observation of the reciprocal space emission. In panel b we show a typical emission in k-space coming from a region right outside the one which oscillations take place; unfortunately, for practical reason, this figure doesn't belongs exactly to the same set of measurements than the one in panel (a), but it represents qualitatively the same situation. We can observe how such signal is emitted from outside the first BZ, mainly from negative k values. It is attributed to polaritons that have jumped up to the second band. The weak signal collected at positive k values derives from some backscattering or reflection from the edge of the wire.

From the real space emission, we extracted the intensity of each of this ejected beams (labelled with number from 1 to 6). In panel c of figure 4.39 we plot the obtained values, normalized to the total intensity integrated in the oscillations region. This does not give us the absolute values of the escaping ratio, but allows to get an idea of its evolution in time.

Indeed, this evolution is compared with the one expected for the Landau-Zener tunnelling probability, estimated applying formula 4.31. We apply such formula considering again an exponential decrease of the gradient F , the same that is used to reproduce the trajectories in real space shown in panel (a) with blue dashed line. Although this remains a rough evaluation and just few experimental points are available, this comparison shows how the fast decrease of the trasmitted ratio is compatible with the interpretation in term of Landau-Zener tunneling.

Conclusion of the second part

This section has been be dedicated to the study of polaritons in a lattice accelerated by an energy gradient. We presented two possible experimental implimentations of such configurations.

The first one was based on the etching of wires with a periodic width modulation combined with a progressive variation of the average width. In such a structures, we have shown how minibands and energy gaps are conserved and we observed signature of the Wannier Stark ladder in the photoluminescence spectra.

The second approach was based on the use of simple modulated wire and the gradient was induced by the excitonic reservoir generated by a large non resonant spot. In this configuration we observed the generation of Bloch oscillation both in real and reciprocal space. The interpretation of the results is confirmed by numerical calculations which reproduce the observed trajectories and in which a single fitting parameter is required. All the other are extracted from the experimental measurements.

Finally, we have given signatures of the Landau-Zener tunneling: both in real and reciprocal space we present good indication of polaritons hopping from the first to the second band, when reaching the edge of the first BZ. Additionally, also the decrease in time of the escaping probability is in accordance with the theoretical picture.

4.8 Polaritons in a quasiperiodic potential

We now study polaritons in a quasiperiodic potential by analyzing the photoluminescence from micro cavity wires in which barrier and potential wells are ordered in a way that reproduces the Fibonacci sequence.

4.8.1 Quasicrystals and the Fibonacci structures

In addition to crystalline and amorphous materials, there exist a third intermediate class consisting of deterministic aperiodic structures, known as Quasicrystals.

They were firstly observed by Shechtman and coworkers in 1984 [225] when X-ray diffraction on an $AlMn$ solid alloy evidenced a five fold but also icosahedral symmetry, forbidden by the rules of crystallography. The observation was explained few months later by Levine and Steinhardt [226] by the aperiodic Penrose tiling, that presents locally small areas of five-fold symmetry, opening a complete new area of research rewarded with the Nobel prize in 2011.

The fascinating features of such kind of structure relies on the fact that although aperiodic, thanks to their long range order, they can still exhibit sharp diffraction patterns and other collective properties not shared by their constituent parts. In particular, they are expected to present a highly fragmented energy spectrum displaying self-similar (fractal) character [227, 228].

The Fibonacci's sequence

Quasi-periodic structures have been deeply investigated especially in 1 dimension[229]: the aperiodic sequence is generally generated starting from two building blocks, represented for instance by region of different potential values. These 2 building blocks are spatially ordered following a given deterministic succession. Several sequences have been studied (Thue-Morse, period-doubling, Rudin-Shapiro, Cantor [230, 231]) but the biggest efforts were focused on the Fibonacci's sequence[232, 233, 234, 235], subject of our experimental studies.

One possible approach to generate the Fibonacci's sequence is based on the method named "substitution". It consists in taking two blocks A and B and apply the iterative rules that reads $A \rightarrow B$ and $B \rightarrow BA$. By starting with the first two blocks B and A and applying the substitution rules several times, we obtain for every n-th iteration a Fibonacci's word S_n of increasing length. The results for the first iteration orders are the followings:

$$\begin{aligned} S_0 &= B \\ S_1 &= A \\ S_2 &= BA \\ S_3 &= ABA \\ S_4 &= BAABA \\ S_5 &= ABABAABA \\ &\dots \end{aligned}$$

The procedure is the analogous of the one that generates the well known numerical Fibonacci series $F_n = F_{n-2} + F_{n-1}$ with $F_0 = F_1 = 1$. The length of the obtained words indeed follows

the Fibonacci numbers 1, 1, 2, 3, 5, 8, ..., while the appearance of A's and B's, respectively N_A and N_B , increases and the ratio N_A/N_B tends to the value $\tau = 2\cos\left(\frac{\pi}{10}\right) = \frac{1+\sqrt{5}}{2} \approx 1.618$, the Golden number.

Let's now consider the diffraction properties and the energy spectrum of a 1D potential built of wells and barriers of length respectively L_A and L_B ordered following the Fibonacci sequence.

The Fourier components of such a 1D potential consist in an arrangement of δ -functions which densely fill the real line. In a diffraction experiment of particles experiencing such a potential, these peaks will appear as Bragg peaks; they will form a countably infinite set and their positions, height and phases can be analytically calculated. In the specific case of $L_A/L_B = \tau$, the Golden ratio, the Bragg peaks corresponds to reciprocal vectors given by the expressions [228]:

$$q_{h,h'} = \frac{2\pi\tau^2}{L_B(\tau^2 + 1)}(h + h'/\tau) \quad (4.35)$$

with h, h' integers numbers. We will discuss later the more general case of finite sequence and arbitrary L_A/L_B ratio.

In analogy to what has been discussed in the beginning of this section, these peaks arise from resonant interference effects, related to the structural self-similarity of Fibonacci sequence, in which some patterns are repeated along the lines ⁴. This guarantees the existence of suitable resonance conditions at any scale.

Each Fourier component $q_{h,h'}$ of the Fibonacci potential couples the two degenerate Bloch waves with $k = \pm q_{h,h'}/2$; in a perturbative approach, the coupling is represented by the matrix:

$$W = \begin{pmatrix} E_k & V_{m,n} \\ V_{m,n} & E_k \end{pmatrix} \quad (4.36)$$

where E_k is the energy of the free particle with wavevector k , and $V_{h,h'}$ the Fourier component of the potential corresponding to $q_{h,h'}$. The states split into $E_k \pm V_{h,h'}$ and a pseudo-gap of $2V_{h,h'}$ is open[231].

The resulting energy spectra is the complementary of the pseudo-gaps. In the case of an infinite sequence, the high density of gaps makes the spectrum to be everywhere not dense: it is a Cantor like spectrum with zero Lebesgue measure[237]. The gaps can be labeled with couples of integer numbers, according with a general theorem on aperiodic structures named "Gap labeling Theorem" [237, 238].

The spectrum strongly influences the localization of the wavefunctions. For energies outside the pseudo-gaps, wavefunctions are indeed neither extended (as Bloch modes in the bands), neither localized (as defect states inside the gap, exponentially decaying), but present an intermediate behaviour, presenting a decay in space weaker than exponential, usually a power law: they are defined as "critically localized" [233, 239].

Quasiperiodic systems are particularly interesting for fundamental studies of localization and propagation of light pulses [227, 240] and of the control of spontaneous emission of quantum emitters[241]. They are also attracting for realization of high Q defect-lasers [242]

⁴The existence of repeated pattern is the subject of the Conway's theorem which reads as the following: given an arbitrary sequence of layers, one will always find a replica at a distance smaller than twice its length [236, 227].

and their peculiar spectral structure makes them suitable for the realization of frequency filters[230] , low absorption mirrors[227] and also for enhancing surface luminescence[243] or increasing sensitivity in biosensing platform [244].

Previous experimental observations

The first experimental implementation of the Fibonacci sequence was realized for electron in 1985 [245]. It consisted in a *GaAs* – *AlAs* superlattice with layers of different lengths arranged in a Fibonacci sequence. X-ray diffraction and Raman scattering gave the first evidence of the characteristic multiple diffraction Bragg peaks discussed above. But the clearest results up to now have been obtained in optical systems.

Photonic Quasicrystals have been investigated in several dimensions but for simplicity both in the implementation and in the theoretical interpretation, the most investigated geometry is the 1-dimensional one. The pioneering experiment in 1D optical Fibonacci structures were performed by Gellerman et al. [232] in 1994: the structure consisted in dielectric layers of *SiO₂* and *TiO₂* of different refractive index arranged in a Fibonacci sequence. In figure 4.40 we report the measured optical transmission through these structures: several transmission peaks appear according with eq. 4.35. Furthermore, by increasing the number of layers (and so the order in the Fibonacci serie) up to S_9 , the self similarity of the spectra appears, showing patterns in the transmission spectra that looks the same when undergoing discrete scale transformation.

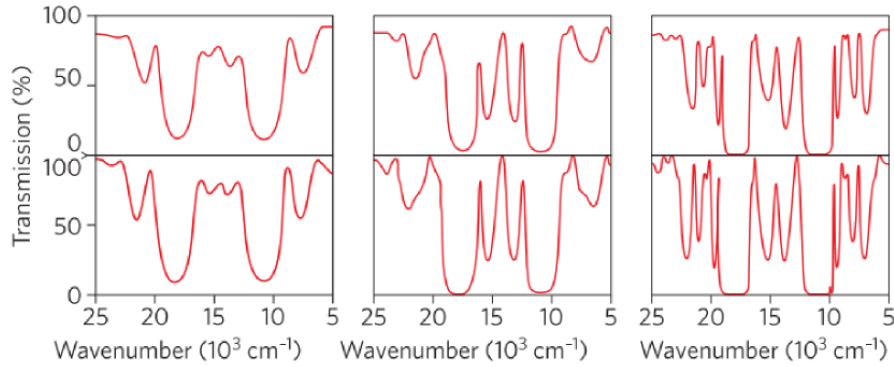


Figure 4.40: Optical transmission spectra (transmission versus wavenumber) for dielectric coating stacks corresponding to the Fibonacci words from S_6 to S_9 (from left to right). The top (bottom) spectra show experimental (calculated) results extracted from [232]. One can observe the appearance of several peaks and increasing the number of layers a triple peaks shape appears repeated at two different energy scale, evidencing the self similarity of the spectra.

This works has been followed by several others, based on different layers compositions, higher order words [246, 235, 247] and even with phononic[230] and plasmonic [248] systems. Nevertheless, the experimental approach remains basically the same, presenting few limitations: the transmission spectra gives a quite indirect informations on the eigenstates of the system and their spatial distribution can only be simulated but it is hardly accessible

experimentally.

In the following pages we will present first results on polaritons in a Fibonacci potential. In a photoluminescence measurement under non resonant excitation, the eigenstates of the system can be directly observed and all the information concerning real and k-space distribution and phase can be accessed. Furthermore, although not studied here, the effects of interactions on the critical localization expected inside the pseudo bands represent an interesting field of investigation.

4.8.2 Fibonacci wire

The shaping of the Fibonacci potential sequence was obtained by properly adjusting the lateral width of the etched microcavity wires, that we will name Fibonacci wire. The height of the potential step can be controlled as well as the size of the A's and B's building blocks of the sequence, and also the length of the words can be, in principle, arbitrary long.

Several Fibonacci wires have been realized and in figure 4.41 we show a SEM image of few of them, together with a scheme of the resulting potential profile.

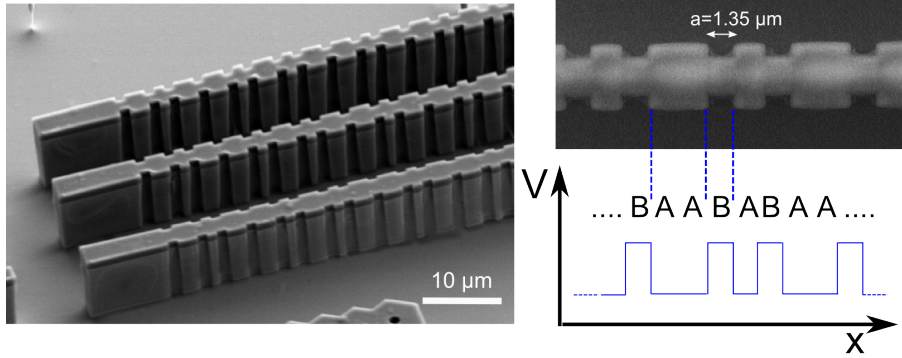


Figure 4.41: SEM image of 3 Fibonacci's wires etched on the sample. The one in the middle will be the one investigated and from which the results presented have been collected. A zoom of the top view of such wire is reported on the upper right panels. On the lower right panels, a scheme of the resulting potential is reported.

The letters A and B correspond to two different values of the potential felt by polaritons, V_A and V_B . The length of all the letters was the same, that means $L_A = L_B = a$. We realized wires of different spatial constant a and potential steps V_0 . More precisely, for every values of V_0 we realized two different families of wires, corresponding to the two possibilities that reads $V_A - V_B = \pm|V_0|$, in which the letter A represents a barrier and B a well or viceversa. The order of the Fibonacci's words sculpted on the structure goes up to S_{12} , that means 233 letters. This corresponds to a sequence of around $200\mu m$ of length.

In analogy to what has been discussed for periodically modulated wires, we can define a recoil energy given by $E_R = \frac{\hbar^2 \pi^2}{2m_p(2a)^2}$. The ratio V_0/E_R will play a role also here : a value of around unity or higher is required to better observe the opening of the pseudogaps and for investigate localization effects.

The results presented in the following pages were obtained on a wire of modulation strength $V_0 = 1.1\text{meV}$ and recoil energy $E_R = 1.15\text{meV}$ with $V_A < V_B$, and a potential pattern corresponding to the Fibonacci word S_{11} .

4.8.3 Dispersion, eigenstates and energy spectrum in a Fibonacci wire

The study of the eigenstates of the wires has been performed by non resonantly exciting them with a *cw* excitation at a power well below condensation threshold. Such excitation condition populates the available states in the system and, as in section 4.4.2, the resulting photoluminescence intensity gives access to the density of states.

Additionally, in this case we excite the wire with a spatially extended spot (with FWHM of $\approx 50\mu\text{m}$) in order to excite a large number of sites and to minimize the effect of the local energy blueshift induced by the reservoir.

The resulting photoluminescence emission, energy and spatially resolved, is reported in figure 4.42.

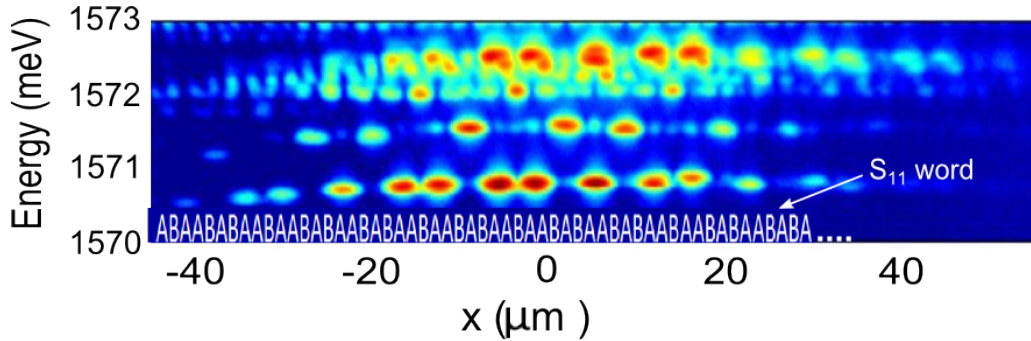


Figure 4.42: Emission from a Fibonacci wire excited at low power with a large non-resonant spot (FWHM of $\approx 50\mu\text{m}$). The low energy part of the emission is reported (corresponding to the bottom of the polariton band). Several localized states appear and in the observed pattern one can identify the final letters of the S_{11} Fibonacci word shaped on the potential, reported in the figure.

The difference with the case of periodically modulated wire is evident: the continuous bands are replaced by a series of discrete localized states, appearing at several energies. The potential is indeed a sequence of wells and barrier and by observing the emission especially at lower energy, one can identify some patterns and directly recognize the corresponding letters of the S_{11} Fibonacci's word expected. A direct visualization of the wave functions is thus possible.

In figure 4.43 the corresponding emission in reciprocal space is reported. Here we notice how the polariton dispersion is modulated and fragmented in a high number of pseudobands divided by pseudogaps. The high number of gaps corresponds indeed to the numerous Bragg peaks discussed in the introduction paragraph.

A theoretical analysis of the eigenstates of the systems was performed in the group of Eric Akkerman in the Tehnion Institute in Haifa. By taking into account the finite size of our system formula 4.35 can be rewritten and the positions of the Bragg peaks is given by:

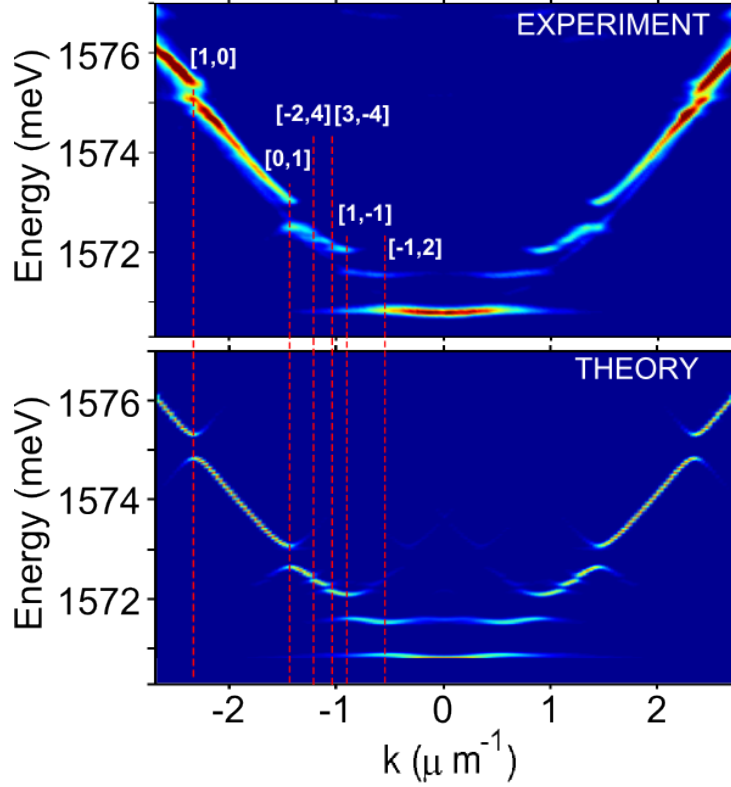


Figure 4.43: On top we report the reciprocal space emission from the Fibonacci wire corresponding to the previous figure 4.42. Several pseudogap and pseudobands appear. We report also the indexing of each pseudo-gap with the couple of integers $[h, h']$, according with eq. 4.37. Below we report the result of the simulated polariton dispersion numerically calculated starting from the parameters used in the experiments.

$$q_{h,h'} = \frac{2\pi}{aF_{j+1}}(F_{j+1}h + F_j h') \quad (4.37)$$

with F_j the j -th Fibonacci number and j the order of the considered sequence.

Additionally, starting from the parameters used in the experiments (including finite length of the microwire and its lateral shape), the polaritons states have been numerically calculated and the polariton dispersion of fig. 4.43 has been exactly reproduced (as shown in fig.4.43).

Thanks to this analysis, we succeed in indexing the different gaps observed in the experimental band structure with the index $[h, h']$, as shown in fig. 4.43, proving the applicability of the "Gap labeling theorem".

Integrated Density Of States

The peculiar structure of the emission spectrum appears more clearly by observing the integrated intensity and the integrated density of states derived from it. This is what we report in figure 4.44 for the low energy part of the spectrum. We observe the appearance of peaks,

corresponding to band edges and deeps corresponding to pseudo gap.

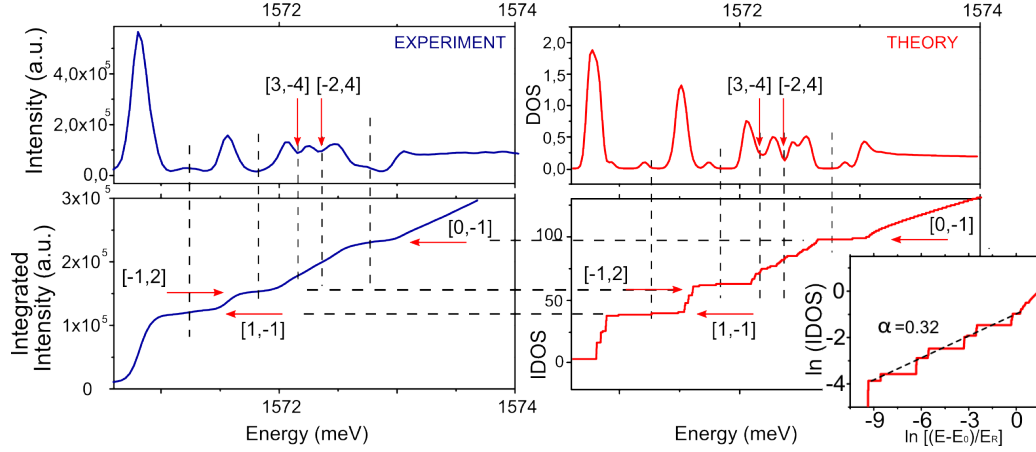


Figure 4.44: On top left we report the integrated intensity spectrum corresponding to the reciprocal space emission of figure 4.43. Below, we report the intensity of the upper curve integrated on the energy axis. Such curve is expected to give an indication of the behavior of the IDOS function. The pseudogaps correspond to flat region of the energy integrated intensity. We identify the main gap observed on the dispersions, identified by red flashes. The small gaps at ≈ 1572.3 meV also appear in the spectrum. All these features are reproduced in the theoretical calculations performed by Akkerman and coworkers, reported on the right column and corresponding the theoretical dispersion shown in fig. 4.43. In the inset on the bottom right, the calculated IDOS in the low energy region is reported in a double-log scale, as a function of $E - E_0/E_R$ (with $E_0 \approx 1570.8$ meV and $E_R = 1.2$ meV). Log-periodic oscillations are visible, modulated by an increasing by a power law with $\alpha = 0.32$ (see formula 4.38).

Additionally, by assuming that this signal is proportional to the density of state, the integration of the curve along the energy scale from the lowest energy up to E' gives integrated density of states: $IDOS(E') = \int_{E_{min}}^{E'} I(E) dE$. The result of this integration is also reported in fig.4.44. We can observe how the pseudogaps correspond to a flattening of the IDOS curve and this flat region corresponds to the energy of a polariton given, in the parabolic approximation, by $\frac{\hbar^2 q_{h,h'}^2}{2m_p}$.

The IDOS is a quantity particularly interesting since it is always well defined and can be convenient to describe different types of spectral singularities [231]. In previous works, the group of E. Akkerman [249] has shown how quantities such as the integrated density of states in a fractal system⁵ present general behavior and can be described by the product of a power function modulated by a log periodic function. This reads:

$$IDOS(E') = |E - E_0|^\alpha F\left(\frac{\ln|E - E_0|}{\ln b}\right) \quad (4.38)$$

where F is a periodic function of unit period, b a scaling parameter and the energy of the lower energy state.

⁵The Fibonacci sequence is more exactly defined as a multifractal, with multiple scaling rules [231]

In the right column of figure 4.44, we report the calculated DOS and IDOS curves. We observe an excellent qualitative agreement with the experimental curves. Also quantitatively the agreement is satisfying, confirming how emission intensity allows to directly access the density of states in the system. Additionally, the high resolution available in the calculation allows to look in detail into the behaviour of the IDOS. In the inset in the bottom of fig. 4.44, we plot in a log-log scale the IDOS as a function of $(E - E_0)/E_R$ (with E_0 the bottom of the band). We observe a log periodicity of the curve modulated by an overall increasing fitted by a power law with exponent $\alpha = 0.32$. The energetic resolution of the experimental spectrum doesn't allow to recognize this pattern in the present structure. Nevertheless, the results obtained in the simulation show a direct indication of the fractal character of the polariton spectrum, besides the finite size of the structure. An optimization of the microcavity structure, thanks to a smaller step size a and a higher potential steps V_0 could allow to resolve also experimentally at least one periodic oscillation in the IDOS.

Conclusion of the third part

In this section we have discussed polariton in potential profile that follows the quasi periodic sequence of Fibonacci. We presented at first few characteristic theoretical features expected for such aperiodic potential profile and we described the microcavity structure used to implement such potential for polaritonic particles. A direct visualization of the eigenstates has been proofed. In real space, a set of confined states has been observed, with an intensity spatial pattern that directly corresponds to the shape of the aperiodic potential. In reciprocal space pseudo bands and pseudogaps can be identified and signature of a Cantor-like spectrum appears. Additionally the position of the pseudo gaps and their labeling by couples of integers nicely follows the theoretical prediction for a quasi periodic crystal and are confirmed by numerical calculation. This work represents a first characterization of these structures that appear as a promising framework for future investigation. A possible direction of investigation consists in the study of polariton localization in such a structure, especially in the non linear regime, where interactions are expected to drive the system into the equivalent of a metal-insulator transition [250, 251, 252].

Chapter 5

A polariton interferometer

5.1 Introduction

In the previous chapter we have shown few examples of how interaction properties of polaritons can be exploited for manipulating the polaritons flow. Especially the exciton-polariton interaction has been demonstrated to provide an efficient all optical way to reshape the polariton potential, to accelerate them, to block and reflect them, and superposed to a periodic potential, to localize them in gap states or drive them to perform Bloch oscillations.

In this chapter we will demonstrate how interactions give a way to control and manipulate the phase of the polariton flow in an all optical way.

To put in evidence this effect we etched polariton interferometers. The proof of the principle will be obtained thanks to a coherent propagation polaritons flow inside a Sagnac interferometer and the effect will be exploited in order to modulate the transmission of a Mach Zehnder interferometer.

We discuss the propagation and precession of polariton pseudospin in both 2D and 1D geometry, and then the behavior of such spin degree of freedom will be analyzed inside the Mach Zehnder interferometer. It is shown how we can also obtain a control of the degree of linear polarization of the outcoming signal.

We conclude discussing the potentiality of this structure as a tool to detect a polariton Berry phase.

5.2 Measuring and controlling the phase

Interferometry is a field that have accompanied most of the major discoveries in the physics of 20th century. Several examples can be presented: Michelson and his interferometer provided a key experiment in the debate of the light propagation in different reference systems[253], Young's experiment still represents one the clearest proof of the wave nature of photons [254] , while Fabry and Perot completely revolutionized the spectroscopic measurements[255].

The advent of quantum mechanics further increased the potentiality of these techniques. The wave nature of every particle predicted by De Broglie has first become visible in interference experiments: fringes formed by electrons scattered by a thin metal film where observed by G.P.

Thomson [256], helium atoms were seen to form density fringes when reflected on a crystal [?] and nowadays the equivalent of the two slit experiment with single electrons or atoms is still one of the most astonishing and appealing proof of quantum mechanics.

Since then, interferometry strongly developed in different directions [257, 258, 259].

Optical interferometers represent not only tools for highly precision measurements [260, 261, 262, 263] but they are also an essential ingredient to investigate fundamental properties of light sources such as spatial and temporal coherence, or to investigate the more subtle behaviours of single photons sources [4], indistinguishable photons [264], entangled states [265].

Additionally, development of photonic materials, waveguides and photonic crystals, allowed the realization of light confinement and guiding at the wavelength scale and below [153, 266, 162]. Interferometers in solid state structure in several geometries became the basis of various integrated optoelectronic devices [267, 268, 269, 270, 271, 152, 272].

Parallely, matter wave interferometer have been realized, thanks to the development of atom optics, based on exotic structures such as mechanical and laser gratings, able to reproduce the equivalent of mirrors and beam-splitters for De Broglie wavelength of typically fractions of Angstrom [257, 258]. Initially conceived as elements of basic research, nowadays atom-interferometers are building blocks for high precision measuring devices, such as atomic clocks or gravimeters.

Interference effects have been also detected in electronic circuits: thanks to high quality quantum conductors and sub-Kelvin temperature operation, interference between a single pair of electrons has been detected [273].

It's also worth to mention the case of cold atom gases: as introduced in the first chapter, the phase transition towards a Bose Einstein condensation manifests itself with the appearance of spatial coherence [92] detectable measuring the spatial correlation function via interferometric measurements. For atomic condensates this property has been proved by splitting a condensate in two trapped ones and letting them expand and interfere with each other [274], or by realizing the equivalent of a two slits experiments [275], and nowadays also on-chip BEC interferometers have been implemented [276, 277].

In the polariton field, optical interferometric techniques has also played a major role, since the phase information of the emitted photons gives a further insight into the polariton states. A good example comes from the measurements of spatial coherence: with respect to atomic condensate, this measurements can be done more easily thanks to optical interferometry on the photons emitted and collected out of the sample. Such measurements represented one of the indication for polariton quasi-condensation in CdTe cavity [?], and later in GaAs [13], and GaN [16] based cavity.

Furthermore, spatial mapping of the phase of the excited polaritons states allowed the identification of topological defects, characterised by phase discontinuities such as vortices [24], half vortices [23], as well as solitons and half solitons [20] and still inspires much other theoretical propositions [278].

In these pages we will show how interference effects in a polariton flow will be visualized directly inside the sample without indirect interferometric measurements of the emitted light and they will be exploited to drive and control the flow by optically modulating the phase itself.

5.2.1 Phase modulation

A two-beam interference pattern shifts according with the path difference between the beams. This can modulate the output intensity of an interferometer that can become a sensible devices for measuring distances, time delay, temperature, acceleration, gravity, magnetic field and many other quantities [279, 280, 260, 263].

But the deterministic control of the accumulated phase in one of the arms opened the way to use them as integrated solid state devices acting as modulator of the signal transmitted trough them (see section 5.5.3). Furthermore, such control can also allow to accurately manipulate quantum states [281, 282, 267] and to generate, ideally, any discrete quantum operator [283].

Concerning optical devices, the optical path $k \cdot x$ is modified generally acting on the wave-vector k via a local variation on the refractive index. Several mechanisms have been investigated in order to modulate the refractive index of a waveguide material. It can be done thermo-optically, based on temperature dependent refractive index material[271], electro-optically, using index change with electrically injected carriers [284], or based on optomechanical induced index changes [285], while we talk about all-optical systems when such variation is driven by a control optical beam.

In most of these cases, the optimization and enhancement of the induced phaseshift is based on two main ingredients.

On the one hand, one needs to use a medium with a refractive index that strongly depends on the control parameters, such that a small variation of the control, highly influence the value of n and so of k . In the case of optical control, this has been obtained by using strongly non linear medium [286], or mainly by adding in the active region carrier confinement, thanks to QWs and especially QDs, to enlarge non linear optical response[287, 269, 270] .

On the other hand, one can engineer its optical mode in order to traduce even a small variation on n , in a big variation in k or of the propagating velocity. Indeed in a dispersive material, in the vicinity of a resonance, light can be strongly slow down and so, going slowly trough this region, can accumulate a large phase shift. This is the essential principle of the structures based on electromagnetic induced transparency [285] , ring resonator [288] and, the most diffused, photonic crystals[153, 266] (see section 5.5.2).

5.2.2 Interaction induced phase shift for polaritons

Now we introduce a different approach for inducing a phaseshift in a polariton flow by optical control but still based on these two principles just mentioned: the mixed light-particle nature of polaritons will provide strong non linearities typical of electronic systems combined with the highly dispersed mode of a photons confined in a micro-cavity.

Let's consider a monochromatic polariton flow propagating along a microwire, with a well defined kinetic energy E_k . In the effective mass approximation, or , in other words, considering a parabolic band, its corresponding wave-vector is given by $k_1 = \frac{\sqrt{2m_p E_k}}{\hbar}$.

We place a non resonant control spot shining on a certain region of the wire. Its intensity

will be kept below condensation threshold so that its main effects will be the local injection of excitons in the reservoir. As mentioned in the previous chapters, the repulsive interaction between polaritons and excitons results in a local shift of the polaritonic resonances of a quantity V , as depicted in figure 5.1. We have already discussed how such a barrier induced by excitonic reservoir could be used to accelerate and decelerate polaritons, and, if the barrier is sufficiently high, to stop and reflect them. In this case we consider a barrier lower than the kinetic energy such that polaritons will cross the region of the non resonant control beam. However, in this region their kinetic energy will locally decrease, $E'_{kin} = E_{kin} - V$, and consequently their wave-vector will decrease to a value $k_2 = \frac{\sqrt{2m_p(E'_k - V)}}{\hbar}$.

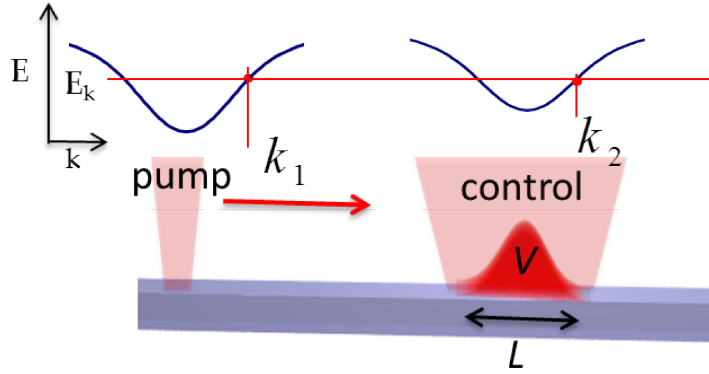


Figure 5.1: Schematic representation of the experimental configuration for inducing a phase shift to a polariton flow by a non-resonant control laser beam. The blue curves schematically represent the polariton dispersion in two different region of the wire: on the region of the control beam the dispersion is locally blue-shifted of a quantity V .

Considering L the diameter of the control spot, the flow acquires a phase-shift with respect to the case of unperturbed propagation equal to:

$$\Delta\phi = L \cdot \Delta k = L \frac{\sqrt{2m_p}}{\hbar} \left(\sqrt{E_k - V} - \sqrt{E_k} \right) \quad (5.1)$$

Since the value of the height of the potential can be controlled by the power density of the control beam P_c , this will provide us an external all optical control of the phase of the polariton flow.

5.3 The interferometer structures

In this section we present polariton interferometers controlled by the described method.

Splitting a condensate into two

The starting point in the realization of almost every kind of interferometer configuration is the realization of a beam splitter to divide in two the incoming signal and then guide each part and recombine them in the output arm, always in a phase-preserving way. This has been realized in several systems and in many different ways. Thanks to quantum point contact for electrons interferometry in circuits or via a double well potential for propagating BECs, while in optics several approaches have been used. In photonic crystals, 0D or 1D confining potential can be created for photons that are guided in the desired direction [162]. Then, strong or weak abrupt variations of the effective optical index provides the possibility of realizing the equivalent of a mirror or of beamsplitter [152]. Alternatively, optical waveguides have been used, when light is strongly confined due to index difference between the guide material and the one in which is embedded or the air and a large variety of optical paths can be realized [289].

Our approach is based on the etching of a 1D microcavity structure consisting in wire split via a y-shaped bifurcation, depicted schematically in fig. 5.2.

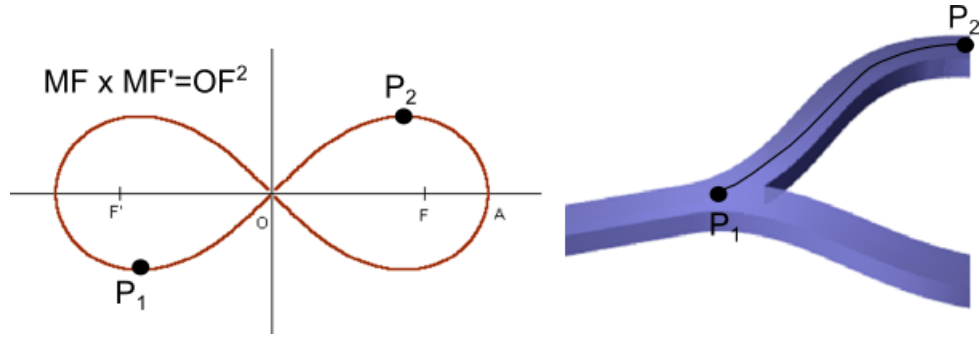


Figure 5.2: Scheme of the bifurcation of the microcavity structure.

The shape of the bifurcation, as well the path of the arms, are designed to present smooth curvatures in order to decrease the probability of backreflections of polaritons at the junctions¹. The efficiency of the injection of the structures will be discussed in details in the following paragraphs, when the coherent propagation inside this structure is studied.

5.3.1 The 2 interferometers

Two different kinds of interferometers have been realized.

The first one (on the top of figure 5.3) is a Sagnac interferometer (that we friendly named “tennis racket”). A simplified scheme of the original Sagnac interferometer [290] is reported on

¹The curvature of the wire follows the shape of a Lemniscate of Bernoulli, described by the equation $(x^2 + y^2)^2 = 2a^2(x^2 - y^2)$

the upper left of the figure: the incoming beam is split into two contra-propagating beams that circulate in the interferometer, superposing their paths. The beams come back to the initial beam splitter and couple out towards a detector.

Our structure is analogous, with the slight difference that our beam splitter redirects the two signal in a single output path.

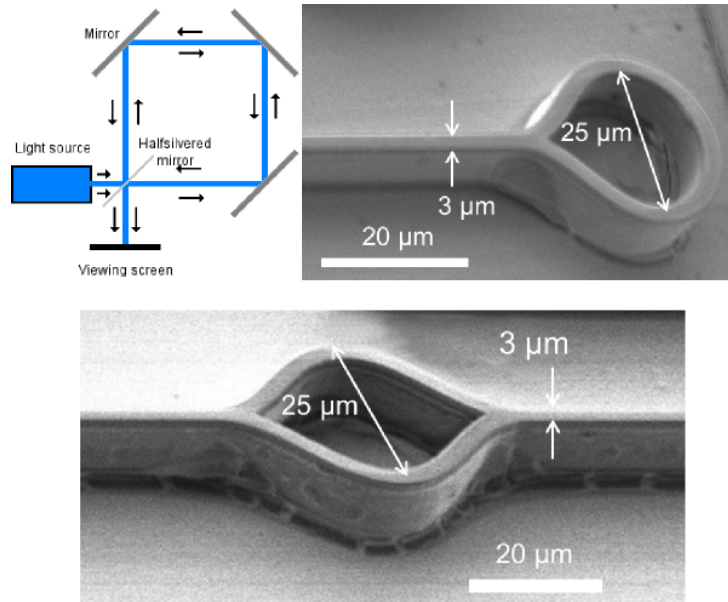


Figure 5.3: Left top: Scheme of the standard configuration for a Sagnac interferometer. Right top: SEM image of our structure, analogous to a Sagnac interferometer. Bottom: The Mach-Zehnder interferometer. Essential parameters are reported in the pictures.

The second one is the well known Mach Zehnder interferometer.

To obtain it, we need the equivalent of two beamsplitters, so in our case two y-shaped coupler. The two beams undergo well separated paths inside the two arms of the interferometer and then recombine at the output.

We realized these two structures in different sizes, varying the arm to arm distance and the width of the wires. In the following pages we will present measurements realized on structures with 25 μm distance between the arms (see figure 5.3) and a 3 μm wire width.

5.4 Optical control of the polariton phase

Let's now investigate the propagation of polaritons inside the Sagnac interferometer, that will be an ideal structure for proving the effect of the phase shift induced by the interaction of flowing polaritons with the reservoir and to directly measure and quantify such an optically induced phase shift.

5.4.1 Interference patterns in the Sagnac interferometer

The experimental configuration is represented on top of figure 5.4.

The structure is excited along the injection arm to create a polariton flow that will propagate inside the structure. In this section we excite the system with a non resonant excitation. The resulting emission from the Sagnac interferometer are reported in figure 5.4 for several power of the non resonant pumping beam.

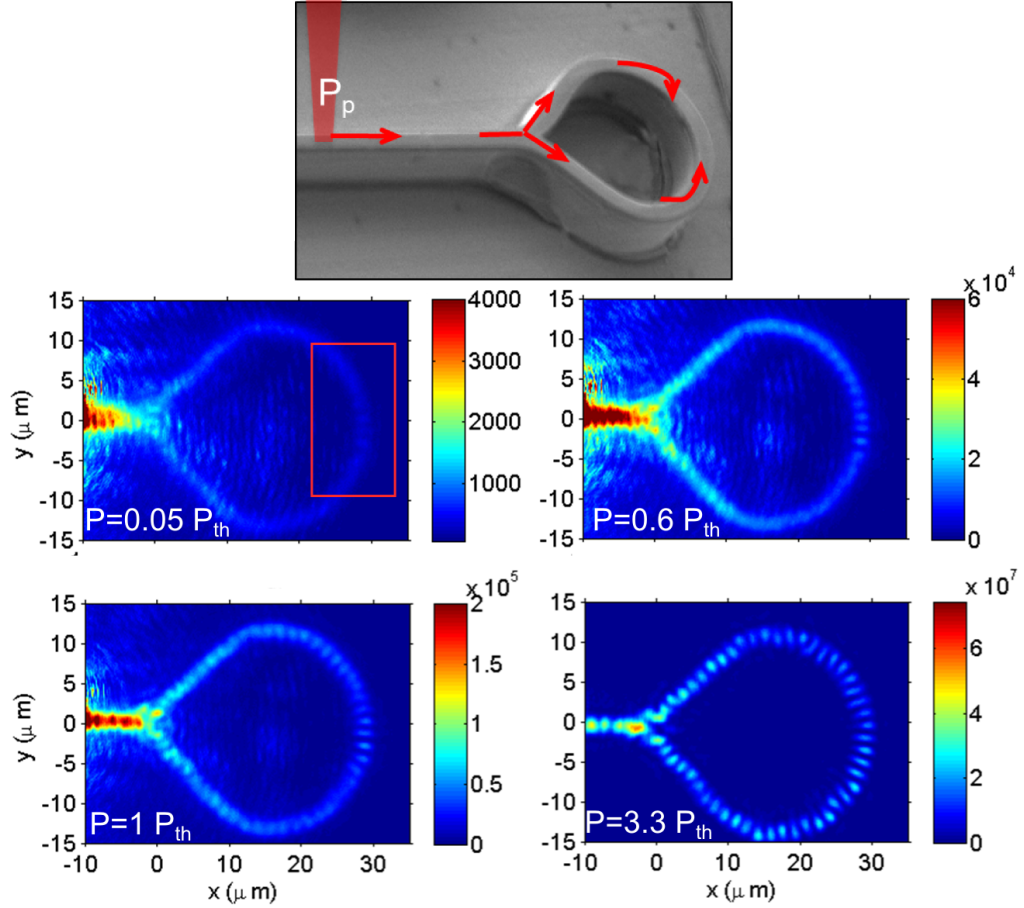


Figure 5.4: Top: Scheme of the experimental configuration. The pump laser P_p is non resonant. Bottom: Real space emission collected from the racket for different excitation power. The red rectangle in the first panel indicates the region from which profile reported in fig. 5.5 are extracted.

Below threshold an incoherent population of polaritons is injected, wide in energy and k space. But we know that, above threshold, we should expect the generation of a monochromatic beam and the build up of a coherent propagation of a monochromatic beam.

What is remarkable is that here in order to detect this transition, we won't need neither an output of the interferometer (as it is normally required) nor a movable arm to control the relative beam path but since all the interference effects are taking place inside the sample, we will simply collect the light escaping from the structure to directly access the polariton

wavefunction and so visualize and quantify the onset of coherence.

Two wave interference

Let's consider a incident signal in the injection arm and that will be splitted. We will have so two signal propagating in the two arm, labelled 1 and 2 . We treat the problem in one dimension, the position along the waveguide, and we consider the two monochromatic wave contrapropagating with opposite wave vector. So we write:

$$\Psi_1 = \sqrt{I_1} \exp^{i(kx - \omega t + \theta_1)} \quad \Psi_2 = \sqrt{I_2} \exp^{i(-kx - \omega t + \theta_2)} \quad (5.2)$$

and the results interference pattern is:

$$I = |\Psi|^2 = I_1 + I_2 + 2g\sqrt{I_1 I_2} \cos(2kx + \theta_1 - \theta_2) \quad (5.3)$$

where we introduced a factor $0 \leq g \leq 1$ to take into account non perfect monochromaticity or a finite coherence between the two beams.

The sum of the first two terms can be seen as a uniform background while the last term is an oscillating terms representing the interference effect: $g = 1$ represents completely coherent waves and $g = 0$ complete incoherent ones. According to the argument of the cosine, intensity will oscillates between a minimum and a maximum of intensities, generating an interference pattern of period π/k , with fringes visibility defined as $\frac{I_{max} - I_{min}}{I_{max} + I_{min}}$. In the case of $I_1 = I_2$, the parameter g corresponds exactly to the fringes visibility.

In formula 5.3 and in the fits that will follow, we are neglecting the spatial decrease of intensity due to finite polariton lifetime along propagation; we can state that, by looking to the interference pattern only in a region of few microns at the top of the interferometer (see red rectangle in fig. 5.4), this spatial decrease can be neglected. Later, in the next sections, we will take it into account.

Expression 5.3 will be used to fit the observed spatial emission profile in the power series corresponding to figure 5.4, where adjusting the parameter g we take into account the transition from an incoherent polariton population below threshold, wide in energy and k , towards monochromatic coherent wave above threshold.

5.4.2 The spontaneous build up of coherence

We plot the spatial profiles of the emission from the Sagnac interferometer for the series of measurements corresponding to figure 5.4. The profiles are extracted from the region indicated by the red rectangle in the figure and are plotted on the left panel of fig. 5.5 for several values of excitation power. Using the formula 5.3 we fit such extracted curves, considering $I_1 = I_2$ and where the adjustable parameters are the coefficient g and the k vector that increases with power.

We observe that, as expected from an energetically broad signal distribution corresponding to below threshold excitation, a quite uniform intensity profile is observed along the device and almost no interference pattern is detectable, corresponding to low value of visibility g . Then the

increase of the visibility and so the onset of the coherence takes place at an excitation power corresponding to a non linear increase of the local polariton density, as reported on the right of fig. 5.5.

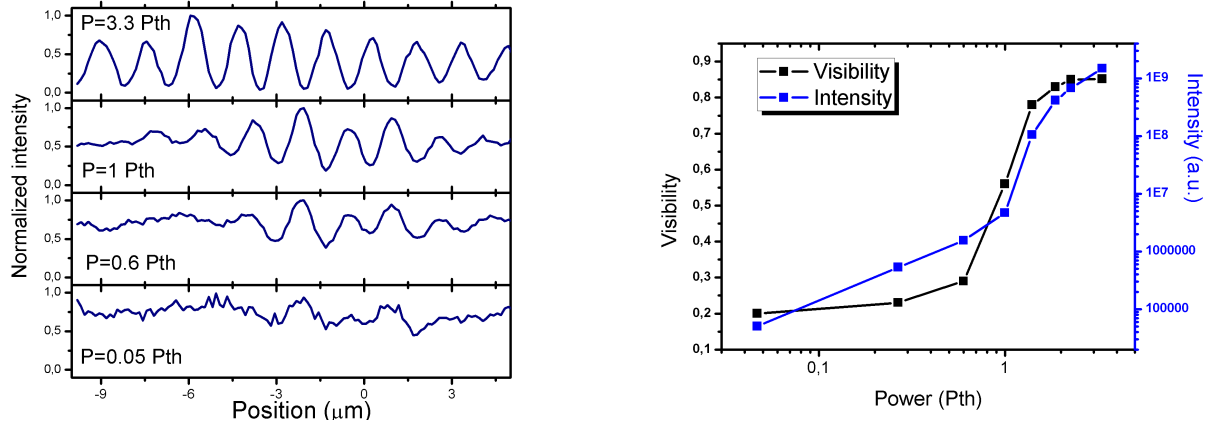


Figure 5.5: Left: Normalized intensity profile extracted from the head of the interferometer corresponding to the panels of fig. 5.4. Right: Visibility of fringes as a function of power (black) and integrated signal intensity at the head of the interferometer as a function of power (blue).

One can interpret these measurements as the equivalent of the ones by E. Wertz, reported in fig. 3.5, where the first order correlation function $g^{(1)}$ was measured by evaluating the visibility of the interference fringes from two points at a distance a along the wire (see figure 3.5).

In the present experiment the point a is the total length of the interferometer, $80\mu\text{m}$. A visibility of 0.85 shown here, was detected only for a distance a of few μm in the Wertz experiment. Although we didn't perform a detail study of the decrease of the fringes visibility with the propagation distance in this sample, we can nevertheless conclude that the present coherent propagation length is longer than the previous investigated sample, in accord with its higher quality factor.

Additionally, one could also argue and demonstrate that the measured values of the visibility are actually a lower limit, since the visibility of the fringes can be lowered by the effect of multiple reflection of the signals inside the interferometer taking place at the beam-splitter and by a not perfectly equal intensity injected in the two arms.

In conclusion, we have shown how such interferometer structure can provide a way to directly visualize and quantitatively analyze the effect of spontaneous build up of coherence under non resonant excitation, giving a more direct confirmation of the previous results obtained on straight wires[38].

5.4.3 The optical-induced phase-shift

After the discussion on the interference pattern appearing inside the ring, let's take advantage of this as a tool for measuring the optically controlled phase shift proposed in the beginning of the chapter.

Let's fix the intensity of the pump beam to $3P_{th}$ placed on the injection arm of the Sagnac interferometer: this corresponds to the injection of a monochromatic polariton flow with a

kinetic energy of 3.1meV . The corresponding k vector, obtained from the far field emission, is $k = 2\mu\text{m}^{-1}$, giving rise to a fringe space of $1.6\mu\text{m}$, in agreement with the fringe spacing of figure 5.6. Now on one arm of the interferometer we place a second non resonant control beam. A beam collimator is placed on the path of this second control beam in order to enlarge its spot size to a higher values with respect to the almost diffraction limited size of the $2\mu\text{m}$ pump beam. In all the reported results of the chapter, the size of the control spot is characterized by a FWHM between 5 and $9\mu\text{m}$. As explained before, this spot will create locally an excitonic reservoir and so a blueshift of the polariton bands. The height of this potential is controlled by the power of the control beam.

In figure 5.6 we report the emission from the interferometer for different control powers. It appears clearly that all the interference patterns shifts progressively with increasing the power of control beam.

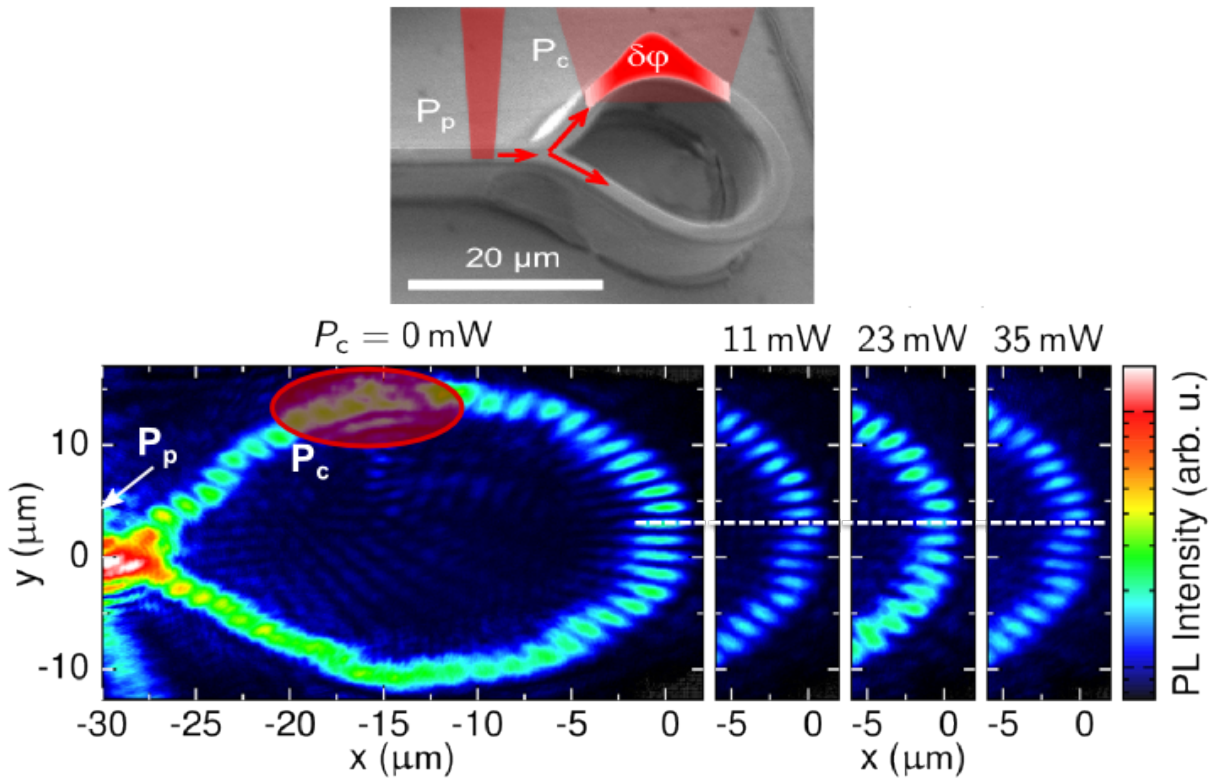


Figure 5.6: Top: Scheme of the experimental configuration: a control non resonant beam is placed on one of the arms. The non resonant pump beam is also indicated and is placed on the injection arm right outside the window. Bottom: Real space emission of the interferometer measured for different values of control beam power P_c , placed on the region indicated with the red circle on the upper arm. A dashed white lines is a guide to the eye to evidence the shift of the interference pattern between the panels.

In figure 5.7 we reported few intensity profiles corresponding to series of measurements of figure 5.6, extracted at the head of the ring. By fitting the curves with the formula 5.3, one can

directly derive the phase shift corresponding to the observed fringe displacements and plot it as a function of the control power: the obtained shift increases almost linearly with the control power to a value higher than 3π (see figure 5.7).

In order to understand and reproduce such a behaviour, also the blueshift induced by the second spot has been measured: the pump beam has been blocked and the emission from the control spot region has been collected energetically resolved. The results, in the inset of the graph of fig. 5.7, presents a linear increase with power.

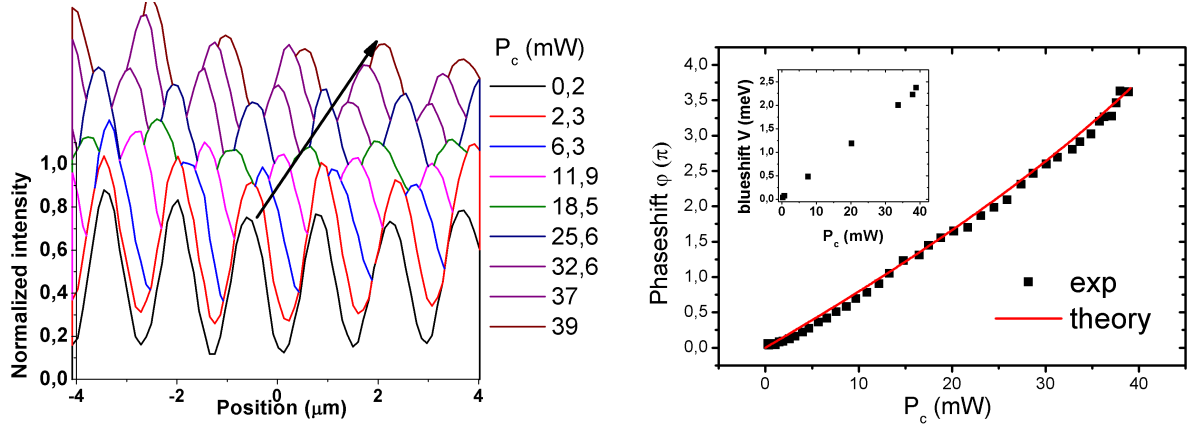


Figure 5.7: Left: Normalized intensity profile extracted from the circular part of the interferometer corresponding to the same series of measurements of fig. 5.6. The arrow indicates the overall shift of the fringes. Right: Phaseshift as a function of the control power extracted by fitting the experimental profiles on the left (black squares). In the inset the measured blueshift induced by the control beam as a function of power. The red curve represents the calculated phaseshift obtained by applying formula 5.1 in a presence of a gaussian shaped potential barrier of size σ and of height given by the experimental values of the blueshift (Parameters: $E_{kin} = 3.1 \text{ meV}$, $\sigma = 4.3 \mu\text{m}$, $m_p = 6 \cdot 10^{-5} m_0$).

To reproduce the measured phaseshift, we apply formula 5.1, in which we consider a gaussian potential barrier of $\sigma = 4.3 \mu\text{m}$ with a height varying with the control power and corresponding to the measured blue-shift reported in the inset of figure 5.7. The red line shows the obtained fit which nicely reproduces the measurements in the whole power range. The dependence observed between phaseshift ϕ and blueshift V appears linear, although we expect a square root dependence $\phi \propto \sqrt{E_{kin} - V}$. This is due to the fact that the kinetic energy is always much higher than the induced blueshift, and so polaritons don't approach the bottom of the band and the effect of the parabolicity of the dispersion is reduced. In the next experiment with the Mach Zehnder interferometer, the polariton kinetic energy will be lower, and a deviation from a linear dependence between ϕ and V will appear.

Decrease and recovery of visibility

We would like now to discuss the observed visibility of the interference fringes when changing the control power.

The left part of figure 5.8 shows the visibility of the fringes as a function of the control beam, obtained by fitting the curves in figure 5.7.

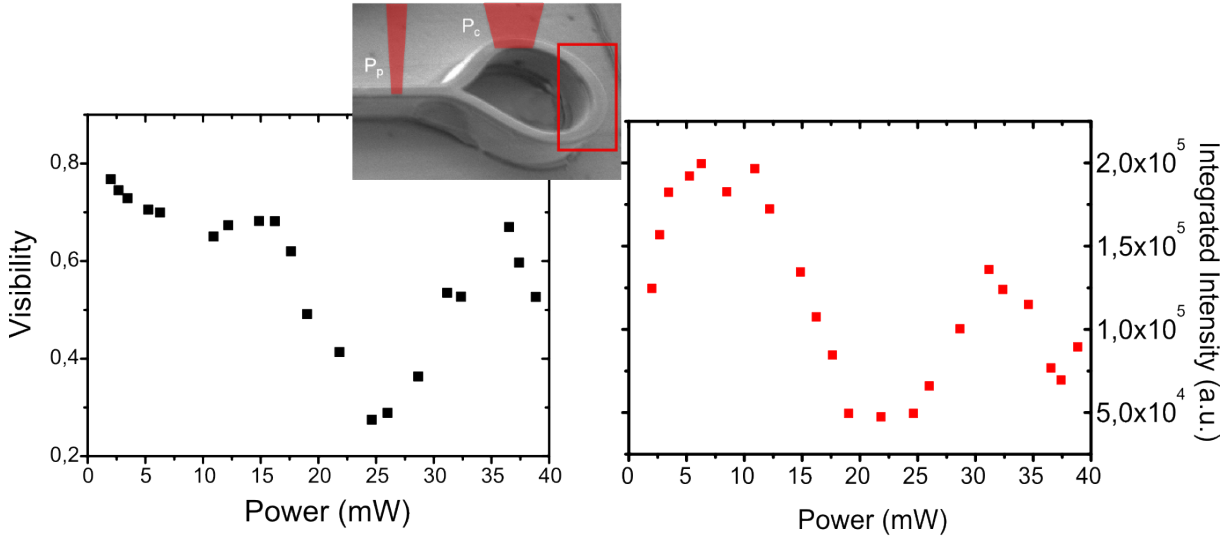


Figure 5.8: Left: Visibility of the fringes at the top of the interferometer (red rectangle in the scheme) as a function of the power of the control beam. Right: Integrated emission intensity collected at the top of the interferometer inside the red rectangle in the scheme.

The visibility starts from the already discussed value of around 0.8, stays quite constant up to 15 mW, then decreases down to 0.25 and later increases again up to 0.7.

To interpret these results, at first one must consider that the control beam can act not only as a source of excitons in the reservoir, inducing the phase shift, but also as source of additional polariton injected in the circuit. For low power, below threshold, the injected polaritons are incoherent and this can represent a background signal that reduces the visibility of the fringes. In general this contribution can be neglected since it's much weaker than the injected coherent signal by the pump beam. On the right of figure 5.8, we report the total integrated signal over the region on top of the interferometer, indicated by red rectangle in the inset. Here we observe how the total injected signal is not independent on the control power, but instead oscillates and can be reduced down to a factor 4.

A possible interpretation of this variation is directly related to the use of non resonant excitation, in which case the formation of the coherent state is spontaneous, and, differently from the case of resonant pumping, the initial phase of the state is not fixed. The geometry of our Sagnac interferometer allows polaritons to travel the whole rings and thanks to a long lifetime and especially, in this situation, to a high propagation speed, they can close the loop, and so tend to form and lock into a stationary wave. This is analogous to what happens for a polariton flux against a barrier [36, 39], in a closed loop [291] or between two spots [111]. In the structure, by varying the induced phaseshift by the control beam, the input injection region will oscillate between a node or an antinode of the standing wave. As a result the efficiency of the injection (and eventually the reflection against the beamsplitter) changes and the total intensity in the ring will oscillates as observed.

This interpretation is confirmed by the period of this oscillation of around 20 mW that

correspond, compared to fig. 5.7, to an induced phase shift of around 2π .

This effect, combined with some incoherent signal introduced by the control beam, explains the observed behavior of the visibility. The weak incoherent signal injected by the control spot have an influence on the visibility only when the injection efficiency of the coherent signal is low, around 25 mW, corresponding to the observed visibility deep.

Notice that these effects affect solely the visibility of the fringes. The phaseshift increases continuously with the control power without presenting any discontinuity.

5.5 The complete Mach Zehnder interferometer: the output modulation

The Sagnac interferometer was an ideal structure to provide a direct visualization and a clear evidence of the principle of the reservoir induced phase shift for a polariton flow. Let's now exploit this effect for controlling the behaviour of a Mach Zehnder interferometer.

It's important to stress that in all the following experiments the condensate will be injected resonantly and the control pump power would be lower. This allow us to fix the phase and the injection efficiency of the incoming beam and also to generate a signal from the pump laser much stronger than the one possibly generated by the control beam and any influence of the signal injected by the control beam will be absolutely negligible.

5.5.1 Propagation inside the Mach Zehnder interferometer

The experimental configuration is summarized in figure 5.9.

Before discussing in details how the device operates, a particular attention must be paid to the band structure of the wire cavity. As shown in the center of figure 5.9, several band are presents. Here we observe the first two order (labeled 1 and 2). Each mode has a TE-TM splitting (as discussed in chapter 2) and so we finally obtain a 4 bands structure.

In the following experiment, we will carefully adjust the kinetic energy of polaritons to a value of $E_k = 0.5meV$, below the TE_1 band, and in order to do so we will use a resonant pump beam. This will assure us the excitation only of the lower band TM_1 .

The resulting emission is reported on the bottom panel of fig. 5.9; where we evidence polariton propagation along the whole device.

The polariton flow is divided almost equally in the two arm of the interferometer by the first beam splitter. Polaritons travels inside the arms and then reaches the second beam splitter. As we will better demonstrate and discuss later, the two paths have almost exactly the same length and so the phase difference between the two beams is expected to be zero: at the reunification point, the second beam-splitter, constructive interference occurs and signal is transmitted outside of the interferometer.

We can define the total transmission of the structure as the ratio between the signal in the output arm I_{out} divided by the one in the input arm I_{in} . These two values are obtained integrating the signal in the region indicated in the figure, and the resulting value for the

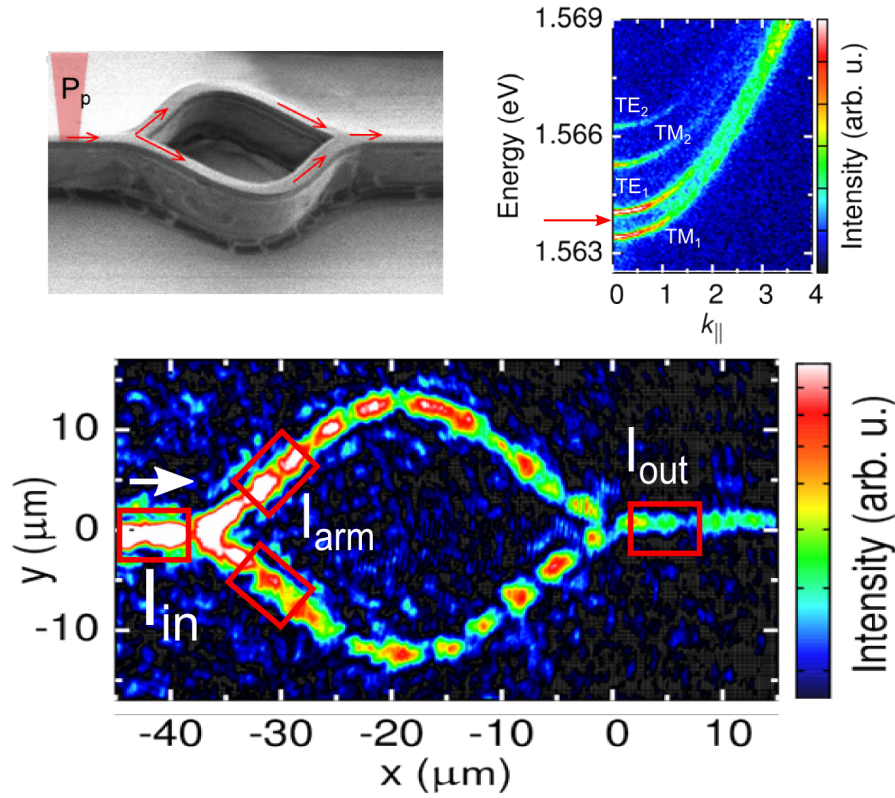


Figure 5.9: Top left: Scheme of the experimental configuration. The pumping laser is now resonant. Top Right: The band structure measured along the injection arm. The red arrow indicates the energy of the pumping laser. Bottom: Emission intensity collected from the MZI interferometer structure. The rectangles indicates some specific regions over which the integrated emission intensity is considered (see text).

transmission is $T = 6.5\%$.

This value, much smaller than unity, can be explained by two effects. On the one hand finite polariton lifetime reduces the overall intensity along the propagation. On the other hand, each beamsplitter generates a ratio of backreflected signal that don't enter the structure or that, once inside undergoes several reflections. The latter effect is confirmed by the observation of clear interference fringes in the arms of the interferometer. These are generated by an incoming signal interfering with contra-propagating signal reflected by the second beam splitter.

In order to give a rough estimation of the efficiency of the beamsplitters and of the loss of polaritons during the propagation, one can derive some analytical expressions for the signal in different points of the structure. In a simplified model, where interference effects are neglected, we can consider that at each beamsplitter, a certain ratio t of the total incident signal is transmitted, and the remaining $r = 1 - t$ is reflected. Afterwards, we can define a damping factor $\gamma \leq 1$, representing the reduction of signal corresponding to the propagation over one arm.

By taking into account and summing all the contributions of possible reflections, we end up

with the following expressions (similar to the ones obtained for a Fabry-Perot):

$$I_{in} = I_0 (1 + r + \gamma^2 r t^2) \frac{1}{1 - \gamma^2 r^2} \quad (5.4)$$

$$I_{arm} = \frac{I_0}{2} t \frac{1 + \gamma^2 r}{1 - \gamma^2 r^2} \quad (5.5)$$

$$I_{out} = I_0 t^2 \gamma \frac{1}{1 - \gamma^2 r^2} \quad (5.6)$$

where I_0 is the injected intensity.

Experimentally, one obtain a value for the quantity $I_{out}/I_{in} = 6.5\%$ (as mentioned before) and $2I_{arm}/I_{in} = 0.5$ (where $2I_{arm}$ is the sum of the intensity measured in the two arms, integrated in the region indicated in the figure). From there, we estimate the values for t and g .

In the 2D colormaps of figure 5.10, we report the calculated values of $2I_{arm}/I_{in} = 0.5$ (on the left), and the transmission I_{out}/I_{in} as a function of all the possible values of t and g . The contoured region (in blue and yellow) represents the parameters combination that are in agreement with the experimental measurements, that is with the requirements $2I_{arm}/I_{in} = 50 \pm 5\%$ and $I_{out}/I_{in} = 6.5 \pm 1.5\%$. Superposing the two conditions, we deduce essentially two possible combinations of parameters, evidenced by green lines on the right colormap of fig. 5.10.

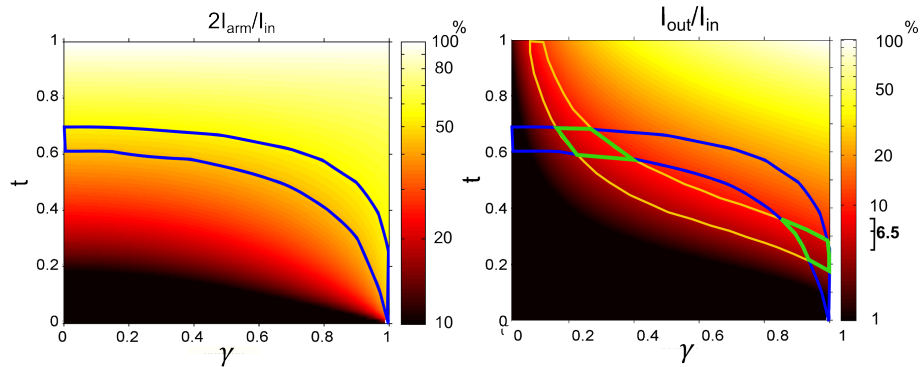


Figure 5.10: 2D color map representing the calculated values of the ratio $2I_{arm}/I_{in}$ (left) and I_{out}/I_{in} (right), varying the parameters t and γ . The evidenced region on the map represents the parameters combination in agreement with the experimental observation. The blue line contours a region in which $2I_{arm}/I_{in} = 50 \pm 5\%$. The yellow contours a region in which $I_{out}/I_{in} = 6.5 \pm 1.5\%$. Regions countoured by black lines on the right map indicates parameters for which both the conditions are satisfied.

We can exclude values of γ of 0.9, that would correspond to polariton lifetime of several hundreds of ps, and also a beam splitter with a transmission of only 20% is not compatible with other experimental evidences. It is then legitimate to consider the map region on the upper left.

We can deduce an estimation for the efficiency of the beam splitter of around 65%. This in the approximation of an equal efficiency for the entrance and the exit of the signal. Furthermore, we extract a reduction of signal during the propagation due to the finite

polariton lifetime, given by γ , of around 0.25.

Considering the length of the arm $l = 55\mu m$, and the polariton group velocity of $v_g = 1.5\mu m/ps$ (corresponding to a kinetic energy of $E_k = 0.5meV$), one can deduce the corresponding lifetime $\frac{l}{v_g \ln(\gamma)} = 30ps$. Considering the negative detuning of the used structure ($\delta = -8meV$), this value corresponds to a polariton lifetime at zero detuning of $\tau_{pol}(\delta = 0) = 42ps$, in quite good agreement with the value of around 40 ps extracted from the decay in a planar cavity.

The overall transmission of the device will be defined for the rest of the chapter as the value $T = I_{out}/I_{in}$. But it's important to keep in mind that, taking the extracted value of the beamsplitter efficacy t , we can correct this value because, in first approximation, $I_{in} = I_0 + (1 - t)I_0$ and so the effective transmission is $T_{correct} = (2 - t)\frac{I_{out}}{I_{in}} \approx 1.4T = 9\%$.

Nevertheless, the limitation on the overall transmission imposed by the polariton lifetime is relevant and represents an handicap for this structure: handicap that although could be partially overcome by a further increase of the polariton lifetime and also by reducing the length of the interferometer arms. Increasing such a transmission value could be of particular importance especially if considering such a polariton Mach Zehnder interferometer integrated in optically driven polaritonic circuits. The cascability indeed is one of the essential features for any circuit element.

In conclusion, we have shown and analyzed the propagation of polaritons inside the Mach Zehnder interferometer, characterizing the main parameters, essentials for the following discussion of the device used as a modulator.

5.5.2 Control of the output intensity

We now address the optical control of our MZI. To induce a control phase-shift, a non-resonant control beam is now focused on the upper arm of the MZI. Its power P_c has been scanned from 0 up to 12 mW and the results are reported in figure 5.11 for few significative powers.

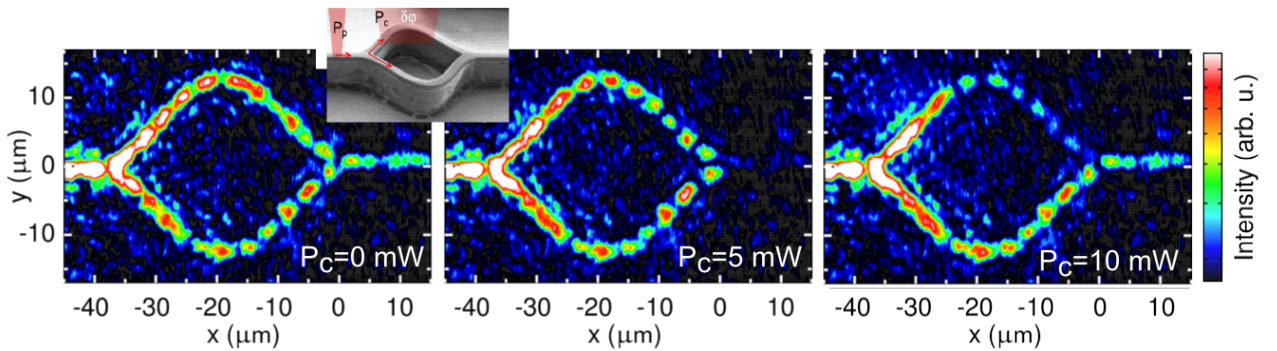


Figure 5.11: Emission intensity from a MZI for different values of the non resonant control beam (scheme of the experiment in the small inset); the transmitted emission is modulated thanks to the phase induced by the control beam.

We can clearly observe how the output intensity can be controlled by the control power beam and its non monotone dependence with P_c is a good indication that we are in presence of an interference effect.

Indeed the second beam induces a phase shift between the two arms. A phase shift of π , corresponding to $P_c = 5mW$, generates destructive interference at exactly the reunification point. The interference pattern will present at this point a minimum and so the coupling with the output arm is close to zero and the signal propagating outside the structure is strongly suppressed.

For a higher power, a 2π phase shift is induced and constructive interference at the beamsplitter position is recovered and so the intensity in the output arm is maximized.

In order to better quantify the modulation of the signal, one can plot the overall transmission of the structure, defined as $T = I_{out}/I_{in}$, as a function of P_c . The results are reported in figure 5.12. We observe how such transmission coefficient is modulated by one order of magnitude. In

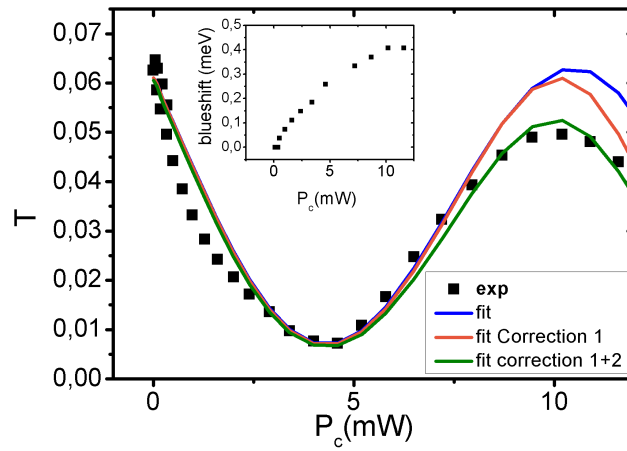


Figure 5.12: Experimental transmission $T = I_{out}/I_{in}$ of the MZI as a function of the power P_c of the non resonant control laser: Experimental point (black squared) and fits (solid colored curves). The 3 fits are obtained using formula 5.7, considering a phaseshift induced by a gaussian barrier with height given the measured blueshift reported in the inset. The first fit (blue) curve is obtained considering $I_1 = I_2$ for every P_c , for the other two a correction to the intensity of I_2 caused by the increase of the potential barrier height is taken into account (see text and appendix for more details B). Fit parameters : $E_{kin} = 0.5meV$, $\sigma = 6\mu m$, $m_p = 6 \cdot 10^{-5}m_0$, $g = 0.8$, $\alpha = 3.5\%$, $\tau = 25ps$.

order to exactly understand the behaviour of the system, we fit the experimental curve with the following model.

We use the standard formula for the intensity resulting from the interferences of two beams with some additional parameters, and so we write the transmission as:

$$T = \frac{\alpha}{I_0} \left[I_1 + \beta I_2 + 2g\sqrt{I_1\beta I_2} \cos(\Delta\phi + \theta_0) \right] \quad (5.7)$$

where:

- g represents the coherence of the beams in the two arms and will take a value of 0.8 in

accordance with what is observed in the Sagnac interferometer since the path over which polaritons go through is approximately the same than fig. 5.6.

- α represents an overall decrease of the signal that takes into account finite polariton lifetime and the reflected signal by the beamsplitters.
- θ_0 is a constant phaseshift between the two beams, in order to take into account an eventual slight asymmetry between the two paths.
- the values of the phase shift $\Delta(\phi)$ depends on the blueshift following the formula 5.1, where the potential is a gaussian with $\sigma = 5.5\mu m$ and height given by the measured blueshift as a function of P_c reported in the inset of fig. 5.12.

The values I_1 and I_2 are supposed both equal to $I_0/2$ for $P_c = 0$ (with I_0 is the measured incoming signal). The coefficient $\beta < 1$ represents a reduction of the intensity on one of the two arms due to the presence of the induced potential barrier. Such a reduction is related to two effects that have been taken into accounts.

Correction 1: Even if a barrier has a height below the kinetic energy of a particle, there's a certain probability that the particle is reflected. This effect is taken into account by modeling the gaussian barrier by a sequence of squared barrier, for which the transmission coefficient can be easily calculated.

Correction 2: Polaritons, passing through the control spot region, are strongly slowed down. This also means the time required for travelling the same path gets longer, and so their density could further decrease. A more complete description of how these two corrections are estimated is found in appendix B.

The results, taking progressively into account the mentioned corrections 1 and 2 are also reported in figure 5.12. The parameters of the fit are reported in the caption.

This good result of the fitting procedure and the parameters used allow us to draw some conclusions.

- The behavior of the system and the transmitted intensity is completely dominated by interference effect and the influence of incoherent signal on the output intensity is weak. The high value of $g = 0.8$ used confirms this, and it's in agreement with previous measurements.
- The small value of $\theta = \pi/10$ confirms our previous statement that the two paths are indeed almost identical. This small asymmetry could come from a slight energy difference of the polariton resonance in the lower and upper band due to the gradient of energy always present over the sample. This effect could eventually be overcome by paying particular attention in the orientation of the etched structure.
- The correction effect to the intensity represented by the factor β becomes important for higher pumping power, when kinetic energy and barrier height are comparable, and this correction reproduces the asymmetry between the height of the two maxima of the

transmission curve. As better shown in appendix B, the main correction comes from the enhanced decay due to the slowing down of polaritons in the control region.

To conclude, we have demonstrated how the behaviour of the structure is controlled optically, and how we can understand qualitatively and quantitatively the operation of the device and the influence of the potential induced by the control beam.

In the following section will discuss our MZI as a possible signal modulator, evidencing advantages and limitation in comparison with other similar devices.

5.5.3 MZI as a modulator

In the framework of a next-generation of electronic and optoelectronic devices, optical switches and modulators are key components[284]. In this context, Mach Zehnder interferometer geometry has been deeply investigated, in several kinds of structures and by exploiting a wide range of mechanisms for inducing relative optical beam phaseshift, with the aim of implementing an intensity signal modulator device. As already mentioned, the phase shift can be induced by several physical effects, mechanically, thermally, electrically, but the case of all optical control is particularly interesting since this could allow to overcome the bottleneck of electro-optic conversion in the integration inside a chip. Whatever mechanism, these modulators should fulfill certain requirements: they should be preferentially small, in order to be highly integrable in a chip, they should be fast, allowing rapid modulation of the out-coming signal, they should be low-energy consuming and operate at room temperature .

In the next paragraph we will discuss the main operating parameters of our system: although still far from applications (due especially to low T functioning and short signal lifetime), it could represent an alternative approach, taking advantages from the strong interaction properties of polaritons.

Functioning parameters

Energy consumption

A parameter characteristic of the functioning of the MZI as a modulator is the power consumption necessary to generate a π phase shift between the two arms or, in other words, the power to switch from on to off the transmitted signal. By looking at the intensity modulation series of Fig. 5.12 , we extract that the blueshift required for inducing a π phase shift is $E_b \approx 0.3$ meV. This corresponds to an estimated exciton density of $n_X = 2.6 \cdot 10^{10} \text{cm}^{-2}$ ². Since the area of pumping is approximately $L \cdot w \approx 21 \mu\text{m}^2$ (with $L \approx 7 \mu\text{m}$, size of modulated region, and $w = 3 \mu\text{m}$ the width of the wire), this values corresponds to a number of exciton per quantum well (12 in total) of $N \approx 5400$. Let's now consider that excitons have a lifetime at low T of $\tau_x = 400 \text{ps}$ [75]. Under a constant cw pumping, their population will follow the rate equation: $dN_X/dt = -N_X/\tau_X + R$ (with R indicating the rate of excitons injection by the pump), which stationary state is given by

²The heighth of the induced potential barrier is given by: $V = |X|^2 n_X 6a_{B^*}^2 E_B$, with X the excitonic Hopfield coefficient of the polariton. This expression is obtained starting from the formula 1.43 for the interaction constant and considering interactions from a polariton in the bottom of the band and a and highly excitonic one ($|X|^2 = 1$).

$N_X = R\tau_X$. The effective power to be injected inside the cavity required to maintain this value of excitons is around $40\mu W$. From Fig.5.12 we can also extract the real power sent on the sample to obtain the π shift, that corresponds to 3 mW. The relevant difference between this two values can be explained taking into account the following factors:

- half of the pump power do not really hits the cavity, since the spot is 2 times wider than the waveguide;
- the control laser spot has a wide angular distribution due to the high numerical aperture objective (NA=0.55) used to focus it. The consequent angular mismatch between the incoming power and the reflectivity deep of the Bragg mirror brings to the fact that only a small part of the signal, estimable at around 5%, is effectively injected in the cavity.

By simply optimizing the spot shape and its angular distribution, a reduction of a factor around 40 could be obtained in the control power values, almost reaching the estimated optimum value. In principle, this pumping condition should be quite easily achievable from the experimental point of view. From the number of excitons per QWs estimated above, we could also deduce what could be the energy needed to be delivered by one laser pulse to induce a π - *shift*, in the case of perfect injection. This is approximately 15 fJ.

Size

The used interferometer structure has a size of approximately $40 \cdot 30 \mu m^2$, but the more significant parameter is the size of the active region, the real lower limit for the device size. In our case is the $L \approx 7 \mu m$ corresponding to the control spot region.

Characteristic time

The speed operation of our MZI is limited by the exciton lifetime in the reservoir, that decays with a lifetime of $\tau_x = 400 ps$ [75].

A higher speed operation could be obtained by a reduction of this limit, for example via an increase of the recombination rate of the excitons, in analogy with what is done for free carrier in photonic crystal structures [292].

Extinction ratio

The intensity modulation between the maximum and the minimum transmitted values obtained goes up to around one order of magnitude. It is common to define it in decibel scale as $\log_{10} \frac{I_{max}}{I_{min}} = 10$. Although extinction ratio can be much higher in other devices (as reported in table 5.5.3), this values is nevertheless enough to clearly distinguish on and off operation. Furthermore, the measured value is a lower limit for the real extinction ratio since the sensitivity in the experiment is limited by noise coming from scattering of the resonant laser.

All characteristics of our device are summarized in the table 5.5.3, reported together with parameters coming from few examples reported in literature and obtained in other MZI modulator, working with different kinds of control mechanisms but most of them based on photonic crystal.

| | π shift power π shift energy | Size | Operation time | Extinction |
|---|---|--------------|-------------------|------------|
| Si Photonic Crystal Thermooptical control [284] | $20mW$ — | $20\mu s$ | $20\mu m$ | 20dB |
| Si Ph. Crys. Eletrical control [266] | $2mW$ — | 100 ns | $10\mu m$ | 15 dB |
| Surface plasmon polaritons (CdSe QDs) - optical control [270] | $2\mu W$ — | 40 ns | $4\mu m$ | — |
| AlGaAs Photonic crystal - optical control [268] | — $1.7nJ$ | 3 ps | $80\mu m$ | — |
| InGaAs Ph.Cr+InAs QDs - optical control [269] | — $100fJ$ | 15 ps | $500\mu m$ | 16 dB |
| Our MZI | 3 mW ($40\mu W_{opt.}$) $15fJ$ | $\sim 400ps$ | $7\mu m$ | 10 dB |

Table 5.1: Summary of the essential operational parameters of our interferometers, reported together with the ones from other kind of MZI interferometers reported in literature.

At first, it's important to underline how all the systems which characteristics are reported in the table operates at room temperature, while our experiments are performed at 10 K. Nevertheless, we can comment how our system, especially after the discussed realistic optimization of the control beam injection, can provide a phase modulation with low energy consumption in extremely short active region and an acceptable extinction ratio value. For a more quantitative comparison let's for example compare our non linearities, with non linearities expected in pure GaAs bulk material.

In our configuration, a π phase shift is induced by energy shift of the mode of $\Delta E = 0.3 \text{ meV}$, and this is obtained sending an effective injected optical density flux of around $f = 3 \cdot 10^6 \text{ W/m}^2$. One can also estimate the equivalent variation Δn of the optical index n which would be required in a bulk material to obtain the same energy shift through the relation $\Delta n/n = \Delta E/E$. This gives $\Delta n \approx 7 \cdot 10^{-4}$. If we now consider bulk GaAs, with a non linear Kerr coefficient $n_2 = 3.3 \cdot 10^{-17} \text{ m}^2 \text{W}^{-1}$, and excited with the same optical flux f , the corresponding variation of the optical index would be $\Delta n = f n_2 \approx 10^{-10}$. Even considering the effect of light confinement by the Bragg mirrors in our structure, that can enhance non linearities of a quantity equals to the cavity factor $Q \approx 10^5$, the equivalent index variation in our experiment is still almost two orders of magnitude higher that the one relative to bulk GaAs. This indeed suggests that polaritons modes and their interaction properties could provide an interesting approach to combine, in the frameworks of optoelectronics, the strong non-linearity of an electronic system (due to exciton-exciton interactions) with the long and

coherent propagation of photons.

But still at least two important limitations needs to be overcome, that are: losses, that reduce the transmission to 9% and limits the cascability, and the low temperature requirements. Concerning the first one, a significant reduction of losses along the propagation could be provided by the use of guided surface polariton modes. Such configuration could be realized in photonic crystal slabs with embedded quantum wells [293] or using laterally confined Bloch surface polaritons [294]. While, to enhance the operating temperature up to room temperature, large band gap semiconductors can be used, such as GaN or ZnO [16, 17], for which the material quality has been strongly improved lately.

5.6 Polarization control

In this section we will show how the MZI structure, under proper conditions, can act as a modulator of the linear polarization degree. But at first, we will discuss and illustrate the effect of pseudo-spin precession in 2D and 1D cavities.

5.6.1 TE-TM splitting and pseudo-spin precession

In chapter 1 we have already introduced the concept of polariton pseudospin and how polaritons can be considered as spin 1/2 particles. The spin state of the polariton inside the microcavity has a one to one relation with the polarization of the photon escaping the cavity.

Now let's discuss what happens when this pseudospin states are not degenerate but there's a finite energy splitting between states with different pseudospin.

Optical Spin Hall effect

We refer to figure 2.7 of chapter 2 to remind the polarization feature of the polariton dispersion. Both in 2D and 1D, polariton bands are splitted in linear polarization, and the two linear polarization eigenstates will be called TE or TM. Such energy splitting Δ_{TE-TM} can be interpreted as equivalent to an effective magnetic field Ω_{TE-TM} in the plane of the cavity, acting on the polariton pseudospin \vec{S} , represented in the Hamiltonian by the term $H_{TE-TM} = -\vec{S} \cdot \vec{\Omega}_{TE-TM}$. The pseudospin can be represented as a unit vector in the Bloch sphere as in figure 5.13. The effective magnetic field have a peculiar dependence with the polariton k-vector given by [70]:

$$\Omega_x = \frac{\Delta_{TE-TM}}{\hbar k^2} (k_x^2 - k_y^2), \quad \Omega_y = \frac{\Delta_{TE-TM}}{\hbar k^2} k_x k_y \quad (5.8)$$

also represented in the figure.

The pseudospin can precess along such an effective magnetic field with a Larmor frequency given by $\omega = \Delta_{TE-TM}/\hbar$. In the case of a polariton with a pseudospin on the x direction, representing a linear polarization parallel to the x or y axis, and k vector lying, for example, along the x spatial axis, no momentum is applied by the field and the spin be conserved. In the other extreme case of spin aligned along the z axis, (representing circular polarization) there will be precession around the magnetic field that lies in the x-y plane. Analogous to the intrinsic

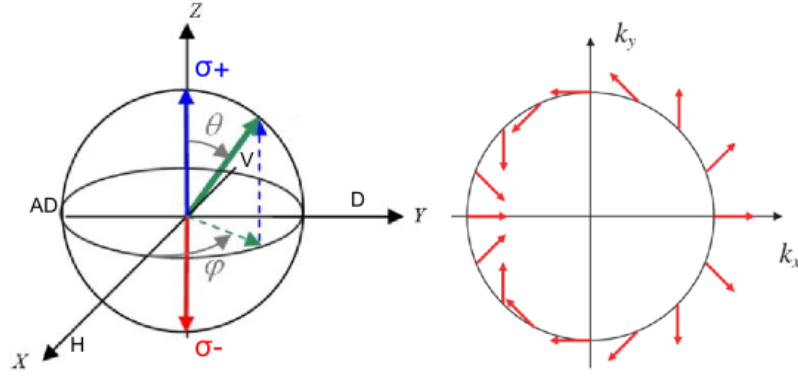


Figure 5.13: Left: Schematic representation of a pseudospin inside the Bloch sphere. The poles, indicated by blue and red arrows, correspond to circular polarizations, respectively σ_+ and σ_- . Figure extracted from [295]. Right: Orientation of the in-plane effective magnetic field generated by the TE-TM splitting, dependent on the direction of the wavevector. Figure extracted from [70].

spin Hall effect in doped quantum wells, where the spin of moving electrons or holes interacts with the Dresselhaus and Rashba fields [296], this polariton pseudo-spin precession effect has been called Optical spin Hall effect [70]. It has been firstly predicted by Shelykh and coworkers [69] and then experimental evidences were obtained in the group of Alberto Bramati in Paris [295] as well as by Langbein and coworkers in Cardiff [114]. But in all the previous experimental observations, polariton lifetime wasn't long enough to allow polariton to undergo a complete precession before decaying.

In the following paragraph we will give experimental evidences of spin precession observed following the polarization degree of the polariton emission along their propagation.

Spin precession in a planar cavity

In figure 5.14 we give an example of the effect of spin rotation in a planar cavity. Polaritons are created at $x = y = 0$ by a $2\mu m$ non resonant laser spot above threshold and propagate radially for few hundreds of microns. In the figure we plot the circular polarization degree of their emission. We will not discuss in detail the initial polarization of the condensate, but what we are interested in is that during propagation polariton pseudospin will precess in time along an effective magnetic field. Then radial ballistic expansion of the polaritons convert this time evolution in the observed spatial polarization pattern.

The radial ballistic motion permits, knowing the group velocity v_g , a direct mapping between radial coordinates and time evolution, and the spin textures observed can so be described by the simple expression [109]:

$$v_g \frac{\delta \vec{S}(\vec{r})}{\delta r} = \vec{S}(\vec{r}) \times \vec{\Omega}_k^{TE-TM} \quad (5.9)$$

In the figure we observe an initial 10% circularly polarized polaritons that radially expand from the excitation region, while their spins precess coherently for at least $300\mu m$. By increasing the excitation power, the polariton kinetic energy increases, and so both the group velocity v_g

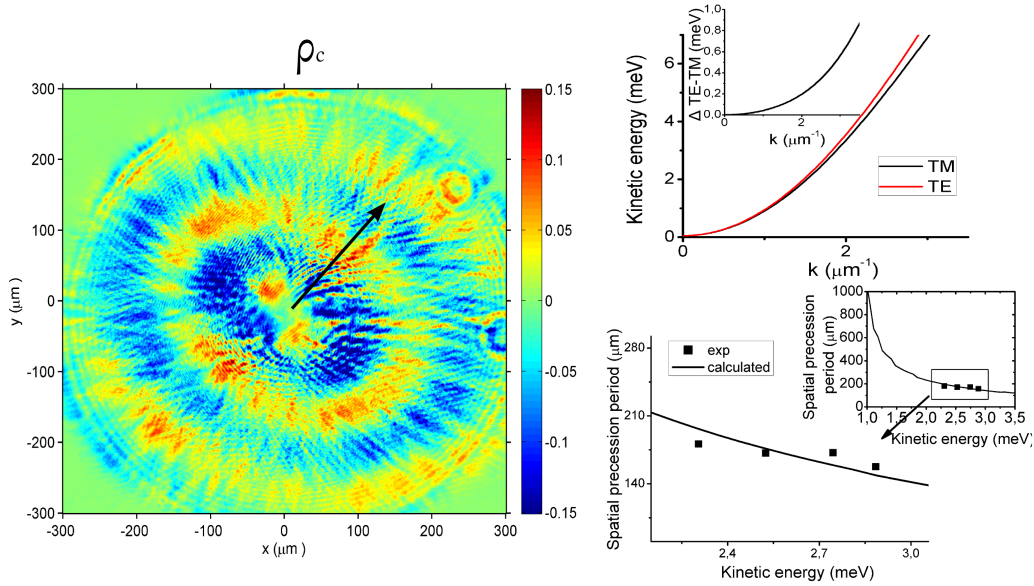


Figure 5.14: Left: Degree of circular polarization of a polariton condensate excited with a $2\mu\text{m}$ non resonant spot in the origin. Polaritons expand radially and the pseudospin precession gives rise to a polarization ring patterns of the emission. Right top: TE and TM polariton bands extracted from fitting the experimental far field emission. In the inset the increase of the TE-TM splitting with the kinetic energy is put in evidence. Right bottom: Solid line: Calculation of the spatial period of the spin precession as a function of the kinetic energy, calculated using 5.9, where values of the TE-TM splitting and of v_g are extracted from the experimental dispersions. Squares: Few experimental values of the spatial precession period measured along the line indicated on the left panel. A good agreement between experiment and calculation is found.

and the TE-TM splitting. By fitting the experimental dispersions (see top right panels of figure 5.14), we can extract these two values for every kinetic energy, and combined with a measure of the blueshift as a function of power, we can calculate the expected behaviour for the spatial precession period. We can see that the few experimental points collected are in good agreement with this calculation.

Analogous results have been obtained and published by E. Kammann [109] and coworkers in Southampton. The Spin Hall effect plays an essential role also in a work we realized in a collaboration between our group and the group of Alberto Bramati in the laboratory LKB in Paris, published in Nature Physics in 2012 [20], and reported in C. In this work, not detailed in this manuscript, the combination of the Optical Spin Hall effect with the spin dependent polariton interactions allowed us to evidence the formation of Half-solitons, interesting topological defect that can be nucleated in wake of a defect. In presence of the effective TE-TM magnetic field, half solitons behave as magnetic monopoles (for more details see appendix C).

Spin precession in wires

The TE-TM splitting in wires has a different origin and a different dependence on the kinetic energy, as discussed in chapter 2 and already shown in figure 5.9. Here the polarization-eigenstates of the system are determined by the direction of the linear polarization with respect to the wire direction (parallel or perpendicular) but the physics involved remains essentially the same, and also the direction dependence of the effective magnetic field with the k vector remains the same of fig. 5.13, but where the only possible direction for the k vector is of course tangent to the wire orientation.

In figure 5.15 we report the effect of spinprecession along a wire, plotting the linear polarization degree of the signal along the propagation. Differently from the previous planar case, here polariton states are excited resonantly, in order to exactly control the energy and the polarization of the initial state. The exciting spot is broad in k space and so will excite all the possible branches present at a given energy. Few examples of the emission resolved in polarization from propagating polaritons along a wire are reported in figure 5.15. When we pump only one of the eigenstates, TM or TE, pseudospin and effective magnetic field are parallel and so no precession is observed (left panel of fig. 5.15). But if the wire is pumped not in an eigenstate, for example

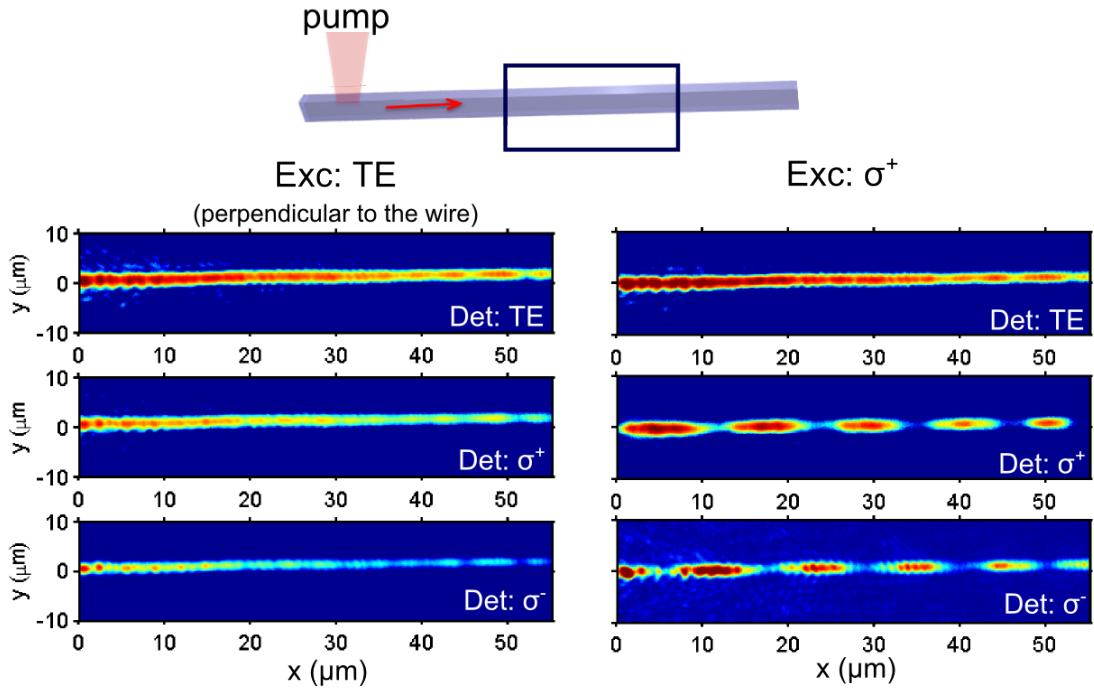


Figure 5.15: A wire is excited resonantly and emission is detected along polariton propagation in the region indicated with a rectangle in the sketch of the experiment. The polarization of the excitation and of the detection is changed in the several panels. In the case of linear excitation, an eigenstates of the system is excited and no intensity oscillation are observed. In the case of circular polarization pumping, the pseudospin will turn in the Bloch sphere from σ_+ to σ_- , but the linear component will remains constant.

with a circular polarized laser, what is excited is a linear superposition of eigenstates, pseudospin

and effective magnetic field are not aligned anymore and we observe precession in space (and so in time) in the circular polarization basis. The intensity in the linear component will remain constant.

The spatial period of the circular polarization precession can be calculated as a function of the kinetic energy. In figure 5.16 we report the results coming from measurements obtained on a $3\mu\text{m}$ wide wire for 3 different kinetic energies. By fitting the dispersions of the TE and TM polariton branches, we extracted the group velocity and the TE-TM splitting, and we calculated the expected spatial oscillation period. The TE-TM splitting now decreases with k so the period increases for higher kinetic energy, differently from the 2D case. The experimental points are quite well fitted by the calculated curve.

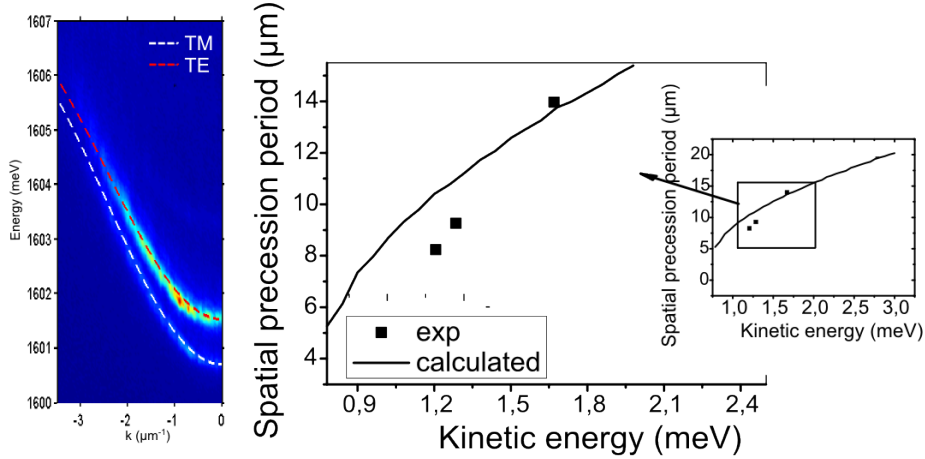


Figure 5.16: Left: Dispersion of a straight $3\mu\text{m}$ width wire. Dashed curve are fits of the two TM and TE bands. Right: Experimental and calculate spatial oscillations period as a function of the kinetic energy. The calculated curve is obtained applying formula 5.9, in which TE-TM splitting and group velocity are derived form the fits of the dispersions.

These observations and the understanding of the spin dynamics will be now essential to understand how can use the polariton MZI as a modulator of the polarization degree.

5.6.2 Pseudospin and phase inside the MZI

We now consider what happens to the pseudospin degree of freedom when the polariton flow enter the MZI. The experimental condition is exactly as before (see fig. 5.9) with the only difference being a higher energy of the excitation laser. We now excite with a laser energy that is above the first TE_1 band and with a TM polarization (pseudospin with $S_x = +1$), so we actually populate only the eigenstates corresponding to the TM_1 band. This signal propagates unperturbed until the beamsplitter. This appears clearly in the figure 5.17, where the emission is now selected in linear polarization, horizontal and vertical (parallel and perpendicular to the longitudinal axis of the interferometer). Once inside the interferometer, the waveguide turns, the magnetic field is no more aligned with the pseudospin (or in other word, horizontal polarization

is no more an eigenstate) and the pseudospin starts to precess and we observe the appearance of a component of the polarization along the vertical direction.

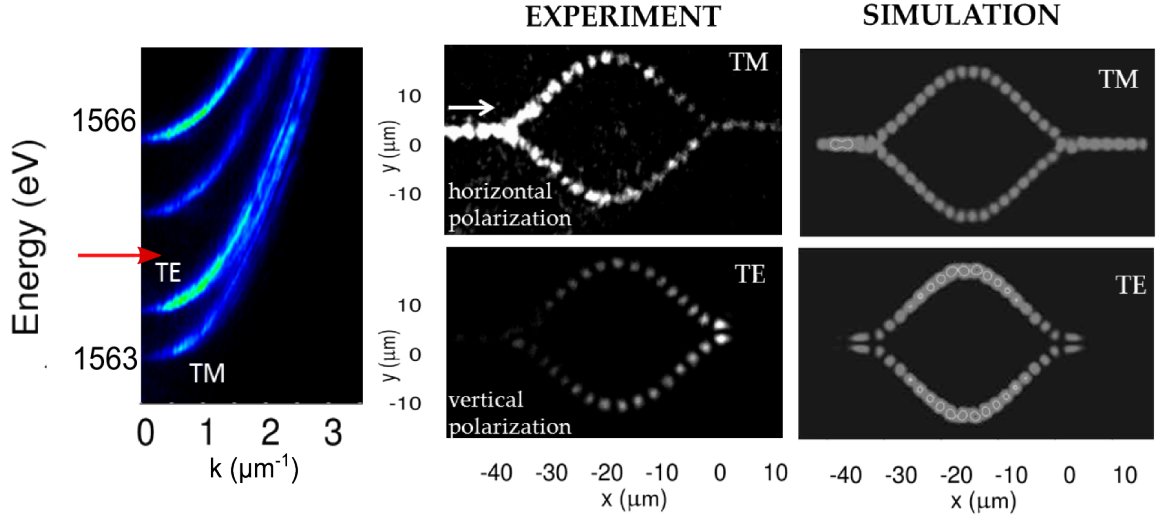


Figure 5.17: Experiment configuration as fig. 5.9 but with a higher energy of the injected polaritons : $E_{kin} = 1.45 meV$, so above the TE band. The pump laser is TM polarized. In the center column, emitted signal along the MZI for horizontal and vertical polarization, corresponding to TM and TE eigenstates of the straight injection arm. On the right, simulations of a polariton states flow inside the MZI, performed by the group of G. Malpuech in Clermont-Ferrand, considering the presence of an effective magnetic field. (Parameters: $\Delta_{TE-TM} = 0.4 meV$, $E_{kin} = 1.85 meV$.)

It appears clearly in both the experimental pictures and in the theoretical ones (obtained in the group of G. Malpuech), that, while TM signal is transmitted, TE signal does not come out from the device. In the TE polarization a two lobes spatial profile is observed both at the entrance and at the exit beamsplitter, typical for a π phase shift between the two arms (to compare with figure 5.11). In order to explain this effect we need to understand how the wave function evolves at the bifurcation.

π shift for TE polarization

Let's consider an initial state in the injection arm linearly polarized along x, the propagation direction. Let's write it in the basis of circular polarization, and so as an in-phase superposition of σ^+ and σ^- , that corresponds to pseudo spin $S_z = +1$ and $S_z = -1$, $\Psi_0 = \frac{1}{\sqrt{2}} \begin{pmatrix} 1 \\ 1 \end{pmatrix}$. Let's

write the 3 Cartesian components of the effective magnetic field as $\vec{B} = \begin{pmatrix} B_0 \cos(2\phi) \\ B_0 \sin(2\phi) \\ 0 \end{pmatrix}$ with

ϕ the angle with respect to the x axis (we remember that the magnetic field turns twice faster than the k-vector, as represented in the scheme of fig. 5.18). The evolution of the pseudospin components is given by the following Schroedinger equation, in which the zero energy level

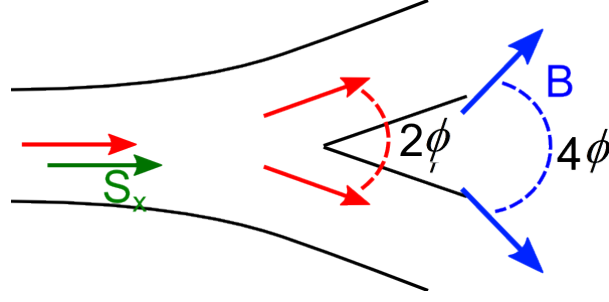


Figure 5.18: Scheme of the beam splitter. Wavevector direction are represented by red arrow. Blues arrows are the direction of the magnetic field, turning twice faster than the k vector. The green arrows represents the initial pseudospin aligned with the injection arm.

corresponds to the spin aligned with the field:

$$i\hbar \frac{\delta}{\delta t} \begin{pmatrix} \Psi^+ \\ \Psi^- \end{pmatrix} = [-\vec{S} \cdot \vec{B} + B_0] \begin{pmatrix} \Psi^+ \\ \Psi^- \end{pmatrix} = \begin{pmatrix} B_0 \Psi^+ - B_0 e^{-i2\phi} \Psi^- \\ B_0 \Psi^- - B_0 e^{i2\phi} \Psi^+ \end{pmatrix} \quad (5.10)$$

where the component of \vec{S} are the Pauli matrices σ_i .

We can observe in this expression how, by starting from a linear polarization and considering a straight wire region ($\phi = 0$), no precession is expected. Now let's see how the wavefunction evolves in presence of a magnetic field that curves following the bifurcation of the wire. We can write the variation of the wavefunction after a short time dt , in the approximation of small angles:

$$\Delta \Psi = \begin{pmatrix} \Delta \Psi^+ \\ \Delta \Psi^- \end{pmatrix} = \frac{-iB_0 dt}{\hbar} \begin{pmatrix} \Psi^+ - \Psi^- + i2\phi \Psi^- \\ \Psi^- - \Psi^+ - i2\phi \Psi^+ \end{pmatrix} \quad (5.11)$$

We now consider the initial condition corresponding to linear polarization $\Psi^+ = \Psi^- = 1/\sqrt{2}$ and we can write:

$$\begin{pmatrix} \Delta \Psi^+ \\ \Delta \Psi^- \end{pmatrix} = \frac{B_0 dt}{\hbar \sqrt{2}} \begin{pmatrix} 2\phi \\ -2\phi \end{pmatrix} \quad (5.12)$$

Since the basis in which we are interested is the linear polarization basis, $\begin{pmatrix} \Psi^H \\ \Psi^V \end{pmatrix} = \frac{1}{\sqrt{2}} \begin{pmatrix} \Psi^+ + \Psi^- \\ i(\Psi^+ - \Psi^-) \end{pmatrix}$, we can write the variation in this basis finally obtaining:

$$\begin{pmatrix} \Delta \Psi^H \\ \Delta \Psi^V \end{pmatrix} = \begin{pmatrix} 0 \\ \frac{iB_0}{\hbar} 2\phi \end{pmatrix} \quad (5.13)$$

This result means that for small t and small angles ϕ , so at the entrance of the interferometer, the horizontal polarization component almost doesn't change, while some signal from the V polarization appears. The sign of the wave-function changes with the sign of ϕ , meaning that it will have opposite sign in the upper and lower arm. In other words, a π -shift for the TE component is induced between the two arms and the wavefunction presents a node at the axis defined by $\phi = 0$. This corresponds to the two lobes observed in the spatial emission image at the beam splitter for the TE polarization.

5.6.3 Control of the output polarization

We want to show here how we can use the polarization dynamic in order to optically control the polarization of the output beam. The possibility of acting on the relative phase of the two beams with the control laser will allow us to invert the situation of constructive and destructive interference for respectively horizontal and vertical polarized signal.

In figure 5.19 where we report the emission from the structure in the two linear polarizations for 3 significative powers P_c of the control beam.

Notice that the signal from outside the structure that is detected around the region where the control beam is placed (panel 2 and 3 of fig. 5.19), is not signal from polariton but it's simply a scattering of the non resonant control laser that is not properly filtered in energy. At $P_c = 7\text{mW}$ the induced blueshift for the TM component corresponds to a phase shift of π : the TM outcoming signal is suppressed and at the reunification we find the two lobe pattern characteristic of destructive interference. For such power of the control beam, TE will also be shifted of π , and so oppositely to TM, will present constructive interference. Vertical polarized signal appears at the output of the device and so the polarization of the outcoming signal switches from TM to TE, driven by the control power.

The TE signal also acquires a π phase shift proofed by the appearance of a vertical polarized signal in the outcoming arm. Then the last column of figure 5.19 shows how,

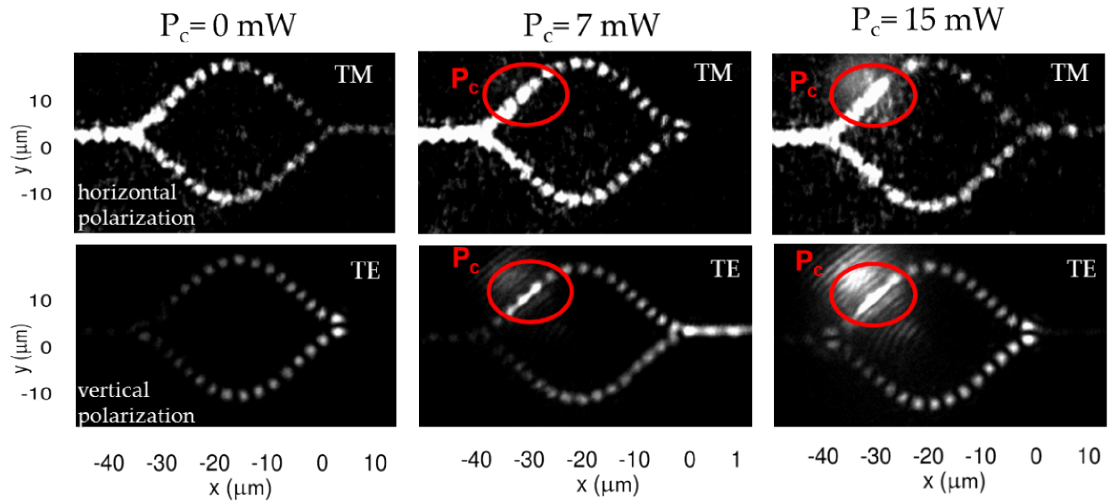


Figure 5.19: Emitted signal along the MZI for horizontal and vertical polarization for different values of the control power beam, placed in the region indicated by the red circle. Constructive and destructive interference are alternatively induced on the two components.

inducing a 2π phase shift on both the component, the same features of the first column, with $P_c = 0$, are recovered.

To better visualize the effect of polarization switch, in figure 5.20 we plot the resulting linear polarization degree, defined as $\frac{I_{hor}-I_{ver}}{I_{hor}+I_{ver}}$, as a function of P_c .

The polarization degree oscillates, controlled by the P_c power, and completely changes sign from +1 to -0.8 when changing P_c from 0 to 7 mW.

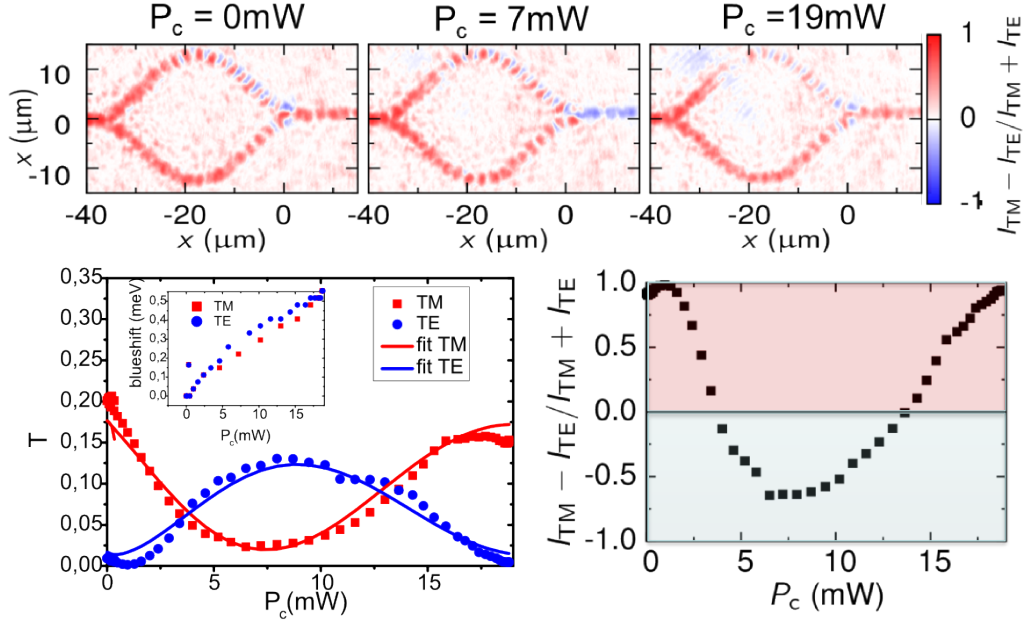


Figure 5.20: Up: Spatial image of the linear polarization degree of the emission from the MZI for 3 different values of P_c (corresponding to the panels of fig. 5.19). Left bottom: Squares and circles: Experimental transmission values, defined as the transmitted intensity divided by the intensity of the TM injected signal, for the two linear polarization. The solid curves are results of a fit obtained using formula 5.7, with parameters explained in the text, considering an initial π shift for the TE component. The phase shift as a function of P_c of each component is deduced taking into account the same blueshift for the two polarization, as confirmed by the experimental point in the inset of the figure. Parameters used: $E_{kin}^{TM} = 1.45 \text{ meV}$, $\Delta_{TE-TM} = 0.4 \text{ meV}$, $\sigma = 6 \mu\text{m}$, $m_p = 6 * 10^{-5} m_0$.

A fitting analogous to the one in figure 5.12, is now applied here to reproduce the transmission intensity in the two polarization.

The fits are obtained by considering two different flows, TM and TE polarized. The same parameters than in the previous fit for the spot size and the induced blueshift are used here. The blueshift below threshold for the two bands is, as expected, the same. Since the kinetic energy is given by the difference between the bottom of the band and energy of the pump laser, two different values for the kinetic energy are used, linked by the relation $E_k^{TE} = E_k^{TM} - \Delta_{TE-TM}$ with $\Delta_{TE-TM} = 0.4 \text{ meV}$ is the measured TE-TM splitting. Also the parameters g is kept equal to the previous case, while the factor γ , indicating the reduction of the signal due to the beamsplitter efficiency and the polariton lifetime, increases with respect to the previous fit up to 0.15, due to the higher polariton kinetic energy.

In agreement with the theoretical explication given above, a phase shift of π at $P_c = 0$ between the two polarization must be introduced to reproduce the curves.

Except this π shift, we also need to introduce some additional correcting phaseshift $\theta_0^{TM} = \pi/10$ and $\theta_0^{TE} = -\pi/6$. These shift could be the results of some asymmetry between the arms, and more specifically some asymmetry of the TE-TM splitting between the upper and lower arm, and to a not perfectly TM polarization of the incoming signal.

To conclude, we have demonstrated how we can optically control the phase of a polariton flow and with this, modulate the intensity of the transmitted trough a Mach Zehnder interferometer device. The pseudo spin and so the linear polarization degree can be controled and modulated.

Another example of mode switching is given in the appendix A: we could induce a switch between the first and the second transverse mode and observe spatial beating between the two.

5.7 Towards Berry phase detection

Here we want to to discuss, in terms of perspectives, how such interferometer structure could be used to measure a geometrical phase acquired by polaritons in the presence of an effective rotating magnetic field.

The concept of geometric phase, also known as Berry phase, is a general concept born in the framework of quantum mechanic, but which can be easily generalized to a large number of classical effects. Its universality lies in its geometric nature. Indeed, this concept can be related to a geometrical phenomenon known as *anholonomy* [297], in which non integrability causes some variables to fail to return to their original values when others, which drive them, are altered around a cycle. As an example, let's consider a quantum system that slowly undergoes a certain trajectories in the parameter space, passing trough a series of intermediate state, and that at the end comes back to the initial state. In this evolution the phase that its wavefunction acquires is a quantum adiabatic geometrical phase, named Berry phase.

We will present the interpretation given by M.V. Berry in 1984 [298] of the Aharonov & Bohm effect as special case of geometric phase. Then we will discuss possible experimental approaches in order to observe a polaritonic Berry phase, taking advantage of our interferometer structure. We will in particular discuss the proposal from Shelykh [299], presenting peculiarities, limitations and possible successful approaches.

5.7.1 The Berry's experiment

Let's initially consider a general Hamiltonian $H(\vec{R})$, that depends on the parameter vector \vec{R} . Let's consider this vector $\vec{R}(t)$ evolving in time, undergoing a closed loop from $t=0$ to T . The hamiltonian $H(\vec{R}(t))$, its eigenstates $|n(\vec{R}(t))\rangle$ and respectively eigenvalues $E_n(t)$ will change in time. We now consider an evolution slow enough that a system, if in an eigenstate $n(\vec{R}(0))$ at $t=0$, will remain in an eigenstate of $H(\vec{R}(t))$ at any time. This is the so-called adiabatic evolution. It can be shown that at the end of the loop C , at time T , the wavefunction can be written as :

$$|\psi(T)\rangle = e^{i\Phi(t)} |n(\vec{R}(t))\rangle \quad (5.14)$$

with the phase term given by:

$$\Phi(T) = -\frac{1}{\hbar} \int_0^T E_n(\vec{R}(t)) dt + i \oint_C d\vec{R} \cdot \langle n(\vec{R}) | \vec{\nabla}_{\vec{R}} | n(\vec{R}) \rangle \quad (5.15)$$

The first term represents the dynamical phase accumulated in the time evolution, while the second term, time independent, represents the geometrical phase. In order to understand the meaning of such expression let's apply it to the example proposed in the original work of Berry [298].

We consider a monoenergetic beam of particles with spins \vec{S} along a magnetic field \vec{B} . Let's split it into two, one undergoing a path in a region where \vec{B} is constant, the other in a region where \vec{B} is constant in magnitude but its direction is varied slowly around a circuit C subtending a solid angle Ω . The dynamical phase factor is the same for both beams because the eigenvalues E_n are insensitive to the direction of \vec{B} . But the rotating \vec{B} will generate a relative phase factor on one of the arm. Let's estimate this phase shift. We consider a magnetic field \vec{B} varying in time; for simplicity we consider it rotating around a given axis, and we express it as follows:

$$\vec{B} = \begin{pmatrix} B_0 \cos \phi \sin \theta(t) \\ B_0 \sin \phi \sin \theta(t) \\ B_0 \cos \theta(t) \end{pmatrix} \quad (5.16)$$

The eigenstates of the hamiltonian $-\vec{B} \cdot \vec{S}$, representing a spin parallel or antiparallel to the field are the following:

$$|+\rangle = \begin{pmatrix} \cos \frac{\theta(t)}{2} \\ e^{i\phi} \sin \frac{\theta(t)}{2} \end{pmatrix} \quad |-\rangle = \begin{pmatrix} \sin \frac{\theta(t)}{2} \\ -e^{i\phi} \sin \frac{\theta(t)}{2} \end{pmatrix} \quad (5.17)$$

By applying the formula 5.18 in which the parameter R corresponds the angle ϕ , we end up with the following expression for the geometric phase associated with spin up component:

$$\Phi_g^+ = - \int_0^{2\pi} \cos^2 \frac{\theta}{2} d\phi = -\pi(1 - \cos \theta) \quad (5.18)$$

The value of this phase has no dependence on physical variables like the strength of the field or the speed of rotation, except from the condition of adiabaticity, and its value is purely geometrical and is proportional to the solid angle Ω enclosed by the path. For example, in the case of a field \vec{B} undergoing an equatorial tour ($\theta = \pi/2$), the corresponding solid angle is indeed the $\Omega = 2\pi$ and corresponds to a maximum of the acquired geometrical phase, while no phase shift is generated in absence of rotation of the vector \vec{B} , corresponding to $\theta = 0$ and $\Omega = 0$.

Let's now try to apply the same reasoning to understand the measurements of a polaritonic Berry phase proposed by Shelykh [299].

5.7.2 A polaritonic Berry phase

Polaritons provide all the essentials ingredient for reproducing the configuration of the experiment of Berry. They have shown coherence propagation hundred of microns and also their pseudospin is maintained for long distances. Furthermore, such a spin interact with both

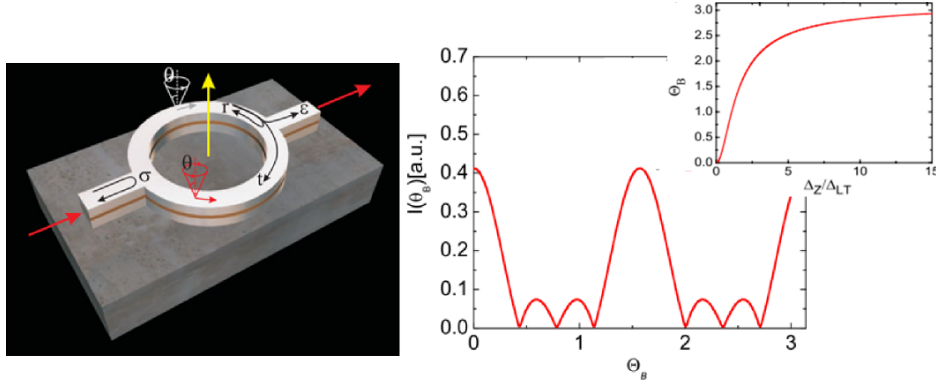


Figure 5.21: Left: Scheme of the proposed experimental configuration by Shelykh [299] for observation of a polaritonic Berry phase. The yellow arrow indicates the direction of the external magnetic field. Pseudospin of polaritons travelling clockwise or anticlockwise in the circuit precess in different directions and they acquire an opposite Berry phase. Right: Intensity of the polariton beam outgoing the interferometer as a function of the Berry phase. In the inset; Berry phase dependence on the ratio Δ_Z/Δ_{TE-TM}

real or effective magnetic fields: these are the main ideas of the work of I. Shelykh, G. Malpuech and coworkers [299].

In analogy with previous experiments realized with electrons, based on coupling Rashba Spin Orbit Interaction and polarization splitting [300], the proposition consists in placing a MZI interferometer like the one presented until now, inside an external magnetic field perpendicular to the cavity surface. The TE-TM splitting Δ_{TE-TM} , combined with the path determined by the circuit, provides a rotating in-plane magnetic field. The external magnetic field provides a constant out of plane component, and induces a Zeeman splitting Δ_Z between pseudospin parallel and antiparallel to its direction. The result is a magnetic field vector precessing around the z axis along the arms of the interferometer, exactly analogous to the Berry configuration. The inclination of this vector θ is given by the ratio between TE-TM and Zeeman splitting, $\arccos\theta = \frac{1}{\sqrt{(\Delta_{TE-TM}/\Delta_Z^2)^2 + 1}}$. Given the geometry of the TE-TM splitting, the magnetic vector will rotate twice faster than the k vector, so it will perform a complete tour around a cone of aperture θ along one arm of the interferometer; additionally the sense of rotation in the two arms of the interferometer will be opposite. The two beams so will undergo opposite phaseshift, that, adapting eq.5.18, is given by:

$$\Phi_g = \pm\pi\left(1 - \frac{\Delta_Z}{\sqrt{\Delta_{TE-TM}^2 + \Delta_Z^2}}\right) \quad (5.19)$$

By varying the external magnetic field, the phase shift between the arms could be modulated and, as demonstrated above, detecting the transmission of the device could give a way to observe and measure such geometric phase.

5.7.3 Experimental requirements and limitation

Let's now consider the applicability of this proposal considering the geometry and the parameters characteristic of our sample. Two main issues must be discussed:

TE-TM Versus Zeeman splitting

By observing eq. 5.19 we can identify several regimes, varying the relative strength of the TE-TM splitting.

- if $\Delta_{TE-TM} \ll \Delta_Z$, the spin-eigenstates along the guide corresponds to spin parallel and antiparallel to the external field and never corresponds to elliptical polarization but always exactly circular; the resulting swipped angle corresponds to $\theta = 0$ and so no phaseshift is induced.
- if $\Delta_{TE-TM} \gg \Delta_Z$, the spin-eigenstates corresponds to in-plane spins all along the guide, and the corresponding polarization is essentially linear; the resulting swipped angle corresponds to an equatorial precession, $\theta = \pi/2$ and so an in-influent relative phase of 4π is induced.
- the interesting regime is the one in which $\Delta_{TE-TM} \sim \Delta_Z$. This could allow to vary the aperture of the cone described by the total magnetic field and so to modulate the induced phaseshift.

By considering the interferometer structure studied in this chapter, the TE-TM splitting is found to be of the order of $\Delta_{TE-TM} \approx 0.5 meV$. The Zeeman splitting for polaritons is given by the expression $\Delta_Z = \beta^2 g \mu_B B$, where μ_B is the Bohr magneton and g the Landé or giromagnetic factor of the exciton and β^2 the excitonic fraction. The g factor strongly depends on the composition and on the size of the QWs. In the present sample we use a 7nm thick GaAs QWs which giromagnetic factor has almost a zero value [301] and we can estimate an upper limit for the Zeeman splitting for a reasonable 10 T magnetic field that is: $\Delta_Z < 30 \mu eV$. We conclude that in this sample we are far from the required regime.

A possible solution consists in using different QW samples.

A new sample based on $In_4\%Ga96\%As$ QW has already been realized. The number of QWs has been reduced to one, and this reduced the TE-TM splitting to $\Delta_{TE-TM} \approx 50 \mu eV$. While a Zeeman splitting of $75 \mu eV$ was measured at 9 Tesla.

The adiabatic regime

We mentioned before that the variation of the magnetic field is required to be slow, in order to give to the system the possibility to follow this rotation and to the state to always be an eigenstate during the evolution, attaining the so called adiabatic regime. But what exactly *slow* means?

There are two timescales involved: one corresponds to the time period T_L for a Larmor precession

of the spin around the magnetic field, and the other is the time for a complete rotation T_r of the magnetic field during the evolution. The requirement so reads:

$$T_r \gg T_L \quad (5.20)$$

More precisely, according with [302], a difference of around one order of magnitude is required. In the case of the presented interferometer the Larmor period is given by $T = \frac{2\pi\hbar}{\Delta_{TE-TM}} \approx 8$ ps. While, since the magnetic field is directly related to the position on the wire, its variation speed is directly related to the polariton propagating speed v_g ; taking into account an approximately value of $v_g = 1\mu m/ps$ and considering the length of the arm around $50\mu m$, we obtain $T_r = 50ps$.

The ratio $\frac{T_L}{T_r} \approx 5$ relative to the 12 GaAs QWs sample could be further reduced by one order of magnitude in the single InGaAs QW sample allowing to completely fulfill also the adiabatic condition.

Our interferometer structure seems to be extremely promising for the observation of a polariton Berry phase: polariton provides pseudo spin that is maintained over hundred of microns; additionally the geometric structure of TE-TM splitting, combined with advantages of pseudospin interaction with an external magnetic field provided by the excitonic polariton component, reproduces exactly the configuration described by Berry. On going experiment performed by Chris Sturm under an external magnetic field might give a confirmation to this proposal.

5.8 Conclusion

In this chapter we presented the realization of two kinds of polariton interferometers. In the first part of the chapter we have discussed the propagation of polaritons inside these structures. We put in evidence a coherent propagation that gives rise to interference effects taking place inside the sample itself. We have demonstrated how we can also directly modulate by optical control the phase of a polariton flow taking advantage of the repulsive interactions between polaritons and excitons. The proof of principle of this method has been obtained in the Sagnac interferometer, in which from the shift of the interference pattern formed inside the structure we deduced a value of the induced phaseshift up to 3π . The mechanism has then been used in a Mach Zehnder interferometer. We obtained a modulation of the output signal of one order of magnitude and we discussed limits and potentialities of the device for future possible applications in all optical controlled circuits.

The evolution of the pseudospin degree of freedom during propagation inside these structure has also been investigated; at first we have evidenced how spin can process along the propagation under the effect of the TE-TM splitting. Then we have shown how the phase modulation can allow controlling the degree of linear polarization of the output signal of the MZI.

Additionally, we have shown how such structures are good candidates for detecting a geometric phase that polaritons acquire along the propagation in the interferometer in the presence of an external magnetic field.

Conclusion and outlooks

In the present thesis we have studied the physical properties of cavity-polaritons inside one-dimensional microcavity structures.

The mixed excitonic and photonic nature of polaritons results in unique possibilities to control their generation, to manipulate their motion and, at the same time, to experimentally detect their behavior.

During this works, we have largely exploited these potentialities. By acting on the confinement of their photonic part, we have reshaped at will the potential in which polaritons move. Additionally, their interaction properties, coming from their excitonic part, provided a further manipulation tools enabling to put polaritons in motion, localize them, block or reflect them and finally, also to control their phase.

By starting from the work of Esther Wertz, who demonstrated for the first time the spontaneous generation of coherent polariton flows inside wire microcavities, we investigated polaritons and polariton quasi-condensates in a variety of one-dimensional geometries.

We have studied polariton motion and their scattering by the disorder, naturally present in the samples. A strong reduction of the backscattering signal has been observed, when the particle density is increased; we proposed an interpretation for this reduced scattering based on the onset of spontaneous parametric processes[139].

Polariton condensation has been investigated in a 1D ridge with periodically modulated size. This lateral modulation gives rise to a periodic potential and results in a strongly modified polariton dispersion, in which mini-bands and forbidden energy gaps appear. This modified dispersion completely changes the spatial behavior of the condensation process. Condensation is triggered towards strongly localized states inside the first energy gap. We have shown, with the theoretical support of the group of Guillaume Malpuech in Clermont-Ferrand, that this localized state is a Bound Gap Solitons, due to a complex interplay between the localized blueshift induced by the excitonic reservoir and polariton-polariton interactions. In time resolved experiments under pulsed non resonant excitation, we have used the different time evolution of the exciton and polariton population to demonstrate a dynamical transition from a pure exponential defect state to a Gap Solitons[110].

This periodic potential has been combined with a constant potential gradient resulting in the acceleration of polaritons. In some specifically etched structures, we have shown how minibands and energy gaps are conserved in presence of such gradient and we observed

characteristic Wannier Stark ladders in the photoluminescence spectra. This potential gradient could also be obtained making use of the interaction energy with the excitonic reservoir in the region where the exciton density spatially varies, i.e. at the edge of the excitation spot. In this configuration we demonstrated polariton Bloch oscillations both in real and reciprocal space, and we presented signatures of polariton Landau-Zener tunneling, jumping non adiabatically from the first to the second mini-band.

The possibility of engineering the potential profile has also been exploited to realize a quasi-periodic lattice, following the Fibonacci sequence. Polariton states in such a potential have been investigated, in collaboration with the group of Eric Akkerman from Technion Israel Institute of Technology. Fibonacci polaritons modes have been imaged both in real and reciprocal space. Their spectrum is a Cantor-like spectrum and their dispersion evidenced appearance of several pseudogaps obeying the gap labeling theorem.

We have finally demonstrated examples of more complex polaritonic circuits, with the realization of both Sagnac and Mach Zehnder interferometers, in which the phase of a coherent polariton flow is changed with a control laser beam. To realize this optical control, we make use of repulsive interactions between polaritons and excitons locally injected by the control laser beam. This repulsive potential locally slows down the polariton flow and thus induces a controlled phaseshift. This mechanism has been applied to control the output signal of a Mach Zehnder interferometer. We have demonstrated the possibility to control both the interferometer output intensity and its degree of linear polarization[303].

All these results illustrate the variety of physical problems that can be addressed using one-dimensional polaritons and open the way to several future research directions . These research perspectives can be envisaged within three main topics.

One direction is surely the continuation of more complex **band engineering** and the study of polaritons in **controlled lattice structures**.

A first example concerns further investigation of the original properties of polaritons in a Fibonacci potential. The study presented in this manuscript is indeed a first characterization of a system that appears promising for further investigation. One possible direction consists in the study of the spreading of time of a wavepacket. In a Fibonacci potential, the time evolution of the width of a wavepacket is expected to follow a power law behavior but modulated by log periodic time oscillations[304, 305]. These oscillations are a direct consequence of the self-similar properties of the Fibonacci potential, in which any partial sequence is always repeated at least ones along the whole series[236, 227].

These oscillations have never been observed, but our system presents the advantage to provide a direct imaging of the particle distribution, not available in other system like electronic superlattices[234] or optical dielectric arrays[228]. The study of the polariton diffusion in a time resolved experiment could give an experimental proof of this effect.

Periodic potential can also be realized using coupled micropillars. This approach is closer

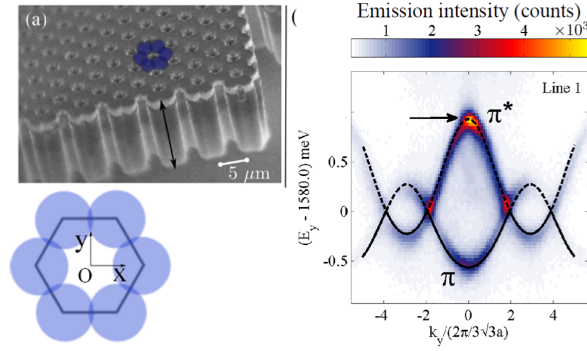


Figure 5.22: Polaritons in honeycomb lattice of coupled micropillars. On the left, SEM image and scheme of the hexagonal disposition of microcavity pillars to form the lattice. Right: Section of the 2D dispersion evidencing the appearance of Dirac cones.

to a tight-binding approach, as opposed to the approach described in this manuscript which is more a perturbation approach to the case of free polaritons. Recently in the group, Thibaut Jacqmin, has observed a graphene-like band structure in a honeycomb lattice of polaritonic pillars (see figure 5.22). Dirac cones, as well as non dispersive bands (flat bands) have been observed, providing a system to study, within the same sample, massless, massive and infinite massive interacting particles[306].

A second interesting direction of investigation is the study of the **hydrodynamics of 1D fluids of interacting bosons**.

One of the structure that I designed during my thesis consists in straight wires with the presence of a controlled defect, represented by barriers or wells of different heights (see figure 5.23). Generation of solitons or other turbulent effects are expected for a flow of interacting bosons against such barrier. Our 1D samples provide a platform to study these effects.

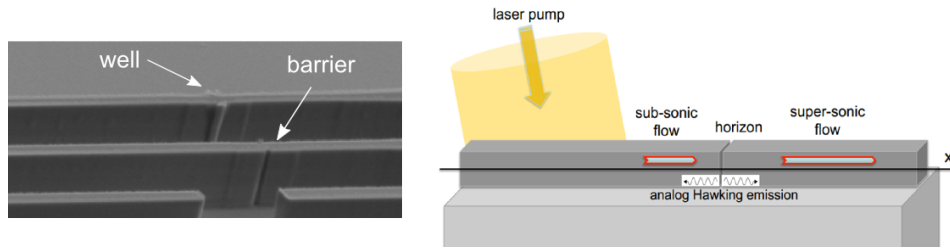


Figure 5.23: Left: SEM image of a straight wire in which a control defect is induced by the etching. This defect can be either a potential barrier or well. Right: Schematic of the theoretical proposal for the generation of an acoustic black hole. Figure extracted from [210].

Recently, a theoretical proposal by Dario Gerace and Iacopo Carusotto presented such configuration as promising for generating the analogous of an acoustic Black hole[210]. An intense superfluid polariton flow is sent onto the barrier. Because of limited transmission through the barrier, one expects an abrupt reduction of the polariton density on the down stream side of the barrier (see figure 5.23). This is proposed to realize the analogous of a black

hole for polaritonic phonons. The region of the barrier provides a horizon between a region of supersonic and a region of subsonic (superfluid) motion. This configuration is proposed for the experimental measurement of stimulated and spontaneous Hawking radiation.

Hai Son Nguyen, post-Doc in the group, is now studying this kind of structures and recently obtained strong indication of the first realization of a polaritonic horizon.

Finally the third main direction is represented by the development of **devices based on polariton non-linearities**.

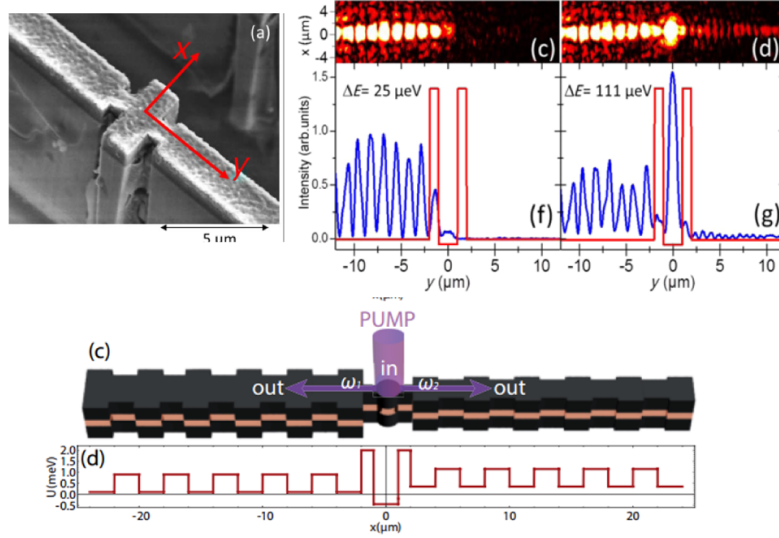


Figure 5.24: Top : On the right, the SEM image of double barrier resonant tunneling diode structure[31]. On the left we show an example of modulation of the transmission through the barriers by varying the induced blueshift inside the trap. Down: Scheme of the structure proposed by Flayac to implement a polariton router. A central trap is pumped and output on the modulated wire on the side is obtained if the discrete energies of the trap match with the band structure of the wires.

Particularly interesting results are expected when coupling 1D and 0D structures, subject of several theoretical proposals[34, 35, 33]. By exploiting the control of barriers and potential wells, Hai Son Nguyen has recently implemented the first polariton tunneling diode [31]. The structure is represented in the figure 5.24 below: it consists in a double barrier structure, which defines a small island in which polaritons are fully confined and thus present discretized states. When a monochromatic polariton flow is sent onto the double barrier structure, polaritons can tunnel resonantly through the island only if there exists a discrete polariton state within the island resonant to the incident flow. Recently Hai Son Nguyen has demonstrated that the transmission of the device can be optically controlled using a non-resonant control beam which tunes the island levels by injecting a small exciton population. The device shows strong non-linearities and a bistable behavior induced by polariton-polariton interactions within the island. This non-linearity can be used to realize optical gates and optical memories.

A similar architecture was recently proposed by Hugo Flayac, also shown in figure 5.24 in

which an island is placed in between two periodically modulated wires with different periods[33]. Controlling the energy of the discrete states of the pillar with respect to the energy gaps on each side, one can obtain resonant tunneling of polaritons from the island into one side of the island or the other. Thus the device, shown in the figure below, can be operated as a router.

Of course for real applications, room temperature is a necessary requirement. The proposed research directions are only demonstrations of proof of principles in the model GaAs system, which is limited to cryogenic temperature. Nevertheless, considering the impressive late improvement of cavity based on large band gap materials, such as GaN[16] or ZnO[17], it may become possible on a longer timescale to develop polaritonic devices operating at room temperature.

Appendix A

Transverse modes switching

In section 5.6.3, we have shown how, by setting the kinetic energy of the signal injected in the interferometer above the first TE band, the output polarization could be controlled, thanks to a switching between the first TM and TE mode driven by the phaseshift induced by the control spot. Both in figure 5.5.2 and 5.19, we can notice how the quenching of the transmission corresponds to a two lobe spatial features at the output beamsplitter. Such intensity profile causes a bad coupling with the first transverse mode, presenting a single lobe in the middle of the waveguide. Since the pumping energy was lower than the energy of the second order transverse mode of the output waveguide, this spatial features corresponded to quenching of transmission out of the device.

Let's see what happens when we pump with an energy higher than the one of the second transverse mode, as shown in the picture A.1.

Such a band corresponds to a polariton modes with a transverse distribution showing two antinodes with opposite phase, and one node at the center, differently from the two first lower bands, as schematized in the sketch of figure A.1.

Because of the gaussian profile of the excitation beam, essentially only the first confined mode (labelled in the figure TM_1 and TE_1) are injected in the interferometer, with a similar k-vector $k_1 \approx 2.2\mu^{-1}$. Such a high k vector, the TE-TM splitting is smaller than 0.2 meV and Due to the fact that in this situation the TE-TM splitting is therefore smaller (0.2 meV) and the propagation speed much higher ($\approx 2.5\mu m/ps$), the discussed effect of polarization precession discussed in section 5.6.3 is not relevant. In the experimental setup, the detection won't be selected in polarization, but all the signal will be collected.

This modes TM_1 and TE_1 will travel inside the interferometer and then recombine at the output. In the absence of control beam, this modes will recombine at the beamsplitter and they will be in phase, and so at the output only first order transverse mode will be excited (see panel c). But applying the control beam, we can induce a π shift between the two beams. The spatial and phase profile obtained at the reunification point perfectly match with the second order transverse mode of the waveguide that now can be excited and it will be the only signal outgoing the device, with its characteristic 2 lobe spatial profile (panel e).

Inducing a 2π shift the initial condition is recovered (panel g), while all the intermediate cases present an excitation of coherent superposition of different order states and consequently the appearance of spatial oscillations between these modes (panels d and f).

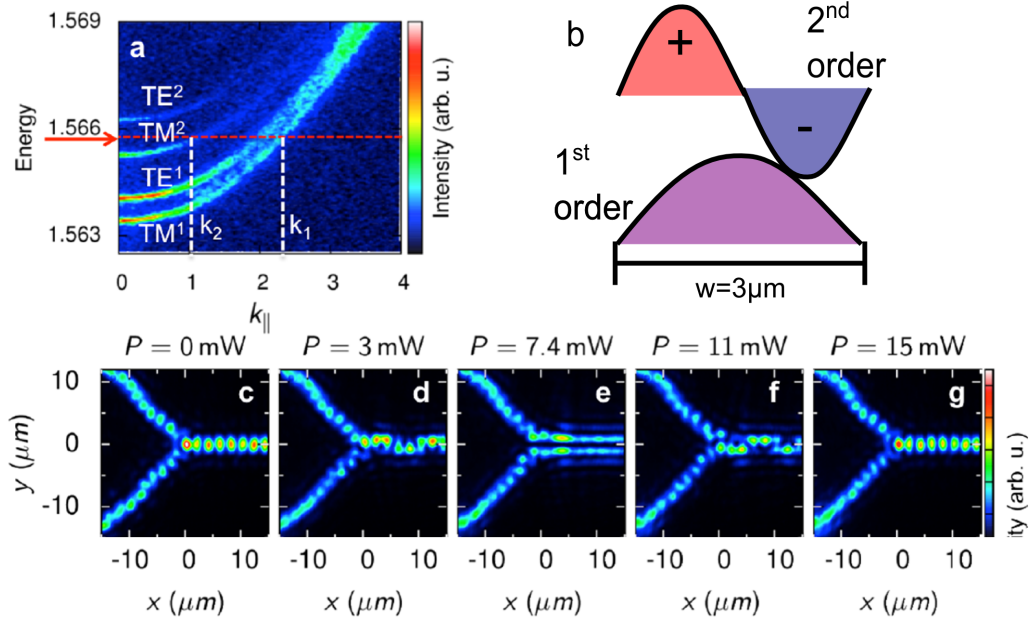


Figure A.1: (a) Polariton dispersion showing, with the red arrow, the energy of the injected polariton flow. The bands are labeled according with their polarization and with the order of confined mode they corresponds to. The white dashed lines indicates the two main wave vectors (k_1 and k_2) of the first and second order 2D confined polariton modes. (b) Sketch of the spatial and phase profile of the first and second order transverse mode in the waveguide of size w . (c-g) Spatially resolved polariton emission at the output of the interferometer for different values of the control power.

Appendix B

Correction to the fit of the MZI interferometer transmission

The fits of the transmission of the MZI interferometer, reported in figure 5.5.2, have been obtained applying the formula 5.7. The factor β appearing in that formula represents a correction to the intensity of the arm where the potential barrier induced by the control beam is created, and results from taking into account two main effects: a partial reflection of the signal by the induced potential barrier and a decrease in the signal attenuation due to the lifetime and the slow down of polaritons.

Here we will better detail how this 2 corrections have been estimated:

Correction 1

Considering a squared potential barrier of height V and length L and an incident particle of kinetic energy E_{kin} (see panel a in the figure), we know that even if $E_{kin} > V_0$, a partial reflection can takes place. The transmission coefficient can be written as:

$$T = \frac{1}{1 + \frac{V^2 \sin^2(k_1 L)}{4E_{kin}(E_{kin} - V_0)}} \quad (\text{B.1})$$

where k_1 is the wavevector in the region of the barrier.

In our fit we consider a gaussian shaped barrier $V(x)$: in order to estimate the total transmission we approximate its shape with a series of squared barriers of size Δx as shown in panel b. In each region of center x_n we can define a local kinetic energy $E_{kin}^n = E_{kin} - V(x_n)$ and a relative wavevector k_n , and a potential barrier between the zone n and $n+1$ equals to $V_0^n = V(x_{n+1}) - V(x_n)$. This allows us to calculate the transmission coefficient for every step T_n and then the total transmission will be given by $T = \prod_n T_n$. Considering the blueshift dependence on power shown in figure 5.5.2, in panel c we plot the attenuation coefficient due to reflection against the barrier. This correction, for the parameters used, is found to be less than 5%.

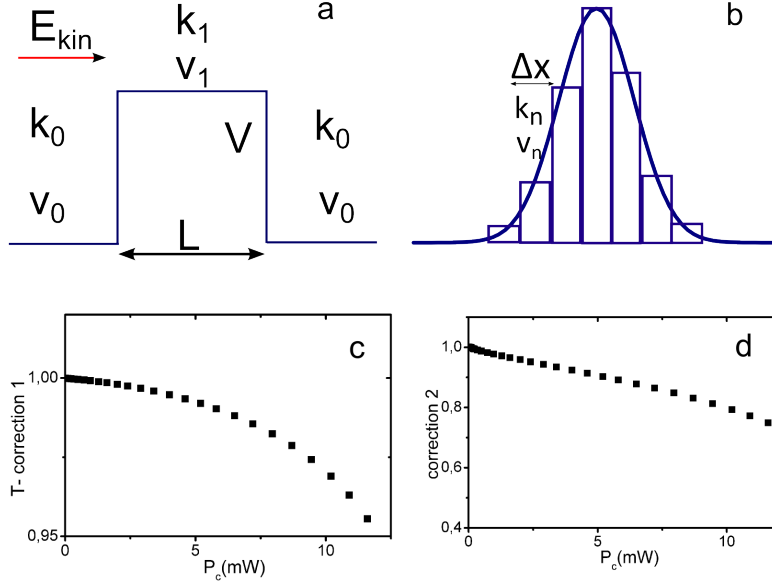


Figure B.1: a) Schematic representation of squared potential barrier. b) Approximation of a gaussian barrier with a sequence of squared barriers. c) Coefficient for correction 1, corresponding to the fraction of reflected signal by the potential barrier generated by control laser beam d) Coefficient for correction 2, corresponding to the attenuation of the signal caused by slow down of polariton in the region modulated by the control power. Parameters used: $E_{kin} = 0.5 meV$, $\sigma = 6 \mu m$, $m_p = 6 * 10^{-5} m_0$, $\tau = 25 ps$, $\Delta x = 1 \mu m$.

Correction 2

When particles are traveling in the control region, they propagate more slowly. In the sketch of panel a, the wavevector on the barrier region is lower, $k_1 < k_0$, and so the velocity. In the parabolic approximation the new velocity is given by $v_1 = \frac{\hbar}{mk_1}$. This means that the time spent by this particle to travel in this region will increase with respect to case of absence of the barrier. The delay will be exactly equal to $\Delta t = L(\frac{1}{v_1} - \frac{1}{v_0})$. Considering that polaritons are finite lifetime particles with lifetime τ , this time delay corresponds to a signal reduction given by: $e^{-\Delta t/\tau}$. Similarly to what done before, we now consider a gaussian shape barrier as a series of squared barrier. In each region of constant potential we can define a given speed v_n and we can compute the total delay as: $\Delta t = \Delta x \sum_n (\frac{1}{v_n} - \frac{1}{v_0})$. Even in this case we plot the reduction coefficient estimated for the experimental configuration of figure 5.5.2 as a function of the power of the control beam. The effect here is more important, and reach a value of around 70%.

Appendix C

Half-solitons

During my PhD I've participated to the experimental observation of polaritons Half Solitons, non linear excitations of a 2-dimensional polaritons gas with mixed spin-phase geometry. The theoretical proposition was elaborated in the group of Guillaume Malpuech, in Clermont-Ferrand and the experimental observation has been realized by Romain Hivet at the Laboratoire Kastler Brossel, in the group of Alberto Bramati. I have collaborated with Romain in several experiments performed at the LKB and few experimental measurements have been performed also at the LPN. The obtained results have been recently described in the PhD thesis of Romain Hivet and they are the subject of an article published in Nature Physics[20] that I report in this appendix.

Half-solitons in a polariton quantum fluid behave like magnetic monopoles

R. Hivet¹, H. Flayac², D. D. Solnyshkov², D. Tanese³, T. Boulier¹, D. Andreoli¹, E. Giacobino¹, J. Bloch³, A. Bramati^{1*}, G. Malpuech² and A. Amo^{3*}

Magnetic monopoles¹ are point-like sources of magnetic field, never observed as fundamental particles. This has triggered the search for monopole analogues in the form of emergent particles in the solid state, with recent observations in spin-ice crystals^{2–4} and one-dimensional ferromagnetic nanowires⁵. Alternatively, topological excitations of spinor Bose–Einstein condensates have been predicted to demonstrate monopole textures^{6–8}. Here we show the formation of monopole analogues in an exciton–polariton spinor condensate hitting a defect potential in a semiconductor microcavity. Oblique dark solitons are nucleated in the wake of the defect^{9,10} in the presence of an effective magnetic field acting on the polariton pseudo-spin¹¹. The field splits the integer soliton into a pair of oblique half-solitons¹² of opposite magnetic charge, subject to opposite effective magnetic forces. These mixed spin-phase excitations thus behave like one-dimensional monopoles¹³. Our results open the way to the generation of stable magnetic currents in photonic quantum fluids.

Magnetic monopoles are the magnetic counterparts of electric charges, characterized by a divergent field. The seminal work of Dirac¹ showed that monopoles are not forbidden by the laws of quantum mechanics. In particular, he considered particles characterized by a wavefunction with a nodal line and a non-integrable phase around it. One route to create an object behaving like a monopole is thus to engineer a wavefunction with such characteristics. A model system to do this is a spinor Bose–Einstein condensate^{14–16}, demonstrating properties such as superfluidity or persistent currents. In reduced dimensions, not only do these quantum fluids support topological defects¹⁷, such as vortices (two dimensional; 2D) or solitons (1D) characterized by a node, but an adequate spin distribution can also provide a vector field with a non-zero divergence, satisfying Maxwell's equations for a point magnetic charge^{6–8}. Monopoles can then be arranged in spinor condensates in the form of mixed spin-phase topological excitations, with a magnetic analogue of the Coulomb force acting on them¹³.

Exciton–polariton (polariton) condensates seem a well-suited system to evidence and study such original effects in quantum fluids. Polaritons are the quasi-particles arising from the strong coupling between excitons and photons confined in planar semiconductor microcavities (InGaAs/GaAs/AlGaAs in our case)¹⁸. Polariton fluids are easy to manipulate with standard optical techniques^{19–22} and they have recently become a model system for the study of quantum fluid effects such as superfluidity²³, vortex formation^{24,25} or oblique solitons^{9,10}. Their spin structure is especially interesting: polaritons are bosons with only two allowed spin projections ± 1 on the growth axis of the sample, which

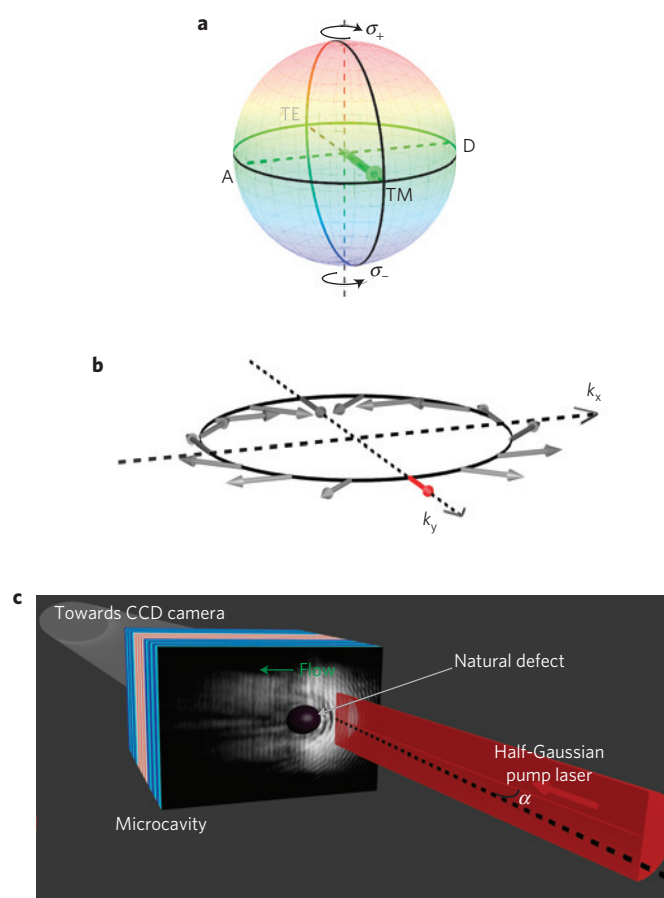


Figure 1 | Polariton pseudospin, effective magnetic field and experimental set-up. a, Bloch sphere representing all of the possible spin configurations of the polariton gas and the associated polarizations: the poles represent circular polarization, the equator represents linearly polarized states and the intermediate latitudes represent elliptically polarized states.

b, Direction of the effective magnetic field created by the TE–TM splitting for polaritons propagating in different directions. **c**, Scheme of the resonant injection of the polariton fluid above a round potential barrier present in the sample. Half-solitons nucleate in its wake. α is the angle of incidence of the excitation beam with respect to the normal to the microcavity plane.

couple to circularly polarized (σ_{\pm}) photons in and out of the cavity. A coherent superposition of different spin populations

¹Laboratoire Kastler Brossel, Université Pierre et Marie Curie, Ecole Normale Supérieure et CNRS, UPMC case 74, 4 place Jussieu, 75005 Paris, France,

²Institut Pascal, PHOTON-N2, Clermont Université, University Blaise Pascal, CNRS, 24 avenue des Landais, 63177 Aubière cedex, France, ³Laboratoire de Photonique et Nanostructures, CNRS, Route de Nozay, 91460 Marcoussis, France. *e-mail: bramati@spectro.jussieu.fr; alberto.amo@lpn.cnrs.fr.

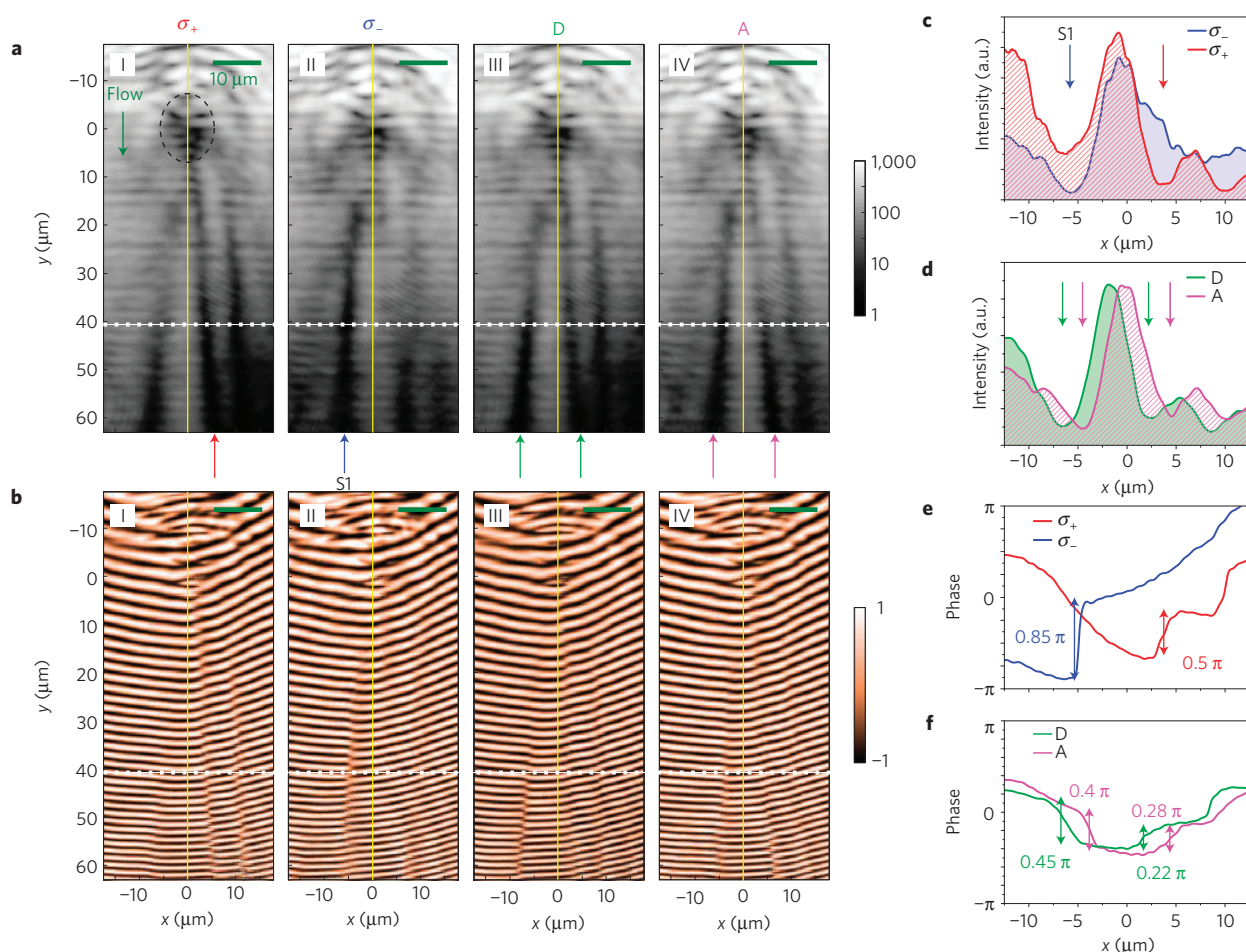


Figure 2 | Density and phase tomography of the half-solitons. **a**, Emitted intensity of the polariton gas in σ_+ (I) and σ_- (II) circularly polarized components and in the diagonal (III) and antidiagonal (IV) linearly polarized components with respect to the TM polarization of injection. Half-solitons spontaneously nucleate in the wake of the potential barrier (dashed circle in **a-I**) and are evidenced as dark traces present only in one circular polarization component (arrows). The yellow line is a guide to the eye. S1 indicates the half-soliton discussed in the text. **b**, Corresponding interferometric images obtained from the interference of the real-space emission with a beam of homogeneous phase. **c,d**, Density profiles of the σ_+ and σ_- (**c**), and diagonal and antidiagonal (**d**) polarized emission along the dotted line in **a-I-IV**. The arrows indicate the position of the inner half-solitons, present only in a given circular polarization and in both diagonal polarizations. **e,f**, Associated phase jump (obtained from **b-I-IV**). The phase jumps observed in diagonal/antidiagonal polarizations have half the value of that measured in circular polarization, hence the term half-solitons. D represents diagonal and A antidiagonal polarized emissions in **d** and **f**. The error bars in the estimation of the phase jumps shown in **e** and **f** represent $\pm 0.08\pi$.

gives rise to polarization states that can be described by a pseudospin vector \mathbf{S} mapped onto a Bloch sphere (Fig. 1a). Another remarkable feature of microcavities is the presence of an effective in-plane magnetic field (Fig. 1b) induced by the polarization splitting between the transverse electric (TE)–transverse magnetic (TM) polarization modes¹¹. The effective field interacts with the polariton pseudospin, adding a magnetic energy term $H_{\text{TE-TM}} = -\mathbf{S} \cdot \mathbf{\Omega}_{\text{TE-TM}}$ to the Hamiltonian (see Supplementary Information) and it provides the analogue of a Coulomb force acting on topological monopoles¹³. Finally, polariton–polariton interactions are strongly spin-anisotropic of the antiferromagnetic type²⁶. This is an absolute requirement for the observation of any stable monopole structure^{7,8}. Indeed, a topological monopole in a two-component spinor condensate is stable against its destruction by an in-plane effective magnetic field if the difference in the interaction energy between the same and opposite spins exceeds the magnetic energy¹³.

One kind of spin-phase topological defect already reported in polariton quantum fluids are the so-called half-vortices^{27,28}. However, no probing of the monopole behaviour has been possible yet, because of the disorder-induced pinning²⁸. The 1D

counterpart of a half-vortex is a dark half-soliton, characterized by a notch in the polariton density of the fluid, and a simultaneous phase and polarization rotation of up to $\pi/2$ in the condensate wavefunction across the soliton¹².

Here, we report on the experimental observation of oblique half-solitons and on their separation and acceleration caused by the effective magnetic field present in semiconductor microcavities. Oblique solitons (or half-solitons in the spinor case) are formed in the wake of a localized potential barrier present in the path of a flowing condensate⁹. They can be seen as the trajectories of 1D solitons in the direction perpendicular to the flow (x), travelling across a 2D flow. The second spatial coordinate (y , parallel to the flow) represents the time coordinate of the 1D system ($t = y/v_f$, where v_f is the flow velocity). This means that the soliton trajectory becomes traceable in a steady state regime²⁹. Studying such trajectories, we demonstrate that an integer oblique soliton separates into a pair of half-solitons of opposite magnetic charge accelerated in opposite directions.

In our experiments we create a polariton fluid in a semiconductor microcavity (see Methods) at a temperature of 10 K by quasi-resonant excitation of the lower polariton branch with a continuous

wave Ti:sapphire monomode laser. Polarization-resolved real-space images of the polariton fluid in the transmission geometry are then recorded on a CCD (charge-coupled device) camera owing to the photons escaping out of the cavity (Fig. 1c). The fluid is injected at supersonic speed (in-plane momentum of $k_p = 1.3 \mu\text{m}^{-1}$, see Methods), upstream from the potential barrier formed by a structural photonic defect present in our sample. Under these conditions, a circularly polarized excitation beam leads to the formation of pairs of oblique dark solitons in the wake of the barrier⁹, characterized by a phase jump close to π across each notch (see Supplementary Information). In the present experiments, we create a polariton gas with linear polarization parallel to the flow (TM polarization, along the y direction). This is a key feature needed to explore the nucleation of spin-phase topological excitations, which can be evidenced by analysing the circularly polarized components of the emission.

First, we demonstrate the formation of half-integer solitons. Figure 2a-I shows the nucleation of two oblique dark solitons to the right of the barrier wake in the σ_+ component of the emission. They can be identified as dark straight notches in the polariton density. These solitons are almost absent in the σ_- component (Fig. 2a-II). In turn, in the σ_- emission, a deep soliton (S1) clearly appears to the left of the barrier wake (blue arrow), where only a very shallow one is present in σ_+ (see the profiles in Fig. 2c). The absence of mirror symmetry between Fig. 2a-I and a-II arises from the specific and uncontrolled form of the natural potential barrier. The individual dark solitons in each of the $S_z = \pm 1$ states of the fluid appear as long spatial traces with a high degree of circular polarization ($\rho_c = (I^+ - I^-)/(I^+ + I^-)$, where I^\pm is the emitted intensity in σ_\pm polarization), as shown in Fig. 3a. Interferometric images obtained by combining the real-space emission with a reference beam of homogeneous phase (Fig. 2b-I and b-II) give access to the phase jump across each soliton. For instance, for the soliton S1 observed in σ_- , 42 μm after the obstacle we measure a phase jump of $\Delta\theta_- = 0.85\pi$ (Fig. 2e; note that it would be π for a strict dark soliton with zero density at its centre⁹), whereas in the same region the phase in the σ_+ component does not change ($\Delta\theta_+ \approx 0$).

A dark soliton present in just one spin component of the fluid is the fingerprint of a half-soliton¹². The mixed spin-phase character of these topological excitations is further evidenced when analysing them in the linear polarization basis. In the regions where the two circular polarizations are of equal intensity (that is, the fluid surrounding the half-solitons) we can define a linear polarization angle $\eta = (\theta_+ - \theta_-)/2$ and a global phase $\phi = (\theta_+ + \theta_-)/2$, where θ_+ and θ_- are the local phases of each circularly polarized component^{12,27}. In our experiments we directly access the phase jump $\Delta\phi$ and the change of η across the solitons by studying the linearly polarized emission in the diagonal and anti-diagonal directions (polarization plane rotated by $+45^\circ$ and -45° with respect to the TM direction). Figure 2d,f shows that the half-soliton S1 is also present in these polarizations with a phase jump of $\Delta\phi \approx 0.4\pi$. This confirms that across the half-solitons, ϕ undergoes a jump $\Delta\phi \approx 0.85\pi/2 \approx (\Delta\theta_+ + \Delta\theta_-)/2$, that is, one-half the phase jump observed in the circularly polarized component in which the soliton is present. We also expect a similar jump $\Delta\eta$ of the direction of polarization. This is demonstrated in Fig. 3b, where all the half-solitons present in our fluid (dashed lines extracted from Fig. 2a-I and a-II) appear as walls between domains of diagonal (magenta) and anti-diagonal (green) polarization. Mapping the linear polarization vector in the vicinity of soliton S1 (Fig. 4a), we deduce a jump of the polarization direction of $\Delta\eta \approx 0.32\pi$ (Fig. 4c), close to $\Delta\phi$, the ideal expected value.

Analysing the half-soliton trajectory from polarization-resolved real-space measurements, we study their acceleration in the field $\Omega_{\text{TE-TM}}$ originating from the TE-TM splitting present in the structure¹¹, pointing in the direction of the flow (y , red arrow in Fig. 1b). The acceleration arises from the interaction between this

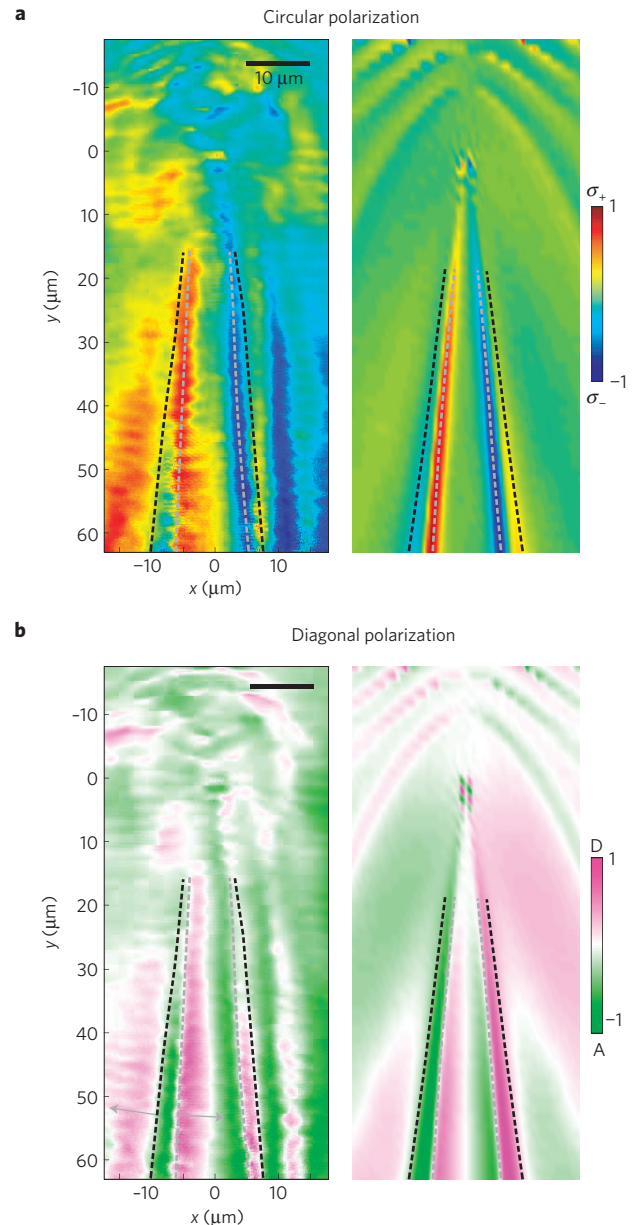


Figure 3 | Polarization texture of half-solitons. **a, b**, Left panels, the measured degree of circular and diagonal polarizations, respectively; right panels, the calculated patterns from the solution of the nonlinear spin-dependent Schrödinger equation describing the system in the conditions of the experiment (see Supplementary Information). The dashed lines show the trajectory of the inner (grey) and outer (black) half-solitons extracted from Fig. 2a-I and a-II. The trajectories of the half-solitons appear as extremes of circular polarization, and as domain walls in diagonal polarization. The grey arrows in **b** indicate the direction of acceleration of the half-solitons induced by the effective magnetic field.

magnetic field and the pseudospin texture of the half-soliton, shown in Fig. 4b for S1. In the direction perpendicular to the soliton (dotted line), the in-plane pseudospin \mathbf{S} is divergent, because it points away from S1 on both sides, as expected for a magnetic charge.

We are able to evaluate the force acting on the half-soliton as the gradient of the magnetic energy with respect to the half-soliton position x_0 . The magnetic energy per unit length is $\int -\mathbf{S}(x' - x_0) \cdot \Omega_{\text{TE-TM}} dx'$, where the integral is performed along the x' transverse direction, perpendicular to the half-soliton located at x_0 . The energy has a positive contribution from the left of the

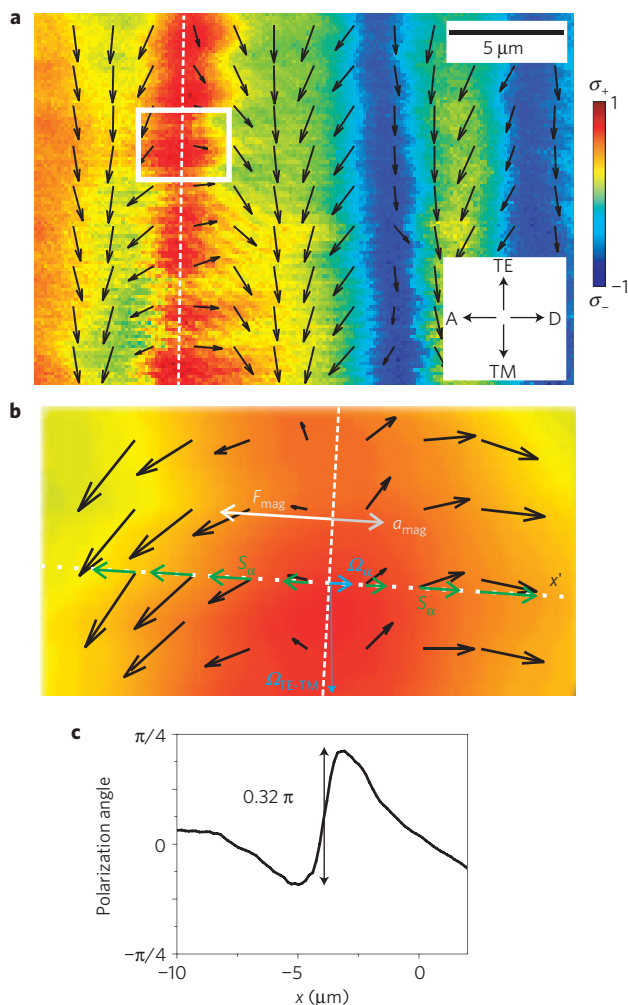


Figure 4 | Magnetic force acting on the half-solitons. **a**, Complete spin texture of the polariton fluid in the region between 30 and 50 μm below the barrier. The colour scale indicates the degree of circular polarization (latitude in the Bloch sphere), and the arrows the direction of the linear polarization as defined in the equator of the Bloch sphere. **b**, Higher magnification of the area outlined by a white rectangle in **a**. The half-soliton, marked by a white dashed line in **a** and **b**, provides a pseudospin field analogous to that of a point charge in the direction perpendicular to its trajectory (white dotted line). The TE-TM effective magnetic field ($\Omega_{\text{TE-TM}}$) has a component Ω_a perpendicular to the half-soliton, which exerts a force F_{mag} causing it to accelerate at a_{mag} . **c**, Angle of the linear polarization plane measured along the direction perpendicular to the half-soliton (shown in **b** as green arrows along the dotted white line). The angle jumps from the antidiagonal to the diagonal direction when crossing the half-soliton.

half-soliton (\mathbf{S} and $\Omega_{\text{TE-TM}}$ pointing in opposite directions), and a negative one from the right (\mathbf{S} and $\Omega_{\text{TE-TM}}$ having the same direction). For the magnetic energy to be minimized, a magnetic force appears, pushing the half-soliton towards the left, increasing the negative contribution. As solitons are density notches, their effective mass is negative¹⁷ and, therefore, the acceleration is in the direction opposite to the force. Thus, the half-soliton S1 that appears in the σ_- component of the fluid accelerates towards the right, as sketched in Fig. 4b. The direction of the acceleration is opposite for the soliton present in the σ_+ component (see arrows in Fig. 3b).

The monopole dynamics allows an understanding of the mechanisms of formation of the half-solitons in our experiments.

An integer soliton nucleated right behind the obstacle can be seen as a superposition of two half-solitons of opposite magnetic charges. The presence of the TE-TM effective magnetic field makes them experience opposite magnetic forces, leading to their separation and to the curved trajectories depicted as dashed lines in Fig. 3, a behaviour similar to the monopole separation in spin ice under a magnetic field³. The half-solitons pushed towards the centre are slowed down, gaining stability and becoming darker as the trajectory becomes parallel to the field. Those pushed outwards gain velocity and become shallower until they eventually disappear (see Supplementary Information and the black dashed lines in Fig. 3). The trajectories of these expelled secondary half-solitons are perturbed far from the obstacle axis by the presence of further solitons nucleated by the large barrier, particularly on the right side of the images. The monopole behaviour and soliton separation are well reproduced by a nonlinear Schrödinger equation including spin and the effective magnetic field present in our microcavities (see Fig. 3 and Supplementary Information). The analogy of half-solitons with magnetic monopoles goes well beyond the behaviour reported here under an applied magnetic field. Our theoretical model predicts repulsive and attractive interactions between half-solitons depending on their respective charges (see Supplementary Information).

A remarkable feature of half-soliton monopoles is that they can be thought of as charged partly photonic quasiparticles, propagating with a high velocity in a fluid that supports superflow²³. Their generation can be well controlled by the phase and density engineering of the polariton wavefunction, their trajectories can be easily followed using standard optical techniques and their dynamics can be controlled by applying strain or external electric fields, which modify the effective magnetic field³⁰. Furthermore, owing to the developed engineering of the polariton landscape^{19,20}, we open the way to the realization of magnetronic circuits in a polariton chip.

Methods

Sample description. The experimental observations have been performed at 10 K in a 2 λ GaAs microcavity containing three In_{0.05}Ga_{0.95}As quantum wells. The top and bottom Bragg mirrors embedding the cavity have, respectively, 21 and 24 pairs of GaAs/AlGaAs alternating layers with an optical thickness of $\lambda/4$, with λ being the wavelength of the confined cavity mode. The resulting Rabi splitting is 5.1 meV, and the polariton lifetime is about 10 ps. During the molecular beam epitaxy growth of the distributed Bragg reflectors, the slight mismatch between the lattice constants of each layer results in an accumulated stress that relaxes in the form of structural defects. These photonic defects create high potential barriers in the polariton energy landscape.

Excitation scheme. To create a polariton fluid we excite the microcavity with a continuous-wave single-mode Ti:sapphire laser resonant with the lower polariton branch. We use a confocal excitation scheme in which the laser is focused in an intermediate plane where a mask is placed to hide the upper part of the Gaussian spot. Then, an image of this intermediate plane is created on the sample, producing a spot with the shape of a half-Gaussian. Polaritons are resonantly injected into the microcavity with a well-defined wave vector, in the region above the defect. In these conditions, polaritons move out of the excitation spot with a free phase, no longer imposed by the pump beam. This is essential for the observation of quantum hydrodynamic effects involving topological excitations with phase discontinuities⁹.

The momentum of the injected polaritons is set by the angle of incidence α of the excitation laser on the microcavity. This allows us to control the in-plane wave vector of the polariton fluid through the relation $k = k_0 \sin(\alpha)$, where k_0 is the wave vector of the laser field. At the injected polariton momentum $k = 1.3 \mu\text{m}^{-1}$, the polariton velocity is $v_l = \hbar k / m_{\text{pol}} = 1.5 \mu\text{m ps}^{-1}$ ($m_{\text{pol}} = 10^{-4} m_{\text{electron}}$). This velocity is higher than the speed of sound of the fluid for the polariton densities of our experiments, as evidenced by the presence of ship waves upstream of the obstacle in Fig. 2a (see ref. 23). For this value of the momentum, we measure a TE-TM splitting of 20 μeV , resulting in the effective magnetic field sketched in Fig. 1b.

Polaritons are photogenerated in our microcavity with TM linear polarization. This corresponds to a pseudospin pointing in the direction of the flow as marked by the arrow in Fig. 1a.

Detection scheme. The observations reported in this work require the complete knowledge of the polariton spin. To gain this, a complete polarization tomography

of the emission is performed through the measurement of the three Stokes parameters $S_1 = (I_{TE} - I_{TM})/I_{tot}$, $S_2 = (I_D - I_A)/I_{tot}$ and $S_3 = (I_{\sigma+} - I_{\sigma-})/I_{tot}$, where I_j is the light intensity emitted with polarization j , and I_{tot} is the total emitted intensity. This requires measuring six different polarizations: I_H , I_V , I_{+45} , I_{-45} , $I_{\sigma+}$ and $I_{\sigma-}$, which, respectively, represent linear horizontal, linear vertical, linear diagonal, linear anti-diagonal, left circularly and right circularly polarized emitted intensity. A combination of wave plates and polarizing beam splitters is used to image each of the polarization components of the emitted light on a CCD camera.

Received 13 March 2012; accepted 19 July 2012; published online 26 August 2012

References

1. Dirac, P. A. M. Quantised singularities in the electromagnetic field. *Proc. R. Soc. Lond. A* **133**, 60–72 (1931).
2. Morris, D. J. P. *et al.* Strings and magnetic monopoles in the spin ice $\text{Dy}_2\text{Ti}_2\text{O}_7$. *Science* **326**, 411–414 (2009).
3. Bramwell, S. T. *et al.* Measurement of the charge and current of magnetic monopoles in spin ice. *Nature* **461**, 956–959 (2009).
4. Fennell, T. *et al.* Magnetic Coulomb phase in the spin ice $\text{Ho}_2\text{Ti}_2\text{O}_7$. *Science* **326**, 415–417 (2009).
5. Ono, T. *et al.* Propagation of a magnetic domain wall in a submicrometer magnetic wire. *Science* **284**, 468–470 (1999).
6. Busch, T. & Anglin, J. R. Wave-function monopoles in Bose–Einstein condensates. *Phys. Rev. A* **60**, R2669–R2672 (1999).
7. Stoof, H. T. C., Vliegen, E. & Al Khawaja, U. Monopoles in an antiferromagnetic Bose–Einstein condensate. *Phys. Rev. Lett.* **87**, 120407 (2001).
8. Pietilä, V. & Möttönen, M. Creation of Dirac monopoles in spinor Bose–Einstein condensates. *Phys. Rev. Lett.* **103**, 030401 (2009).
9. Amo, A. *et al.* Polariton superfluids reveal quantum hydrodynamic solitons. *Science* **332**, 1167–1170 (2011).
10. Grosso, G., Nardin, G., Morier-Genoud, F., Léger, Y. & Deveaud-Plédran, B. Soliton instabilities and vortex street formation in a polariton quantum fluid. *Phys. Rev. Lett.* **107**, 245301 (2011).
11. Kavokin, A., Malpuech, G. & Glazov, M. Optical spin Hall effect. *Phys. Rev. Lett.* **95**, 136601 (2005).
12. Flayac, H., Solnyshkov, D. D. & Malpuech, G. Oblique half-solitons and their generation in exciton–polariton condensates. *Phys. Rev. B* **83**, 193305 (2011).
13. Solnyshkov, D. D., Flayac, H. & Malpuech, G. Stable magnetic monopoles in spinor polariton condensates. *Phys. Rev. B* **85**, 073105 (2012).
14. Stenger, J. *et al.* Spin domains in ground-state Bose–Einstein condensates. *Nature* **396**, 345–348 (1998).
15. Leanhardt, A. E., Shin, Y., Kielpinski, D., Pritchard, D. E. & Ketterle, W. Coreless vortex formation in a spinor Bose–Einstein condensate. *Phys. Rev. Lett.* **90**, 140403 (2003).
16. Sadler, L. E., Higbie, J. M., Leslie, S. R., Vengalattore, M. & Stamper-Kurn, D. M. Spontaneous symmetry breaking in a quenched ferromagnetic spinor Bose–Einstein condensate. *Nature* **443**, 312–315 (2006).
17. Pitaevskii, L. & Strindgari, S. *Bose–Einstein Condensation* (Clarendon, 2003).
18. Kavokin, A., Baumberg, J. J., Malpuech, G. & Laussy, F. P. *Microcavities* (Oxford Univ. Press, 2007).
19. Amo, A. *et al.* Light engineering of the polariton landscape in semiconductor microcavities. *Phys. Rev. B* **82**, 081301 (2010).
20. Wertz, E. *et al.* Spontaneous formation and optical manipulation of extended polariton condensates. *Nature Phys.* **6**, 860–864 (2010).
21. Sanvitto, D. *et al.* All-optical control of the quantum flow of a polariton superfluid. *Nature Photon.* **5**, 610–614 (2011).
22. Tosi, G. *et al.* Sculpting oscillators with light within a nonlinear quantum fluid. *Nature Phys.* **8**, 190–194 (2012).
23. Amo, A. *et al.* Superfluidity of polaritons in semiconductor microcavities. *Nature Phys.* **5**, 805–810 (2009).
24. Lagoudakis, K. G. *et al.* Quantized vortices in an exciton–polariton condensate. *Nature Phys.* **4**, 706–710 (2008).
25. Nardin, G. *et al.* Hydrodynamic nucleation of quantized vortex pairs in a polariton quantum fluid. *Nature Phys.* **7**, 635–641 (2011).
26. Renucci, P. *et al.* Microcavity polariton spin quantum beats without a magnetic field: A manifestation of Coulomb exchange in dense and polarized polariton systems. *Phys. Rev. B* **72**, 075317 (2005).
27. Rubo, Y. G. Half vortices in exciton polariton condensates. *Phys. Rev. Lett.* **99**, 106401–106404 (2007).
28. Lagoudakis, K. G. *et al.* Observation of half-quantum vortices in an exciton–polariton condensate. *Science* **326**, 974–976 (2009).
29. El, G. A., Gammal, A. & Kamchatnov, A. M. Oblique dark solitons in supersonic flow of a Bose–Einstein condensate. *Phys. Rev. Lett.* **97**, 180405 (2006).
30. Malpuech, G., Glazov, M. M., Shelykh, I. A., Bigenwald, P. & Kavokin, K. V. Electronic control of the polarization of light emitted by polariton lasers. *Appl. Phys. Lett.* **88**, 111118 (2006).

Acknowledgements

We thank R. Houdré for the microcavity sample and P. Voisin for fruitful discussions. This work was supported by the Agence Nationale de la Recherche (contract ANR-11-BS10-001), the RTRA (contract Boseflow1D), IFRAF, the FP7 ITNs Clermont4 (235114) and Spin-Optronics (237252), and the FP7 IRSES ‘Polaphen’ (246912). A.B. is a member of the Institut Universitaire de France.

Author contributions

All authors contributed to all aspects of this work.

Additional information

Supplementary information is available in the online version of the paper. Reprints and permissions information is available online at www.nature.com/reprints. Correspondence and requests for materials should be addressed to A.B. or A.A.

Competing financial interests

The authors declare no competing financial interests.

List of Publications

- Tanese, D., D.D. Solnyshkov, A. Amo, L.Ferrier, E. Bernet-Rollande, E. Wertz, I. Sagnes, A. Lemaître, P. Senellart, G. Malpuech, J. Bloch, 2012. *Backscattering Suppression in Supersonic 1D Polariton Condensates*. Physical Review Letters 108 (3) (January): 036405
- Galbiati, M., L. Ferrier, D.D. Solnyshkov, D. Tanese, E. Wertz, A. Amo, M. Abbarchi, P. Senellart, A. Lemaître, E. Galopin, G. Malpuech, J. Bloch. 2012. *Polariton Condensation in Photonic Molecules*. Physical Review Letters 108 (12) (March): 126403.
- Hivet, R., H. Flayac, D. D. Solnyshkov, D. Tanese, T. Boulier, D. Andreoli, E. Giacobino, J. Bloch, A. Bramati, A.Amo. 2012. *Half-solitons in a Polariton Quantum Fluid Behave Like Magnetic Monopoles*. Nature Physics 8 (10) (August 26): 724-728.
- Tanese, D., H. Flayac, D. Solnyshkov, A. Amo, A. Lemaître, E. Galopin, R. Braive, P. Senellart, I. Sagnes, G. Malpuech, J. Bloch. 2013. *Polariton Condensation in Solitonic Gap States in a One-dimensional Periodic Potential*. Nature Communications 4 (January): 1749.
- Sturm, C., Tanese, D., H. S. Nguyen, H. Flayac, A. Amo, E. Galopin, A. Lemaître, I. Sagnes, D. D. Solnyshkov, A. Amo, G. Malpuech, J. Bloch. 2013. *All optical phase modulation in a cavity-polariton Mach-Zehnder interferometer*, under second review of Nature Communications)
- Nguyen, H.S., D. Vishnevsky, C. Sturm, D. Tanese, D. Solnyshkov, E. Galopin, A. Lemaître, I. Sagnes, A. Amo, G. Malpuech, and J. Bloch. 2013. *Realization of a double-barrier resonant tunneling diode for cavity polaritons* Physical Review Letters 110(23): 236601.
- Tanese, D., E. Gurevich, A. Lemaître, E. Galopin, I. Sagnes, A. Amo, J. Bloch, E. Akkerman 2013. *Fractal energy spectrum of a polariton gas in a Fibonacci quasi-periodic potential*. submitted to Physical Review Letters

Bibliography

- [1] E. Purcell, H. Torrey, and R. Pound. Resonance absorption by nuclear magnetic moments in a solid. *Physical Review*, 69(1-2):37–38, January 1946.
- [2] A. Dousse, L. Lanco, J. Suffczynski, E. Semenova, A. Miard, A. Lemaitre, I. Sagnes, C. Roblin, J. Bloch, and P. Senellart. Controlled Light Matter Coupling for a Single Quantum Dot Embedded in a Pillar Microcavity Using Far Field Optical Lithography. *Physical Review Letters*, 101(26):267404, December 2008.
- [3] O. Gazzano, S. Michaelis de Vasconcellos, C. Arnold, A. Nowak, E. Galopin, I. Sagnes, L. Lanco, A. Lemaitre, and P. Senellart. Bright solid-state sources of indistinguishable single photons. *Nature communications*, 4:1425, January 2013.
- [4] B. Lounis and M. Orrit. Single-photon sources. *Reports on Progress in Physics*, 68(5):1129–1179, May 2005.
- [5] Y. Kaluzny, P. Goy, M. Gross, J. Raimond, and S. Haroche. Observation of self induced rabi oscillations in two level atoms excited inside a resonant cavity: The ringing regime of superradiance. *Physical Review Letters*, 51(13):1175–1178, September 1983.
- [6] M. Raizen, R. Thompson, R. Brecha, H. Kimble, and H. Carmichael. Normal mode splitting and linewidth averaging for two state atoms in an optical cavity. *Physical Review Letters*, 63(3):240–243, July 1989.
- [7] C. Weisbuch, M. Nishioka, A. Ishikawa, and Y. Arakawa. Observation of the coupled exciton-photon mode splitting in a semiconductor quantum microcavity. *Physical Review Letters*, 69(23):3314–3317, December 1992.
- [8] M. Saba, C. Ciuti, J. Bloch, V. Thierry-Mieg, R. André, le S. Dang, S. Kundermann, A. Mura, G. Bongiovanni, J. L. Staehli, and B. Deveaud. High-temperature ultrafast polariton parametric amplification in semiconductor microcavities. *Nature*, 414(6865):731–5, December 2001.
- [9] P. Savvidis, J. Baumberg, R. Stevenson, M. Skolnick, D. Whittaker, and J. Roberts. Angle-resonant stimulated polariton amplifier. *Physical Review Letters*, 84(7):1547–1550, February 2000.
- [10] R.M. Stevenson, V.N. Astratov, M.S. Skolnick, D.M. Whittaker, M. Emam-Ismael, A.I. Tartakovskii, P.G. Savvidis, J.J. Baumberg, and J.S. Roberts. Continuous wave

- observation of massive polariton redistribution by stimulated scattering in semiconductor microcavities. *Physical review letters*, 85(17):3680–3, October 2000.
- [11] A Imamoglu, R.J. Ram, S. Pau, and Y. Yamamoto. Nonequilibrium condensates and lasers without inversion: Exciton-polariton lasers. *Physical review. A*, 53(6):4250–4253, June 1996.
- [12] J. Kasprzak, M. Richard, S. Kundermann, A. Baas, P. Jeambrun, J.M.J. Keeling, F.M. Marchetti, M .H. Szymanska, R. André, J.L. Staehli, V. Savona, P.B. Littlewood, L. Dang, and B. Deveaud. Bose-Einstein condensation of exciton polaritons. *Nature*, 443(7110):409–14, September 2006.
- [13] H. Deng, G. Solomon, R. Hey, K. Ploog, and Y. Yamamoto. Spatial coherence of a polariton condensate. *Physical Review Letters*, 99(12):126403, September 2007.
- [14] R. Balili, V. Hartwell, D. Snoke, L. Pfeiffer, and K. West. Bose Einstein condensation of microcavity polaritons in a trap. *Science*, 316(5827):1007–10, May 2007.
- [15] D. Bajoni, P. Senellart, E. Wertz, I. Sagnes, A. Miard, A. Lemaître, and J. Bloch. Polariton laser using single micropillar GaAs-GaAlAs semiconductor cavities. *Physical Review Letters*, 100(4):047401, January 2008.
- [16] S. Christopoulos, G. von Hagersthal, A. Grundy, P. Lagoudakis, A. Kavokin, J. Baumberg, G. Christmann, Butte, E. Feltin, J.-F. Carlin, and N. Grandjean. Room-temperature polariton lasing in semiconductor microcavities. *Physical Review Letters*, 98(12):126405, March 2007.
- [17] F. Li, L. Orosz, O. Kamoun, S. Bouchoule, C. Brimont, P. Disseix, T. Guillet, X. Lafosse, M. Leroux, J. Leymarie, M. Mexis, M. Mihailovic, G. Patriarche, F. Réveret, D. Solnyshkov, J. Zuniga-Perez, and G. Malpuech. From Excitonic to Photonic Polariton Condensate in a ZnO-Based Microcavity. *Physical Review Letters*, 110(19):196406, May 2013.
- [18] I. Carusotto and C. Ciuti. Quantum fluids of light. *Reviews of Modern Physics*, 85(1):299–366, February 2013.
- [19] Al. Amo, J. Lefrère, S. Pigeon, C. Adrados, C. Ciuti, I. Carusotto, R. Houdré, E. Giacobino, and A. Bramati. Superfluidity of polaritons in semiconductor microcavities. *Nature Physics*, 5(11):805–810, September 2009.
- [20] R. Hivet, H. Flayac, D. D. Solnyshkov, D. Tanese, T. Boulier, D. Andreoli, E. Giacobino, J. Bloch, A. Bramati, G. Malpuech, and A. Amo. Half-solitons in a polariton quantum fluid behave like magnetic monopoles. *Nature Physics*, 8(10):724–728, August 2012.
- [21] A. Amo, S. Pigeon, D. Sanvitto, V .G. Sala, R. Hivet, I. Carusotto, F. Pisanello, G. Leménager, R. Houdré, E. Giacobino, C. Ciuti, and A. Bramati. Polariton superfluids reveal quantum hydrodynamic solitons. *Science*, 332(6034):1167–70, June 2011.

- [22] M. Sich, D.N. Krizhanovskii, M.S. Skolnick, A.V. Gorbach, R. Hartley, D.V. Skryabin, E.A. Cerda-Méndez, K. Biermann, R. Hey, and P.V. Santos. Observation of bright polariton solitons in a semiconductor microcavity. *Nature Photonics*, 6(1):50–55, November 2011.
- [23] K.G. Lagoudakis, T. Ostatnický, A.V. Kavokin, Y.G. Rubo, R. André, and B. Deveaud-Plédran. Observation of half-quantum vortices in an exciton-polariton condensate. *Science*, 326(5955):974–6, November 2009.
- [24] K.G. Lagoudakis, M. Wouters, M. Richard, A. Baas, I. Carusotto, R. André, Le Si Dang, and B. Deveaud-Plédran. Quantized vortices in an exciton polariton condensate. *Nature Physics*, 4(9):706–710, August 2008.
- [25] M. Wouters and I. Carusotto. Superfluidity and critical velocities in nonequilibrium Bose-Einstein condensates. *Physical Review Letters*, 105(2):020602, July 2010.
- [26] M. Romanelli, C. Leyder, J. Karr, E. Giacobino, and A. Bramati. Four Wave Mixing Oscillation in a Semiconductor Microcavity: Generation of Two Correlated Polariton Populations. *Physical Review Letters*, 98(10):106401, March 2007.
- [27] T.K. Paraïso, M. Wouters, Y. Léger, F. Morier-Genoud, and B. Deveaud-Plédran. Multistability of a coherent spin ensemble in a semiconductor microcavity. *Nature materials*, 9(8):655–60, August 2010.
- [28] A. Amo, T. C. H. Liew, C. Adrados, R. Houdré, E. Giacobino, A.V. Kavokin, and A. Bramati. Exciton polariton spin switches. *Nature Photonics*, 4(6):361–366, April 2010.
- [29] D. Ballarini, M. De Giorgi, E. Cancellieri, R. Houdré, E. Giacobino, R. Cingolani, and A. Bramati. Alloptical polariton transistor. *Nature communications*, 4(1778), 2013.
- [30] T. Gao, P.S. Eldridge, T.C.H. Liew, S.I. Tsintzos, G. Stavriniadis, G. Deligeorgis, Z. Hatzopoulos, and P.G. Savvidis. Polariton condensate transistor switch. *Physical Review B*, 85(23):235102, June 2012.
- [31] H.S. Nguyen, D. Vishnevsky, C. Sturm, D. Tanese, D. Solnyshkov, E. Galopin, A. Lemaître, I. Sagnes, A. Amo, G. Malpuech, and J. Bloch. Realization of a double-barrier resonant tunneling diode for cavity polaritons. *Physical Review Letters*, 110(23):236601, June 2013.
- [32] H. Flayac, D.D. Solnyshkov, and G. Malpuech. Bloch oscillations of exciton polaritons and photons for the generation of an alternating terahertz spin signal. *Physical Review B*, 84(12):125314, September 2011.
- [33] Hugo Flayac and Ivan G Savenko. An all-optical spin selective quantum router with frequency elevation. *Arxiv: 1307.6552*, (d):5, July 2013.
- [34] T. Liew, A. Kavokin, and I. Shelykh. Optical circuits based on polariton neurons in semiconductor microcavities. *Physical Review Letters*, 101(1):016402, July 2008.

- [35] T. Espinosa-Ortega and T. C. H. Liew. Complete architecture of integrated photonic circuits based on and and not logic gates of exciton polaritons in semiconductor microcavities. *Physical Review B*, 87(19):195305, May 2013.
- [36] L. Ferrier, E. Wertz, R. Johne, D.D Solnyshkov, P. Senellart, I. Sagnes, A. Lemaître, G. Malpuech, and J. Bloch. Interactions in confined polariton condensates. *Physical review letters*, 106(12):126401, March 2011.
- [37] M. Abbarchi, A. Amo, V.G. Sala, D.D. Solnyshkov, H. Flayac, L. Ferrier, I. Sagnes, E. Galopin, A. Lemaître, G. Malpuech, and J. Bloch. Macroscopic quantum self-trapping and Josephson oscillations of exciton polaritons. *Nature Physics*, 9(5):275–279, April 2013.
- [38] E. Wertz, L. Ferrier, D.D. Solnyshkov, P. Senellart, D. Bajoni, A. Miard, A. Lemaître, G. Malpuech, and J. Bloch. Spontaneous formation of a polariton condensate in a planar GaAs microcavity. *Applied Physics Letters*, 95(5):051108, 2009.
- [39] E. Wertz, L. Ferrier, D.D. Solnyshkov, R. Johne, D. Sanvitto, A. Lemaître, I. Sagnes, R. Grousson, A.V. Kavokin, P. Senellart, G. Malpuech, and J. Bloch. Spontaneous formation and optical manipulation of extended polariton condensates. *Nature Physics*, 6(11):860–864, August 2010.
- [40] N.D. Mermin and N.W. Ashcroft. *Solid State Physics*. 1976.
- [41] F. Bloch. Über die quantenmechanik der elektronen in kristallgittern. *Zeitschrift für Physik*, 52(7-8):555–600, July 1929.
- [42] J. Frenkel. On the Transformation of light into Heat in Solids. I. *Physical Review*, 37(1):17–44, January 1931.
- [43] G. Wannier. The Structure of Electronic Excitation Levels in Insulating Crystals. *Physical Review*, 52(3):191–197, August 1937.
- [44] V. Savona, C. Piermarocchi, A. Quattropani, P. Schwendimann, and F. Tassone. Optical properties of microcavity polaritons. *Phase Transitions*, 68(1):169–279, February 1999.
- [45] J.H. Davies. *The physics of low dimensional semiconductors: an introduction*. Cambridge express, 1998.
- [46] G. Rochat, C. Ciuti, V. Savona, C. Piermarocchi, a. Quattropani, and P. Schwendimann. Excitonic Bloch equations for a two-dimensional system of interacting excitons. *Physical Review B*, 61(20):13856–13862, May 2000.
- [47] S. Schmitt-Rink, D. Chemla, and D. Miller. Theory of transient excitonic optical nonlinearities in semiconductor quantum-well structures. *Physical Review B*, 32(10):6601–6609, November 1985.
- [48] R. Houdre, J. Gibernon, P. Pellandini, R. Stanley, U. Oesterle, C. Weisbuch, J. O’Gorman, B. Roycroft, and M. Ilegems. Saturation of the strong coupling regime in a semiconductor microcavity: Free carrier bleaching of cavity polaritons. *Physical Review B*, 52(11):7810–7813, September 1995.

- [49] R. Butte, G. Delalleau, A. Tartakovskii, M. Skolnick, V. Astratov, J. Baumberg, G. Malpuech, A. Di Carlo, A. Kavokin, and J. Roberts. Transition from strong to weak coupling and the onset of lasing in semiconductor microcavities. *Physical Review B*, 65(20):205310, April 2002.
- [50] G. Bastard. *Wave mechanics applied to semiconductor heterostructures*. Les Éditions de Physique, 1988.
- [51] L.C. Andreani. Optical transitions, excitons, and polaritons in bulk and low-dimensional semiconductor structures. In *Confined Electrons and Photons*, pages 57–112. 1995.
- [52] E. Wertz. *Formation spontanée de condensats de polaritons dans des microcavités à base de GaAs*. PhD thesis, Univ. Paris Sud, 2010.
- [53] M. Perrin. *Relaxation de polaritons dans une microcavité contenant un gaz d'électrons*. PhD thesis, Univ. Paris VI, 2006.
- [54] A. Kavokin, J.J. Baumberg, G. Malpuech, and F.P. Laussy. *Microcavities*. Oxford University Press, journal un edition, 2007.
- [55] Jacques Dupont-Roc et Gilbert Grynberg Claude Cohen-Tannoudji. *Processus d'interaction entre photons et atomes*. Savoirs ac edition, 1988.
- [56] Y. Yamamoto, F. Tassone, and H. Cao. *Semiconductor Cavity Quantum Electrodynamics*. Springer Tracts in Modern Physics, 2000.
- [57] J.M. Gérard and B. Gayral. InAs quantum dots: artificial atoms for solid state cavity quantum electrodynamics. *Physica E: Low dimensional Systems and Nanostructures*, 9(1):131–139, January 2001.
- [58] P. Goy, J. Raimond, M. Gross, and S. Haroche. Observation of cavity-enhanced single-atom spontaneous emission. *Physical Review Letters*, 50(24):1903–1906, June 1983.
- [59] J. Hopfield. Theory of the contribution of excitons to the complex dielectric constant of crystals. *Physical Review*, 112(5):1555–1567, December 1958.
- [60] D. Sell, R. Dingle, S. Stokowski, and J. DiLorenzo. Observation of polaritons in GaAs: A new interpretation of the free-exciton reflectance and luminescence. *Physical Review Letters*, 27(24):1644–1647, December 1971.
- [61] C. Guillaume, A. Bonnot, and J. Debever. Luminescence from polaritons. *Physical Review Letters*, 24(22):1235–1238, June 1970.
- [62] C. Weisbuch and R. Ulbrich. Resonant polariton fluorescence in Gallium Arsenide. *Physical Review Letters*, 39(10):654–656, September 1977.
- [63] R.G. Ulbrich and C. Weisbuch. Resonant brillouin scattering of excitonic polaritons in Gallium Arsenide. *Physical Review Letters*, 38(15):865–868, April 1977.

- [64] B. Sermage and G. Fishman. Resonant brillouin scattering of polaritons in ZnSe: heavy and light excitons. *Physical Review Letters*, 43(14):1043–1046, October 1979.
- [65] E.T. Jaynes and F.W. Cummings. Comparison of quantum and semiclassical radiation theories with application to the beam maser. *Proceedings of the IEEE*, 51(1):89–109, 1963.
- [66] B. Sermage, S. Long, I. Abram, and J. Y. Marzin. Time-resolved spontaneous emission of excitons in a microcavity: Behavior of the individual exciton-photon mixed states. *Physical Review B*, 53(24):16516–16523, June 1996.
- [67] B Sermage, S Long, H Eskinazi, M Stellmacher, J.Y. Marzin, J Bloch, V. Thierry-Mieg, and R Planel. Exciton dynamics in quantum-well microcavities. *Superlattices and Microstructures*, 22(3):375–381, October 1997.
- [68] J. Kasprzak. *Condensation of exciton polaritons*. PhD thesis, Univ. Joseph Fourier-Grenoble, 2006.
- [69] I. Shelykh, G. Malpuech, K. Kavokin, A. Kavokin, and P. Bigenwald. Spin dynamics of interacting exciton polaritons in microcavities. *Physical Review B*, 70(11):115301, September 2004.
- [70] A. Kavokin, G. Malpuech, and M. Glazov. Optical spin Hall effect. *Physical Review Letters*, 95(13):136601, September 2005.
- [71] G Malpuech, Y. G. Rubo, F. P. Laussy, P. Bigenwald, and A. V. Kavokin. Polariton laser: thermodynamics and quantum kinetic theory. *Semiconductor Science and Technology*, 18(10):S395–S404, October 2003.
- [72] D. Porras, C. Ciuti, J. Baumberg, and C. Tejedor. Polariton dynamics and Bose-Einstein condensation in semiconductor microcavities. *Physical Review B*, 66(8):085304, August 2002.
- [73] F. Tassone, C Piermarocchi, and V Savona. Bottleneck effects in the relaxation and photoluminescence of microcavity polaritons. *Physical Review B*, 56(12):7554–7563, 1997.
- [74] A. Tartakovskii, M. Emam-Ismail, R. Stevenson, M. Skolnick, V. Astratov, D. Whittaker, J. Baumberg, and J. Roberts. Relaxation bottleneck and its suppression in semiconductor microcavities. *Physical Review B*, 62(4):R2283–R2286, July 2000.
- [75] D. Bajoni, M. Perrin, P. Senellart, A. Lemaître, B. Sermage, and J. Bloch. Dynamics of microcavity polaritons in the presence of an electron gas. *Physical Review B*, 73(20):205344, May 2006.
- [76] M. Perrin, P. Senellart, A. Lemaître, and J. Bloch. Polariton relaxation in semiconductor microcavities: Efficiency of electron-polariton scattering. *Physical Review B*, 72(7):075340, August 2005.
- [77] R. P. Stanley, S. Pau, U. Oesterle, R. Houdré, and M. Illegems. Resonant photoluminescence of semiconductor microcavities: The role of acoustic phonons in polariton relaxation. *Physical Review B*, 55(8):R4867–R4870, February 1997.

- [78] P. Senellart, J. Bloch, B. Sermage, and J. Marzin. Microcavity polariton depopulation as evidence for stimulated scattering. *Physical Review B*, 62(24):R16263–R16266, December 2000.
- [79] Le Dang, D. Heger, R. Andre, F. Boeuf, and R. Romestain. Stimulation of Polariton Photoluminescence in Semiconductor Microcavity. *Physical Review Letters*, 81(18):3920–3923, November 1998.
- [80] G. Christmann, R. Butte, E. Feltn, J. Carlin, and N. Grandjean. Room temperature polariton lasing in a GaN/AlGaIn multiple quantum well microcavity. *Applied Physics Letters*, 93(5):051102, 2008.
- [81] H. Deng, G. Weihs, C. Santori, J. Bloch, and Y. Yamamoto. Condensation of semiconductor microcavity exciton polaritons. *Science*, 298(5591):199–202, October 2002.
- [82] M. Galbiati, L. Ferrier, D.D. Solnyshkov, D. Tanese, E. Wertz, A. Amo, M. Abbarchi, P. Senellart, I. Sagnes, A. Lemaître, E. Galopin, G. Malpuech, and J. Bloch. Polariton condensation in photonic molecules. *Physical Review Letters*, 108(12):126403, March 2012.
- [83] E. Wertz, A. Amo, D.D. Solnyshkov, L. Ferrier, T.C.H. Liew, D. Sanvitto, P. Senellart, I. Sagnes, A. Lemaître, A.V. Kavokin, G. Malpuech, and J. Bloch. Propagation and amplification dynamics of 1D polariton condensates. *Physical Review Letters*, 109(21):216404, November 2012.
- [84] C. Ciuti. Theory of polariton parametric interactions in semiconductor microcavities. *Semiconductor Science and Technology*, 279, 2003.
- [85] C. Ciuti, V. Savona, C. Piermarocchi, A. Quattropani, and P. Schwendimann. Role of the exchange of carriers in elastic exciton-exciton scattering in quantum wells. *Physical Review B*, 58(12):7926–7933, September 1998.
- [86] M. Vladimirova, S. Cronenberger, D. Scalbert, K.V. Kavokin, A. Miard, A. Lemaître, J. Bloch, D. Solnyshkov, G. Malpuech, and A.V. Kavokin. Polariton-polariton interaction constants in microcavities. *Physical Review B*, 82(7):075301, August 2010.
- [87] M.M. Glazov, H. Ouerdane, and L. Piloizzi. Polariton-polariton scattering in microcavities: A microscopic theory. *Physical Review B*, pages 1–14, 2009.
- [88] D. Sarkar, S.S. Gavrilov, M. Sich, J.H. Quilter, R.A. Bradley, N.A. Gippius, K. Guda, V.D. Kulakovskii, M.S. Skolnick, and D.N. Krizhanovskii. Polarization bistability and resultant spin rings in semiconductor microcavities. *Physical Review Letters*, 105(21):216402, November 2010.
- [89] C. Adrados, A. Amo, T.C.H. Liew, R. Hivet, R. Houdré, E. Giacobino, A.V. Kavokin, and A. Bramati. Spin rings in bistable planar semiconductor microcavities. *Physical Review Letters*, 105(21):216403, November 2010.
- [90] E.P. Gross. Structure of a quantized vortex in boson systems. *Il Nuovo Cimento*, 20(3), 1961.

- [91] L.P. Pitaevskii. The problem of the form of the spectrum of elementary excitation in liquid Helium II. *Soviet Physics JETP-USSR*, 13(2), 1961.
- [92] L. Pitaevskii and S. Stringari. *Bose-Einstein Condensation*. Press, Oxford University, 2003.
- [93] C. Sun, S. Jia, C. Barsi, S. Rica, A. Picozzi, and J.W. Fleischer. Observation of the kinetic condensation of classical waves. *Nature Physics*, 8(6):471–475, April 2012.
- [94] M. Wouters and I. Carusotto. Excitations in a nonequilibrium Bose-Einstein condensate of exciton polaritons. *Physical Review Letters*, 99(14):140402, October 2007.
- [95] M. Cross and P. Hohenberg. Pattern formation outside of equilibrium. *Reviews of Modern Physics*, 65(3):851–1112, July 1993.
- [96] G. Grosso, G. Nardin, F. Morier-Genoud, Y. Léger, and B. Deveaud-Plédran. Soliton instabilities and vortex street formation in a polariton quantum fluid. *Physical Review Letters*, 107(24):245301, December 2011.
- [97] D. Sanvitto, S. Pigeon, A. Amo, D. Ballarini, M. De Giorgi, I. Carusotto, R. Hivet, F. Pisanello, V.G. Sala, P.S.S. Guimaraes, R. Houdré, E. Giacobino, C. Ciuti, A. Bramati, and G. Gigli. All-optical control of the quantum flow of a polariton condensate. *Nature Photonics*, 5(10):610–614, September 2011.
- [98] S. Pau, G. Björk, and J. Jacobson. Microcavity exciton-polariton splitting in the linear regime. *Physical Review B*, 51(20), 1995.
- [99] T. Lecomte. *Microcavités semiconductrices structurées pour la génération paramétrique optique*. PhD thesis, Univ. Paris VI, 2011.
- [100] V.G. Sala. *PhD Thesis*. PhD thesis, Univ. Paris VI, 2013.
- [101] G. Panzarini, L.C. Andreani, and A. Armitage. Exciton-light coupling in single and coupled semiconductor microcavities: Polariton dispersion and polarization splitting. *Physical Review B*, 59(7):5082–5089, 1999.
- [102] C. Diederichs. *Oscillation paramétrique optique et génération de photons jumeaux dans des microcavités de semiconducteurs*. PhD thesis, Univ. Paris VI, 2007.
- [103] V. Ardizzone. *Diffusion paramétrique dans les microcavités de semiconducteurs*. PhD thesis, Univ. Paris VI, 2013.
- [104] A. Kuther, M. Bayer, T. Gutbrod, A. Forchel, P. Knipp, T. Reinecke, and R. Werner. Confined optical modes in photonic wires. *Physical Review B*, 58(23):15744–15748, December 1998.
- [105] G. Dasbach, A. Dremin, M. Bayer, V. Kulakovskii, N. Gippius, and A. Forchel. Oscillations in the differential transmission of a semiconductor microcavity with reduced symmetry. *Physical Review B*, 65(24):245316, June 2002.

- [106] R. Balili, B. Nelsen, D.W. Snoke, R.H. Reid, L. Pfeiffer, and K. West. Huge splitting of polariton states in microcavities under stress. *Physical Review B*, 81(12):125311, March 2010.
- [107] M. Saba, C. Ciuti, J. Bloch, and V. Thierry-Mieg. High-temperature ultrafast polariton parametric amplification in semiconductor microcavities. *Nature*, pages 731–735, 2001.
- [108] T. Freixanet, B. Sermage, a. Tiberj, and R. Planel. In-plane propagation of excitonic cavity polaritons. *Physical Review B*, 61(11):7233–7236, March 2000.
- [109] E. Kammann, T.C.H. Liew, H. Ohadi, P. Cilibrizzi, P. Tsotsis, Z. Hatzopoulos, P.G. Savvidis, A.V. Kavokin, and P.G. Lagoudakis. Nonlinear optical spin Hall Effect and long-range spin transport in polariton lasers. *Physical Review Letters*, 109(3):036404, July 2012.
- [110] D. Tanese, H. Flayac, D. Solnyshkov, A. Amo, A. Lemaître, E. Galopin, R. Braive, P. Senellart, I. Sagnes, G. Malpuech, and J. Bloch. Polariton condensation in solitonic gap states in a one-dimensional periodic potential. *Nature communications*, 4:1749, January 2013.
- [111] G. Tosi, G. Christmann, N.G. Berloff, P. Tsotsis, T. Gao, Z. Hatzopoulos, P.G. Savvidis, and J.J. Baumberg. Sculpting oscillators with light within a nonlinear quantum fluid. *Nature Physics*, 8(3):190–194, 2012.
- [112] D. Snoke. Long distance propagation of long lifetime polaritons in microcavities. In *6th International conference of spontaneous coherence in excitonic systems*, 2012.
- [113] T. Guillet. Strongly excitonic polariton condensates in a ZnO microcavity. In *14th International conference on light matter coupling in nanostructures*, 2013.
- [114] W. Langbein, I. Shelykh, D. Solnyshkov, G. Malpuech, Yu. Rubo, and a. Kavokin. Polarization beats in ballistic propagation of exciton-polaritons in microcavities. *Physical Review B*, 75(7):075323, February 2007.
- [115] A. Amo, D. Sanvitto, F.P. Laussy, D. Ballarini, E. del Valle, M.D. Martin, A. Lemaître, J. Bloch, D.N. Krizhanovskii, M.S. Skolnick, C. Tejedor, and L. Viña. Collective fluid dynamics of a polariton condensate in a semiconductor microcavity. *Nature*, 457(7227):291–5, January 2009.
- [116] D. Whittaker. Classical treatment of parametric processes in a strong-coupling planar microcavity. *Physical Review B*, 63(19):193305, April 2001.
- [117] C. Diederichs, J. Tignon, G. Dasbach, C. Ciuti, A. Lemaître, J. Bloch, Ph. Roussignol, and C. Delalande. Parametric oscillation in vertical triple microcavities. *Nature*, 440(7086):904–7, April 2006.
- [118] J. Baumberg, P. Savvidis, R. Stevenson, a. Tartakovskii, M. Skolnick, D. Whittaker, and J. Roberts. Parametric oscillation in a vertical microcavity: A polariton condensate or

- micro-optical parametric oscillation. *Physical Review B*, 62(24):R16247–R16250, December 2000.
- [119] A. Amo. *Dynamics of excitons, polaritons and collective excitations in semiconductors and semiconductor microcavities*. PhD thesis, Univ. Autonoma de Madrid, 2008.
 - [120] M. Wouters, I. Carusotto, and C. Ciuti. Spatial and spectral shape of inhomogeneous nonequilibrium exciton-polariton condensates. *Physical Review B*, 77(11):115340, March 2008.
 - [121] M. Portella-Oberli, V. Ciulin, S. Haacke, J.-D. Ganière, P. Kossacki, M. Kutrowski, T. Wojtowicz, and B. Deveaud. Diffusion, localization, and dephasing of trions and excitons in CdTe quantum wells. *Physical Review B*, 66(15):155305, October 2002.
 - [122] W. Langbein, E. Runge, V. Savona, and R. Zimmermann. Enhanced resonant backscattering of excitons in disordered quantum wells. *Physical Review Letters*, 89(15):157401, September 2002.
 - [123] J.M. Zajac and W. Langbein. Structure and zero-dimensional polariton spectrum of natural defects in GaAs/AlAs microcavities. *Physical Review B*, 86(19):195401, November 2012.
 - [124] J.M. Zajac, W. Langbein, M. Hugues, and M. Hopkinson. Polariton states bound to defects in GaAs/AlAs planar microcavities. *Physical Review B*, 85(16):165309, April 2012.
 - [125] J.M. Zajac, E. Clarke, and W. Langbein. Suppression of cross-hatched polariton disorder in GaAs/AlAs microcavities by strain compensation. *Applied Physics Letters*, 041114:1–5, 2012.
 - [126] M. Wouters, T. C. H. Liew, and V. Savona. Energy relaxation in one-dimensional polariton condensates. *Physical Review B*, 82(24):245315, December 2010.
 - [127] J.F. Allen and A.D. Misener. Flow of liquid helium II. *Nature*, 141:75–75, 1938.
 - [128] P. Kapitza. Viscosity of liquid helium below the l-point. *Nature*, 141:74, 1938.
 - [129] A.J. Leggett. Superfluidity. *Reviews of Modern Physics*, 71(2):318–323, 1999.
 - [130] I. Carusotto and C. Ciuti. Probing microcavity polariton superfluidity through resonant rayleigh scattering. *Physical Review Letters*, 93(16):166401, October 2004.
 - [131] L. Landau. Theory of the Superfluidity of Helium II. *Physical Review*, 60(4):356–358, August 1941.
 - [132] L.D. Landau and E.M. Lifshitz. *Statistical Physics I*. 1980.
 - [133] I.L. Aleiner, B.L. Altshuler, and G.V. Shlyapnikov. A finite-temperature phase transition for disordered weakly interacting bosons in one dimension. *Nature Physics*, 6(11):900–904, September 2010.

- [134] T. Paul, P. Schlagheck, P. Leboeuf, and N. Pavloff. Superfluidity versus Anderson localization in a dilute Bose Gas. *Physical Review Letters*, 98(21):210602, May 2007.
- [135] A. Lagendijk, B. van Tiggelen, and D. Wiersma. Notes on Anderson localization. *Physics Today*, 65(5):3–5, 2012.
- [136] J. Billy, V. Josse, Z. Zuo, A. Bernard, B. Hambrecht, P. Lugan, D. Clément, L. Sanchez-Palencia, Ph. Bouyer, and A. Aspect. Direct observation of Anderson localization of matter waves in a controlled disorder. *Nature*, 453(7197):891–4, June 2008.
- [137] G. Roati, C. D’Errico, L. Fallani, M. Fattori, C. Fort, M. Zaccanti, G. Modugno, M. Modugno, and M. Inguscio. Anderson localization of a non-interacting Bose-Einstein condensate. *Nature*, 453(7197):895–8, July 2008.
- [138] B. Deissler, M. Zaccanti, G. Roati, C.D. Errico, M. Fattori, M. Modugno, G. Modugno, and M. Inguscio. Delocalization of a disordered bosonic system by repulsive interactions. *Nature Physics*, 6(5):354–358, 2010.
- [139] D. Tanese, D.D. Solnyshkov, A. Amo, L. Ferrier, E. Bernet-Rollande, E. Wertz, I. Sagnes, A. Lemaître, P. Senellart, G. Malpuech, and J. Bloch. Backscattering suppression in supersonic 1D polariton condensates. *Physical Review Letters*, 108(3):036405, January 2012.
- [140] J. Dalibard. *Atomes et rayonnement, cours au Collège de France*. 2013.
- [141] R. de L. Kronig and W.G. Penney. Quantum mechanics of electrons in crystal lattices. *Proceedings of the Royal Society of London*.
- [142] D.A. Mcquarrie. The Kronig-Penney Model. *The Chemical Educator*, 1(1):1–10, 1996.
- [143] M. Ben Dahan. *Transport et relaxation d’atomes de Césium: oscillations de Bloch et résonance de diffusion*. PhD thesis, Univ. Paris VI, 1997.
- [144] C. Kittel. *Introduction to Solid State Physics*. 1996.
- [145] G. Wannier. The structure of electronic excitation levels in insulating crystals. *Physical Review*, 52(3):191–197, August 1937.
- [146] A. Davydov. *Quantum Mechanics*. Pergamon Press, Oxford, 1976.
- [147] F. Abdullaev, A. Abdumalikov, and R. Galimzyanov. Gap solitons in Bose Einstein condensates in linear and nonlinear optical lattices. *Physics Letters A*, 367(1-2):149–155, July 2007.
- [148] D. Mandelik, R. Morandotti, J. Aitchison, and Y. Silberberg. Gap Solitons in Waveguide Arrays. *Physical Review Letters*, 92(9):093904, March 2004.
- [149] I. Spielman, W. Phillips, and J. Porto. Mott-Insulator Transition in a Two-Dimensional Atomic Bose Gas. *Physical Review Letters*, 98(8):080404, February 2007.

- [150] Immanuel Bloch and Wilhelm Zwerger. Many-body physics with ultracold gases. *Reviews of Modern Physics*, 80(3):885–964, July 2008.
- [151] J. Struck, M. Weinberg, C. Olschlager, P. Windpassinger, J. Simonet, K. Sengstock, R. Hoppner, P. Hauke, A. Eckardt, M. Lewenstein, and L. Mathey. Engineering Ising-XY spin-models in a triangular lattice using tunable artificial gauge fields. *Nature Physics*, September 2013.
- [152] H.M. Nguyen, M.A. Dundar, R.W. van der Heijden, E.W.J.M. van der Drift, H.W.M. Salemink, S. Rogge, and J. Caro. Compact Mach-Zehnder interferometer based on self-collimation of light in a silicon photonic crystal. *Optics express*, 18(7):6437–46, March 2010.
- [153] Al. Figotin and I. Vitebskiy. Slow light in photonic crystals. *Waves in Random and Complex Media*, 16(3):293–382, August 2006.
- [154] T. Yamamoto and M. Notomi. Design of a high-Q air-slot cavity based on a width-modulated line-defect in a photonic crystal slab. *Optics express*, 16(18):13809–13817, 2008.
- [155] C. Monat, M. de Sterke, and B.J. Eggleton. Slow light enhanced nonlinear optics in periodic structures. *Journal of Optics*, 12(10):104003, October 2010.
- [156] A. Jones. Coupling of optical fibers and scattering in fibers. *Journal of the Optical Society of America*, 55(3):261, March 1965.
- [157] S. Somekh, E. Garmire, A. Yariv, H.L. Garvin, and R.G. Hunsperge. Channel optical waveguides and directional couplers in GaAs imbedded and ridged. *Applied Optics*, 13(2), 1974.
- [158] D.N. Christodoulides, F. Lederer, and Y. Silberberg. Discretizing light behaviour in linear and nonlinear waveguide lattices. *Nature*, 424(6950):817–23, August 2003.
- [159] S. Ogawa, M. Imada, S. Yoshimoto, M. Okano, and S. Noda. Control of light emission by 3D photonic crystals. *Science*, 305(5681):227–9, July 2004.
- [160] B. K. Smith S. Y. Lin, J. G. Fleming, D. L. Hetherington, W. Zubrzycki R. Biswas, K. M. Ho, M. M. Sigalas, S. R. Kurtz et Bur, and Jim. A three-dimensional photonic crystal operating at infrared wavelengths. *Nature*, 394:251–253, 1998.
- [161] C. Grillet, C. Monat, C.L. Smith, M.W. Lee, S. Tomljenovic-Hanic, C. Karnutsch, and B.J. Eggleton. Reconfigurable photonic crystal circuits. *Laser & Photonics Reviews*, 4(2):192–204, February 2010.
- [162] M. Notomi. Manipulating light with strongly modulated photonic crystals. *Reports on Progress in Physics*, 73(9):096501, September 2010.
- [163] Y. Liu and X. Zhang. Metamaterials: a new frontier of science and technology. *Chemical Society reviews*, 40(5):2494–507, May 2011.

- [164] L. Esaki and R. Tsu. Superlattice and negative differential conductivity in semiconductors. *IBM Journal of Research and Development*, 1856, 1970.
- [165] C. Waschke, H.G. Roskos, R. Schwedler, K. Leo, H. Kurz, and K. Kohler. Coherent submillimeter wave emission from Bloch oscillations in a semiconductor superlattice. *Physical Review Letters*, 70(21):3319–3322, 1993.
- [166] T. Dekorsy, R. Ott, H. Kurz, and K. Köhler. Bloch oscillations at room temperature. *Physical Review B*, 51(23):17275–17278, June 1995.
- [167] C. Orzel, A.K. Tuchman, M.L. Fenselau, M. Yasuda, and M.A. Kasevich. Squeezed states in a Bose-Einstein condensate. *Science*, 291(5512):2386–9, March 2001.
- [168] S. Fölling, A. Widera, T. Müller, F. Gerbier, and I. Bloch. Formation of spatial shell structure in the superfluid to Mott insulator transition. *Physical Review Letters*, 97(6):060403, August 2006.
- [169] O. Morsch, J. Müller, M. Cristiani, D. Ciampini, and E. Arimondo. Bloch oscillations and Mean-Field effects of Bose-Einstein condensates in 1D optical lattices. *Physical Review Letters*, 87(14):140402, September 2001.
- [170] M. Cristiani, O. Morsch, J. Müller, D. Ciampini, and E. Arimondo. Experimental properties of Bose-Einstein condensates in one-dimensional optical lattices: Bloch oscillations, Landau-Zener tunneling, and mean-field effects. *Physical Review A*, 65(6):063612, June 2002.
- [171] P.G. Kevrekidis, D.J. Frantzeskakis, and R. Carretero-González, editors. *Emergent Nonlinear Phenomena in Bose-Einstein Condensates*, volume 45 of *Atomic, Optical, and Plasma Physics*. Springer Berlin Heidelberg, Berlin, Heidelberg, 2008.
- [172] Y.V. Kartashov, V.V. Konotop, V.A. Vysloukh, and L. Torner. Dissipative defect modes in periodic structures. *Optics Letters*, 32(10), 2010.
- [173] X. Li, Y. Jiang, and L. Xu. A historical narrative of study of fiber grating solitons. *Communications and Network*, 2(1), 2010.
- [174] K. Dossou, L. Botten, R. McPhedran, C. Poulton, a. Asatryan, and C. Martijn de Sterke. Shallow defect states in two-dimensional photonic crystals. *Physical Review A*, 77(6):063839, June 2008.
- [175] R. Sapienza. *Photonic nano materials: anisotropic transport and optical Bloch oscillations*. PhD thesis, Univ. Paris VI - Univ. di Firenze, 2002.
- [176] S. Tomljenovic-Hanic, M.J. Steel, C. Martijn de Sterke, and D.J. Moss. High-Q cavities in photosensitive photonic crystals. *Optics letters*, 32(5):542–4, March 2007.
- [177] M. Notomi and H. Taniyama. On-demand ultrahigh-Q cavity formation and photon pinning via dynamic waveguide tuning. *Optics express*, 16(23):18657–66, November 2008.

- [178] C. Grillet, C. Monat, C.L. Smith, M.W. Lee, S. Tomljenovic-Hanic, C. Karnutsch, and B.J. Eggleton. Reconfigurable photonic crystal circuits. *Laser & Photonics Reviews*, 4(2):192–204, February 2010.
- [179] E.A. Ostrovskaya, M.K. Oberthaler, and Y.S. Kivshar. Nonlinear Localization of BECs in Optical Lattices. In *Emergent Nonlinear Phenomena in Bose-Einstein Condensates*. Springer Berlin Heidelberg, 2008.
- [180] P. Louis, E. Ostrovskaya, C. Savage, and Y. Kivshar. Bose-Einstein condensates in optical lattices: Band-gap structure and solitons. *Physical Review A*, 67(1):013602, January 2003.
- [181] Th. Anker, M. Albiez, R. Gati, S. Hunsmann, B. Eiermann, A. Trombettoni, and M. Oberthaler. Nonlinear self-trapping of matter waves in periodic potentials. *Physical Review Letters*, 94(2):020403, January 2005.
- [182] J. Wang, J. Yang, T. Alexander, and Y. Kivshar. Truncated-Bloch-wave solitons in optical lattices. *Physical Review A*, 79(4):043610, April 2009.
- [183] Y.S. Kivshar. Self-localization in arrays of defocusing waveguides. *Optics letters*, 18(14):1147, July 1993.
- [184] F.H. Bennet, T.J. Alexander, F. Haslinger, A. Mitchell, D.N. Neshev, and Y.S. Kivshar. Observation of nonlinear self-trapping of broad beams in defocusing waveguide arrays. *Physical Review Letters*, 106(9):093901, February 2011.
- [185] J.E. Sipe. Gap Solitons. In *Guided Wave Nonlinear Optics*, pages 305–318. Springer Netherlands, 1992.
- [186] D.N. Christodoulides and R.I. Joseph. Discrete self-focusing in nonlinear arrays of coupled waveguides. *Optics letters*, 13(9):794–6, September 1988.
- [187] H. Eisenberg, Y. Silberberg, R. Morandotti, A. Boyd, and J. Aitchison. Discrete spatial optical solitons in waveguide arrays. *Physical Review Letters*, 81(16):3383–3386, October 1998.
- [188] J.W. Fleischer, T. Carmon, and M. Segev. Observation of discrete solitons in optically induced real time waveguide arrays. *Physical Review Letters*, pages 1–4, 2003.
- [189] J.W. Fleischer, M. Segev, N.K. Efremidis, and D.N. Christodoulides. Observation of two-dimensional discrete solitons in optically induced nonlinear photonic lattices. *Nature*, 422(6928):147–50, March 2003.
- [190] B. Eiermann, Th. Anker, M. Albiez, M. Taglieber, P. Treutlein, K.-P. Marzlin, and M. Oberthaler. Bright Bose-Einstein gap solitons of atoms with repulsive interaction. *Physical Review Letters*, 92(23):230401, June 2004.
- [191] B. Eiermann, P. Treutlein, Th. Anker, M. Albiez, M. Taglieber, K.-P. Marzlin, and M. Oberthaler. Dispersion management for atomic matter waves. *Physical Review Letters*, 91(6):060402, August 2003.

- [192] C.W. Lai, N.Y. Kim, S. Utsunomiya, G. Roumpos, H. Deng, M.D. Fraser, T. Byrnes, P. Recher, N. Kumada, T. Fujisawa, and Y. Yamamoto. Coherent zero state and pi state in an exciton-polariton condensate array. *Nature*, 450(7169):529–32, November 2007.
- [193] N.Y. Kim, K. Kusudo, A. Löffler, S. Höfling, A. Forchel, and Y. Yamamoto. Exciton polariton condensates near the Dirac point in a triangular lattice. *New Journal of Physics*, 15(3):035032, March 2013.
- [194] N. Masumoto, N.Y. Kim, Ti. Byrnes, K. Kusudo, A. Löffler, S. Höfling, A. Forchel, and Y. Yamamoto. Exciton polariton condensates with flat bands in a two-dimensional kagome lattice. *New Journal of Physics*, 14(6):065002, June 2012.
- [195] N.Y. Kim, K. Kusudo, C. Wu, N. Masumoto, A. Löffler, S. Höfling, N. Kumada, L. Worschech, A. Forchel, and Y. Yamamoto. Dynamical d-wave condensation of exciton polaritons in a two dimensional square-lattice potential. *Nature Physics*, 7(9):681–686, June 2011.
- [196] E. Cerda Méndez, D. Krizhanovskii, M. Wouters, R. Bradley, K. Biermann, K. Guda, R. Hey, P. Santos, D. Sarkar, and M. Skolnick. Polariton condensation in dynamic acoustic lattices. *Physical Review Letters*, 105(11):1–4, September 2010.
- [197] E.A. Cerda-Méndez, D.N. Krizhanovskii, K. Biermann, R. Hey, M.S. Skolnick, and P. V. Santos. Wavefunction of polariton condensates in a tunable acoustic lattice. *New Journal of Physics*, 14(7):075011, July 2012.
- [198] R. Idrissi Kaitouni, O. El Daïf, A. Baas, M. Richard, T. Paraiso, P. Lugan, T. Guillet, F. Morier-Genoud, J. Ganière, J. Staehli, V. Savona, and B. Deveaud. Engineering the spatial confinement of exciton polaritons in semiconductors. *Physical Review B*, 74(15):155311, October 2006.
- [199] L. Van Hove. The occurrence of singularities in the elastic frequency distribution of a crystal. *Physical Review*, 89(6):1189–1193, March 1953.
- [200] F. Bassani and G.P. Parravicini. *Electron States and Optical Transitions in Solids*. Pergamon Press, Oxford, 1975.
- [201] R. Saito, A. Gruneis, G.G. Samsonidze, G. Dresselhaus, M.S. Dresselhaus, A. Jorio, L.G. Cancado, M.A. Pimenta, and A.G. Souza Filho. Optical absorption of graphite and single-wall carbon nanotubes. *Applied Physics A: Materials Science & Processing*, 78(8):1099–1105, May 2004.
- [202] G. Li, A. Luican, J.M.B. Lopes dos Santos, A.H. Castro Neto, A. Reina, J. Kong, and E.Y. Andrei. Observation of Van Hove singularities in twisted graphene layers. *Nature Physics*, 6(2):109–113, November 2009.
- [203] H. Kataura, Y. Kumazawa, Y. Maniwa, I. Umezu, S. Suzuki, Y. Ohtsuka, and Y. Achiba. Optical properties of single-wall carbon nanotubes. *Synthetic Metals*, 103(1-3):2555–2558, June 1999.

- [204] K. G. Lagoudakis, B. Pietka, M. Wouters, R. André, and B. Deveaud-Plédran. Coherent Oscillations in an Exciton-Polariton Josephson Junction. *Physical Review Letters*, 105(12):120403, September 2010.
- [205] B.D. Josephson. Possible new effects in superconductive tunnelling. *Physics Letters*, 1(7):251–253, July 1962.
- [206] F.S. Cataliotti, S. Burger, C. Fort, P. Maddaloni, F. Minardi, A. Trombettoni, A. Smerzi, and M. Inguscio. Josephson junction arrays with Bose-Einstein condensates. *Science*, 293(5531):843–6, August 2001.
- [207] S. Raghavan, a. Smerzi, S. Fantoni, and S. Shenoy. Coherent oscillations between two weakly coupled Bose-Einstein condensates: Josephson effects, π oscillations, and macroscopic quantum self-trapping. *Physical Review A*, 59(1):620–633, January 1999.
- [208] S. Backhaus, S. Pereverzev, and R.W. Simmonds. Discovery of a metastable π -state in a superfluid ^3He weak link. *Nature*, pages 687–690, 1998.
- [209] T. Iizuka and de Sterke C.M. Corrections to coupled mode theory for deep gratings. *Physical review. E*, 61(4 Pt B):4491–9, April 2000.
- [210] D. Gerace and I. Carusotto. Analog Hawking radiation from an acoustic black hole in a flowing polariton superfluid. *Physical Review B*, 86(14):144505, October 2012.
- [211] H. Flayac, D.D. Solnyshkov, and G. Malpuech. Bloch oscillations of an exciton-polariton Bose-Einstein condensate. *Physical Review B*, 83(4):045412, January 2011.
- [212] C. Zener. A theory of the electrical breakdown of solid dielectrics. *Proceedings of the Royal Society A: Mathematical, Physical and Engineering Sciences*, 145(855):523–529, July 1934.
- [213] T. Hartmann, F. Keck, H.J. Korsch, and S. Mossmann. Dynamics of Bloch oscillations. *New Journal of Physics*, 6:2–2, January 2004.
- [214] M. Gluck, A.R. Kolovsky, and H.J. Korsch. Wannier Stark resonances in optical and semiconductor superlattices. *Physics reports*, 366:103–182, 2002.
- [215] P. Voisin, J. Bleuse, C. Bouche, S. Gaillard, C. Alibert, and A. Regreny. Observation of the Wannier Stark Quantization in a Semiconductor Superlattice. *Physical Review Letters*, 61(14):1639–1642, October 1988.
- [216] S.R. Wilkinson, C.F. Bharucha, K.W. Madison, Q. Niu, and M.G. Raizen. Observation of atomic Wannier Stark ladders in an accelerating optical potential. *Physical review letters*, 76(24):4512–4515, June 1996.
- [217] R. Sapienza, P. Costantino, D. Wiersma, M. Ghulinyan, C. Oton, and L. Pavesi. Optical analogue of electronic Bloch oscillations. *Physical Review Letters*, 91(26):263902, December 2003.

- [218] J.O. Estevez, J. Arriaga, A. Mendez-Blas, E. Reyes-Ayona, J. Escorcia, and V. Agarwal. Demonstration of photon Bloch oscillations and Wannier Stark ladders in dual periodical multilayer structures based on porous silicon. *Nanoscale research letters*, 7(1):413, January 2012.
- [219] K. Leo, P.H. Bolivar, F. Brüggemann, R. Schwedler, and K. Köhler. Observation of Bloch oscillations in a semiconductor superlattice. *Solid State Communications*, 84(10):943–946, December 1992.
- [220] M. Gustavsson, E. Haller, M. Mark, J. Danzl, G. Rojas-Kopeinig, and H.-C. Nägerl. Control of interaction-induced dephasing of Bloch oscillations. *Physical Review Letters*, 100(8):080404, February 2008.
- [221] Ben Dahan M., E. Peik, J. Reichel, Y. Castin, and C. Salomon. Bloch oscillations of atoms in an optical potential. *Physical review letters*, 76(24):4508–4511, June 1996.
- [222] R. Morandotti, U. Peschel, J. Aitchison, H. Eisenberg, and Y. Silberberg. Experimental observation of linear and nonlinear optical Bloch oscillations. *Physical Review Letters*, 83(23):4756–4759, December 1999.
- [223] T. Pertsch, P. Dannberg, W. Elfle, A. Bräuer, and F. Lederer. Optical Bloch oscillations in temperature tuned waveguide arrays. *Physical Review Letters*, 83(23):4752–4755, December 1999.
- [224] A. Kavokin, G. Malpuech, A Di Carlo, P. Lugli, and F. Rossi. Photonic Bloch oscillations in laterally confined Bragg mirrors. *Physical Review B*, 61(7):4413–4416, 2000.
- [225] D. Shechtman, I. Blech, D. Gratias, and J. Cahn. Metallic phase with long-range orientational order and no translational symmetry. *Physical Review Letters*, 53(20):1951–1953, November 1984.
- [226] Dov Levine and Paul Steinhardt. Quasicrystals: A New Class of Ordered Structures. *Physical Review Letters*, 53(26):2477–2480, December 1984.
- [227] E. Maciá. Exploiting aperiodic designs in nanophotonic devices. *Reports on progress in physics. Physical Society*, 75(3):036502, March 2012.
- [228] Z.V Vardeny, A. Nahata, and A. Agrawal. Optics of photonic quasicrystals. *Nature Photonics*, 7, 2013.
- [229] E. Maciá. The role of aperiodic order in science and technology. *Reports on Progress in Physics*, 69(2):397–441, February 2006.
- [230] W. Steurer and D. Sutter-Widmer. Photonic and phononic quasicrystals. *Journal of Physics D: Applied Physics*, 40(13):R229–R247, July 2007.
- [231] J. Luck. Cantor spectra and scaling of gap widths in deterministic aperiodic systems. *Physical Review B*, 39(9):5834–5849, March 1989.

- [232] W. Gellerman, M. Kohmoto, B. Sutherland, and P.C. Taylor. Localization of light waves in Fibonacci dielectric multilayers. *Physical Review Letters*, 72(5):633–636, 1994.
- [233] M. Kohmoto and B. Sutherland. Critical wavefunction and a Cantorset spectrum of a one dimensional quasicrystal model. *Physical Review B*, 35(3), 1987.
- [234] J. Hendrickson, B.C. Richards, J. Sweet, G. Khitrova, A.N. Poddubny, E.L. Ivchenko, M. Wegener, and H.M. Gibbs. Excitonic polaritons in Fibonacci quasicrystals. *Optics express*, 16(20):15382–7, September 2008.
- [235] M. Ghulinyan, C. Oton, L. Dal Negro, L. Pavesi, R. Sapienza, M. Colocci, and D. Wiersma. Light-pulse propagation in Fibonacci quasicrystals. *Physical Review B*, 71(9):094204, March 2005.
- [236] M. Gardner. Mathematical Games. *Scientific American*, 236(1):110–221, January 1977.
- [237] J. Bellissard, A. Bovier, and J.-M. Ghez. Mathematical physics spectral properties of a tight binding Hamiltonian with period doubling potential. *Communications in Mathematical Physics*, 399:379–399, 1991.
- [238] B. Simon. Almost periodic Schrodinger operators : A review. *Advances in Applied Mathematics*, 490:463–490, 1982.
- [239] D.S. Wiersma, R. Sapienza, S. Mujumdar, M. Colocci, M. Ghulinyan, and L. Pavesi. Optics of nanostructured dielectrics. *Journal of Optics A: Pure and Applied Optics*, 7(2):S190–S197, February 2005.
- [240] R. Lifshitz and S. Mandel. Observation of log-periodic oscillations in the quantum dynamics of electrons on the one dimensional Fibonacci quasicrystal. *Philosophical Magazine*, 91(19-21):2792–2800, July 2011.
- [241] E. Akkermans and E. Gurevich. Spontaneous emission from a fractal vacuum. (4):1–5, 2012.
- [242] K. Nozaki and T. Baba. Quasiperiodic photonic crystal microcavity lasers. *Applied Physics Letters*, 84(24):4875, 2004.
- [243] A. Gopinath, S.V. Boriskina, S. Yerci, R. Li, and L. Dal Negro. Enhancement of the 1.54 μm Er³⁺ emission from quasiperiodic plasmonic arrays. *Applied Physics Letters*, 96(7):071113, 2010.
- [244] S.Y. Lee, J.J. Amsden, S.V. Boriskina, A. Gopinath, A. Mitropolous, D.L. Kaplan, F.G. Omenetto, and L. Dal Negro. Spatial and spectral detection of protein monolayers with deterministic aperiodic arrays of metal nanoparticles. *Proceedings of the National Academy of Sciences of the United States of America*, 107(27):12086–90, July 2010.
- [245] R. Merlin, K. Bajema, and R. Clarke. Quasiperiodic gas-alas heterostructures. *Physical Review Letters*, 55(17):1768–1770, 1985.

- [246] T. Hattori and N. Tsurumachi. Photonic dispersion relation in a one-dimensional quasicrystal. *Physical Review . . .*, 50(6):4220–4223, 1994.
- [247] L. Dal Negro, C. Oton, Z. Gaburro, L. Pavesi, P. Johnson, A. Lagendijk, R. Righini, M. Colocci, and D. Wiersma. Light transport through the band-edge states of Fibonacci quasicrystals. *Physical Review Letters*, 90(5):055501, February 2003.
- [248] A. Gopinath, S.V. Boriskina, N.N. Feng, B.M. Reinhard, and L. Dal Negro. Photonic plasmonic scattering resonances in deterministic aperiodic structures. *Nano letters*, 8(8):2423–31, August 2008.
- [249] E. Akkermans. Statistical Mechanics and Quantum Fields on Fractals. *arXiv preprint arXiv:1210.6763*, (924):1–21, 2012.
- [250] P. Ribeiro, M. Haque, and A. Lazarides. Strongly interacting bosons in multichromatic potentials supporting mobility edges: Localization, quasicondensation, and expansion dynamics. *Physical Review A*, 87(4):043635, April 2013.
- [251] J. Vidal, D. Mouhanna, and T. Giamarchi. Correlated fermions in a one dimensional quasiperiodic potential. *Physical Review Letters*, 83(19):3908–3911, November 1999.
- [252] J. Vidal, D. Mouhanna, and T. Giamarchi. Interacting fermions in self similar potentials. *Physical Review B*, 65(1):014201, November 2001.
- [253] A. Michelson and E. Morley. On the relative motion of the Earth and the luminiferous Ether. *American Journal of Science*, pages 33–345, 1887.
- [254] T. Young. Physics, experiments and calculation relative to optical. *Philosophical Transactions of the Royal Society of London*, 94, 1804.
- [255] A. Perot and Ch. Fabry. Théorie et applications d’une nouvelle méthode de spectroscopie interférentielle. *Annales de Chimie et de Physique*, 16, 1899.
- [256] G.P. Thomson. *The wave mechanics of free electrons*. 1930.
- [257] P.R. Berman. *Atom Interferometry*. Academic Press, 1997.
- [258] M. Arndt, A. Ekers, W. Von Klitzing, and H. Ulbricht. Focus on modern frontiers of matter wave optics and interferometry. *New Journal of Physics*, 14(12):125006, December 2012.
- [259] P. Hariharan. *Optical Interferometry*. Academic Press, 2003.
- [260] F. Pereira and A. Landragin. Getting the measure of atom interferometry. *Physics World*, 2007.
- [261] J.D. Monnier. Optical interferometry in astronomy. *Reports on Progress in Physics*, 66(789), 2003.
- [262] P.R. Griffiths and J.A. de Haseth. Fourier Transform Infrared Spectrometry. 391(7):2379–2380, May 2008.

- [263] B.J. Luff, J.S. Wilkinson, J. Piehler, U. Hollenbach, J. Ingenhoff, and N. Fabricius. Integrated optical Mach-Zehnder biosensor. *Journal of Lightwave Technology*, 16(4):583–592, April 1998.
- [264] C. Santori, D. Fattal, J. Vuković, G.S. Solomon, and Y. Yamamoto. Indistinguishable photons from a single-photon device. *Nature*, 419:594–597, 2002.
- [265] V. Giovannetti, S. Lloyd, and L. Maccone. Quantum-enhanced measurements: Beating the standard quantum limit. *Science*, 306, 2004.
- [266] Y. Vlasov, M. O’Boyle, H.F. Hamann, and S.J. McNab. Active control of slow light on a chip with photonic crystal waveguides. *Nature*, 438(7064):65–9, November 2005.
- [267] D. Bonneau, E. Engin, K. Ohira, N. Suzuki, H. Yoshida, N. Iizuka, M. Ezaki, C.M. Natarajan, M.G. Tanner, R.H. Hadfield, S.N. Dorenbos, V. Zwiller, J.L. O’Brien, and M.G. Thompson. Quantum interference and manipulation of entanglement in silicon wire waveguide quantum circuits. *New Journal of Physics*, 14(4):045003, April 2012.
- [268] D. M. Szymanski, B. D. Jones, M. S. Skolnick, A. M. Fox, D. O’Brien, T. F. Krauss, and J. S. Roberts. Ultrafast alloptical switching in AlGaAs photonic crystal waveguide interferometers. *Applied Physics Letters*, 95(14):141108, October 2009.
- [269] K. Asakawa, Y. Sugimoto, Y. Watanabe, and Et Al. Photonic crystal and quantum dot technologies for alloptical switch and logic device. *New Journal of Physics*, 8(9):208–208, September 2006.
- [270] D. Pacifici, H. Lezec, and H.A. Atwater. Alloptical modulation by plasmonic excitation of CdSe quantum dots. *Nature Photonics*, 1(7):402–406, July 2007.
- [271] E. Camargo, H. Chong, and R. De La Rue. 2D Photonic crystal thermo-optic switch based on AlGaAs/GaAs epitaxial structure. *Optics express*, 12(4):588–92, February 2004.
- [272] I. Glesk, P.J. Bock, P. Cheben, J.H. Schmid, J. Lapointe, and S. Janz. All-optical switching using nonlinear subwavelength Mach-Zehnder on silicon. *Optics express*, 19(15):14031–9, July 2011.
- [273] E. Bocquillon, V. Freulon, J.-M. Berroir, P. Degiovanni, B. Plaçais, A. Cavanna, Y. Jin, and G. Fève. Coherence and indistinguishability of single electrons emitted by independent sources. *Science*, 339(6123):1054–7, March 2013.
- [274] M.R. Andrews, C.G. Townsend, H.-J. Miesner, D.S. Durfee, D.M. Kurn, and W. Ketterle. Observation of interference between two Bose condensates. *Science*, 275(5300):637–641, January 1997.
- [275] I. Bloch, T.W. Hansch, and T. Esslinger. Measurement of the spatial coherence of a trapped Bose gas at the phase transition. *Nature*, 403(6766):166–70, January 2000.

- [276] R.J. Sewell, J. Dingjan, F. Baumgärtner, I. Llorente-García, S. Eriksson, E.A. Hinds, G. Lewis, P. Srinivasan, Z. Moktadir, C.O. Gollasch, and M. Kraft. Atom chip for BEC interferometry. *Journal of Physics B: Atomic, Molecular and Optical Physics*, 43(5):051003, March 2010.
- [277] T. Schumm, S. Hofferberth, L. M. Andersson, S. Wildermuth, S. Groth, I. Bar-Joseph, J. Schmiedmayer, and P. Krüger. Matter-wave interferometry in a double well on an atom chip. *Nature Physics*, 1(1):57–62, September 2005.
- [278] H. Flayac, D.D. Solnyshkov, I.A. Shelykh, and G. Malpuech. Transmutation of Skyrmions to Half-Solitons driven by the nonlinear optical spin Hall effect. *Physical review letters*, pages 2–6, 2013.
- [279] B. Ineichen and R. Muller. Measurement of three-dimensional temperature fields by heterodyne holographic interferometry. *International Journal of Energetic Materials and Chemical Propulsion*, 3(1-6):271–284, 1994.
- [280] M. Tinto and S.V. Dhurandhar. Time-delay interferometry. *Living Reviews in Relativity*, 8, 2005.
- [281] E. Andersson and S. Barnett. Bell-state analyzer with channeled atomic particles. *Physical Review A*, 62(5):052311, October 2000.
- [282] R. Folman, P. Kruger, J. Schmiedmayer, J. Denschlag, and C. Henkel. Microscopic atom optics: From wires to an atom chip. *Advanced in atomic, molecular, and optical physics*, Vol. 48, 48:263–356, 2002.
- [283] M. Reck, A. Zeilinger, H.J. Bernstein, and P. Bertani. Experimental realization of any discrete unitary operator. *Physical Review Letters*, 73(1), 1994.
- [284] L. O’Faolain, D.M. Beggs, T.P. White, T. Kampfrath, K. Kuipers, and T.F. Krauss. Compact Optical Switches and Modulators Based on Dispersion Engineered Photonic Crystals. *IEEE Photonics Journal*, 2(3):404–414, June 2010.
- [285] A.H. Safavi-Naeini, T.P. Mayer Alegre, J. Chan, M. Eichenfield, M. Winger, Q. Lin, J.T. Hill, D.E. Chang, and O. Painter. Electromagnetically induced transparency and slow light with optomechanics. *Nature*, 472(7341):69–73, April 2011.
- [286] E.L. Wooten and K.M. Kissa. A review of lithium niobate modulators for fiber-optic communications systems. *IEEE Journal of Selected Topics in Quantum Electronics*, 6(1):69–82, 2000.
- [287] D.N. Christodoulides, I.C. Khoo, G.J. Salamo, G.I. Stegeman, and E.W. Van Stryland. Nonlinear refraction and absorption: mechanisms and magnitudes. *Advances in Optics and Photonics*, 2(1):60, January 2010.
- [288] F. Wang, Xi. Wang, H. Zhou, Q. Zhou, Yi. Hao, Xi. Jiang, M. Wang, and J. Yang. Fano-resonance-based Mach-Zehnder optical switch employing dual-bus coupled ring resonator as two-beam interferometer. *Optics express*, 17(9):7708–16, April 2009.

- [289] S. Weng, L. Pei, R. Zhao, J. Yang, and Yi. Wang. Optical devices based on multilayer optical waveguide. *Frontiers of Optoelectronics*, 6(2):146–152, April 2013.
- [290] G. Sagnac. Luminous ether demonstrated by the effect of relative wind of ether in a uniform rotation of an interferometer. *Comptes Rendus Hebdomadaires des Séances de l'Académie des Sciences*, 157:708–710, 1913.
- [291] P. Cristofolini, A. Dreismann, G. Christmann, G. Franchetti, N.G. Berloff, P. Tsotsis, Z. Hatzopoulos, P.G. Savvidis, and J.J. Baumberg. Optical superfluid phase transitions and trapping of polariton condensates. *Physical Review Letters*, 110(18):186403, May 2013.
- [292] P. Murzyn, A.Z. Garcia-Deniz, D.O. Kundys, A.M. Fox, J.-P.R. Wells, D.M. Whittaker, M.S. Skolnick, T.F. Krauss, and J.S. Roberts. Control of the nonlinear carrier response time of AlGaAs photonic crystal waveguides by sample design. *Applied Physics Letters*, 88(14):141104, 2006.
- [293] S. Azzini, D. Gerace, M. Galli, I. Sagnes, R. Braive, A. Lemaître, J. Bloch, and D. Bajoni. Ultralow threshold polariton lasing in photonic crystal cavities. *Applied Physics Letters*, 99(11):111106, September 2011.
- [294] M. Liscidini, D. Gerace, D. Sanvitto, and D. Bajoni. Guided Bloch surface wave polaritons. *Applied Physics Letters*, 98(12):121118, March 2011.
- [295] C. Leyder, M. Romanelli, J. Ph. Karr, E. Giacobino, T.C.H. Liew, M.M. Glazov, A.V. Kavokin, G. Malpuech, and A. Bramati. Observation of the optical spin Hall effect. *Nature Physics*, 3:628–631, 2007.
- [296] S. Murakami, N. Nagaosa, and S.-C. Zhang. Dissipationless quantum spin current at room temperature. *Science*, 301(5638):1348–51, September 2003.
- [297] M.V. Berry. The quantum phase, five years after. *Geometric phases in physics*, 1989.
- [298] M. V. Berry. Quantal phase factors accompanying adiabatic changes. *Proceedings of the Royal Society A: Mathematical, Physical and Engineering Sciences*, 392(1802):45–57, March 1984.
- [299] I. Shelykh, G. Pavlovic, D. Solnyshkov, and G. Malpuech. Proposal for a mesoscopic optical Berry-phase interferometer. *Physical Review Letters*, 102(4):046407, January 2009.
- [300] M. König, H. Buhmann, L.W. Molenkamp, T. Hughes, C.-X. Liu, X.-L. Qi, and S.-C. Zhang. The quantum spin Hall effect: Theory and experiment. *Journal of the Physical Society of Japan*, 77(3):031007, March 2008.
- [301] E. Reyes-Gomez, N. Porras-Montenegro, C.A. Perdomo-Leiva, H.S. Brandi, and L.E. Oliveira. Electron Lande' g factor in GaAs- (Ga,Al)As quantum wells under applied magnetic fields: Effects of Dresselhaus spin splitting. *Journal of Applied Physics*, 104(2):023704, 2008.

- [302] S. Filipp. *New Aspects of the Quantum Geometric Phase*. PhD thesis, Technischen Universität Wien, 2006.
- [303] C Sturm, D Tanese, H. S. Nguyen, H. Flayac, E. Galopin, A. Lemaître, I. Sagnes, D. Solnyshkov, A. Amo, G. Malpuech, and J. Bloch. Giant phase modulation in a Mach Zehnder exciton polariton interferometer. *arXiv:1303.1649*, page 18, March 2013.
- [304] Italo Guarnieri and Giorgio Mantica. Multifractal Energy Spectra and Their Dynamical Implications. 73(25):3379–3382, 1994.
- [305] Shuji Abe and Hisashi Hiramoto. Fractal dynamics of electron wave packets in one-dimensional quasiperiodic systems. *Physical Review A*, 36(11):5349–5352, December 1987.
- [306] T. Jacqmin, I. Carusotto, I. Sagnes, M. Abbarchi, D. Solnyshkov, G. Malpuech, E. Galopin, A. Lemaître, J. Bloch, and A. Amo. Direct observation of Dirac cones and a flatband in a honeycomb lattice for polaritons. *submitted to Physical Review Letters (arXiv:1310.8105)*, 2013.